DIMENSIONALLY REDUCED MODELING AND GRADIENT-BASED DESIGN OF MICROCHANNEL COOLING NETWORKS

BY

MARCUS HWAI YIK TAN

DISSERTATION

Submitted in partial fulfillment of the requirements
for the degree of Doctor of Philosophy in Theoretical and Applied Mechanics
with a concentration in Computational Science and Engineering
in the Graduate College of the
University of Illinois at Urbana-Champaign, 2017

Urbana, Illinois

Doctoral Committee:

Professor Anthony M. Jacobi, Chair
Professor Philippe H. Geubelle, Director of Research
Professor Carlos Armando Duarte
Professor Scott R. White

Abstract

Microvascular composites constitute a novel class of biomemetic materials with the ability to perform multiple functions such as dynamic tuning of electromagnetic properties, self-healing and thermal management depending on the fluid circulated in the embedded microchannels. Recent breakthroughs in the vaporization of sacrificial component (VaSC) manufacturing technique have allowed for the creation of intricate microchannel networks and large scale production of these composites. As the design of these networks is key to the performance of the composites and designer's intuition is insufficient to achieve optimal performance, the development of "automated" design tools is of paramount importance.

The primary goal of this work is to fulfill that need in the specific application of thermal management. To that end, we develop three ingredients: dimensionally reduced thermal and hydraulic models, a numerical solver and a shape optimization scheme. Another goal of this project is to verify and validate the dimensionally reduced models against a commercial computational fluid dynamics software package and experiments. The final goal is to apply the design tool to various 2D and 3D problems.

In the dimensionally reduced thermal model, the microchannels are collapsed into lines/curves to simplify mesh generation and their thermal impacts are added to the heat equation. Two versions of the thermal model are considered: (i) a linear model that does not involve radiative heat exchange or linearizes the Stefan-Boltzman radiation equation and (ii) a nonlinear model that incorporates the original radiation equation. The hydraulic model uses the Hagen-Poiseuille law to describe the flow rates and pressure drops in the microchannel networks.

To capture the gradient discontinuity in the temperature field due to the microchannels, we employ the interface-enriched generalized finite element method (IGFEM) as the numerical solver, which greatly simplifies mesh generation by allowing for the use of meshes that do not conform to the microchannel network. While previous IGFEM works are based on polynomial enrichment functions, we demonstrate the flexibility of the IGFEM by developing non-uniform rational B-splines (NURBS) enrichment functions for branched network of curved microchannels.

We then develop a method to address the convergence issue due to the singularity associated with the thermal model in 3D and combine that method with polynomial IGFEM. The thermal fields obtained from the resulting modified IGFEM agree with those of the significantly more complex and costly ANSYS FLUENT conjugate heat transfer simulations.

The final ingredient involves the development of analytical IGFEM-based shape sensitivity analyses for both linear and nonlinear models. These analyses allow the design tool to efficiently exploit existing powerful gradient-based optimization algorithms, especially for large number of design parameters.

We then apply the gradient-based shape optimization scheme to solve a diverse range of problems, which demonstrate two key advantages of the scheme due to the use of stationary nonconforming meshes by (i) eliminating the cumulative mesh generation cost and (ii) avoiding severe mesh distortion issues as the microchannel geometry evolves during the optimization process. The first problem involves parallel networks of microchannels for 2D microvascular composite battery cooling panels. Using a differentiable alternative to the maximum temperature (the p-norm of the temperature field) of a cooling panel as an objective function, we obtain optimized designs superior to the reference designs in terms of cooling performance. We also extensively validate the IGFEM solutions associated with the designs against ANSYS FLUENT simulations and experiments.

We further extend the uses of the tool to include multi-objective optimization, pressure drop as objective function, channel diameters as design parameters and localized heat sources. In the multi-objective optimization, the Pareto fronts of the maximum temperatures and the pressure drops across the networks are generated using the normalized normal constraint method.

Next, we apply the optimization scheme to design blockage-tolerant cooling networks embedded in 2D PDMS panels. In this novel application, a minmax problem that minimizes the worst case of a set of predetermined blockage scenarios is formulated and converted to a simpler single-objective optimization problem. In the worst blockage scenario, the designs optimized in this manner exhibit substantial reduction of cooling performance loss compared with designs optimized without considering blockages, with greater reduction as the redundancy of the network decreases. The designs are also validated against experiments.

Another novel application of the optimization scheme is related to the design of 2D microvascular panels for nanosatellite. In this application, the sensitivity analysis based on the nonlinear thermal model is used since the nonlinear effect of radiation cannot be neglected. Taking advantage of the optimization tool, two formulations are proposed to satisfy the design constraints. We perform extensive benchmarking of the results obtained from the dimensionally reduced models against those from ANSYS FLUENT, and provide analytical estimates of the thermal performance of optimized designs.

In the final application, we design multiple parallel microchannels embedded in 3D microvascular panels using the modified-IGFEM-based optimization scheme. Due to the importance of the straight microchannel design, we propose a semi-analytical model of the maximum temperature in a panel with multiple straight channels.

To my parents,
for their unconditional love and support.

Acknowledgments

This dissertation would not be possible without the guidance and support of my PhD advisor, Prof. Philippe H. Geubelle, who is also the current head of the Aerospace Engineering department. I am greatly indebted to him for providing interesting, challenging and quality projects that allowed me to build crucial skills for my future career. Specifically, I am very thankful for the valuable opportunity to develop and implement new scientific computing methods, and use these tools for real-world applications. Furthermore, I thank him for encouraging internships in the industry, where I learnt a great deal about applying advanced finite element methods to solve industrial problems. At the same time, I highly value the presentation and communication skills that he diligently emphasized and shared with his students. I also appreciate his effort in securing funding and computer resources that were essential for this work.

This work would have limited applications if not for Prof. Scott R. White, the leader of the Autonomous Materials Systems (AMS) group at this university. I am grateful to him for facilitating extensive collaboration with the experimental microvascular composite subgroup, whose work underpins the applications in this dissertation. I would also like to thank him for his valuable inputs at the subgroup and AMS group meetings, and for serving in my preliminary and final exam committees. Another faculty whose feedback at the meetings I would like to acknowledge is Prof. Nancy Sottos.

On the numerical aspect of my work, I greatly appreciate the discussion with Prof. Carlos Armando Duarte of the Civil and Environmental Engineering department as I dealt with the formidable issue of numerical singularity. In addition, I am grateful for his service as a member of my preliminary and final exam committees.

I thank Prof. Anthony M. Jacobi, the current head of the Mechanical Science and Engineering department, for chairing my preliminary and final exam committees. I would also like to thank him in his capacity as an instructor of the Convective Heat Transfer course (ME521), in which I learnt important fundamentals that helped me to understand the physics of the problems in this work.

This dissertation is a highly collaborative effort involving a number of individuals from whom I received help. I am very grateful to my former colleague Dr. Ahmad R. Najafi for sharing with me his knowledge of interface-enriched generalized finite element method (IGFEM) and IGFEM-based sensitivity analysis. His pioneering work in IGFEM-based sensitivity analysis for interface problems has laid the foundation for the IGFEM-based sensitivity analysis in this work. I enjoyed

the insightful discourse that we often had in the lab.

Of equal importance to this dissertation is the work done by my collaborator Stephen J. Pety of the AMS microvascular composite subgroup. I am greatly thankful to him for performing all experiments in this work and for developing new experimental techniques that made the validation studies possible. In addition, I acknowledge the ANSYS FLUENT simulations he carried out in the validation exercise associated with microvascular composite battery cooling panels. His fondness of the software application brought my attention to its power as an alternative validation tool, which I subsequently utilized extensively in this dissertation. I would also like to express my gratitude to him for demonstrating the use of SolidWorks to generate models for the microvascular composite panels.

I acknowledge other former members of Prof. Geubelle's group for their help. In particular, I thank Dr. Masoud Safdari (former postdoc) for initiating the use of non-uniform rational B-splines (NURBS) as IGFEM enrichment functions and Yuxuan Lu (former undergraduate assistant) for helping to generalize the 3D IGFEM code to handle input files from the finite element software package Abaqus.

Pertaining to the nanosatellite microvascular composite panel radiator project, I thank Dr. Ghosh for introducing this design problem to us and my collaborator in this project, Devin Bunce. I am grateful to them for helping to identify the design requirements of the radiators.

I am fortunate and grateful to have received funding throughout this project. Until the end of 2012, this work was supported by the Air Force Office of Scientific Research Multidisciplinary University Research Initiative (Grant No. FA9550-09-1-0686). The later part was funded by the DEMS Program of the NSF Division of Civil, Mechanical and Manufacturing Innovation (Award No. 1436720).

I acknowledge the use of computing resources at the University of Illinois, Urbana-Champaign. The SSM machines and Taub Campus Cluster computing nodes owned by Prof. Geubelle's group were used to implement and run the tools developed in this work. At the Beckman Visualization Lab, SolidWorks and ANSYS were used for the validation studies.

Throughout my journey in graduate school, I owe a great deal to my parents (Siew Kheng Tan and Swee Khiam Tan), especially my mother, for their moral and financial support. They deserve my utmost gratitude for sharing the joy of my successes, encouraging me to persevere in the face of setbacks and motivating me to complete this PhD study. I also gratefully acknowledge my brothers and friends who made this long and challenging journey much less draining and much more enjoyable.

Table of Contents

1 Introduction

1.1 Multifunctional materials

The relentless quest for greater efficiency in material use has been predominantly achieved through weight saving of monofunctional materials. More recently, multifunctional materials have been extensively developed to further improve efficiency. Most multifunctional materials are composites, which are defined as artificial materials consisting of at least two physically or chemically distinct components and possessing properties that are different from any of the components in isolation [1]. Hence we use the terms multifunctional material and multifunction composite interchangeably. Material properties and material structures are two primary ways through which the material achieves the intended functions. Thus, multifunctional materials are sometimes referred to as multifunctional structures [2]. Important target functions of multifunctional materials are structural support, healing, sensing, actuation, morphing, vibration damaping, energy storage, signal transmission and reception, electromagnetic shielding, electrical conduction and thermal management [2, 3, 4].

A large number of multifunctional composites exist today, with the majority of them appearing in the 21st century [2, 3, 5]. One of the earliest multifunctional composites that have allowed for large scale manufacturing is probably the piezeoelectric fiber composite developed in the early 1990s [6]. Electroceramic fiber composite plies together with porous interlaminar electrodes were inserted between standard composite plies, thus enabling large scale sensing and actuation, and load-bearing. During the early 2000s, development of multifunctional composites were accelerated by the Defense Advanced Research Project Agency (DARPA) through the introduction of the research program Synthetic Multifunctional Materials [5]. Under the program, much work was done to develop structure-power materials for unmanned air vehicle (UAV) systems, motivated by the prediction that reducing the weight by a given percentage would result in a significantly greater increase in the aircraft range compared with that resulting from the same percentage increase in propulsion energy [7]. Three concepts were explored: combining battery and structure, allowing the structure to be consumed as fuel, and enabling the structure to morph with fuel consumption [7]. The first concept still survives today and has been applied to structure-battery panels used for electric vehicles [3]. The third concept, though not successful for structure-power materials, has

continued to inspire research in multifunctional shape morphing structures such as morphing wings that could adapt to the flight conditions for optimal performance (see [3] or [8] and the references therein).

Just as moprhing structures mimic the shape-changing ability of nature, so too autonomous multifunctional composites imitate the ability of biological systems to perform multiple functions including healing without manual intervention [2, 3]. A precursor of autonomous material is the microcapsuled-based self-healing composite developed in 2001 [9]. The authors achieved autonomic self-healing by embedding microcapsules in a catalyst-infused epoxy matrix. They have shown that when the microcapsules are softer than the matrix, crack preferentially propagates through the microcapsules, breaking them and releasing the healing agent.

The limited number of healing cycles of a microcapsule-based composite motivated the development of the next generation of self-healing materials: microvascular materials, a new class of materials containing intricately embedded microchannel networks. A landmark work that has inspired microvascular composite manufacturing techniques is the direct-write assembly method for embedding 3D microvascular network in a material using fugitive ink [10]. First, a network scaffold was created by robotic deposition of a fugitive ink, which had the right viscoelastic properties to simultaneously allow flow during deposition and shape retention after deposition. Next, the scaffold was infused with an epoxy resin, left to cure at ambient temperature and then heated to evacuate the scaffold. This method was subsequently used to make self-healing materials, which consisted of epoxy coatings embedded with catalyst deposited on subtrates containing microvascular networks supplied with healing agents [11].

While the direct-write assembly method is capable of creating complex networks of interconnected microchannels, it is not suited for large-scale production. A breakthrough manufacturing technique referred to as the vaporization of sacrificial components (VaSC) was recently proposed to overcome this limitation while still maintaining the ability to create intricate vascular networks [12]. First, catalyst-impregnated polylactide (PLA) sacrificial fibers were woven into the composite preform, which was then infused with epoxy resin via vaccum-assisted resin transfer molding. During the subsequent curing process, the sacrifical fibers remained solid since the curing temperature was kept below the PLA depolymerization temperature. After trimming the cured sample to expose the ends of the sacrifical fibers, the sample was then heated above the depolymerization temperature but below the epoxy degradation temperature to vaporize the PLA material, leaving hollow microchannels in the composites. Lastly, the microchannels were filled with various fluids to endow the resulting composite with multiple functions such as dynamic tuning of electromagnetic signature and electrical conductivity, in situ chemical reaction as well as thermal management. Recently, the versatility of VaSc has been demonstrated with multidimensional ("0D–3D") sacrificial templates, thus opening the door to much more complex embedded structures than that

available to sacrificial fiber-based VaSc [13]. Furthermore, VaSc has also been shown to be feasible for a shape memory alloy-polymer composite that forms the innermost layer of a highly complex structural skin for future hypersonic vehicles [14].

1.2 Active cooling with microchannels

Among the multiple functions of microvascular composites, this dissertation focuses on the highly successful function of thermal management. The use of microchannels for active cooling was first proposed for high-heat-flux electronics cooling by Tuckerman and Pease [15], who observed that the conductive resistance between the chip to the substrate and the resistance associated with the heat absorption by the flowing coolant (inverse of the product of mass flow rate and coolant heat capacity) can be made "very small by obvious means" ([15], p. 126), while the convective thermal resistance between the channel wall and the coolant (inverse of the product of the convection coefficient and the total surface area of the channels) becomes dominant. Since the convection coefficient is inversely proportional to the diameter for fully-developed heat flow, the convective thermal resistance can be decreased significantly by reducing the diameter of the channels. In another study on microchannel heat sinks [16], Phillips suggested applications to diode laser arrays and high-energy-laser mirrors.

While early microchannel designs for electronics cooling consisted of many straight parallel running channels, more complicated designs with few inlets and outlets such as serpentine and bifurcating/treelike have been applied to fuel cell cooling plates [17]. Bifurcating designs have been shown to alleviate the increase in pressure drop due to small diameters and fewer inlets and outlets. It has also been carefully demonstrated that, despite the laminar nature of the flow, bents and branching of the more complicated designs enhance heat transfer not just by increasing mixing but by also creating vortices [18]. To date, a large number of designs for cooling plates used for fuel cells and comparable applications such as battery stacks and concentrated solar panels have been developed [19, 20, 21, 22, 23]. It is also observed that some of these designs are similar to the designs of channels embedded in the bipolar plates of a polymer electrolyte membrane fuel cell for uniformly distributing reactants on and effectively removing reaction products from the membrane electrode assembly [24, 25, 26].

Around the same time as rising interest in cooling plate research, experiments on microvascular polymer fins at flow rates of 10 ml/min or less have demonstrated one to two orders of magnitude increase in effective heat transfer coefficient compared with the no flow case [27]. The heat transfer enhancement was also studied by other authors experimentally [28] and computationally [29, 30, 31]. Careful experiments have also shown the highly beneficial effect of active cooling

on the retention of microvascular composite structural properties in high temperature environment [32]. For example, an actively cooled microvascular polymer matrix composite with microchannels closed to the surface has been shown to successfully retain 90% of its flexural stiffness even after prolong exposure to an environment at the epoxy degradation temperature 325 °C.

Very recently, the use of additive manufacturing or more specifically direct metal laser sintering (DMLS) to create microchannels for gas turbine cooling has been demonstrated [33, 34]. Unlike microvascular composites, the turbine parts manufactured with DMLS are not expected to be used for load bearing since the sintering process produces materials with "uncertain" properties ([33], p.051006-1). In [33], Snyder et al. experimentally studied the effect of build direction on the resulting cross-sectional shape, pressure loss and heat transfer in multiple straight channels embedded in coupons. Such effect is of interest because the flow is expected to operate in the turbulent regime, where the details of the channel walls would significantly affect the flow characteristics. In [34], Kirsch and Thole experimentally and computationally investigated the pressure drop and heat transfer characteristics of undulating channels with different wavelengths.

1.3 Design approaches for microchannels

Since the coolant is expected to convect much of the heat away in an active-cooling application, the design of the microchannels is critical to their thermal performance. Designer's intuition, though important, is often not sufficient to obtain the targeted performance. Hence a number of approaches have been developed: (i) resistance-based analytical modeling, (ii) size optimization, (iii) constructal theory, (iv) parametric study, (v) shape optimization and (vi) topology optimization. Each of these approaches requires different degree of designer's intuition but ultimately aims to optimize single or multiple objective functions subject to constraints.

Analytical modeling was first used to design straight microchannels for high-power electronics cooling [15]. The study chose the sum of the wall-coolant convective thermal resistance and the resistance associated with the absorption of heat by the coolant as the objective function, and the channel width, channel spacing and channel aspect ratios as the design parameters. This approach was extended in [35] to cover various flow conditions, channel surface roughness and other effects.

While the analytical approach provides very useful physical insights, a more accurate approach is size optimization, which appears to have been only applied to straight channels in microelectronics cooling [36, 37, 38]. In [36], Ryu et al. combined the finite voume method and the steepest descent algorithm to minimize the thermal resistance of straight channels using the channel width, fin thickness and inlet to oulet width ratio as design parameters. The gradient/sensitivity of the objective function with respect to the design parameters was calculated with the finite difference

method. Also using similar objective function and design parameters, Husain and Kim employed the finite volume method and surrogate methods for optimization of the channels [38]. The methods first sampled design points using design of experiment techniques. Then, surrogate models such as a response surface were constructed and an optimization algorithm used to search for an optimal point.

An approach called constructal theory was also proposed [39, 40, 41]. According to the theory, "for a flow system to persist in time, it must evolve in such a way that it provides easier and easier access to the currents that flow through it." ([41], p. 041301-1) The theory was applied to produce a treelike design of high conductivity network paths or flow channels for cooling with the lowest global resistance.

Given a base design, parametric study can also be carried out. For example, in [30], the effect of the wavelength of an undulating channel on the heat transfer performance of actively cooled microvascular composite was investigated. However, this approach quickly becomes intractable as the number of design parameters increases. To overcome this limitation, one possible approach is to use shape optimization techniques. While shape optimization has been applied extensively to structural design, its application to microchannel design for active cooling remains limited. To the best of our knowledge, the only shape optimization study prior to the works presented in this dissertation is that of a spiral channel in battery cooling panels [20]. In the study, the corner coordinates of the spiral were the design parameters and either pressure drop, average temperature or standard deviation of the temperature field was used as an objective function. The commercial software ANSYS FLUENT was chosen as the solver and the sequential quadratic program was selected as the optimization algorithm, with the finite difference method used to calcuate the sensitivity of the objective function.

Another design approach that requires an optimization algorithm is topology optimization. Originally invented for and widely used in structural optimization, the approach discretizes space into smaller elements, each of which has a density that is also a design parameter [42]. The density determines the type of material occupying an element. For example, in structural optimization, a value close to zero represents a void while a value approaching unity represents a solid. The material property of interest is then related to the density field using various interpolation functions such as the Simple Isotropic Material with Penalization (SIMP) [43]. An early work related to heat conduction is a finite volumed-based method developed to optimize the distribution of a material with respect to a "heat" cost function analogous to compliance in structural mechanics [44]. Topology optimization for conjugate heat transfer design problems have also been developed [45, 46]. Since the fluid or solid region is not known a priori, the same governing equations need to be applied to the entire domain. The approach that has been adopted is to use the Navier-Stokes equation and Darcy's law with zero and maximum inverse permeability for the fluid and solid

regions, respectively. The energy equation also needs to be modified to interpolate between the fluid and solid. Recently, a variant based on the level set method has been developed specifically for those problems [47]. The work used an unusual objective function "assumed to represent the heat exchange between the fluid and solid domains" ([47], p. 881) and a regularization scheme to control the geometric complexity. In a level set-based topology optimization, the level set function replaces the density and an evolution equation for the level set function is the optimization algorithm.

A method inspired by truss-based topology optimization adapted for flow networks [48] has been developed for microvascular composite design problems [29, 49, 50]. The method creates a network template consisting of lattice points in space and potential channel paths connecting them. Associated with each channel is a set of discrete diameters selected as design parameters. These studies used genetic algorithm to search for optimal solutions. Although very interesting networks were produced, excessive details such as very short channels and jaggedness substantially reduced their manufacturability.

1.4 Objectives

This dissertation has three main objectives. The first objective is to develop a design tool for microchannel cooling networks based on three ingredients: (i) dimensionally reduced models, (ii) a solver and (iii) a shape optimization scheme. Another objective is to verify and validate the results of the models against those obtained from a commercial computational fluid dynamics software package and experiments. The final goal is to apply the tool to various 2D and 3D problems.

We begin in Chapter 2 by describing the dimensionally reduced thermal and hydraulic models, followed by carefully investigation of the assumptions underlying these models. Chapter 3 presents an overview of the previously developed polynomial interface-enriched generalized finite element (IGFEM) scheme and the newly developed 2D non-uniform rational B-spline (NURBS)-based IGFEM. The latter is adapted from the article "A NURBS-based interface-enriched generalized finite element scheme for the thermal analysis and design of microvascular composites" published in *Computer Methods for Applied Mechanics and Engineering* [51]. In Chapter 4, we describe a modified IGFEM method that addresses the numerical issues due to the singularity associated with the dimensionally reduced thermal model in 3D. The chapter is adapted from a recently submitted article. To exploit gradient-based algorithms for shape optimizations in later chapters, we develop in Chapter 5 sensitivity analyses based on the IGFEM, and the linear and nonlinear thermal models.

The next five chapters present applications of the design tool. In Chapter 6, the optimization scheme is applied to design parallel microchannels embedded in microvascular composite panels

intended for battery cooling. The chapter, which is based on the article "Gradient-based design of actively cooled microvascular composite panels" published in the *International Journal of Heat and Mass Transfer* [52], also shows extensive validation of the dimensionally reduced models against ANSYS FLUENT simulations and experiments performed by Stephen J. Pety. Chapter 7 describes multi-objective optimization and other uses of the 2D computational design tool. A novel application of the optimization scheme to the design of 2D blockage-tolerant microchannel networks embedded in PDMS panels is presented in Chapter 8, with further validation of the numerical models. We also present in Chapter 9 another application of the tool: the optimization of nanosatellite microvascular composite radiator panels, where the nonlinear effect of radiation must be considered. Optimization problems are formulated to satisfy the design constraints associated with the radiator coolant and solved with the 2D design tool. The solution of the dimensionally reduced models is extensively benchmarked against that of ANSYS FLUENT. Analytical estimates of the coolant temperatures associated with designs satisfying certain assumptions are derived to facilitate the design process. The last application described in Chapter 10 concerns the design of 3D actively cooled microvascular composites using the modified-IGFEM-based optimization scheme. The chapter also presents a semi-analytical model of the maximum temperatures of 3D panels containing parallel straight channels.

In the concluding chapter (Chapter 11), we summarize the contributions of this dissertation and provide recommendations for future research. An overview of the implementation is presented in the appendix. In this dissertation, all experimental results and the ANSYS FLUENT simulations in Chapter 6 are the work of Stephen J. Pety.

2 Thermal and Fluid Models

2.1 Dimensionally reduced thermal model

A number of approaches can be used to model the temperature distribution of an actively cooled microvascular composite. The most detailed (conjugate heat transfer) approach consists in modeling the solid with the heat conduction equation and the coolant with the Navier-Stokes and energy equations [17, 20, 21, 36, 53, 54], which together constitute a set of coupled nonlinear equations. Another approach is to circumvent the Navier-Stokes equations by assuming a parabolic velocity profile in the fluid [30, 31, 55]. However, both approaches model the microchannels with non-zero diameters, thus increasing the model complexity and the mesh generation burden. For brevity, let the term "channel" hereafter implies "microchannel".

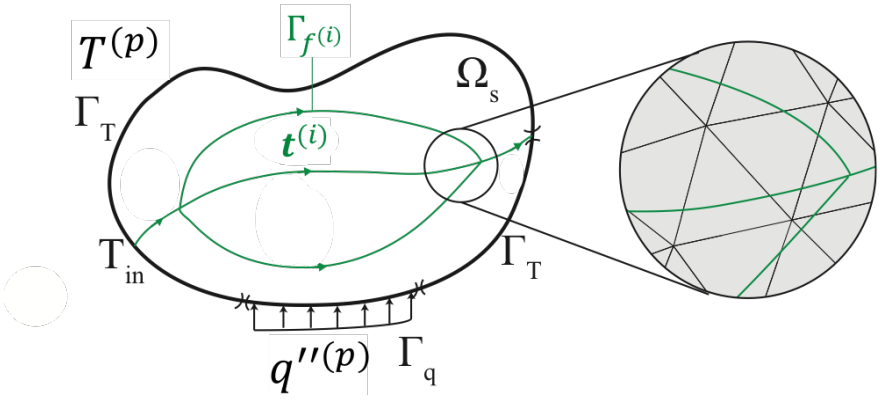

Figure 2.1 – Schematic of the geometry and boundary conditions of the model problem. The domain consists of a solid Ω_s and a network of channels Γ_f. The direction of the flow at each point of Γ_f is specified by the unit tangent vector $\hat{\boldsymbol{t}}$. The inlet temperature T_{in} is prescribed. The inset schematically shows a portion of an unstructured non-conforming mesh.

The abovementioned modeling approaches can quickly become prohibitively expensive for composites embedded with complex networks made possible with advanced manufacturing techniques described in Section 1.1, especially in optimization studies, where the evaluation of large number of channel configurations is involved. Hence, a simpler approach that reduces the channels to line

sources/sinks $\Gamma_{f^{(i)}}$, $i = 1, 2, ...$ as shown in Figure 2.1 and has been used elsewhere [29, 50, 56] is adopted throughout this work. This simplification is possible because the channel diameters are typically much smaller than the distance between them and other characteristic dimensions of the problem.

For the description of the model, consider a channel with cross-sectional area A, axial velocity u and average velocity u_{ave}. Let T_m be the mixed-mean fluid temperature, defined as $\int uT\mathrm{d}A/(Au_{\text{ave}})$ [57]. Further, let s, $\dot{m}$ and c_p respectively denote the parametric coordinate along the channel in the flow direction, the mass flow rate and the specific heat capacity of the fluid at constant pressure. By performing a simple energy balance over an infinitesimal portion of a channel, we obtain the following expression for the heat flow rate per unit length of the channel [57]:

$$q' = \dot{m}c_p \frac{\mathrm{d}T_m}{\mathrm{d}s}. \tag{2.1}$$

2.2 Governing equation

Let Ω denote the domain, which consists of a solid part Ω_s and a network of n_{ch} channels. Denote the curve representing channel i, the parametric representation of the curve, its unit tangent vector in the flow direction and the channel flow rate by $\Gamma_f^{(i)}$, $\boldsymbol{x}^{(i)}(s)$, $\boldsymbol{t}^{(i)}$ and $\dot{m}^{(i)}$, respectively. Given the thermal conductivity tensor $\boldsymbol{\kappa}$ of the solid Ω_s, a distributed heat source $f(\boldsymbol{x})$, the convection coefficient $\tilde{h}$, the emissivity ϵ and an ambient temperature T_∞, and denoting the Stefan-Boltzmann constant by σ_B, the following heat equation holds in Ω:

$$\nabla \cdot (\boldsymbol{\kappa}\nabla T) + f(\boldsymbol{x}) = \sum_{i=1}^{n_{ch}} \delta^{(i)}(\boldsymbol{x})\gamma^{(i)}\boldsymbol{t}^{(i)} \cdot \nabla T + \tilde{h}(T - T_\infty) + \epsilon\sigma_B(T^4 - T_\infty^4), \tag{2.2}$$

where $\gamma^{(i)} = \dot{m}^{(i)}c_p$ and $\delta^{(i)}(\boldsymbol{x}) = \int_{\Gamma_f^{(i)}} \delta(\boldsymbol{x} - \boldsymbol{x}^{(i)}(s))\mathrm{d}s$ is the line Dirac delta function associated with channel i. With the exception of Chapters 8 and 9, other chapters linearize the radiation term and include the resulting coefficient in $\tilde{h}$, or assume that $\tilde{h} = \epsilon = 0$. This simplification will be made clear in the relevant chapters. In the 3D case, the last two terms of (2.2) appear as boundary conditions.

2.3 Assumptions

A key assumption behind (2.2) is that the mixed-mean fluid temperature T_m is approximately equal to the channel wall temperature T_w. However, a temperature gradient must exist in the cross-

sectional plane for fluid-solid heat exchange to occur. Hence, in reality, $T_w \neq T_m$ with $T_w > T_m$ when the fluid is heated and $T_w < T_m$ otherwise. The difference $\Delta T_{wm} = T_w - T_m$ is an estimate of the error resulting from the assumption and can be quantified as follows: using (2.1), the definition of the Nusselt number $\mathrm{Nu} = \tilde{h}_o D_h/\kappa_f$ and $q' = 4A\tilde{h}_o \Delta T_{wm}/D_h$, where $\tilde{h}_o, D_h, \kappa_f$ respectively denote the convection coefficient between the wall and the fluid, the hydraulic diameter of the channel and conductivity of the fluid, one can show that

$$\Delta T_{wm} = \frac{D_h^2 \dot{m} c_p}{4A\kappa_f \mathrm{Nu}} \frac{\mathrm{d}T_m}{\mathrm{d}s}. \tag{2.3}$$

Given a net heat transfer Q into a channel of length L_{ch}, $\mathrm{d}T_m/\mathrm{d}s \approx Q/(\dot{m} c_p L_{ch})$. Hence

$$\Delta T_{wm} \approx \frac{D_h^2}{4A} \frac{Q}{\kappa_f \mathrm{Nu} L_{ch}}. \tag{2.4}$$

This derivation assumes that Nu is constant, which is true only when the heat flow is fully developed. When a significant portion of the heat flow is not fully developed, we expect the estimate for ΔT_{wm} to hold for an average Nu higher than that of a fully developed heat flow since Nu decreases away from the entrance. This observation implies that the right hand side of (2.4) would provide a larger estimate of ΔT_{wm} when the heat flow is not fully developed throughout the channels or equivalently, when the flow rate is small. We also note that, when the flow rate is very small, another source of error due to neglecting axial conduction along the fluid, which is described later, becomes more dominant than the error due to ΔT_{wm}, and therefore ΔT_{wm} is no longer a good estimate of the total error due to the thermal model.

Let us determine the typical hydrodynamic and thermal entrance lengths for our system. A typical channel considered in this work has a square cross section with an average width of 0.75 mm. A commonly used coolant is an aqueous ethylene glycol with density $\rho = 1065\,\mathrm{kg/m^3}$, kinematic viscosity $\nu = 3\times10^{-6}\,\mathrm{m^2/s}$, thermal conductivity $\kappa_f = 0.419\,\mathrm{W/mK}$ and heat capacity $c_p = 3494\,\mathrm{J/kgK}$. The coolant is pumped through the channels with a characteristic total flow rate of 28.2 ml/min. Hence the corresponding Reynolds and Prandtl numbers are $\mathrm{Re} = u_{ave} D_h/\nu = 200$ and $\mathrm{Pr} = \nu\rho c_p/\kappa_f = 26.6$, respectively. This yields approximate hydrodynamic and thermal entrance lengths of $0.05\mathrm{Re}D_h = 0.0075$ m and $0.05\mathrm{RePr}D_h = 0.2$ m, respectively, compared with a typical total channel length $L_{ch} = 1.5$ m. For a fully developed flow in a square tube with constant axial wall heat flux and peripheral wall temperature boundary conditions, $\mathrm{Nu} \approx 3.61$ [58]. Depending on the application, the boundary conditions of a composite, the flow rate and the channel design, the amount of heat absorbed by the embedded channel network Q can vary significantly. For this calculation, we use $Q = 15\,\mathrm{W}$, which is the total heat supplied to a battery cooling panel in Chapter 6. Hence (2.4) gives $\Delta T_{wm} \approx 1.7\,^\circ\mathrm{C}$.

An additional assumption underlying the model is that the viscous heating of the fluid is negligible, which ensures that the temperature rise in the channels due to this mechanism is insignificant. The temperature rise can be estimated as $\Delta T = \Delta P/(\rho c_p)$ [59], where ΔP is the pressure drop across the channel. Taking the density and heat capacity from the previous section and the high end pressure drop $\Delta P = 100\,\mathrm{kPa}$, $\Delta T = 0.027\,^\circ\mathrm{C}$, justifying the assumption.

Since the channels are collapsed into lines and curves, the thermal conductivity of the coolant does not affect the solution to (2.2). This can also be deduced from the weak form of that equation presented in the next section, where any finite jump in the conductivity along a channel does not contribute to the diffusive term since the channel has zero measure in the integral. Hence we need to assume that the axial advection is much larger than the axial conduction so that the axial conduction can be neglected. This assumption is valid because the Péclet number $\mathrm{Pe} := \mathrm{RePr} = 5,320 \gg 1$ [60] using the Reynolds and Prandtl numbers from the preceding paragraphs.

2.4 Weak form of governing equation

Let the domain boundary $\partial\Omega$ shown in Figure 2.1 be divided into two parts, Γ_T and Γ_q, where Dirichlet and Neumann boundary conditions are specified, respectively. Denoting the prescribed heat flux as $q''^{(p)}$, the weak form of (2.2) is: Find the temperature field T satisfying the Dirichlet boundary condition $T_{|\Gamma_T} = T^{(p)}$ such that $\forall v \in \mathbb{V}$,

$$\begin{aligned} 0 = &- \int_{\Omega_s} \nabla v \cdot \boldsymbol{\kappa} \nabla T \mathrm{d}\Omega - \int_{\Omega_s} v(\tilde{h}T + \epsilon\sigma_B T^4)\mathrm{d}\Omega - \sum_{i=1}^{n_{ch}} \int_{\Gamma_f^{(i)}} v\gamma^{(i)} \boldsymbol{t}^{(i)} \cdot \nabla T \mathrm{d}\Gamma \\ &+ \int_{\Omega_s} vf\mathrm{d}\Omega + + \int_{\Omega_s} v(\tilde{h}T_\infty + \epsilon\sigma_B T_\infty^4)\mathrm{d}\Omega + \int_{\Gamma_q} vq''^{(p)}\mathrm{d}\Gamma, \end{aligned} \tag{2.5}$$

where $\mathbb{V}$ is the space of weight functions.

In some of the chapters, the following linearized version of (2.5) is used:

$$\begin{aligned} 0 = &- \int_{\Omega_s} \nabla v \cdot \boldsymbol{\kappa} \nabla T \mathrm{d}\Omega - \int_{\Omega_s} v\tilde{h}_{eff} T \mathrm{d}\Omega - \sum_{i=1}^{n_{ch}} \int_{\Gamma_f^{(i)}} v\gamma^{(i)} \boldsymbol{t}^{(i)} \cdot \nabla T \mathrm{d}\Gamma \\ &+ \int_{\Omega_s} vf\mathrm{d}\Omega + \int_{\Omega_s} v\tilde{h}_{eff} T_\infty \mathrm{d}\Omega + \int_{\Gamma_q} vq''^{(p)}\mathrm{d}\Gamma, \end{aligned} \tag{2.6}$$

where $\tilde{h}_{eff} = \tilde{h} + 4\epsilon\sigma_B T_\infty^3$. The second term of the effective convection coefficient $\tilde{h}_{eff}$ results from the linearization of the radiation term about T_∞.

In the 3D case, since Dirichlet and Neumann boundary conditions are applied to surfaces, we rewrite Γ_T and Γ_q as S_T and S_q, respectively. In addition, let S_h be the additional part of the

domain boundary where the surface convection and/or radiation is applied. Then (2.5) and (2.6) continue to apply with Ω_s of the terms involving $\tilde{h}, \epsilon, \tilde{h}_{eff}$ replaced with S_h.

The presence of the second convective term in (2.5) or (2.6) implies that the associated stiffness matrix is not symmetric. With the exception of Chapter 3, when multiple channels with branching are present in the domain, we observe numerical oscillations in the solution similar to those that appear when modeling the channels with non-zero diameters [31] at the flow rates of interest in this study. To remove the oscillations, we employ the streamline upwind/Petrov-Galerkin (SUPG) method [61], which modifies the weight function while maintaining equivalence with the original weak form. Throughout this work, we assume an isotropic conductivity, i.e, $\boldsymbol{\kappa} = \kappa \boldsymbol{I}$. In 2D, this assumption is valid as only balanced plain-weave composites [62] or PDMS material is considered. In 3D, κ can be thought of as an average value when a composite is used. Denoting the total number of the nodes in the mesh by n_n and the shape function associated with node j by N_j, we replace v in (2.5) by

$$w = v + \sum_{i=1}^{n_{ch}} \tau_e^{(i)} u_{\text{ave}}^{(i)} \boldsymbol{t}^{(i)} \cdot \nabla v, \tag{2.7}$$

where

$$\tau_e^{(i)} = \frac{h_e^{(i)}}{2u_{\text{ave}}^{(i)}} \left[\coth\left(\frac{u_{\text{ave}}^{(i)} h_e^{(i)} \rho c_p}{2\kappa} \right) - \frac{2\kappa}{u_{\text{ave}}^{(i)} h_e^{(i)} \rho c_p} \right], \tag{2.8}$$

and

$$\frac{2}{h_e^{(i)}} = \sum_{j=1}^{n_n} |\boldsymbol{t^{(i)}} \cdot \nabla_x N_j|. \tag{2.9}$$

Note that the streamline upwind contribution (second term of (2.7)) is understood to vanish at the boundaries [61]. Because linear triangular elements are used in this work, $\nabla_{xx} v = 0$, which implies that $\nabla_x w = \nabla_x v$. Since our simplified model depends explicitly on $\dot{m}^{(i)}$ rather than $u_{\text{ave}}^{(i)}$, and $u_{\text{ave}}^{(i)}$ arbitrarily depends on the assumed cross-sectional area, we eliminate $u_{\text{ave}}^{(i)}$ from (2.8) by assuming $u_{\text{ave}}^{(i)} h_e^{(i)} \rho c_p / \kappa \gg 1$. This assumption is valid because $u_{\text{ave}}^{(i)} h_e^{(i)} \rho c_p / \kappa \gg 1$ throughout this work. Therefore, (2.8) simplifies to $\tau_e^{(i)} = h_e^{(i)} / (2u_{\text{ave}}^{(i)})$ and (2.7) becomes

$$w = v + \sum_{i=1}^{n_{ch}} \frac{h_e^{(i)}}{2} \boldsymbol{t^{(i)}} \cdot \nabla_x v. \tag{2.10}$$

2.5 Hydraulic model

Unless stated otherwise, the hydraulic model based on Hagen-Poiseuille relation is used throughout this dissertation. To obtain the mass flow rate in channel i, $\dot{m}^{(i)}$, we first solve for the pressure P_j

at each end point or node of the channel network using a system of hydraulics equations given by

$$[G]\{P\} = \{S\}. \tag{2.11}$$

The equations are assembled from the following relation between the nodal pressures, P_j, P_k of channel i and the contribution of its flow rate $S_j^{(i)}, S_k^{(i)}$ to the nodes j, k [63]:

$$g^{(i)} \begin{bmatrix} 1 & -1 \\ -1 & 1 \end{bmatrix} \begin{Bmatrix} P_j \\ P_k \end{Bmatrix} = \begin{Bmatrix} S_j^{(i)} \\ S_k^{(i)} \end{Bmatrix}, \tag{2.12}$$

where $g^{(i)}$ is the conductance of channel i.

For a square cross section of width D or a circular cross section of diameter D, a channel length L_{ch} and a uniform kinematic viscosity of ν, the conductance is given by [64]

$$g = \frac{CD^4}{\nu L_{ch}}. \tag{2.13}$$

For square cross sections, $C = 1/28.46$ while for circular cross sections, $C = \pi/128 \approx 1/40.74$ [64, 58]. For rectangular cross sections with height a and width b ($b \geq a$), we have [64]

$$g = \frac{1}{\nu L_{ch}} \frac{a^3 b}{4} \left[\frac{1}{3} - \frac{64a}{\pi^5 b} \tanh\left(\frac{\pi b}{2a} \right) \right]. \tag{2.14}$$

It is worth noting that (2.14) agrees closely with the expression developed by Shah and London [58]. If P_j and P_k are the pressures at the two nodes of channel i, then $\dot{m}^{(i)} = g^{(i)}|P_j - P_k|$.

Two key assumptions are made to decouple the thermal and hydraulic models: (i) c_p is constant (equal to the average over the expected operating temperature range of the coolant) and (ii) ν is uniform. These assumptions allow the flow rates to be calculated first using (2.11), followed by the solution of (2.5) for the temperature field. Lastly, ν is evaluated at an average temperature and the pressure drop scaled according to the ratio of the new to old viscosity values. While the average temperature is taken to be that of the panel in Chapters 6 and 7, the average temperature along the network are used in Chapters 8 and 9 to obtain more accurate pressure drops.

3 2D NURBS-Based IGFEM

This chapter is adapted from the article published in *Computer Methods for Applied Mechanics and Engineering* [51], titled "A NURBS-based interface-enriched generalized finite element scheme for the thermal analysis and design of microvascular composites" by M. H. Y. Tan, M. Safdari, A. R. Najafi and P. H. Geubelle.

3.1 Introduction

In many of the applications of microvascular composites (thermal, structural, electromagnetic), the presence of the microchannels results in fields with discontinuous gradients in the material. Hence, the computational analysis and design of microvascular composites require a method capable of capturing weakly discontinuous solution fields, i.e., solutions that are C^0-continuous with finite gradient jumps.

Standard finite element methods (SFEM) can be applied to solve such problems provided a mesh that conforms to the geometry of the microchannels is used. Solutions obtained with non-conforming meshes have poor accuracy as the error bound of the a priori error estimate shows that a weakly discontinuous solution field converges suboptimally. With a conforming mesh, the C^0 continuity of the FEM solution across the element boundaries naturally captures the discontinuity of the gradient fields and optimal convergence can be recovered. However, generating a conforming mesh with good-quality elements can be a challenging process especially for complex networks of embedded microchannels. For transient [65] or optimization [29, 50] problems, reconstructing a conforming mesh at each iteration can be a formidable and inefficient process, and might violate energy conservation [66].

The generalized FEM (GFEM) [67] and extended FEM (XFEM) [68] are widely-used and successful methods to handle weakly or strongly discontinuous fields with non-conforming meshes. These methods are based on the partition of unity method, in which enrichment functions that closely approximate the true solution are multiplied by the partition of unity functions to construct the local enrichment functions [69, 70, 71]. The GFEM/XFEM has been developed to handle strongly discontinuous problems such as crack propagation [66, 68, 72] and weakly discontinuous problems such as material interface [73] and intense thermal loading due to shockwave [65].

Closely related to this work is a GFEM developed to capture weakly discontinuous temperature field in the thermal analysis, design and optimization of microvascular materials [29, 50, 56].

Recently, an interface-enriched generalized FEM (IGFEM) that has some advantages over GFEM has been proposed [74, 75]. In the method, enrichment nodes are introduced at the intersections between the non-conforming elements and the interface, and associated with them are the enrichment functions. This approach allows local enrichment functions to be constructed without using partition of unity functions. The advantages of this method over GFEM are straightforward application of essential boundary conditions and a lower number of degrees of freedom. However, interfaces are still approximated as line segments in the original IGFEM method.

The aforementioned improvement in manufacturing techniques have allowed the creation of microvascular materials with complex curved microchannels [12, 76]. In this regard, an XFEM that has been developed for curved strong and weak discontinuities [77] could potentially be applied in the analysis of microvascular composites. The approach summarized in [77] describes the interface by a level set function, which is then approximated by standard finite element interpolation.

In this chapter, we adopt a different approach and develop a non-uniform rational B-spline (NURBS)-based IGFEM for triangular linear elements to handle curved microchannels described by NURBS. NURBS include B-splines as a special case. Among the many advantages of using NURBS are their ability to model complicated geometry with high accuracy, the abundance of algorithms and methods for manipulating NURBS, as well as being the standard of Computer Aided Design (CAD) [78, 79].

The use of NURBS enrichment functions is inspired by a series of methods that incorporate NURBS in FEM, including isogeometric analysis [80]. Isogeometric analysis provides a seamless integration with CAD by using NURBS for both the geometrical description of the domain and the construction of the basis functions of the finite element solution. To handle complex geometries, the domain has to be decomposed into patches that conform to the curved boundaries. In addition, one must ensure that the mapping and parameterization in adjoining patch faces are identical in the coarsest mesh and subsequent mesh refinement must also ensure continuity of the solution between the patches [81]. This may be very challenging in the presence of patches with complex geometry. To overcome these issues, the NURBS-enhanced FEM (NEFEM) has been proposed to handle curved boundaries [82]. In that method, curved triangular elements are constructed along curved boundaries and handled with NEFEM while other elements are treated with SFEM. Exact geometrical mapping from a reference element to a curved triangular element is defined using the NURBS description of the curved boundaries. Consistency in the approximation is also ensured by using Cartesian shape functions, i.e., the degree of polynomial interpolation in physical space is the same as the degree of the shape functions. Hence the NEFEM overcomes the geometric inaccuracy in Cartesian FEM and the lack of consistency in p-FEM [82]. However, the method

still requires the generation of a mesh that conforms to the geometry of the curved boundary.

NURBS-based XFEM have also been proposed to represent curved integration subdomains exactly by NURBS [83, 84]. For example, the approach described in [83] represents the integration subdomains with NURBS surfaces. The interfaces are described by level set functions, which are then discretized and approximated by NURBS curves to generate the NURBS surfaces. In addition, this method requires the use of quadratic or higher-order shape functions as linear shape functions cannot ensure the continuity of the displacement field across the interface of deformed elements.

In contrast to NEFEM and the methods described in [77, 83], the NURBS-based IGFEM proposed hereafter uses linear shape functions associated with the original nodes of a non-conforming triangular element and places the enrichment nodes strategically on or near the curved interface, thus reducing the number of new degrees of freedom. Similar to [83], the integration subdomains are represented by NURBS surfaces. However, unlike [77, 83], we use NURBS enrichment functions instead of enrichment functions based on the level set functions. Therefore, a NURBS representation of a curved interface can be used at the outset, obviating the need for approximation of the curved interface. Similar to isogeometrical analysis, the key advantage of using NURBS is that the microchannel geometry can be imported from and exported to CAD programs without loss of geometrical information.

The chapter is organized as follows: we begin by giving a brief overview of IGFEM in Section 3.2. In Section 3.3, we show how NURBS enrichment functions are constructed. We then perform in Section 3.4 a detailed convergence study using the method of manufactured solution for semi-circular microchannels and for branching microchannels. Finally, we apply the NURBS-based IGFEM in Section 3.5 to solve heat transfer problems in actively-cooled microvascular materials with various microchannel geometries.

3.2 IGFEM formulation

In the finite element method, the weak form of the thermal equation (2.5) is solved by approximating $\mathbb{V}$ by a finite-dimensional space. The finite-dimensional space throughout this work is built using the IGFEM developed previously for interface problems, where different regions of the domain contain different materials [74, 75]. While different material properties in interface problems give rise to weak discontinuity (discontinuity in gradient of a solution field) across the interface, the weak discontinuity here arises from the channels.

Let there be n_{on} original nodes in the non-conforming mesh shown in Figure 3.1a with T_i and $N_i(\boldsymbol{x})$ respectively denoting the nodal value and the Lagragian shape function associated with

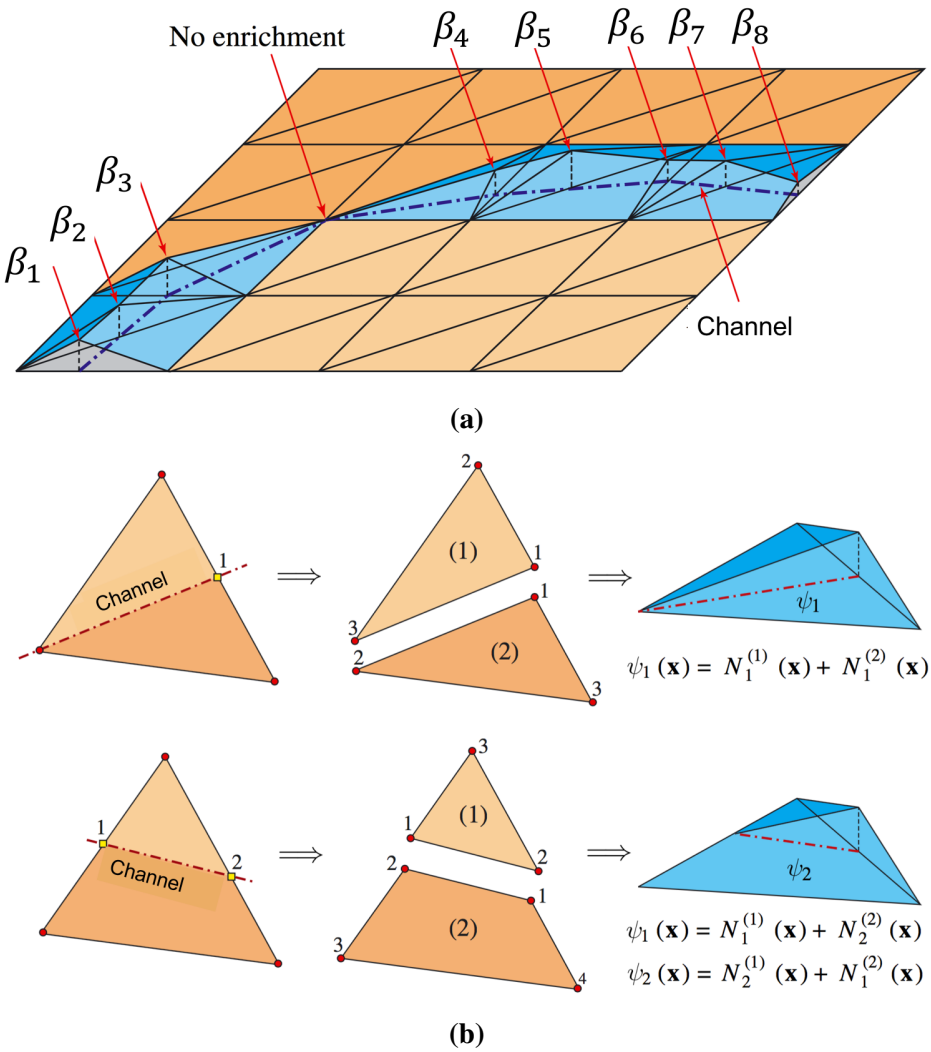

Figure 3.1 – (a) Schematic of a non-conforming mesh used for polynomial IGFEM, and the associated enrichment nodes and functions introduced along the channel. (b) Construction of polynomial enrichment functions in two different scenarios (top and bottom) based on the manner in which the channel crosses a triangular element. Adapted from [74].

node i. In the IGFEM formulation, n_{en} enrichment nodes are added along the channels to yield the following approximation to the temperature field:

$$T^{(h)}(\boldsymbol{x}) = \sum_{i=1}^{n_{on}} T_i N_i(\boldsymbol{x}) + \sum_{j=1}^{n_{en}} \beta_j \psi_j(\boldsymbol{x}) = \begin{Bmatrix} \{N(\boldsymbol{x})\} \\ \{\psi(\boldsymbol{x})\} \end{Bmatrix}' \begin{Bmatrix} \{T\} \\ \{\beta\} \end{Bmatrix}, \tag{3.1}$$

where ψ_j is the enrichment function associated with enrichment node j, β_j is the generalized degree of freedom and $\{\cdot\}'$ denotes the transpose of the vector $\{\cdot\}$. The construction of the polynomial enrichment functions, developed previously in [74], is illustrated in Figure 3.1b.

For simplicity in presenting the nonlinear solution method in Section 3.2.1 and the sensitivity analysis in Chapter 5, we hereafter omit the distinction between original and enrichment degrees of freedom as well as between original shape functions and enrichment functions, and write (3.1) as:

$$T^{(h)}(\boldsymbol{x}) = \{N(\boldsymbol{x})\}'\{T\}. \tag{3.2}$$

From (2.10), the SUPG weight function has the form

$$w^{(h)}(\boldsymbol{x}) = \{W(\boldsymbol{x})\}'\{V\}, \tag{3.3}$$

where

$$\{W\} = \{N\} + \sum_{i=1}^{n_{ch}} \frac{h_e^{(i)}}{2}[B]\{t^{(i)}\}, \tag{3.4}$$

and $[B]$ is the matrix of the spatial derivative of $\{N\}$ with each column corresponding to the derivative with respect to a coordinate. The second term of (3.4) is understood to vanish at element boundaries [61].

Substituting the approximate temperature field (3.1) and weight function into the weak form (2.5), the discretized weak form is given by

$$[K(\{T\})]\{T\} = \{F\}, \tag{3.5}$$

where

$$[K(\{T\})] = \int_{\Omega_s} [B][\kappa][B]'\mathrm{d}\Omega + \int_{\Omega_s} (\tilde{h} + \epsilon\sigma_B T^{(h)3})\{W\}\{N\}'\mathrm{d}\Omega + \sum_{i=1}^{n_{ch}} \int_{\Gamma_f^{(i)}} \{W\}([B]\gamma^{(i)}\{t^{(i)}\})'\mathrm{d}\Gamma, \tag{3.6}$$

and

$$\{F\} = \int_{\Omega_s} \{W\} f \mathrm{d}\Omega + \int_{\Omega_s} \{W\}(\tilde{h}T_\infty + \epsilon\sigma_B T_\infty^4)\mathrm{d}\Omega + \int_{\Gamma_q} \{N\} q''^{(p)}\mathrm{d}\Gamma. \tag{3.7}$$

The expressions of the stiffness matrix $[K(\{T\})]$ and load vector $\{F\}$ for IGFEM can be found in [85]. Section 3.2.1 describes the methods used to solve the system of equations in the general nonlinear case.

Since the focus of this chapter is the development of a NURBS-based IGFEM, the flow rates in the network of channels are imposed with mass conservation satisfied at every branching point. To reflect this, the mass flow rate in channel i is written as $\dot{m}_i$ instead of $\dot{m}^{(i)}$. No SUPG is applied in this chapter since no oscillation is observed for the flow rates of interest.

3.2.1 Solution of nonlinear thermal model

In the nonlinear case, (3.5) is solved using the procedure outlined in Algorithm 1. Unlike nonlinear structural mechanics, no incremental loading is required.

Algorithm 1 Iterative procedure for solving nonlinear equation, where $\|\cdot\|_2$ denotes the 2-norm of a vector and $\{T^{(n)}\}$ indicates the temperature solution at iteration n.

Set termination tolerance ε
Initialize $\{T^{(0)}\}$
$n = 0, d_0 = 1, l_0 = 0$
while $d_n > \varepsilon l_n$ **do**
  Use Newton-Raphson method to obtain $\{T^{(n+1)}\}$
  $l_n = \|\{T^{(n+1)}\}\|_2$
  $d_n = \|\{T^{(n+1)}\} - \{T^{(n)}\}\|_2$
  $n = n + 1$
end while

The Newton-Raphson (NR) method obtains the solution at iteration $n + 1$ by linearizing the system of equations about the solution at iteration n to yield the following equation:

$$[J(\{T^{(n)}\})](\{T^{(n+1)}\} - \{T^{(n)}\}) = \{R(\{T^{(n)}\})\}, \tag{3.8}$$

where

$$J_{ik}(\{T^{(n)}\}) = K_{ik}(\{T^{(n)}\}) + \frac{\partial K_{ij}}{\partial T_k^{(n)}} T_j^{(n)}, \tag{3.9}$$

and

$$\{R(\{T^{(n)}\})\} = \{F\} - [K(\{T^{(n)}\})]\{T^{(n)}\}. \tag{3.10}$$

It is noted that the Jacobian $[J]$ also arises in the sensitivity analysis described in Section 5.3.

As a rough measure of the computational cost associated with Algorithm 1 and the NR method, we compare the time taken to solve the nonlinear thermal equation (2.5) with that needed to solve the linearized thermal equation (2.6), using the 3×3 O_T optimized design and the setup described in Chapter 9. With a termination tolerance $\varepsilon = 10^{-6}$ and a mesh containing 4800 elements, it took approximately 7.5 seconds for 16 iterations to solve the nonlinear equation on a single 2.2 GHz Intel i7 processor. On the other hand, the solution of the linearized thermal equation needed about 5.5 seconds.

The remainer of this chapter assumes convection and radiation are absent. Therefore, the model problem is governed by (2.5) with $\tilde{h} = \epsilon = 0$, leading to $[K(\{T\})] = [K]$ and a linear system of equations.

3.3 NURBS-based IGFEM formulation

Instead of the polynomial enrichment functions adopted previously [74], we develop NURBS enrichment functions in the remainder of this chapter. We begin by briefly introducing NURBS curves and surfaces, covering only the needed concepts and terminologies. The reader is referred to [78, 79, 81] for a detailed explanation of NURBS relevant to this work.

A NURBS curve is defined by

$$\boldsymbol{C}(\xi) = \sum_{i=1}^{n} \boldsymbol{B_i} R_i^p(\xi), \tag{3.11}$$

where $\boldsymbol{B_i}$ is the i-th control point and R_i^p is the degree p rational B-spline basis function associated with the control point. The basis functions R_i^p are defined as

$$R_i^p(\xi) = \frac{N_i^p(\xi) w_i}{\sum_{j=1}^{n} N_j^p(\xi) w_j}, \tag{3.12}$$

where N_i^p are B-spline basis functions, which can be generated by a recursion formula [78, 79, 81]. The shape of the curve can be changed by adjusting the location of the control points and the weights w_i, thus allowing the exact representation of complex geometries that cannot be represented by B-spline curves such as conics. Moreover, the geometry is also controlled by a set of $n + p + 1$ coordinates/knots/break points in parametric space called the knot vector $\boldsymbol{\xi} = \{\xi_1, \xi_2, ..., \xi_{n+p+1}\}$. The knot vector determines the form, support and smoothness of N_i^p. The curve is only defined on the interval $\xi \in [\xi_1, \xi_{n+p+1}]$. In this work, only open knot vectors, which are standard in CAD [79], are considered. In an open knot vector, the first and last knots appear $p + 1$ times.

A NURBS surface is defined analogously by

$$\boldsymbol{S}(\xi, \eta) = \sum_{i=1}^{n} \sum_{j=1}^{m} \boldsymbol{B_{ij}} R_{i,j}^{p,q}(\xi, \eta), \tag{3.13}$$

where

$$R_{i,j}^{p,q}(\xi, \eta) = \frac{N_i^p(\xi) M_j^q(\eta) w_{i,j}}{\sum_{k}^{n} \sum_{l}^{m} N_k^p(\xi) M_l^q(\eta) w_{k,l}}. \tag{3.14}$$

The set of control points $\{\boldsymbol{B_{ij}}\}$ is called the control net and associated with each control point is a weight $w_{i,j}$. The rational basis functions $R_{i,j}^{p,q}$ consist of tensor products of 1D B-spline basis functions $N_i^p(\xi)$ and $M_j^q(\eta)$. Instead of a single knot vector, two knot vectors $\boldsymbol{\xi} = \{\xi_1, \xi_2, ..., \xi_{n+p+1}\}$ and $\boldsymbol{\eta} = \{\eta_1, \eta_2, ..., \eta_{m+q+1}\}$ are needed to define the surface, which is only defined in $[\xi_1, \xi_{n+p+1}] \times [\eta_1, \eta_{m+q+1}]$.

The construction of the NURBS enrichment function consists of four steps:

1. Finding the intersections between the microchannels and the non-conforming elements.
2. Extracting the NURBS representation of a segment of a microchannel in an element.
3. Constructing the NURBS representation of the integration subdomains of a parent element, defined as an element cut by a microchannel.
4. Using some of the rational basis functions of the NURBS representation of the integration subdomains as enrichment functions.

These four steps are summarized next, followed by a description of the integration scheme.

3.3.1 Intersection between the microchannels and the elements

In this work, the non-conforming meshes are made of triangular elements. Due to the many different ways in which a curved microchannel can intersect an element, we restrict our work to cases in which each edge of an element intersects with each microchannel at most once. When this condition is not satisfied, it is an indication that the curvature of the microchannel is likely too high in the region containing the element. In this case, local mesh adaptation such as mesh refinement, mesh reconnection and mesh movement [86] can be carried out until the condition is satisfied. We also assume that at most one branch point appears on the boundary or the interior of an element.

The intersection between the edge of an element and a curved microchannel is found by using a non-linear solver. The search direction is found by the Levenberg–Marquardt algorithm [87]. To drastically reduce the number of iterations required to find the solution as well as ensuring that the non-linear solver does not miss the solution due to a poor initial guess, the curved microchannel is discretized into a series of linear segments to obtain an initial guess close to the true solution (if it exists). The end point of a linear segment closest to the edge is taken as the initial guess. To prevent unnecessary work in finding the intersections when they do not exist, a convex hull tightly containing the NURBS curve and determined by the control points of the NURBS curve can be used [78]. An edge that lies outside of the convex hull is immediately excluded from consideration.

3.3.2 Extraction of NURBS curve segment

Suppose a NURBS curve of degree p with knot vector $\boldsymbol{\xi} = \{\xi_1, \xi_2, ..., \xi_{n+p+1}\}$ intersects an element at $\xi = a \in (\xi_k, \xi_{k+1}]$ and $\xi = b \in (\xi_l, \xi_{l+1}]$ with $b > a$. Using Figure 3.2 as illustration, the NURBS curve is defined by the control points $\boldsymbol{B}_1, ...\boldsymbol{B}_4$ and the knot vector $\boldsymbol{\xi} = \{0, 0, 0, 0.5, 1, 1, 1\}$. Let

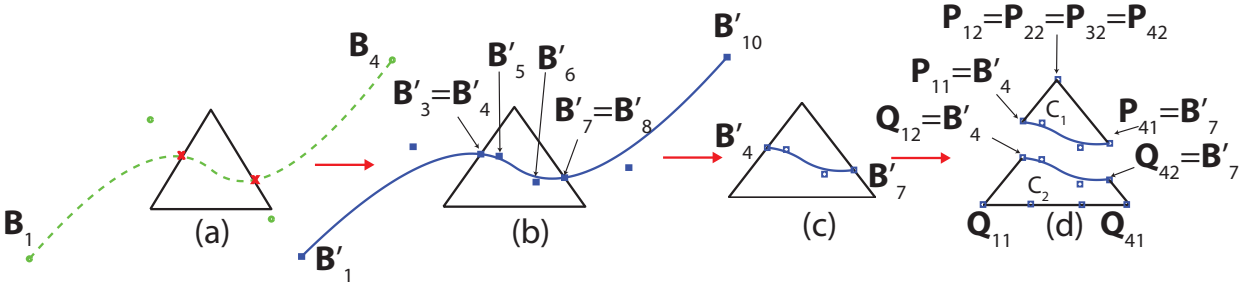

Figure 3.2 – Extraction of a NURBS curve segment and construction of integration subdomains. When there is no branching in the interior of the element, (a) find intersections of a curve with the element edges, (b) perform knot insertions, (c) extract the curve segment and (d) construct the integration subdomains.

us also assume in this illustrative example that the intersections with the element occur at $\xi = 0.39$ and 0.65 on the NURBS curve. The curve segment can be extracted in the following manner:

1. Insert knots at $\xi = a$ and $\xi = b$ using a knot insertion algorithm described in [79, 80] until there are $p + 1$ knots at $\xi = a$ and $\xi = b$ in the resulting knot vector. The knot insertion algorithm adds a control point with every knot insertion and the resulting curve is exactly the same as the original curve with the same smoothness as before. After the multiple knot insertions, the resulting knot vector is $\boldsymbol{\xi'} = \{0, 0, 0, 0.39, 0.39, 0.39, 0.5, 0.65, 0.65, 0.65, 1, 1, 1\}$ and there will be two coincident control points $\boldsymbol{B'}_3, \boldsymbol{B'}_4$ exactly at the intersection corresponding to $\xi = a$ and two other coincident control points $\boldsymbol{B'}_7, \boldsymbol{B'}_8$ at $\xi = b$. Let $i_{\min} = \min(i)$ such that $\xi'_i \geq a$ and $i_{\max} = \max(i)$ such that $\xi'_i \leq b$. In general the pairs of coincident control points are $\boldsymbol{B'}_{i_{\min}-1}, \boldsymbol{B'}_{i_{\min}}$ and $\boldsymbol{B'}_{i_{\max}-p-1}, \boldsymbol{B'}_{i_{\max}-p}$.

2. The curve segment within the element can then be represented exactly by the control points $\boldsymbol{B'}_4$ to $\boldsymbol{B'}_7$ and the knot vector $\overline{\boldsymbol{\xi}} = \{0.39, 0.39, 0.39,$ $0.5, 0.65, 0.65, 0.65\}$. In general, the control points of the extracted curve segment are $\boldsymbol{B'}_i$, $i = i_{\min}, ..., i_{\max} - p - 1$ and the knot vector is $\overline{\boldsymbol{\xi}} = \{\xi'_{i_{\min}}, ..., \xi'_{i_{\max}}\}$

Note that the weights can be extracted in exactly the same fashion as the control points.

3.3.3 Construction of NURBS representation of an integration subdomain

Two general cases need to be handled given the restriction that each edge of an element has at most one intersection with a microchannel. The first case occurs when there is no branching in the parent element as shown in Figure 3.2. To construct the NURBS enrichment function, we need the NURBS representations of the integration subdomains shown in Figure 3.2d. The NURBS

representation of the triangular integration subdomain (C_1) is given by

$$\boldsymbol{S}_{\mathrm{C}_1}(\xi,\eta) = \sum_{i=1}^{n}\sum_{j=1}^{2} \boldsymbol{P_{ij}} \overline{R}^{p,1}_{i,j}(\xi,\eta), \tag{3.15}$$

with $n = 4$, $p = 2$, $\boldsymbol{P}_{11} = \boldsymbol{B'}_4$, $\boldsymbol{P}_{21} = \boldsymbol{B'}_5$, $\boldsymbol{P}_{31} = \boldsymbol{B'}_6$, $\boldsymbol{P}_{41} = \boldsymbol{B'}_7$ and the other control points coinciding with the apex of C_1. The NURBS representation of the quadrilateral integration subdomain (C_2) is given by

$$\boldsymbol{S}_{C_2}(\xi,\eta) = \sum_{i=1}^{n}\sum_{j=1}^{2} \boldsymbol{Q_{ij}} \tilde{R}^{p,1}_{i,j}(\xi,\eta), \tag{3.16}$$

with $n = 4$, $p = 2$, $\boldsymbol{Q}_{12} = \boldsymbol{B'}_4$, $\boldsymbol{Q}_{22} = \boldsymbol{B'}_5$, $\boldsymbol{Q}_{32} = \boldsymbol{B'}_6$, $\boldsymbol{Q}_{42} = \boldsymbol{B'}_7$ and the other control points are equally spaced along the bottom edge. For both (3.15) and (3.16), the knot vector $\overline{\boldsymbol{\xi}}$ is the knot vector of the extracted curve segment, i.e., $\overline{\boldsymbol{\xi}} = \{0.39, 0.39, 0.39, 0.5, 0.65, 0.65, 0.65\}$ in this example and the other knot vector is $\overline{\boldsymbol{\eta}} = \{0, 0, 1, 1\}$. It is worth noting that as long as each microchannel does not intersect an element edge more than once, the method described here can be extended readily to the case of multiple microchannels in an element by splitting the parent element into more than two integration subdomains with some of the integration subdomains having more than one curved boundaries.

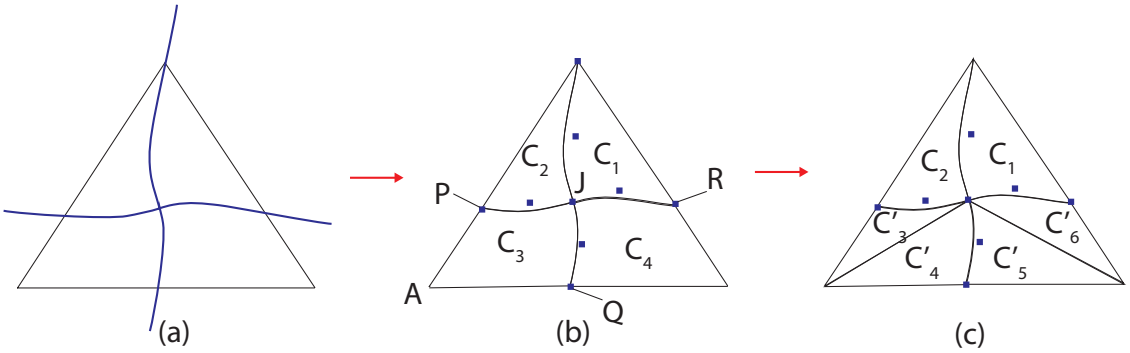

Figure 3.3 – When there is branching in the interior of the element, (a) intersections are determined, (b) curve segments are extracted, (c) quadrilateral subdomains are triangulated.

The second case involves a branching point in the interior of the non-conforming element as shown in Figure 3.3. As before, the intersection points are determined and the curves are extracted. The quadrilateral integration subdomains C_3 and C_4 as shown in Figure 3(b) has to be further triangulated to produce enrichment functions that have inter-element continuity. Details on the definition of the enrichment functions and the integration scheme for this case are provided in the next section.

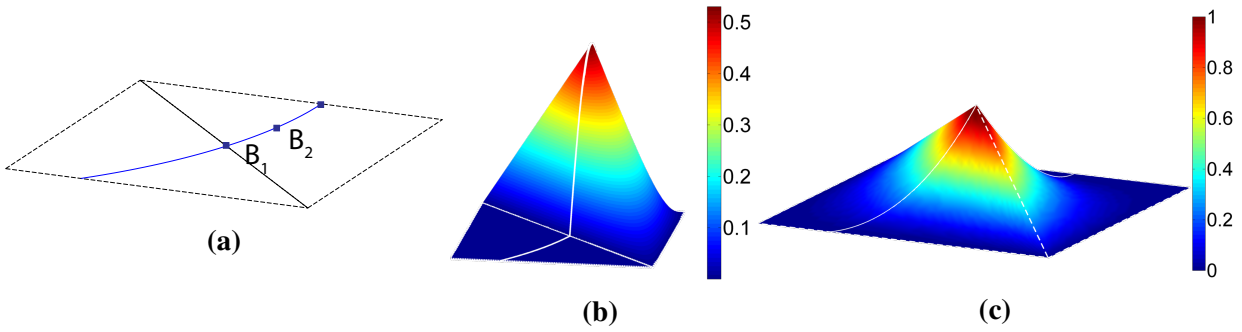

(a) **(b)** **(c)**

Figure 3.4 – (a) A pair of triangular elements cut by a circular arc. (b) and (c): Enrichment functions for enrichment nodes B_2 and B_1, respectively.

3.3.4 Construction of NURBS enrichment functions

The central idea of the construction of NURBS enrichment functions is to use the control points describing the microchannel edge of the integration subdomains as enrichment nodes and the basis functions associated with these control points as enrichment nodes in the same spirit as the original IGFEM. The choice of these basis functions as enrichment functions is straightforward and is motivated by the fact that the enrichment functions have C^0 continuity across the integration subdomains and across the elements as we will explain later. Moreover, the discontinuous gradient in an enrichment function occurs exactly on the channel. We again refer to the example in Figure 3.2 for illustration. Enrichment nodes are introduced at the control points along the microchannel, i.e., at $\boldsymbol{B'}_4, ..., \boldsymbol{B'}_7$. The enrichment functions associated with these nodes are $\overline{R}^{2,1}_{1,1}$, $\overline{R}^{2,1}_{2,1}$, $\overline{R}^{2,1}_{3,1}$ and $\overline{R}^{2,1}_{4,1}$ in C_1 and $\tilde{R}^{2,1}_{1,2}$, $\tilde{R}^{2,1}_{2,2}$, $\tilde{R}^{2,1}_{3,2}$ and $\tilde{R}^{2,1}_{4,2}$ in C_2.

The enrichment function associated with an interior enrichment node such as $\boldsymbol{B'}_5$ in Figure 3.2 or $\boldsymbol{B_2}$ in Figure 3.4a is continuous across the integration subdomains because the subdomains share the same curve segment used to construct their NURBS surfaces. It is also continuous across the elements simply because it vanishes at the edges of the element as shown in Figure 3.4b. That the enrichment function associated with an exterior enrichment node is continuous across elements can be explained by an example. Consider the enrichment node $\boldsymbol{B'}_4$ in Figure 3.2. The basis functions associated with $\boldsymbol{B'}_4$ of the NURBS surfaces C_1 and C_2 vary linearly along the edges $\boldsymbol{P}_{12}\boldsymbol{B'}_4$ and $\boldsymbol{Q}_{11}\boldsymbol{B'}_4$, respectively, are unity at $\boldsymbol{B'}_4$ and vanish along the other edges of the element. Similarly, the basis functions of the integration subdomains in the element adjacent to the edge $\boldsymbol{P}_{12}\boldsymbol{Q}_{11}$ have the same property by construction. The same argument applies to enrichment node $\boldsymbol{B_1}$ in Figure 3.4a. Hence these enrichment functions also have inter-element continuity, which can clearly be observed in Figure 3.4c. Comparing with the linear polynomial IGFEM enrichment nodes and functions shown in Figure 3.1b, we observe that additional interior enrichment nodes are introduced in the NURBS-based IGFEM and the NURBS enrichment function is nonlinear with

respect to the spatial coordinates.

The construction of enrichment function for an element with a branching point is the same as before, except that care must be taken to ensure that the enrichment function is continuous between elements. If two adjacent edges of a quadrilateral integration subdomain are described by curve segments with more than 2 control points, the enrichment function constructed in this manner is not continuous across the element. For illustration, consider integration subdomain C_3 of Figure 3.3(b), the basis functions associated with P is non-linear along the straight edge PA. However, the basis function associated with P of the NURBS surface describing the adjacent integration subdomain in the neighbor element is linear along PA. Hence the enrichment function is discontinuous. To prevent this problem, the quadrilateral integration subdomain has to be further subdivided as shown in Figure 3.3(c). The basis function associated with P of integration subdomain C_3' is then a linear function along edge PA and inter-element continuity is ensured.

3.3.5 Integration over a parent element

Work on the optimal quadrature rule for NURBS is still an active area of research [88]. It is known that Gaussian quadrature is not an optimal rule as it does not utilize the smoothness of the NURBS function between knot spans [88]. An optimal rule called the "half-point rule", which corresponds to one integration point every two basis functions regardless of degree has been developed for the exact integration of B-splines in 1D [88]. The half-point rule will result in huge savings in isogeometric analysis because NURBS quadrature is carried out everywhere in the domain. In our case, we only need to perform quadrature of NURBS in enriched elements and hence an optimal rule is not critical to our method. Because the "half-point rule" has not been tested on piecewise rational polynomials and for simplicity, we use Gaussian quadrature.

Similar to the original IGFEM [74], integration is performed separately in each integration subdomain. However, when using a NURBS enrichment function, two Jacobians are needed [81]. The geometrical mapping from the physical space to the NURBS parametric space in (3.15) or (3.16) is used to calculate the first Jacobian. The derivative of rational B-splines can be calculated according to the method described in [78]. A linear mapping from a knot span to the usual local coordinate space should be defined so that Gaussian quadrature can be performed. This mapping gives rise to the second Jacobian.

Given a knot vector $\boldsymbol{\xi} = \{\xi_1, \xi_2, ..., \xi_{n+p+1}\}$, the knot spans are the sub-intervals $[\xi_i, \xi_{i+1}]$. The Gaussian quadrature is applied separately in each knot span with non-zero width. For example, if the integration subdomain is described by a NURBS with knot vectors $\boldsymbol{\xi} = \{0, 0, 0, 0.5, 1, 1, 1\}$ and $\boldsymbol{\eta} = \{0, 0, 1, 1\}$ and the number of Gauss points per knot span in the ξ- and η-directions are n_ξ and n_η, respectively, then the total number of Gauss points is $2n_\xi \times n_\eta$. The number of Gauss

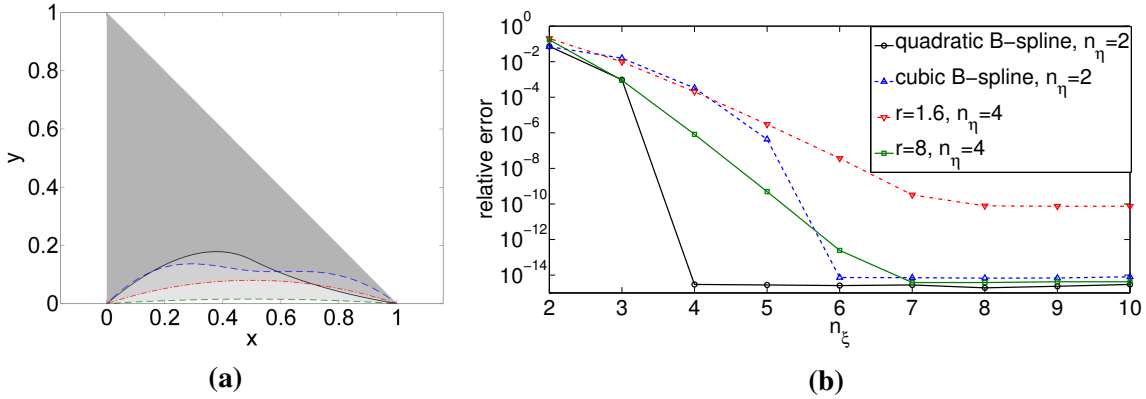

Figure 3.5 – (a) A triangular domain with one curved edge for the numerical integration study. (b) The relative error of the numerical integration of (3.18) using Gaussian quadrature.

points per knot span depends on the degree of the NURBS surface in the direction of the knot vector. In general the higher the degree, the higher the number of Gauss points per knot span. In this subsection, we perform a simple study on the number of Gauss points required for integration specific to our work. The appropriate selection of quadrature rule in the general case warrants a separate study on its own.

Consider a triangular integration subdomain as shown in Figure 3.5a with one curved edge. Consider a typical term in our element stiffness matrix given by

$$\int\int_{[0,1]^2} \nabla_{\boldsymbol{x}}^T \psi_i(\xi,\eta) \nabla_{\boldsymbol{x}} \psi_j(\xi,\eta) J(\xi,\eta) \mathrm{d}\xi \mathrm{d}\eta, \tag{3.17}$$

where ψ_i, ψ_j are enrichment functions and $J(\xi,\eta)$ is the determinant of the Jacobian from the physical space to the NURBS parameter space. A common practice when integrating such a term in isogeometric analysis is to assume that the Jacobian is a constant and if ψ_i and ψ_j are rational piecewise polynomials, that the denominator varies slowly compared to the numerator that it can be assumed constant. This practice is based on standard FEM, where the integration order required is deduced by assuming an undistorted element.

However, in our study, we do not assume that the Jacobian is constant. Because the derivative of a NURBS basis function with respect to physical space in a curved integration subdomain results in an unknown function type, we assume that the derivative has the same degree as the basis function itself. Note that this has also been done for isogeometric analysis when determining an appropriate integration order for the stiffness matrix [88]. Hence, in lieu of the term in (3.17), we perform an integration study over a triangular integration subdomain with a curved edge represented by

NURBS as shown in Figure 3.5a on a term given by

$$\int\int_{[0,1]^2} \psi(\xi,\eta)^2 J(\xi,\eta) \mathrm{d}\xi \mathrm{d}\eta, \tag{3.18}$$

where ψ is chosen as one of the enrichment functions associated with the interior enrichment nodes. The curved edge is a quadratic B-spline, a cubic B-spline and two rational NURBS circular arcs of different radii. The control points of the curves can be found in Table A.1 of the appendix. The different radii are chosen based on the radius to mesh size ratios of the semicircular channel problem in Section 3.4.1.

Figure 3.5b shows how the relative error changes with respected to the number of Gauss points in the direction ξ, n_ξ while fixing n_η. ξ and η are chosen to be in the directions of the curved and straight edges, respectively. Because the basis function in η for the B-splines is a linear piecewise polynomial, $n_\eta = 2$ is the necessary minimal number of Gauss points required to integrate (3.18) exactly. Figure 3.5b shows that $n_\xi = 4$ and 6 are required to integrate the quadratic and cubic B-splines, respectively. This is expected because the integrand in (3.18) has degrees 6 and 10 for quadratic and cubic B-splines, respectively.

On the other hand, the quadrature rule for a rational NURBS is not straightforward. We base our selection of number of quadrature points on the finite element solution error in Section 3.4.1. For the NURBS curves, $n_\eta = 4$ is chosen because $n_\eta = 2$ or 3 will limit the relative error of the integration to between 10^{-2} to 10^{-3}, which may be insufficient when the radius of curvature is high. Figure 3.5b shows that the relative error at $n_\xi = 4$ for the smaller radius of $r = 1.6$ is slightly greater than 10^{-4}, which is smaller than the finite element solution error presented in Section 3.4.1. As the mesh size becomes smaller, the ratio of the radius to the mesh size becomes larger and the relative error of the quadrature decreases. For the larger radius of $r = 8$ and at $n_\xi = 4$, the relative error decreases to a value slightly greater than 10^{-6}, which is much smaller than the finite element solution error. Therefore, we recommend a $n_\xi = n_\eta = 4$ quadrature rule for a radius to mesh size ratio greater than 1.6. The numerical integration study here is also valid for a quadrilateral element with one curved edge.

Other than the usual first term in the stiffness matrix defined in (3.6), a third term arises due to the contribution of the microchannels. In an integration subdomain, this integration is only performed over the edge of the subdomain coinciding with a microchannel. Since there are two integration subdomains sharing a microchannel, the contribution of this integral is halved for each subdomain to avoid double counting.

3.3.6 Computational cost

The creation of meshes that conform to complex microstructural details such as material interfaces and embedded microchannels often represents a challenging and time-consuming task. This is especially the case in 3D settings and/or for problems that require the simulation of multiple realizations of the virtual microstructure such as in multiscale modeling (for which multiple realizations are needed to extract some of the statistics of the homogenized response) or mesoscale shape optimization (during which multiple simulations of the evolving microstructure have to be performed). The ability to perform multiple simulations with a single non-conforming mesh, thereby avoiding the complexity and cost of meshing, is undoubtedly one of the attractive features of the NURBS-based IGFEM scheme. Although it often represents the major time consuming part of a finite element analysis, the mesh generation process does not usually enter the assessment of the efficiency of a solution method. It is therefore difficult to perform a direct comparison between the NURBS-based IGFEM and the standard FEM.

As far as the solution step itself, the key computational costs involved with the IGFEM are associated with (i) finding the intersection points, (ii) constructing the enrichment functions, (iii) assembling the stiffness matrix and (iv) solving the system of equations. With regards to the first operation, efficient algorithms to find the intersection of NURBS with element edges and faces, such as implicitization, subdivision and Bézier clipping, are widely available [89, 90, 91, 92]. Furthermore, finding the intersection points and constructing the enrichment functions can be readily parallelized. While the numerical integration associated with the computation of the stiffness matrix in the IGFEM is more expensive than its standard FEM counterpart, this step can be further improved as the Gaussian quadrature rule for integration of NURBS is not optimal because it does not utilize the smoothness of the curve between knot spans [88]. It should be noted that, unlike isogeometric analysis, NURBS-based IGFEM only requires integration of NURBS in the enriched elements, which typically represent a relatively small fraction of the entire mesh. In most large size problems, the solution of the resulting system of equations constitutes by far the most time-intensive part of the analysis.

3.4 Convergence study

We use the method of manufactured solutions for a problem with a curved microchannel without branching and a second problem with straight branched microchannels to study the convergence and accuracy of IGFEM with NURBS enrichment functions. Dirichlet boundary conditions are imposed at the boundary based on the manufactured solutions. The study is carried out using the

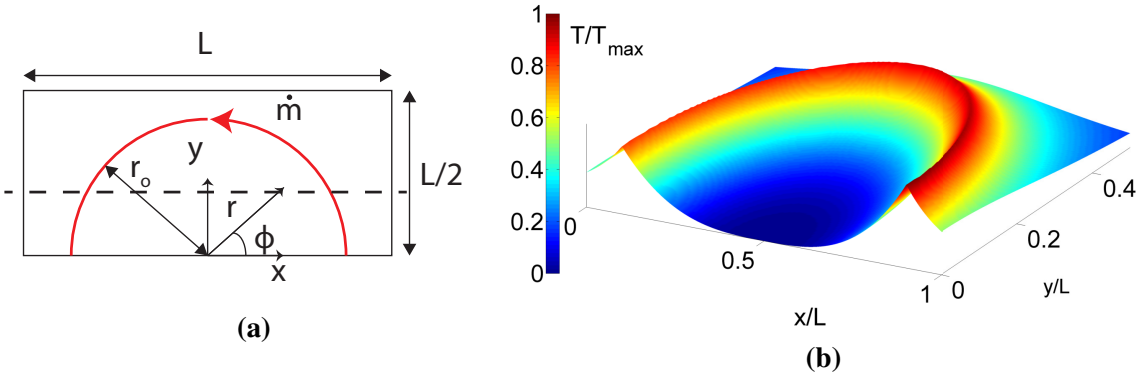

Figure 3.6 – (a) Domain geometry for Verification Problem 1. (b) 3D surface plot of the analytical solution for $k = 3$, $\alpha = 90$ and $r_o = 0.4$. The temperature has been normalized by the maximum temperature in the domain, $T_{\max}$.

L^2- and H^1-norms of the error defined as

$$\|T - T^h\|_{L^2(\Omega)} = \sqrt{\int_\Omega (T - T^h)^2 \mathrm{d}\Omega}, \tag{3.19}$$

and

$$\|T - T^h\|_{H^1(\Omega)} = \sqrt{\int_\Omega \left[(T - T^h)^2 + \left(\|\nabla T - \nabla T^h\|_2\right)^2\right] \mathrm{d}\Omega}. \tag{3.20}$$

We also study the effect of curvature on the relative error of the solution. The problems in the remaining sections involve a homogeneous solid of uniform thermal conductivity κ, with the weak discontinuity in the temperature field solely due to the presence of the microchannels.

3.4.1 Verification Problem 1: Semicircular Channel

Consider a semicircular channel of radius r_o centered at $(L/2, 0)$ with mass flow rate $\dot{m}_f$ and uniform heat capacity c_f in a rectangular domain of length L and width $L/2$ as shown in Figure 3.6a. The semicircle can be described by the control points $(L/2+r_o, 0), (L/2+r_o, r_o), (L/2, r_o), (L/2-r_o, r_o), (L/2-r_o, 0)$ with corresponding weights $1, 1/\sqrt{2}, 1, 1/\sqrt{2}, 1$ and knot vector $\{0, 0, 0, 1, 1, 2, 2, 2\}$. By choosing a characteristic temperature ($T_{\max}$) and a characteristic length (L), the weak form (2.5) can be expressed in terms of a single dimensionless parameter given by

$$\alpha = \frac{\dot{m} c_f}{\kappa}. \tag{3.21}$$

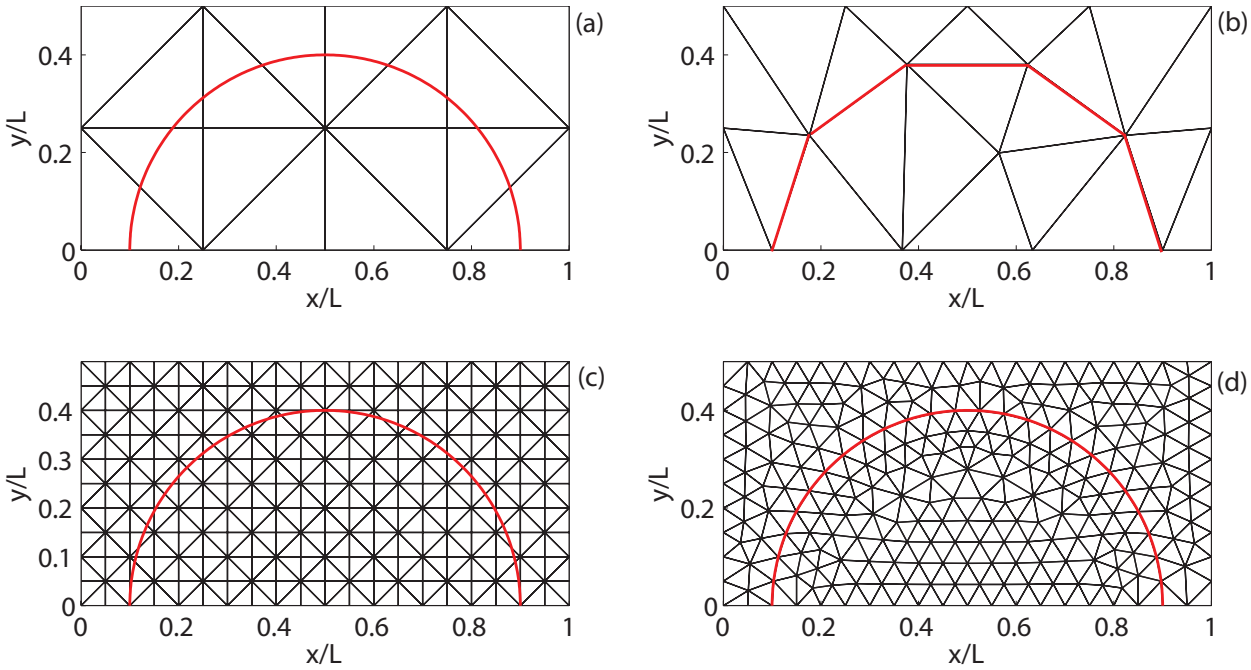

Figure 3.7 – Non-conforming and conforming meshes for verification problem 1. (a) and (b): Coarsest non-conforming and conforming meshes. (c) and (d): Finer non-conforming and conforming meshes.

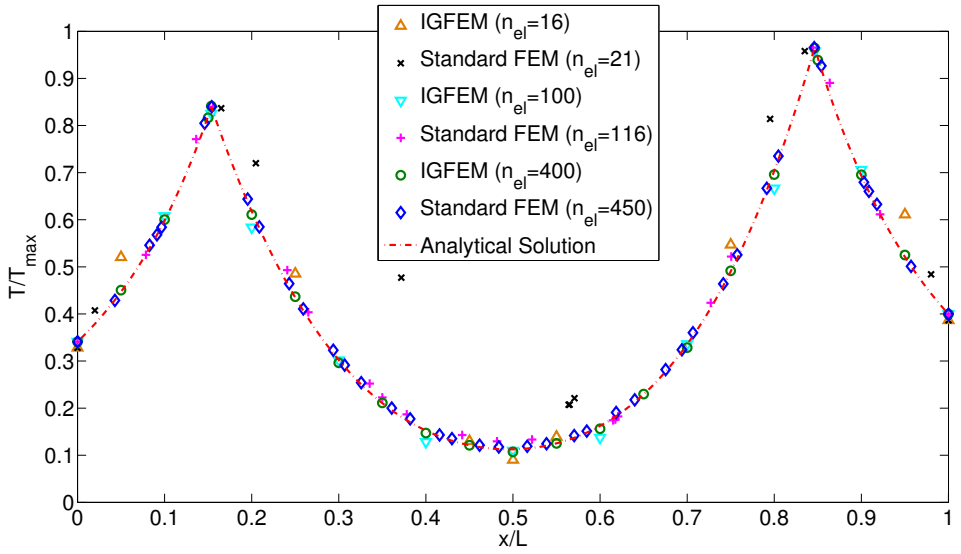

Figure 3.8 – Comparison of IGFEM and SFEM solutions with analytical solution along the line $y = 0.2L$ (dashed line in Figure 3.6a) for different number of elements n_{el}.

If the following distributed heat source is applied to Ω_s:

$$f(r,\phi) = \begin{cases} -(k^2+\lambda^2) r_o^2 \left(\frac{r}{r_o}\right)^{k-2} \mathrm{e}^{-\lambda\phi} & r < r_o, \\ -(k^2+\lambda^2) r_o^{-2} \left(\frac{r_o}{r}\right)^{k+2} \mathrm{e}^{-\lambda\phi} & r > r_o, \end{cases} \tag{3.22}$$

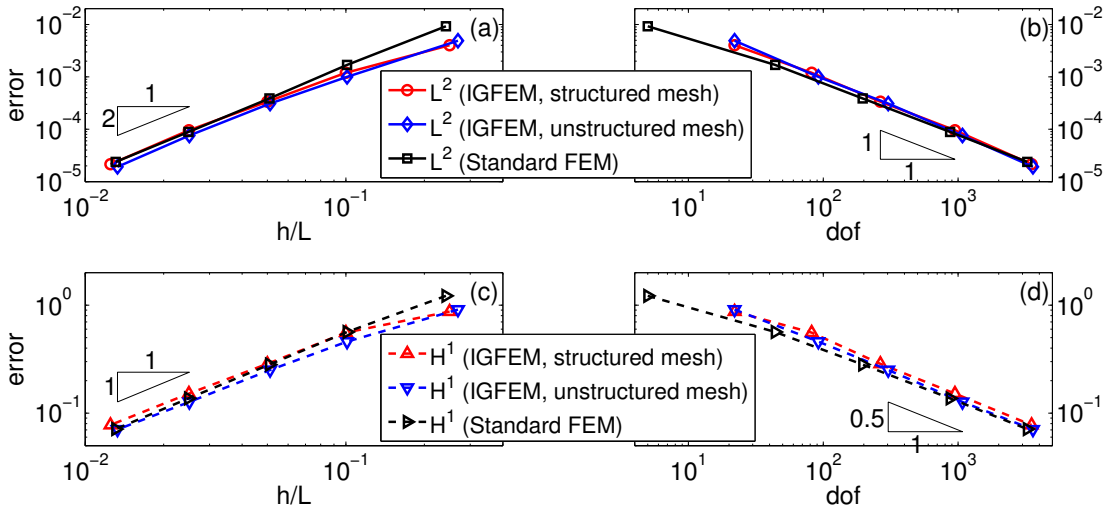

Figure 3.9 – Convergence study: L^2 (top) and H^1 (bottom) errors for Verification Problem 1 (with $r_o = 0.4L$, $k = 3$ and $\alpha = 90$).

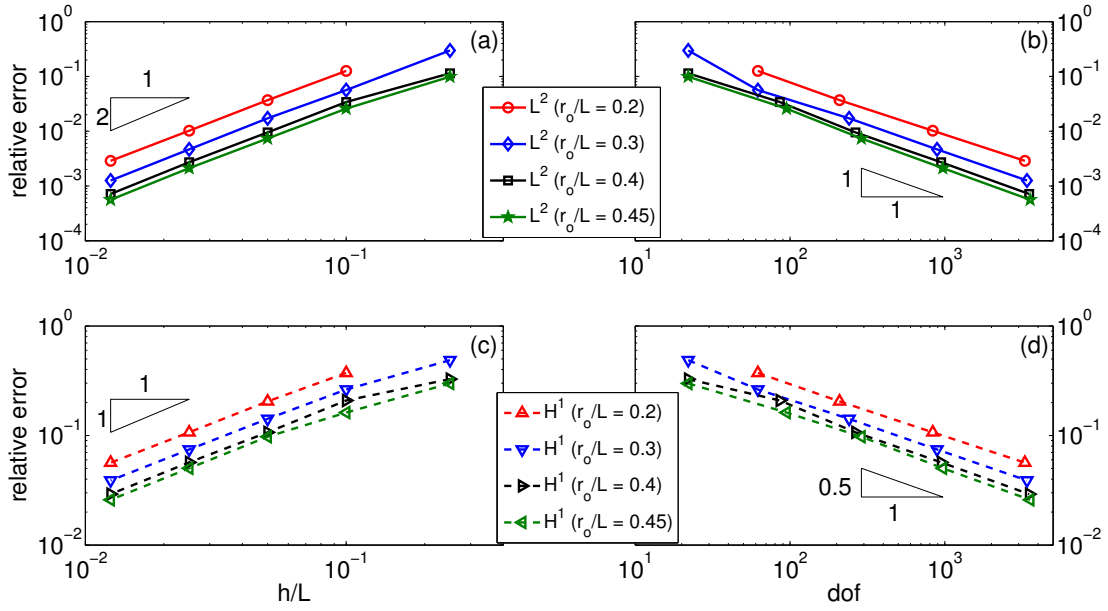

Figure 3.10 – Effect of curvature on the L^2 and H^1 relative errors for Verification Problem 1 with semicircular channels of different radii, $k = 3$ and $\alpha = 90$.

with the cylindrical coordinates (r, ϕ) shown in Figure 3.6a, the solution to (2.5) is given by

$$T(r,\phi) = \begin{cases} \left(\frac{r}{r_o}\right)^k \mathrm{e}^{-\lambda\phi} & r \le r_o, \\ \left(\frac{r_o}{r}\right)^k \mathrm{e}^{-\lambda\phi} & r > r_o, \end{cases} \tag{3.23}$$

where $\lambda = \frac{2k}{\alpha}$. The manufactured solution is thus described by the two parameters k and α. As apparent in Figure 3.6b, the temperature gradient is discontinuous across the microchannel but is continuous along the microchannel. The temperature decays slowly in the counter-clockwise direction due to the relatively small value of λ.

Some of the structured non-conforming meshes and the unstructured conforming meshes used in this study are shown in Figure 3.7. Unstructured non-conforming meshes have also been used for the NURBS-based IGFEM. By setting $k = 3$ and $\alpha = 90$, the solutions obtained from the two coarsest structured non-conforming mesh are compared with those obtained from the two coarsest conforming mesh along the line $y = 0.2L$ in Figure 3.8. It can be seen that IGFEM is able to capture the two weak discontinuities at $x = 0.15L$ and $0.85L$ with a relatively coarse mesh and that no significant difference between IGFEM and SFEM is observed as the mesh becomes finer.

The errors in the L^2- and H^1-norms for both IGFEM and SFEM with respect to the minimum edge length for structured meshes or average edge length for unstructured meshes h are compared in Figures 3.9a,c. As alluded to in Figure 3.8, the solution obtained by IGFEM is significantly more accurate for coarse meshes. By fitting the model $||T - T^h|| = Ah^\beta$ to the last 4 data points, the asymptotic convergence rates of IGFEM with unstructured mesh in the L^2 norm and H^1 norm are 1.95 and 0.93, respectively. With structured mesh, the convergence rates are 1.85 and 0.94 respectively. If the last two data points were used, the convergence rates are 1.93 and 0.96, respectively. The slightly lower accuracy of the structured mesh is due to the higher percentage of very slender integration subdomains, which causes problem in the derivative of the temperature. Note that this problem also occurs in GFEM/XFEM [71, 93]. Unlike conventional GFEM for sharp thermal gradient [65], the accuracy of IGFEM is essentially independent of the mesh orientation. On the other hand, the convergence rates of SFEM are 2.09 and 1 respectively. Due to the slightly higher convergence rate of SFEM, its accuracy will eventually become better than IGFEM as the mesh becomes finer. The mesh size at which this happens, h_o will become smaller as the microchannel effect becomes more important, i.e., as α and/or k increase.

A comparison of the error of IGFEM and that of SFEM with respect to the number of degrees of freedom (total number of nodes less the prescribed nodes) is also shown in Figures 3.9b,d. The accuracy of both methods are comparable to each other for a given number of dofs, with the slightly higher convergence rate of IGFEM due to the strategic placement of the dofs near the microchannel. However, SFEM has a slightly better accuracy compared to IGFEM for a given dof due to the greater number of elements near the channel and the fact that the total error does not just come from elements cut by the channel but also elements near the channel.

The effect of curvature on the relative error of the solution ($||T - T^h||/||T||$) is also investigated using IGFEM with a structured mesh by changing the radius of the semicircular channel. Figure 3.10 shows that the relative error increases with curvature $1/r_o$ but the convergence rate is

essentially unchanged as expected.

3.4.2 Verification Problem 2: Straight Channels with Branching

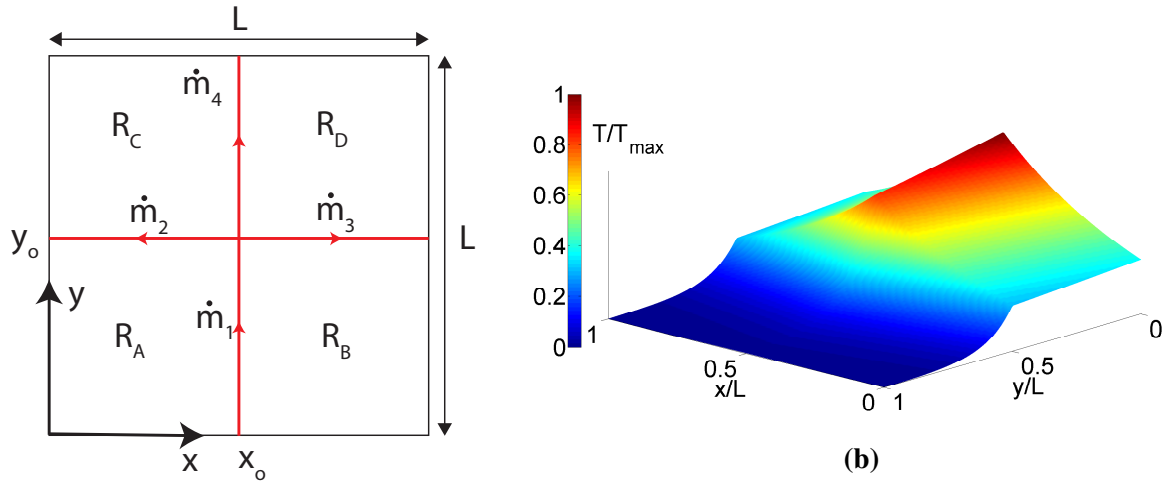

Figure 3.11 – (a) Domain geometry of Verification Problem 2. (b) 3D surface plot of the analytical temperature field. The temperature is normalized by the maximum temperature in the domain, $T_{\max}$.

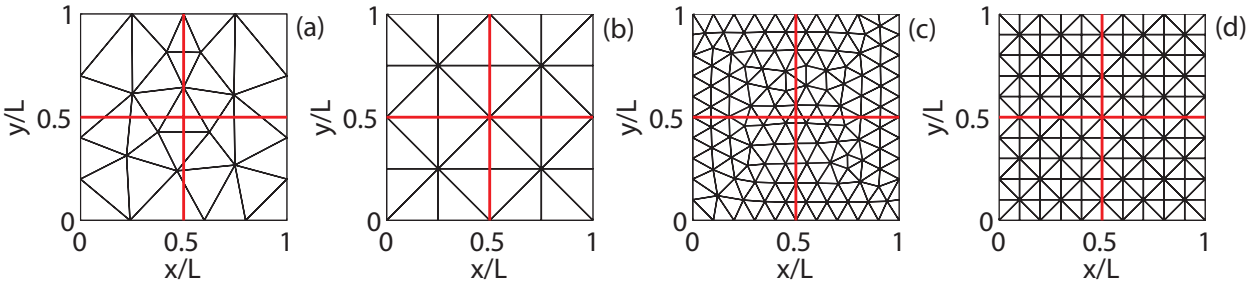

Figure 3.12 – Non-conforming and conforming meshes for Verification Problem 2. (a) and (b): Coarsest non-conforming and conforming meshes. (c) and (d): Finer non-conforming and conforming meshes.

Consider the network of branched straight channels in a square domain of length L illustrated in Figure 3.11a. The junction is located at $x_o = y_o = L/2$. A flow $\dot{m}_1$ enters the domain from point $(x_o, 0)$ and splits into 3 microchannels with flow rates $\dot{m}_2, \dot{m}_3, \dot{m}_4$ such that $\dot{m}_1 = \dot{m}_2 + \dot{m}_3 + \dot{m}_4$. Let the dimensionless parameters defined in (3.21) be $\alpha_i = \dot{m}_i c_f / \kappa$ for channels $i = 1, 2, 3, 4$.

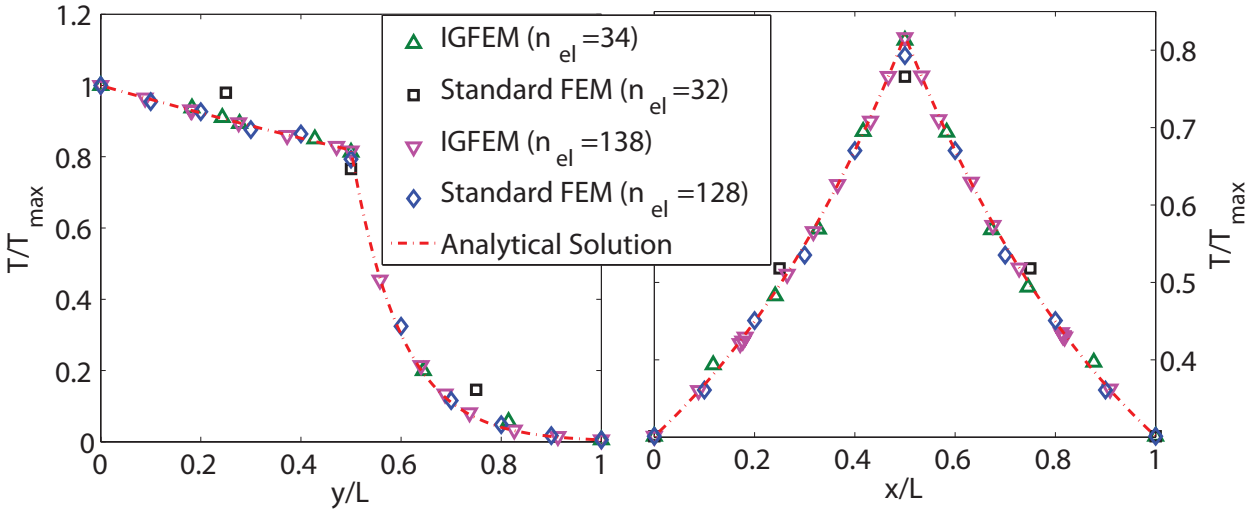

Figure 3.13 – Comparison of IGFEM and SFEM solutions along the microchannels $x = 0.5L$ (left) and $y = 0.5L$ (right) in Figure 3.11a for different number of elements n_{el}.

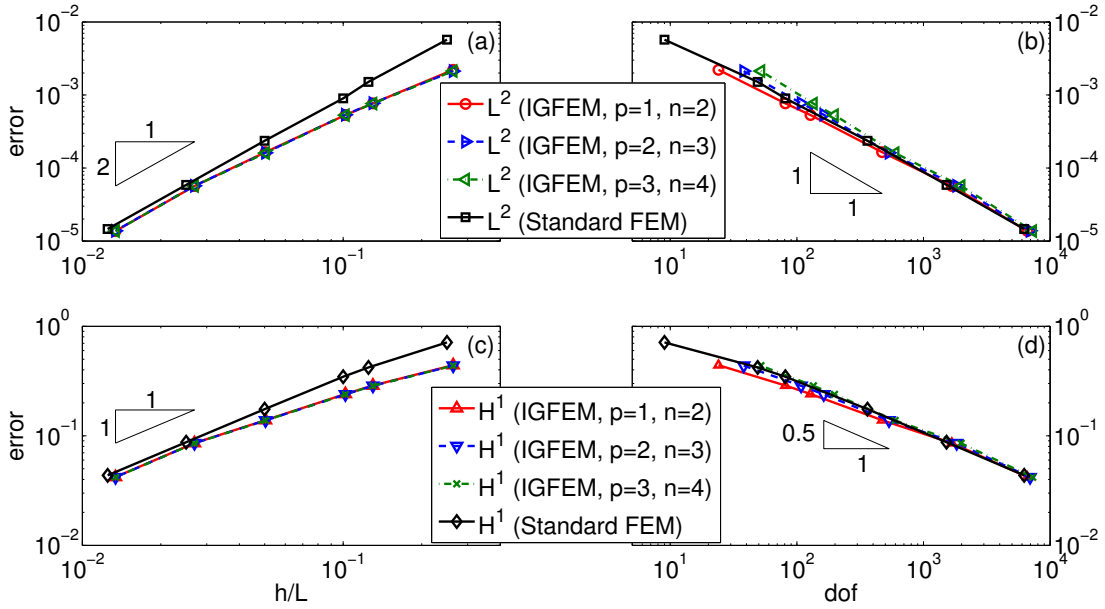

Figure 3.14 – Convergence analysis: L^2 and H^1 errors for Verification Problem 2. Effect of the degree of NURBS, p, and the number of control points of each microchannel, n, on the L^2 and H^1 errors.

For the following distributed heat sources:

$$f(x,y) = \begin{cases} -C(\lambda_1^2+\lambda_2^2)\mathrm{e}^{\lambda_2 x-\lambda_1 y} & \text{on} \quad R_A, \\ -C(\lambda_1^2+\lambda_3^2)\mathrm{e}^{\lambda_2 x_o+\lambda_3(x_o-x)-\lambda_1 y} & \text{on} \quad R_B, \\ -C(\lambda_2^2+\lambda_4^2)\mathrm{e}^{\lambda_2 x+\lambda_4(y_o-y)-\lambda_1 y_o} & \text{on} \quad R_C, \\ -C(\lambda_3^2+\lambda_4^2)\mathrm{e}^{\lambda_2 x_o+\lambda_3(x_o-x)+\lambda_4(y_o-y)-\lambda_1 y_o} & \text{on} \quad R_D, \end{cases} \tag{3.24}$$

where the subdomains R_A, R_B, R_C and R_D are shown in Figure 3.11a, the solution to (2.5) with the appropriate Dirichlet boundary conditions is given by

$$T(x,y) = \begin{cases} C\mathrm{e}^{\lambda_2 x - \lambda_1 y} & \text{on} \quad R_A, \\ C\mathrm{e}^{\lambda_2 x_o + \lambda_3 (x_o - x) - \lambda_1 y} & \text{on} \quad R_B, \\ C\mathrm{e}^{\lambda_2 x + \lambda_4 (y_o - y) - \lambda_1 y_o} & \text{on} \quad R_C, \\ C\mathrm{e}^{\lambda_2 x_o + \lambda_3 (x_o - x) + \lambda_4 (y_o - y) - \lambda_1 y_o} & \text{on} \quad R_D, \end{cases} \tag{3.25}$$

provided the following relations are satisfied: $\lambda_1\alpha_1 = \lambda_4\alpha_4 = \lambda_2 + \lambda_3, \lambda_2\alpha_2 = \lambda_3\alpha_3 = \lambda_4 - \lambda_1, \alpha_1 = \alpha_2 + \alpha_3 + \alpha_4$. The problem is thus defined by 3 parameters, for which we choose $\alpha_1 = 10$, $\alpha_4 = 0.4$ and $\lambda_2 = 20$. Hence $\lambda_1 = 4$, $\lambda_3 = 20$, $\lambda_4 = 100$, $\alpha_2 = \alpha_3 = 4.8$. Figure 3.11b shows the exact temperature field. Steep jumps in thermal gradient are observed along channels $i = 2, 3, 4$.

We use NURBS with different number of control points n and degree p to describe the straight channels as shown in Table A.2 of the appendix. The purpose of doing this is to verify that our method works even for different degree NURBS. Note that the degree of the NURBS enrichment is given by the degree of NURBS curve used to describe the geometry of the microchannel. In general, a lower degree NURBS curve can be integrated more accurately with a given Gaussian quadrature scheme.

Some of the non-conforming and conforming meshes used in this problem are shown in Figure 3.12. The solutions obtained with IGFEM with $n = 2, p = 1$ and SFEM are compared in Figure 3.13, showing that IGFEM achieves a significantly more accurate solution for very coarse meshes.

The error of the IGFEM solution with different n and p is compared with that of SFEM in Figure 3.14a,c. In spite of the suboptimal convergence rate for large element size h, IGFEM is significantly more accurate than SFEM for moderate to large h. The asymptotic convergence rates of IGFEM with respect to h in the L^2 and H^1 norms using the last two points are 2.04 and 1.03, respectively, regardless of n and p. This result shows that the NURBS-based IGFEM is able to handle NURBS curves of different degrees.

For a given number of dofs, the IGFEM with $n = 2, p = 1$ has slightly better accuracy than the SFEM. However, for straight channels, using a higher number of enrichment nodes or degree of enrichment functions does not improve the accuracy and incurs greater computational cost.

3.5 Applications

As indicated in the introduction, recent advances in the manufacturing of microvascular materials allow for very complex curved microchannels to be embedded in polymeric and composite components [12, 76]. In the examples presented hereafter, we show that IGFEM is capable of handling many types of complex microchannel configurations.

3.5.1 Application 1: Wavy channel in active cooling of microvascular materials

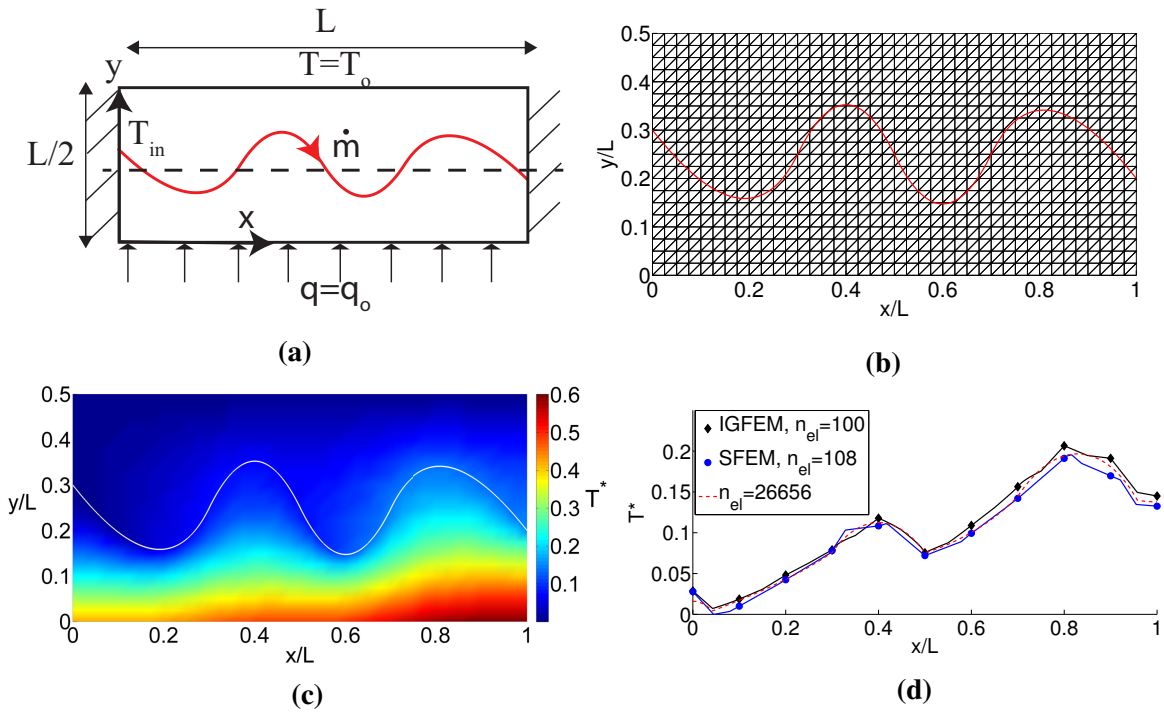

Figure 3.15 – (a) Domain geometry and boundary conditions for Application Problem 1. (b) Non-conforming mesh used by IGFEM to produce the temperature field in (c). (d) Temperature along the line $y = 0.25L$ (dashed line in (a)). The parameters are $\alpha = \dot{m}c_f/\kappa = 10$ and $T_{\text{in}} = T_o$.

Inspired by the microchannel design study summarized in [30], we apply the NURBS-based IGFEM to a $L\times L/2$ domain with a curved microchannel as shown in Figure 3.15a. The microchannel is described by a degree-2 NURBS with the control points (0,0.3), (0.2,0.045), (0.4,0.455), (0.6,0.045), (0.8,0.455), (1,0.2) and knot vector $\{0, 0, 0, 1, 2, 3, 4, 4, 4\}$. Note that the coordinates of the control points are expressed in terms of the characteristic length L and all weights associated with the control points are unity. A heat flux q_o is applied along the bottom edge of the domain and the temperature is fixed ($T = T_o$) along the top edge. The temperature at the inlet of the channel,

T_{in} is prescribed. The solution is expressed in terms of the dimensionless temperature

$$T^* = \frac{2\kappa}{q_o L}(T - T_o), \tag{3.26}$$

where $\frac{q_o L}{2\kappa} + T_o$ is the maximum temperature in the absence of the microchannel. The temperature distribution in Figure 3.15c obtained using the mesh in Figure 3.15b shows that fluid flow in the microchannel reduces the maximum temperature relative to that without the microchannel.

The IGFEM solutions are compared with SFEM solutions obtained with coarser conforming meshes of the same sizes as the structured meshes and a very fine conforming mesh in Figure 3.15d along the line $y = 0.25L$. Both IGFEM and SFEM are able to obtain the solution with rather coarse meshes. The reference maximum temperature is 0.604. For IGFEM, the predicted maximum temperature with 100 elements has a relative error of 1.3% compared to 3.14% for SFEM with 108 elements and the same mesh size.

3.5.2 Application 2: Serpentine microchannel

Motivated by the use of serpentine channels employed in battery cooling plates [20], we use the IGFEM thermal solver to analyze the temperature distribution in a thin microvascular domain represented by a square domain of length L with a serpentine microchannel as shown in Figure 3.16a with different flow rates, $\dot{m}_f = \dot{m}, 2\dot{m}, 4\dot{m}$. The microchannel is represented by a single quadratic NURBS curve with control points (0,0.1), (0.89,0.039), (0.89,0.69), (0.3,0.69), (0.3,0.5), (0.7,0.6), (0.6,0.25), (0.19,0.25), (0.19,0.98), (1,0.9) and knot vector $\{0, 0, 0, 1, 2, 3, 4, 5, 6, 7, 8, 8, 8\}$. As before, the weights associated with the control points are unity. All sides of Ω are insulated except at one point where the temperature of the microchannel at the inlet, T_{in} is prescribed. The heat flux on the flat face of Ω is modeled as a uniform distributed source, i.e., $f(x, y) = Q_b$ in (2.5). The solution is expressed in terms of a dimensionless temperature defined by

$$T^* = \frac{T - T_{\text{in}}}{T_c}, \tag{3.27}$$

where the characteristic temperature is defined as $T_c = Q_b L^2/\kappa$. Hence, the dimensionless distributed heat source, $Q_b L^2/\kappa T_c$ is 1. The effect of increasing the flow rate is clearly seen in Figures 3.16b–d.

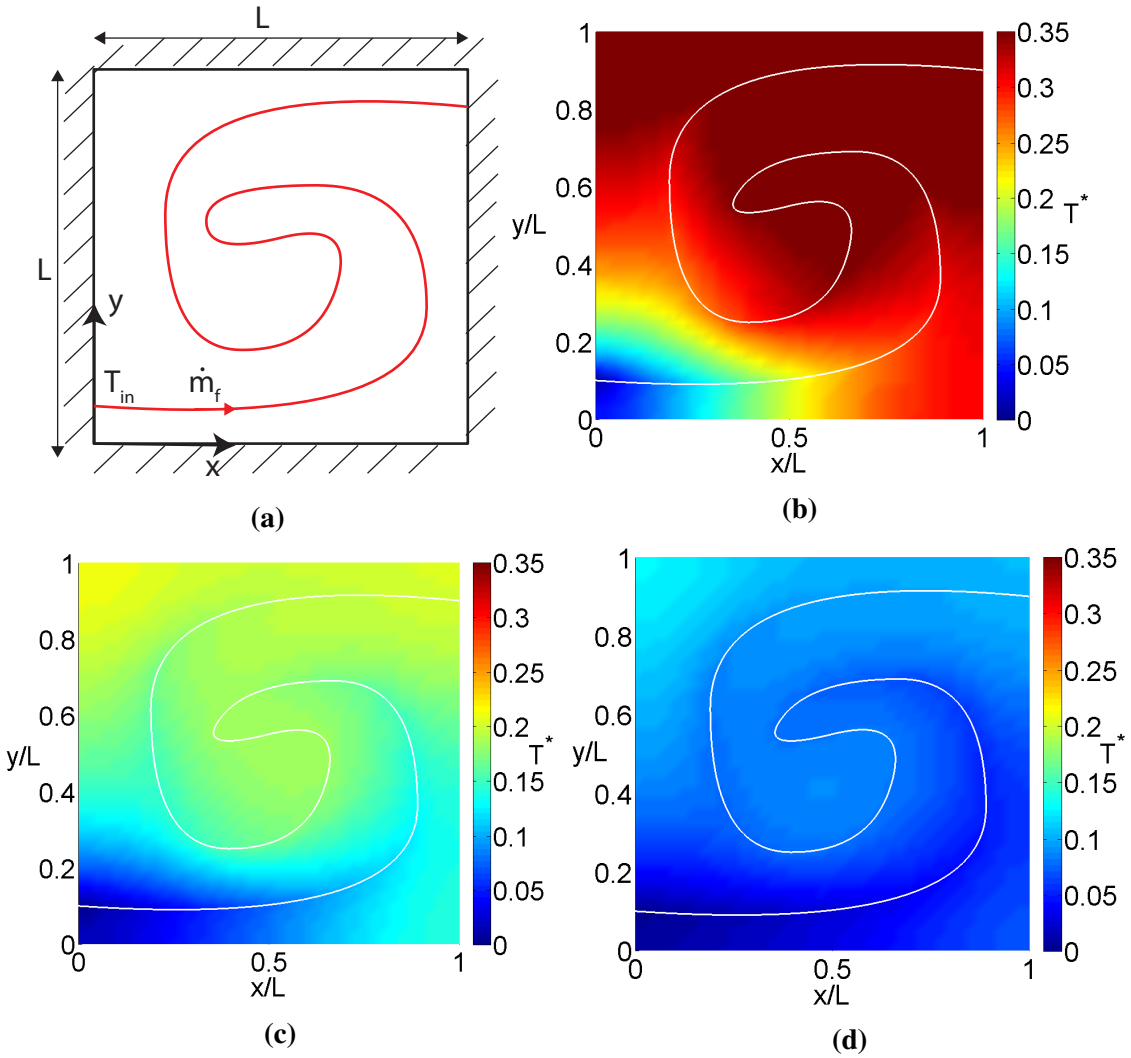

Figure 3.16 – (a) Domain geometry and boundary conditions of a material with a serpentine microchannel and uniform body source, Q_b. The temperature fields obtained using a structured mesh with 3200 elements for (b) $\dot{m}_f = \dot{m}$, $\alpha = 2.5$, (c) $\dot{m}_f = 2\dot{m}$, $\alpha = 5$ and (d) $\dot{m}_f = 4\dot{m}$, $\alpha = 10$, where $\alpha = \dot{m}_f c_f / \kappa$.

3.5.3 Application 3: Embedded network of wavy channels

The design optimization of the microchannels in a microvascular material to minimize objective functions such as global flow resistance, void volume fraction and maximum temperature has been a subject of a number of studies [29, 50, 30, 94]. One notable result is that to minimize the global flow resistance, it is more efficient to bathe a region with a single stream of microchannels with branching than multiple streams of microchannels [94]. In this final application, we replace the single microchannel in Figure 3.15a with a network of microchannels as shown in Figure 3.17a. The knot vectors and the control points are shown in Table A.3 of the appendix. A single stream of

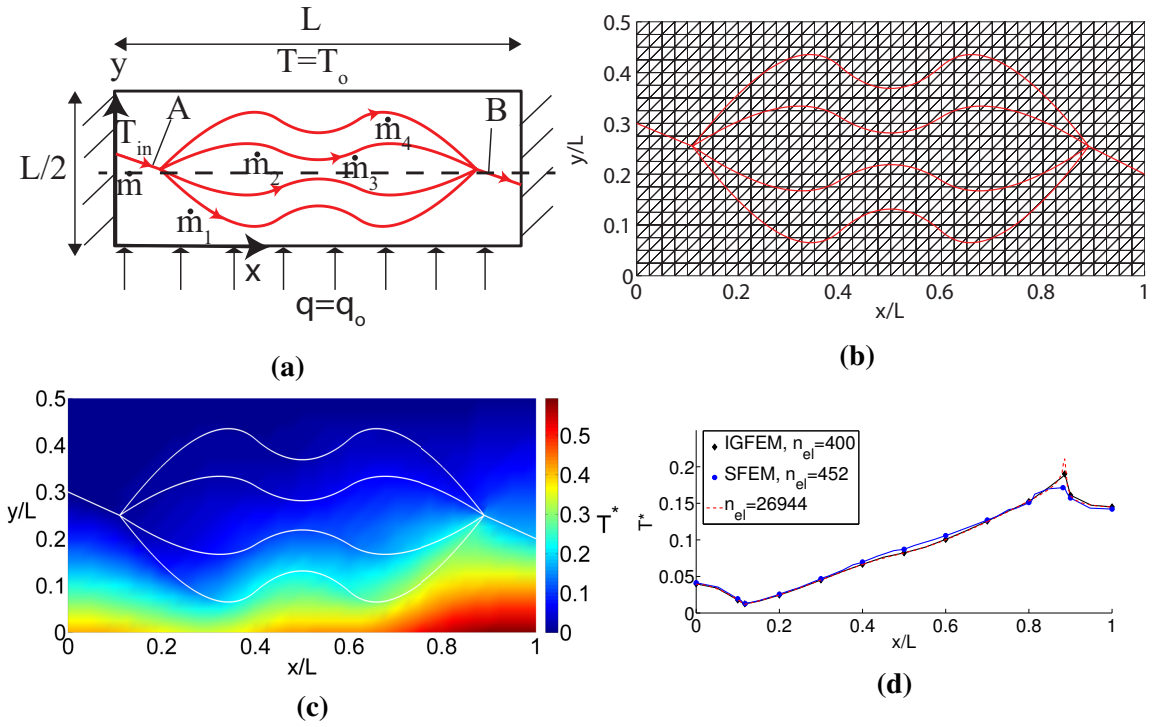

Figure 3.17 – (a) Domain geometry and boundary conditions for Application Problem 3. (b) Non-conforming mesh used by IGFEM solver to obtain the temperature field show in (c). (d) The temperature along the line $y = 0.25L$ (dashed line in (a)). The parameters are $\alpha = \dot{m}c_f/\kappa = 10$, $\dot{m}_i = \dot{m}/4,\ (i = 1, 2, 3, 4)$, $T_{\text{in}} = T_o$.

mass flow rate $\dot{m}$ is split into four microchannels each having the same mass flow rate of $\dot{m}/4$. The solution is expressed in terms of the dimensionless temperature defined in (3.26). The temperature distribution in Figure 3.17c obtained using the non-conforming mesh in Figure 3.17b clearly shows the cooling effect of the microchannels.

A comparison of the IGFEM and SFEM solutions along the line $y = 0.25L$ in Figure 3.17d shows that both methods with relatively coarse meshes agree with the reference solution obtained with a fine conforming mesh. A closer look at the spike at around $x = 0.9L$ close to a branching point shows that IGFEM is able to model the spike more accurately than SFEM. Using the maximum temperature of 0.597 provided by the reference solution as the reference, the error of the maximum temperature predicted by IGFEM with 400 elements is 0.088%, compared to 2.3% predicted by SFEM with 452 elements.

3.6 Conclusions

An overview of the IGFEM was provided in this chapter. The formulation and implementation of a NURBS-based IGFEM for the thermal analysis of a material containing curved microchannels based on a dimensionally reduced thermal model were then presented. By using enrichment functions constructed from some of the basis functions of the NURBS description of the integration subdomains, we showed that the method preserves the exact geometrical description of the curved microchannels and has the ability to handle branching in the interior of an element. In the convergence studies, we demonstrated that the rate of convergence associated with the method is close-to-optimal even for curved microchannel and its accuracy is comparable to that of SFEM. Lastly, the method was applied to solve a number of problems with complex microchannel configurations.

4 3D IGFEM

This chapter is adapted from a recently submitted article titled "3D dimensionally reduced modeling and gradient-based optimization of microchannel cooling networks" by M. H. Y. Tan and P. H. Geubelle.

4.1 Introduction

While much work has been done on the dimensionally reduced model in 2D, its extension to 3D has been complicated by the existence of a logarithmic singularity along the lines (see [95] and Section 4.3 of this chapter). In [50], Aragón et al. reported an extension of the dimensionally reduced thermal model to 3D but the convergence issue was not addressed. Related to this line of work is a dimensionally reduced model for mass transport in heterogenous media such as blood flow through vessels embedded in tissues [96, 97] or the delivery of drugs into tumors [98]. That model reduces the embedded channels to curves and assumes that the driving force for diffusion at a point on a channel is proportional to the difference between the pressure at a point and the average pressure over a circle normal to the tangent and centered at that point. However, convergence has only been observed when the mesh size in the vicinity of a channel is smaller than the radius of the circle [95, 99]. It should be noted that this averaging approach eliminates the advantages of the dimensionally reduced thermal model because the radius of the averaging circle, being equal to the microchannel radius, is orders of magnitude smaller than the dimensions of the domain. Hence, a graded mesh similar to the one used for the aforementioned finite cross-section models of the microchannels is required for convergence.

Another related approach is the extended finite element method (XFEM) for the simulation of quasi-3D mutiphase flows in porous media such as carbon dioxide leakage through abandoned wells in aquifer systems, where the abandoned wells are modeled as lines [100, 101]. Since a true logarithmic function, which is not a H^1 function, cannot be used as an enrichment function, a truncated logarithmic function with the neighborhood of the singularity replaced with a constant was used in those studies instead. The convergence of the well leakage solution for this special form of the XFEM has been shown to be significantly faster than that obtained with the standard finite element method (SFEM) [100] but it is unclear whether the pressure field as a whole converges

faster than SFEM.

The present chapter develops a special dimensionally reduced model of an actively cooled composite based on a 3D generalized finite element scheme. We show that optimal convergence rate can be recovered by correcting the dimensionally reduced model using a method developed in wire-based electromagnetics [102, 103], which uses the fact that an infinitesimally thin wire has a mesh-dependent numerical effective radius. By changing the electric permittivity and magnetic permeability of the elements surrounding the wires, the effective radius is adjusted to the physical radius of the wire. In contrast to the foregoing averaging approach, the method allows for mesh sizes substantially larger than the physical radius of the microchannel.

This chapter is organized as follows: In Section 4.2, we describe the numerical model. In Section 4.3, we adapt the wire-based electromagnetics method to the thermal model, referring to the resulting method as the *correction method*. We then compare in Section 4.4 the IGFEM solutions with and without the correction scheme. The simulated temperature field is next benchmarked in Section 4.5 against the solution of the 3D nonlinear, coupled analysis performed with ANSYS FLUENT v14.0. Lastly, we apply the IGFEM with the correction method to problems with a more complicated domain geometry in Section 4.6.

4.2 Weak form

In the general 3D case, the weak form (2.5) continues to hold with minor modifications: Γ_T and Γ_q are respectively rewritten as S_T and S_q, while Ω_s and $\{W\}$ of the terms involving $\tilde{h}$ or ϵ are respectively substituted with S_h and $\{N\}$. The corresponding equations for the stiffness matrix and load vector can be readily obtained from (3.6) and (3.7), respectively, with identical modifications.

In the remainder of this chapter, radiation is absent and surface convective is only imposed in Section 4.6, resulting in the following weak form:

$$\begin{aligned} 0 = &- \int_{\Omega_s} \nabla v \cdot \boldsymbol{\kappa} \nabla T \mathrm{d}\Omega + \int_{S_h} v\tilde{h} T \mathrm{d}S - \sum_{i=1}^{n_{ch}} \int_{\Gamma_f^{(i)}} v\gamma^{(i)} \boldsymbol{t}^{(i)} \cdot \nabla T \mathrm{d}\Gamma \\ &+ \int_{\Omega_s} v f \mathrm{d}\Omega + \int_{S_q} v q''^{(p)} \mathrm{d}S + \int_{S_h} v\tilde{h} T_\infty \mathrm{d}S. \end{aligned} \tag{4.1}$$

4.3 Singular solution and correction method

Consider a short segment of a single channel and a small cylindrical region with its axis coinciding with the segment as shown in Figure 4.1. Assuming cylindrical symmetry, we express the

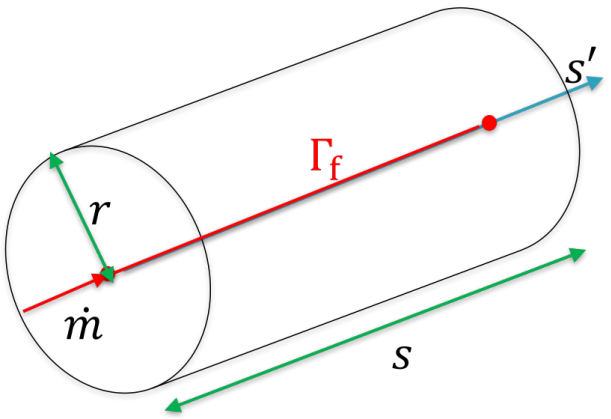

Figure 4.1 – A short segment of a microchannel and a small surrounding cylindrical region, in which an approximate solution is derived.

governing equation for the temperature field as

$$\frac{1}{r}\frac{\partial}{\partial r}\left(r\frac{\partial T}{\partial r}\right)+\frac{\partial^2 T}{\partial s'^2}=\delta^{(\Gamma_f)}r_c\frac{\partial T}{\partial s'}, \tag{4.2}$$

where the line Dirac delta function $\delta^{(\Gamma_f)}$ was introduced in (2.2) and $r_c=\dot{m}c_p/\kappa$. Integrating the governing equation (4.2) over the small cylinder and applying the Gauss divergence theorem, we have

$$2\pi r\int_0^s\frac{\partial T}{\partial r}\mathrm{d}s'+\Phi_{\text{ends}}=r_c\int_0^s\frac{\partial T}{\partial s'}\mathrm{d}s', \tag{4.3}$$

where Φ_{ends} is a term involving the relevant integrals over the ends of the cylinder.

Differentiation of (4.3) with respect to s yields the following jump condition as $r\to 0$:

$$\frac{\partial T}{\partial r}=\frac{r_c}{2\pi r}\frac{\partial T}{\partial s}, \tag{4.4}$$

which is valid for small $r>0$. Using the method of characteristics and denoting an arbitrary differentiable function by ϕ, we arrive at the following approximate general solution in the vicinity of the channel segment:

$$T(r,s)=\phi\left(s+\frac{r_c}{2\pi}\log r\right). \tag{4.5}$$

Substitution of (4.5) into (4.2) then yields a more specific form of the approximate general solution for small $r>0$ given by

$$T(r,s)=G\left(s+\frac{r_c}{2\pi}\log r\right)+C_o, \tag{4.6}$$

where G and C_o are integration constants.

Due to the logarithmic singularity implied by (4.6), the channel has a mesh-dependent effective

radius, thus making the solution sensitive to the mesh size. To alleviate the problem, we modify the thermal conductivity of the elements in the vicinity based on the finite element modeling of thin wires in electromagnetics [102, 103]. As shown in Section 4.3.2, elements with nodes lying within a perpendicular distance r_n from a channel of physical radius r_{phy} are assigned a modified thermal conductivity given by

$$\kappa_m = \kappa \frac{\log \gamma}{\log (r_{phy}/h)}, \tag{4.7}$$

where h is a representative size of the mesh taken as the average of the element edge lengths, and γ is the ratio of the effective size of the channel to the representative mesh size. In this chapter, structured non-conforming meshes are used and h is taken to be the average of the element edge lengths. With this choice of h and by taking $r_n = h$, γ is shown hereafter to be a constant approximately equal to 0.1272. Note that, with $\gamma < 1$, the modified conducitivity $\kappa_m > 0$ if and only if $h > r_{phy}$.

4.3.1 Ratio of effective channel size to mesh size

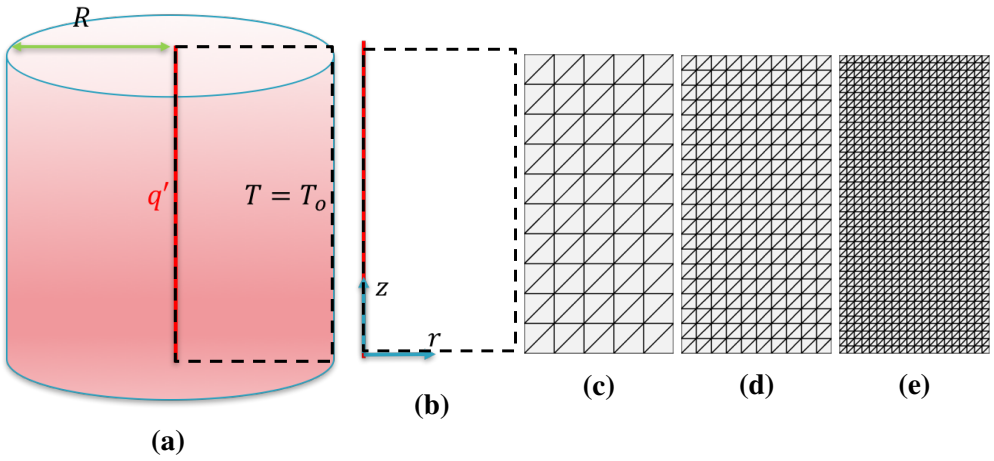

Figure 4.2 – (a) Line source problem and its axisymmetric representation (b) solved using the structured meshes shown in (c)–(e).

Consider an infinitely long cylindrical domain of conductivity κ and radius R, with a line source of strength q' along its axis and surface temperature T_o as shown in Figure 4.2a. The analytical solution for this problem is given by

$$T = -\frac{q'}{2\pi\kappa} \log r + T_o. \tag{4.8}$$

However, the temperature T_{LS} along the line source using the finite element method is finite.

Hence, from (4.8), the line source has an effective radius given by

$$r_{eff} = R \exp \frac{2\pi\kappa(T_o - T_{LS})}{q'}. \tag{4.9}$$

The axisymmetric problem is solved with the 2D structured meshes shown in Figures 4.2c–4.2e by imposing periodic boundary conditions on the two ends perpendicular to the z-axis, and setting $\kappa = 1\,\mathrm{Wm^{-1}K^{-1}}$, $q' = 100\,\mathrm{Wm^{-1}}$ and $T_o = 127\,^{\circ}\mathrm{C}$. Table 4.1 shows that the ratio of effective radius r_{eff} to average element edge length h is almost constant and equal to 0.1272, which is within the range 1/7.2–1/8.4 reported in [102, 103].

Table 4.1 – Ratio of effective radius to average element edge length for the axisymmetric line heat source problem shown in Figure 4.2a.

r_{eff}/R	h/R	$\gamma = r_{eff}/h$
0.0280	0.22021	0.12727447
0.0140	0.11023	0.12728811
0.00702	0.05515	0.12725447
0.00351	0.02758	0.12722742
0.00175	0.01379	0.12721134
0.000877	0.0069	0.12720265

4.3.2 Derivation of the modified conductivity

Consider again the axisymmetric problem shown in Figure 4.2a, where the line source is now replaced with a cylindrical source of radius r_s as shown in Figure 4.3a or b. The solution (4.8) continues to hold for $r_s \leq r \leq R$. If the cylindrical source represents the physical channel, i.e., $r_s = r_{phy}$ as in Figure 4.3a, then the temperature difference between $r = r_{phy}$ and $r = h$ is given by

$$\Delta T_{phy} = -\frac{q'}{2\pi\kappa} \log \frac{h}{r_{phy}}. \tag{4.10}$$

For the numerical channel shown in Figure 4.3b, the temperature difference between $r = r_{eff}$ and $r = h$ is similarly expressed as

$$\Delta T_{num} = -\frac{q'}{2\pi\kappa_m} \log \gamma. \tag{4.11}$$

The modified conductivity κ_m in (4.7) is then obtained by setting $\Delta T_{phy} = \Delta T_{num}$.

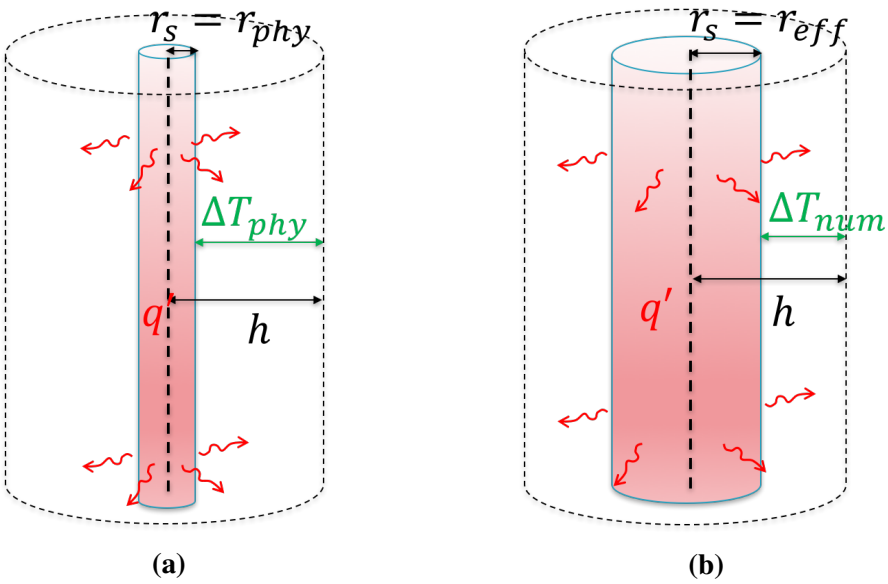

Figure 4.3 – Axisymmetric problems with cylindrical sources of radius r_{phy} and r_{eff}, respectively, representing (a) a physical channel and (b) a numerical channel.

4.4 Convergence study

For the remainder of this dissertation, we refer to the IGFEM with and without the correction as the *modified IGFEM* and *standard IGFEM*, respectively. The convergence properties of the standard and modified IGFEM are compared using the setup shown in Figure 4.4a. The domain, which contains a solid with conductivity $\kappa = 1.0\,\mathrm{Wm^{-1}K^{-1}}$, is subjected to a uniform heat flux along its bottom face and a fixed temperature on the top face while the other faces (faces with normals in the x- and y-directions) are insulated. Embedded in the domain is a channel consisting of piecewise circular arcs of radius 0.005 m. The meshes used are non-conforming tetrahedral structured $n_x \times n_y \times n_z$ meshes, where n_x, n_y, n_z respectively denote the number of divisions in the x-, y- and z-directions. Figure 4.4b and c show the $20 \times 4 \times 4$ and $40 \times 8 \times 8$ meshes used in the convergence study. Defining h_{min} as the minimum element edge length, these two meshes have corresponding h_{min}/L of 0.05 and 0.025, respectively.

As shown in Figure 4.5a, while it captures the gradient discontinuity across the channels, the standard IGFEM solution is strongly mesh dependent. In contrast, the modified IGFEM solution in Figure 4.5b shows little change when the mesh is $40 \times 8 \times 8$ or finer. Denoting a reference solution by T_{ref}, we define the error in the L^2-norm of the finite element temperature field $T^{(h)}$ as $\sqrt{\int_\Omega (T^{(h)} - T_{ref})^2 \mathrm{d}\boldsymbol{x}}$, where the reference solutions for the standard and modified IGFEM are calculated with a $160 \times 32 \times 32$ mesh for which $h_{min}/L = 0.00625$. The plot of L^2-norm of the error in Figure 4.5c shows that, while the standard IGFEM shows suboptimal convergence, the modified IGFEM recovers the optimal convergence rate. For the standard IGFEM, the convergence

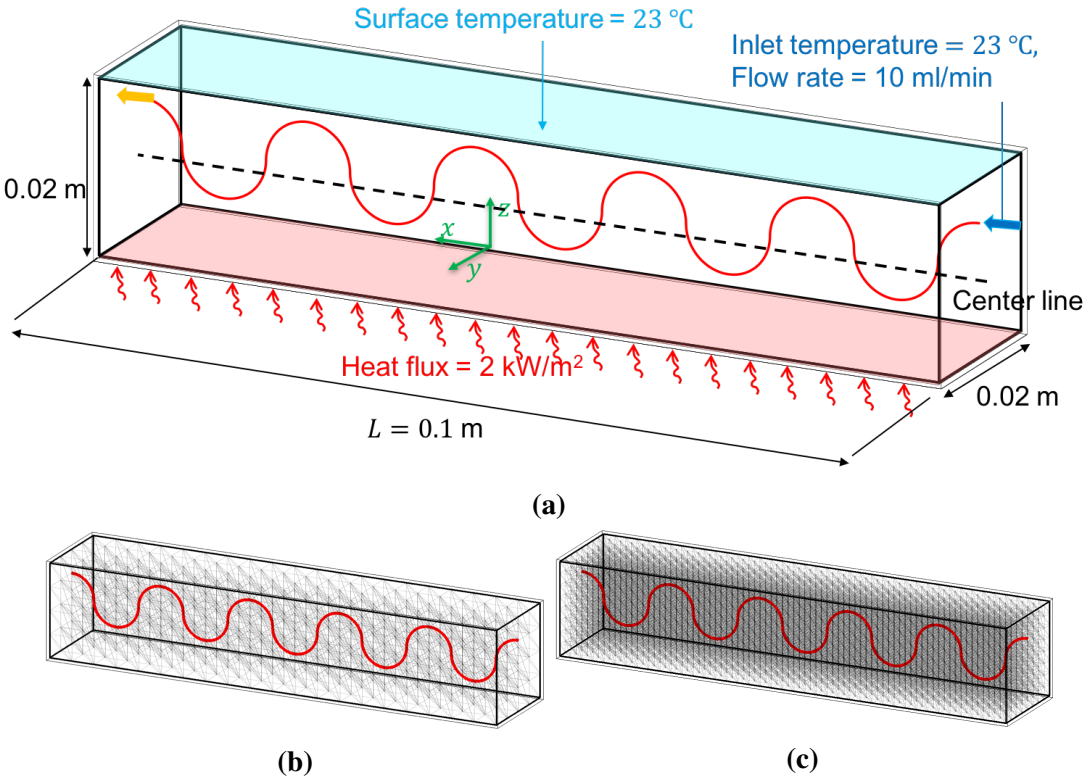

Figure 4.4 – (a) Simulation setup for the convergence study. The side, front and back faces are insulated. (b), (c) $20 \times 4 \times 4$ and $40 \times 8 \times 8$ structured meshes.

rate measured with the average slope of the errors associated with the three finest meshes is 0.67. The modified IGFEM convergence rates are 2.2, 2.3, 2.5 and 2.2 for the physical radii $0.1, 0.2, 0.4$ and 0.5 mm, respectively. The apparent reduction in the convergence rate at small h_{min} for the $r_{phy} = 0.5$ mm case is an artifact of the error in the reference solution, which is obtained with a mesh size $h_{min}/L = 0.00625$ close to the physical radius $r_{phy}/L = 0.005$. At a given mesh size, the error with respect to the corresponding reference solution decreases as the physical radius increases. For all radii and a relatively coarse mesh, the errors associated with the modified IGFEM are substantially smaller.

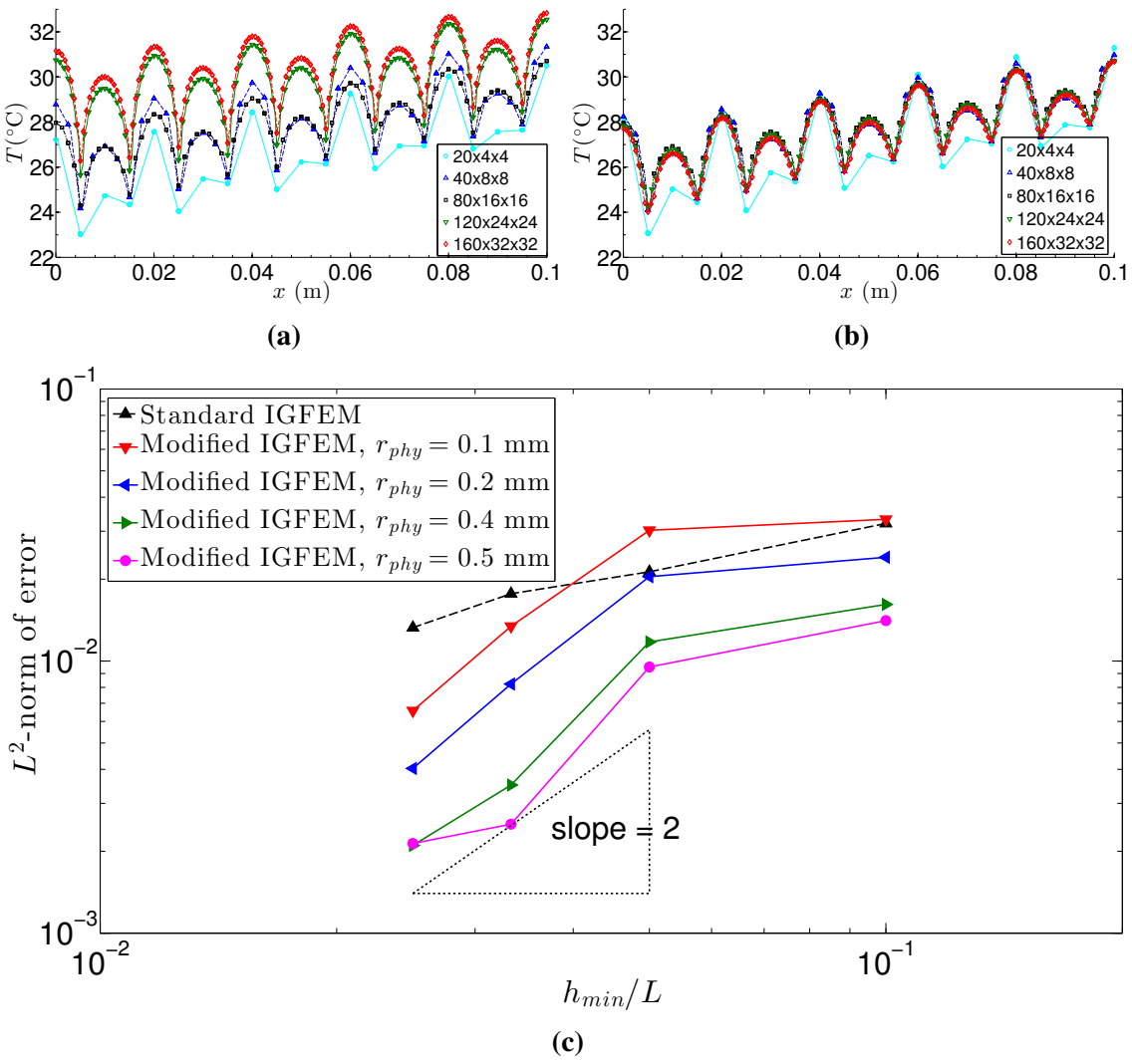

Figure 4.5 – (a) Standard IGFEM and (b) modified IGFEM temperature solutions along the center line indicated by the dashed line in Figure 4.4a for different mesh sizes. (c) L^2-norm of the error of the temperature field as a function of normalized minimum element edge length, where the finest and coarsest meshes are $40 \times 8 \times 8$ and $10 \times 2 \times 2$, respectively.

4.5 Comparison with FLUENT

The modified IGFEM solution is also compared with that obtained using ANSYS FLUENT v14.0 for the two problems shown in Figures 4.6a and c. The boundary conditions are the same for all cases. Taking advantage of symmetry about the midplane normal to the y-direction, half the domain is simulated in FLUENT. The single channel has a circular cross section of diameter 0.001 m while the channels of the branched network have square cross sections of width 0.001 m. A coolant of thermal conductivity 0.419 $\mathrm{Wm^{-1}K^{-1}}$ circulates in the channel. As apparent in Figures 4.6b and d, a large number of elements (> 1.5 million) is required in the FLUENT simulations due

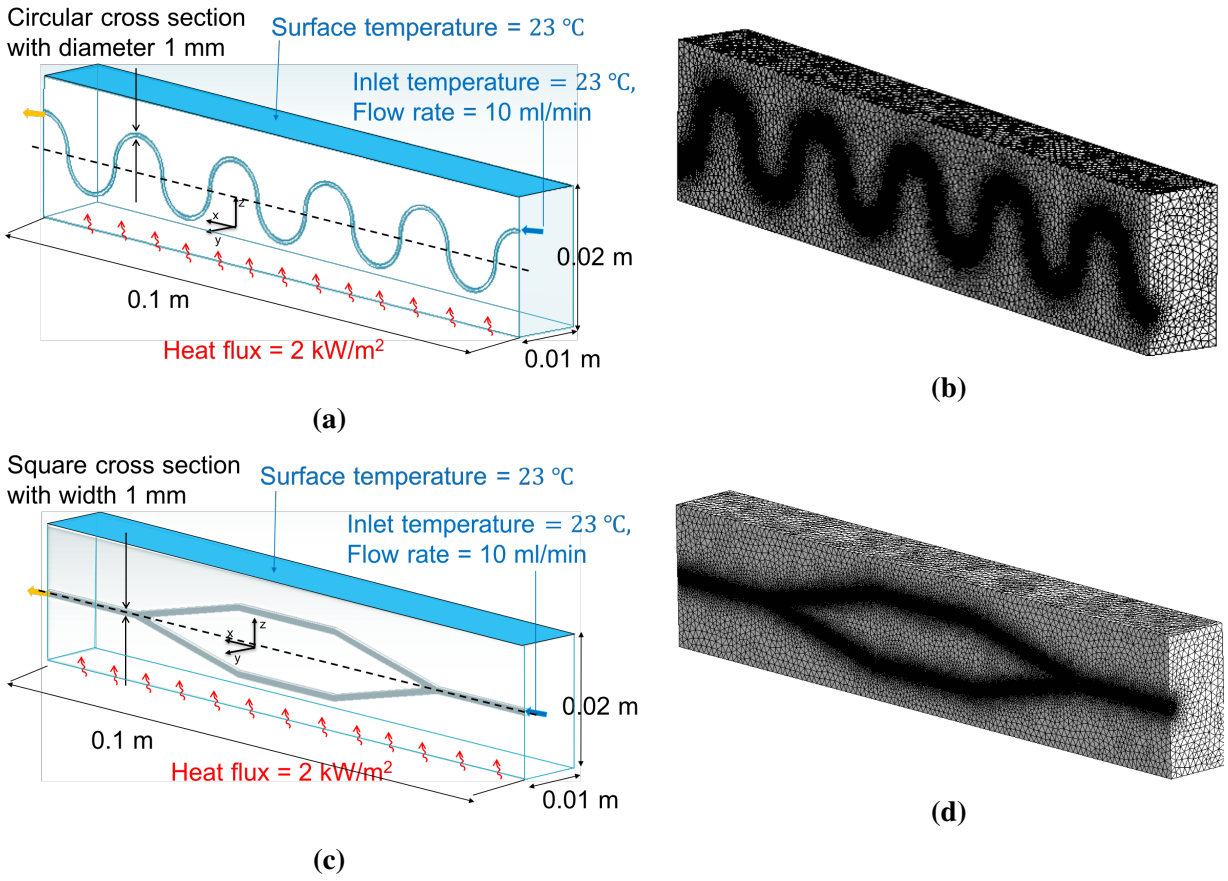

Figure 4.6 – (a), (c): Problem setups with an embedded single channel and branched network of channels. (b), (d): Corresponding FLUENT meshes with 1.5 and 1.7 million elements, respectively.

to the length scale disparity between the channel cross section and the domain size. In contrast, the modified IGFEM uses a structured $40 \times 8 \times 8$ mesh with only 15,360 elements. Further, while the FLUENT simulations involve solving the nonlinear Navier-Stokes and energy equations, the dimensionally reduced model used in IGFEM only requires the solution of the linear weak form given by (4.1), yielding a speed-up of about two orders of magnitude.

A comparison between the IGFEM and FLUENT thermal solutions is presented in Figure 4.7 for the single (Figures 4.7a–c) and branched (Figures 4.7d–f) channel cases. Figures 4.7a and b show that the IGFEM temperature qualitatively agrees with that of FLUENT. As shown in Figure 4.7c, a closer inspection of the IGFEM and FLUENT temperature solutions along the path described in the figure caption reveals that the dimensionally reduced model underpredicts the temperature by about 2 °C. The path is chosen to pass through the wall of the channel since the dimensionally reduced model attempts to model the solid temperature rather than the coolant temperature. The maximum temperature predicted by IGFEM is 48.1 °C compared with 49.5 °C predicted by FLUENT. For

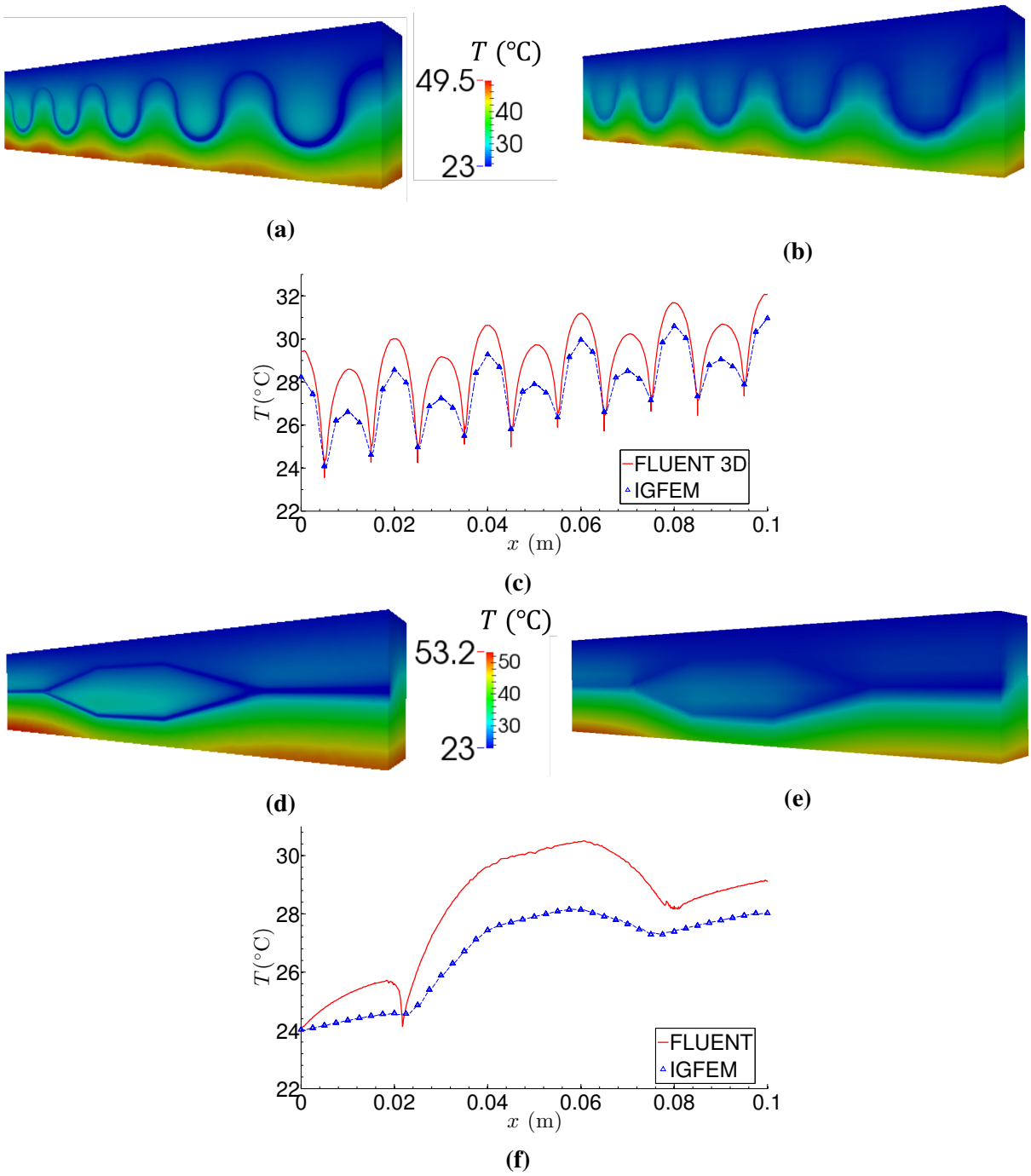

Figure 4.7 – (a), (d) FLUENT and (b), (e) modified IGFEM temperature distributions for the embedded single channel and branched network problems shown in Figure 4.6. (c), (f) IGFEM temperatures compared with the FLUENT temperature along a line offset from the center dashed lines on the plane of symmetry indicated in Figures 4.6a and 4.6c by half the diameter or width in the y-direction.

the branched network, Figures 4.7d–f show that the preceding observation also holds with the maximum temperatures 51.6 °C and 53.2 °C predicted by IGFEM and FLUENT, respectively. These maximum temperature differences are consistent with the predicted difference between the wall temperature of the channel and the mixed mean temperature of the coolant given by (2.4).

4.6 Application to more complex geometries

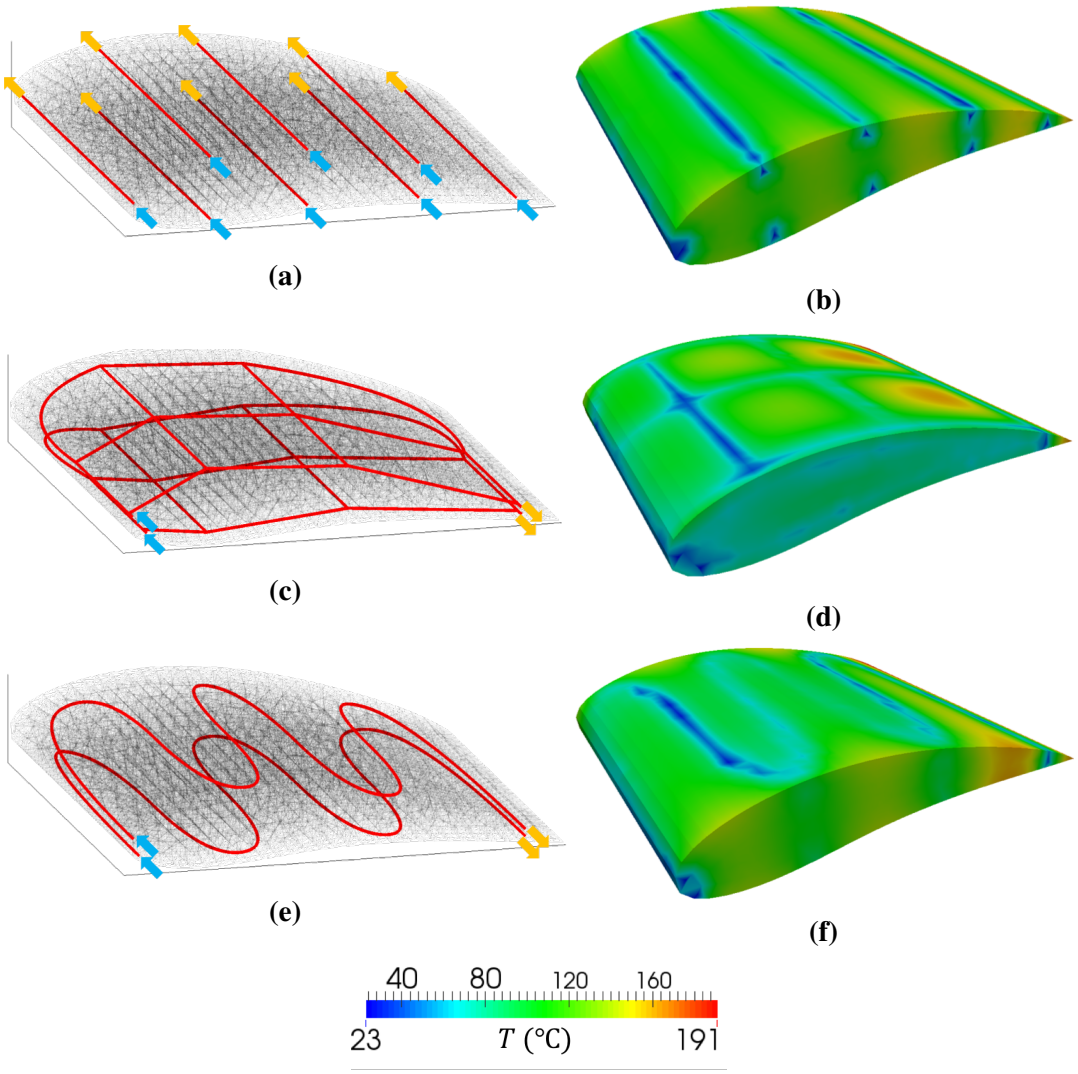

Figure 4.8 – Non-conforming mesh generated by Abaqus for an airfoil subject to convective heating and actively cooled with either (a) parallel straights channels, (b) two branched networks or (c) two serpentine channels. The associated thermal fields are shown in (b), (d) and (f).

We demonstrate in this section that the 3D computational tool we have developed can handle non-conforming meshes associated with more complicated domain geometries. A microvascular composite airfoil with each of the three channels configurations — parallel straight channels, double branched networks and double serpentine channels — as shown in Figure 4.8a, c and e, respectively, is selected for this demonstration. The airfoil is subject to convective heating with convective coefficient $\tilde{h} = 10\,\mathrm{W}/(\mathrm{m}^2\mathrm{K})$ and ambient temperature $T_\infty = 200$ °C. For each channel configuration, a coolant at temperature 22 °C and total flow rate 225.6 ml/min is distributed evenly to each of the inlet. Hence, each of the straight channels has a flow rate of 28.2 ml/min, while a branched network or serpentine channel has 112.8 ml/min.

As apparent in Figures 4.8b, d and f, the temperature distribution associated with the straight channel configuration is more uniform than those of the other two configurations. This result is expected because the former has more inlets and the uniform arrangement of the straight channels allows the coolant to be evenly distributed over the airfoil. Indeed, the maximum temperature corresponding to the straight channel design is 174 °C compared with 191 and 188 °C for the branched and serpentine designs, respectively. The branched design performs slightly worse than the serpentine design because while both geometry and flow rate distribution in the branched networks can be improved, only the geometry of the serpentine design has not been optimized.

4.7 Conclusions

In this chapter, we have developed a novel numerical scheme for the 3D analysis of actively cooled microvascular composites. The thermal solver relies on a dimensionally reduced model of the thermal effect of the embedded microchannels, an interface-enriched generalized finite element method and a modified value of the thermal conductivity of the elements surrounding the channels. The modified IGFEM allowed for the computation of the thermal field in the actively cooled microvascular composites with coarse meshes that did not conform to the microchannels while avoiding convergence issues associated with the logarithmic singularity of the solution in the vicinity of the channels. Solution of problems with more complicated domain geometries was also demonstrated using microvascular airfoils as examples.

5 Adjoint-Based Sensitivity Analysis for Shape Optimization

5.1 Optimization formulation

In a typical design problem, multiple competing objectives need to be considered subject to constraints. Let n_d and n_o respectively be the number of design parameters and objectives. Denoting the design parameters by $\boldsymbol{d} = \{d_1, ..., d_{n_d}\}$, the nodal coordinates of the mesh by $\boldsymbol{X}$ and the multiple objectives as a vector of functions $\boldsymbol{\theta} = \{\theta_1, ..., \theta_{n_o}\}$, the problem can be formulated as the following multi-objective optimization problem:

$$\begin{aligned} \min_{\boldsymbol{d}} \quad & \boldsymbol{\theta}(T^{(h)}(\boldsymbol{X}(\boldsymbol{d}), \boldsymbol{d}), \boldsymbol{X}(\boldsymbol{d}), \boldsymbol{d}), \\ \text{such that} \quad & \boldsymbol{g}(T^{(h)}(\boldsymbol{X}(\boldsymbol{d}), \boldsymbol{d}), \boldsymbol{X}(\boldsymbol{d}), \boldsymbol{d}) \leq 0, \end{aligned} \tag{5.1}$$

where $\boldsymbol{g} \leq 0$ is a vector of constraints and $T^{(h)}(\boldsymbol{X}(\boldsymbol{d}), \boldsymbol{d})$ is obtained from the finite element method.

5.2 Sensitivity analysis of linear discretized weak form

The linear IGFEM-based sensitivity analysis for shape optimization of interface problems was developed in a previous work by Dr. Ahmad Najafi [85]. IGFEM possesses key advantages over standard FEM in shape optimization: (i) similar to other Eulerian-based methods, it does not suffer from severe mesh distortion during the optimization process [85, 104], and (ii) the velocities associated with the original nodes are zero and hence very little computation needs to be done in elements not cut by the channels.

In this section, we develop the IGFEM sensitivity analysis for the shape optimization of embedded channel problems. Throughout this dissertation, the primary objective function considered is the p-norm of the temperature field defined as

$$\|T(\omega)\|_p = \left(\int_\omega T^{(h)p} \mathrm{d}\omega \right)^{1/p}, \tag{5.2}$$

or equivalently, for a fixed ω and p, the p-mean of the temperature field given by

$$\langle T(\omega)\rangle_p := \left(\frac{1}{|\omega|}\int_\omega T^{(h)p}\mathrm{d}\omega\right)^{1/p}, \tag{5.3}$$

where ω refers to a subset of the domain and $|\omega|$ is the size of the subset. For example, ω and $|\omega|$ can be the domain and its volume (or area in 2D), the surface of the domain in 3D and its total surface area, or the channel network and its total length. We often omit ω and write $\langle T\rangle_p$ for brevity after ω has been declared. When $p = 1$, we recover the standard definition of the average. We write $\langle T\rangle_1$ to emphasize that it is the IGFEM average and use $\langle T\rangle$ when it also refers to the average obtained by another method.

The sensitivity of $\|T(\omega)\|_p$ or $\langle T(\omega)\rangle_p$ can be readily computed via the chain rule by first computing the sensitivity of the following function:

$$\tilde{\theta} := |\omega|\langle T(\omega)\rangle_p^p = \|T(\omega)\|_p^p = \int_\omega T^{(h)p}\mathrm{d}\omega = \int_\omega (\{N\}'\{T\})^p\mathrm{d}\omega. \tag{5.4}$$

We develop the sensitivity of $\tilde{\theta}$ based on an IGFEM-based sensitivity analysis developed for interface problems [85], where details on the evaluation of terms such as the derivatives of the shape functions with respect to design parameters and the design velocity field can be found. Without loss of generality, we restrict the following discussion to a single design parameter d. Given a function $\phi(\boldsymbol{x}, d)$ and the shape velocity field $\boldsymbol{v}(\boldsymbol{x}, d) := \partial\boldsymbol{x}/\partial d$, where $\boldsymbol{x}$ denotes the spatial coordinates, the total shape derivative is defined as $\overset{*}{\phi} = (\nabla_x\phi)'\boldsymbol{v} + \partial\phi/\partial d$. Using the Reynolds transport formula and the chain rule $\overset{*}{\overline{\phi_1\phi_2}} = \phi_1\overset{*}{\phi}_2 + \overset{*}{\phi}_1\phi_2$, the derivative of (5.4) with respect to the design parameter d is given by

$$\begin{aligned}
\frac{\partial\tilde{\theta}}{\partial d} &= \int_\omega \left[\overset{*}{\overline{(\{N\}'\{T\})^p}} + (\{N\}'\{T\})^p\nabla_\omega\cdot\boldsymbol{v}\right]\mathrm{d}\omega \\
&= \int_\omega \left[p(\{N\}'\{T\})^{p-1}\overset{*}{\overline{\{N\}'\{T\}}} + (\{N\}'\{T\})^p\nabla_\omega\cdot\boldsymbol{v}\right]\mathrm{d}\omega \\
&= \int_\omega \Bigg[p(\{N\}'\{T\})^{p-1}\left(\left\{\frac{\partial N}{\partial d}\right\}'\{T\} + \{N\}'\overset{*}{\{T\}}\right) \\
&\qquad + (\{N\}'\{T\})^p\nabla_\omega\cdot\boldsymbol{v}\Bigg]\mathrm{d}\omega,
\end{aligned} \tag{5.5}$$

where $\nabla_\omega\cdot$ is the projection of the standard divergence onto ω. For example, if ω has the same dimensionality as the domain, then $\nabla_\omega\cdot = \nabla_x\cdot$, i.e, the operator is simply the standard divergence. If ω is a surface with unit normal vector $\boldsymbol{n}$, then the operator is the surface divergence defined as

$\nabla_\omega \cdot \boldsymbol{\phi} = \mathrm{tr}[(\nabla_x \boldsymbol{\phi})'(\boldsymbol{I} - \boldsymbol{nn})]$, where the jth column of $\nabla_x \boldsymbol{\phi}$ is the spatial gradient of ϕ_j. If ω is a curve with unit tangent $\boldsymbol{t}$, then the operator is a line divergence given by $\nabla_\omega \cdot \boldsymbol{\phi} = \mathrm{tr}[(\nabla_x \boldsymbol{\phi})'(\boldsymbol{tt})]$. In writing $\{\overset{*}{N}\}$ as $\{\partial N/\partial d\}$, we have implicitly assumed that all the arguments of $\{N\}$ have been expressed explicitly as functions of d. Note that, unlike for the standard FEM, the term $\{\partial N/\partial d\} \neq 0$ in XFEM/GFEM/IGFEM [85]. The term, easily missed if the non-discretized form of (5.4) is differentiated directly, cannot be neglected to obtain the correct derivative.

(5.5) can be rewritten as

$$\frac{\partial \tilde{\theta}}{\partial d} = \{F^{(adj)}\}'\{\overset{*}{T}\} + R, \tag{5.6}$$

where

$$\{F^{(adj)}\} = \int_\omega p(\{N\}'\{T\})^{p-1}\{N\}\mathrm{d}\omega, \tag{5.7}$$

and

$$R = \int_\omega \left[p(\{N\}'\{T\})^{p-1} \left\{ \frac{\partial N}{\partial d} \right\}' \{T\} + (\{N\}'\{T\})^p \nabla_\omega \cdot \boldsymbol{v} \right] \mathrm{d}\omega. \tag{5.8}$$

To obtain $\{\overset{*}{T}\}$, we differentiate the discretized weak form (3.5) with $\epsilon = 0$ in (3.6) to obtain

$$[K]\{\overset{*}{T}\} = \{F^{(pseudo)}\} := -\left[\frac{\partial K}{\partial d}\right]\{T\} + \left\{\frac{\partial F}{\partial d}\right\}, \tag{5.9}$$

where

$$\begin{aligned}
\left[\frac{\partial K}{\partial d}\right] = & \int_{\Omega_s} \left(\left[\frac{\partial B}{\partial d}\right][\kappa][B]' + [B][\kappa]\left[\frac{\partial B}{\partial d}\right]' + [B][\kappa][B]'\nabla_x \cdot \boldsymbol{v} \right) \mathrm{d}\Omega \\
& + \int_{\Omega_s} \tilde{h} \left(\left\{\frac{\partial W}{\partial d}\right\}\{N\}' + \left\{\frac{\partial N}{\partial d}\right\}\{W\}' + \{W\}\{N\}'\nabla_x \cdot \boldsymbol{v} \right) \mathrm{d}\Omega \\
& + \sum_{i=1}^{n_{ch}} \int_{\Gamma_f^{(i)}} \left[\left\{\frac{\partial W}{\partial d}\right\}([B]\gamma^{(i)}\{t^{(i)}\})' + \{W\}([B]\gamma^{(i)}\{t^{(i)}\})'\nabla_{\partial l} \cdot \boldsymbol{v} \right. \\
& \qquad \left. + \{W\}\left(\left[\frac{\partial B}{\partial d}\right]\gamma^{(i)}\{t^{(i)}\} + [B]\frac{\partial \gamma^{(i)}}{\partial d}\{t^{(i)}\} + [B]\gamma^{(i)}\left\{\frac{\partial t^{(i)}}{\partial d}\right\}\right)' \right] \mathrm{d}\Gamma,
\end{aligned} \tag{5.10}$$

and

$$\begin{aligned}
\left\{\frac{\partial F}{\partial d}\right\} = & \int_{\Omega_s} \left(\left\{\frac{\partial W}{\partial d}\right\} f + \{W\}\overset{*}{f} + \{W\} f \nabla_x \cdot \boldsymbol{v} \right) \mathrm{d}\Omega \\
& + \int_{\Omega_s} \tilde{h} T_\infty \left(\left\{\frac{\partial W}{\partial d}\right\} + \{W\}\nabla_x \cdot \boldsymbol{v} \right) \mathrm{d}\Omega \\
& + \int_{\Gamma_q} \left(\left\{\frac{\partial N}{\partial d}\right\} q^{\prime\prime(p)} + \{N\}\overset{*}{q}^{\prime\prime(p)} + \{N\} q^{\prime\prime(p)} \nabla_{\partial l} \cdot \boldsymbol{v} \right) \mathrm{d}\Gamma,
\end{aligned} \tag{5.11}$$

where $\nabla_{\partial l}\cdot$ denotes the line divergence operator defined earlier. The evaluation of $\left\{\partial t^{(i)}/\partial d\right\}$ is straightforward and will not be detailed here, and we describe the calculation of $\{\partial W/\partial d\}$ and $\partial\gamma^{(i)}/\partial d$ in Appendices A.3 and A.4, respectively. With minor modification to the terms involving $\tilde{h}$, (5.10) and (5.11) apply to the 3D case: Γ_T and Γ_q are respectively rewritten as S_T and S_q, while Ω_s, $\{W\}$ and $\nabla_x\cdot$ of the terms involving $\tilde{h}$ are respectively replaced with S_h, $\{N\}$ and the surface divergence.

Let the superscripts (f) and (p) respectively denote the free and prescribed nodal values of the temperature field. $\{\overset{*}{T}\}$ can be partitioned into two parts:

$$\{\overset{*}{T}\} = \begin{Bmatrix} \overset{*}{T^{(f)}} \\ \overset{*}{T^{(p)}} \end{Bmatrix} = \begin{Bmatrix} \overset{*}{T^{(f)}} \\ 0 \end{Bmatrix}, \tag{5.12}$$

where we have used $\overset{*}{T^{(p)}} = 0$. Similarly, by partitioning $[K]$ into four parts, (5.9) becomes

$$[K^{(ff)}]\{\overset{*}{T^{(f)}}\} = \{F^{(pseudo,f)}\}. \tag{5.13}$$

At this point, we can already calculate (5.5) by solving (5.13) for each design parameter. If $n_f \times n_f$ is the size of $[K^{(ff)}]$ and n_d is the number of design parameters, then the number of operations is $O(n_d n_f^2)$. The number of operations can be made independent of n_d by using the adjoint method, in which the product of a multiplier $\{\Lambda^{(f)}\}$ and (5.13) is added to (5.6) to yield

$$\begin{aligned} \frac{\partial\tilde{\theta}}{\partial d} &= \{F^{(adj)}\}'\{\overset{*}{T}\} + R + \{\Lambda^{(f)}\}'\left(-[K^{(ff)}]\{\overset{*}{T^{(f)}}\} + \{F^{(pseudo,f)}\}\right) \\ &= \left(\{F^{(adj,f)}\}' - \{\Lambda^{(f)}\}'[K^{(ff)}]\right)\{\overset{*}{T^{(f)}}\} + \{\Lambda^{(f)}\}'\{F^{(pseudo,f)}\} + R. \end{aligned} \tag{5.14}$$

Upon setting the coefficient of $\{\overset{*}{T^{(f)}}\}$ to zero, we have

$$[K^{(ff)}]'\{\Lambda^{(f)}\} = \{F^{(adj,f)}\} \tag{5.15}$$

and

$$\frac{\partial\tilde{\theta}}{\partial d} = \{\Lambda^{(f)}\}'\{F^{(pseudo,f)}\} + R. \tag{5.16}$$

It should be noted that (5.15) needs to be solved only once regardless of n_d. We also emphasize that $[K^{(ff)}]$ is not symmetric in general due to the convective term. The chain rule the yields the

following expression for the sensitivity of $\theta := \|T\|_p$ or $\theta := \langle T \rangle_p$:

$$\frac{\partial \theta}{\partial d} = \frac{\theta}{p\tilde{\theta}} \frac{\partial \tilde{\theta}}{\partial d}. \tag{5.17}$$

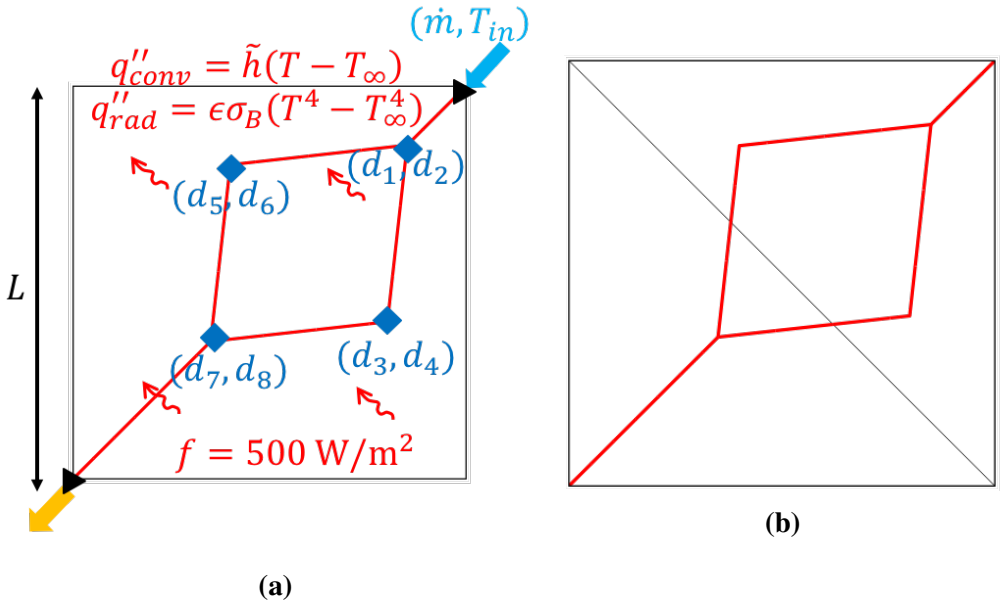

Figure 5.1 – (a) Verification setup for the sensitivity analysis of the linear discretized weak form. The inlet and outlet of the channel represented by the black triangles are fixed while the coordinates of the interior control points $(d_1, ..., d_8)$ are chosen as design parameters. (b) Non-conforming structured mesh used for the verification exercise.

We verify the sensitivity analysis for the linear thermal model with the setup shown in Figure 5.1, using the 8-norm of the temperature field as the objective function and the coordinates of the interior control points as design parameters. A uniform thermal load of $f = 500\,\mathrm{Wm}^{-2}$ is applied to the panel while convective and radiative losses (q''_{conv} and q''_{rad}) are imposed. An aqueous ethylene glycol coolant with the properties listed in Table 5.1a is pumped through the channel network with a flow rate of 0.5 g/s (28.2 ml/min). A nonconforming mesh shown in Figure 5.1b is used for this study. In Table 5.1b, we present the relative differences of the gradients of the objective function computed using the sensitivity analysis and the central finite difference method. Evidently, the two methods are in very good agreement.

Table 5.1 – (a) Parameters for the setup shown in Figure 5.1. (b) Relative differences between the sensitivities of the 8-norm of the panel temperature computed from the sensitivity analysis of the nonlinear discretized weak form and those obtained from the central finite difference method with perturbation size 10^{-7}.

Parameter	Value
Solid thermal conductivity κ	2.04 $\mathrm{Wm^{-1}K^{-1}}$
Panel thickness t	3 mm
Uniform heat source f	500 $\mathrm{Wm^{-2}}$
Convective coefficient $\tilde{h}$	8 $\mathrm{Wm^{-2}K^{-1}}$
Surface emissivity ϵ	1.0
Ambient temperature T_∞	22 °C
Coolant inlet temperature T_{in}	22 °C
Coolant flow rate $\dot{m}$	0.5 g/s
Coolant specific heat capacity c_p	3494 $\mathrm{J/kg \cdot K}$
Coolant kinematic viscosity ν	$3.405 \times 10^{-6}\,\mathrm{m^2/s}$
L	0.1 m

(a)

Design parameter	Initial value	Relative difference
d_1	0.085	3.53e-7
d_2	0.085	1.20e-6
d_3	0.08	4.74e-9
d_4	0.04	5.64e-9
d_5	0.04	1.36e-8
d_6	0.08	1.58e-10
d_7	0.035	6.46e-8
d_8	0.035	5.77e-8

(b)

5.3 Sensitivity analysis of nonlinear discretized weak form

In the nonlinear case, (5.9), (5.10), (5.11), (5.13) and (5.15) need to be modified while (5.6), (5.7), (5.8) and (5.16) remain the same since only the calculation of $\{\overset{*}{T}\}$ is different. To see that, consider the indicial form of (3.5),

$$K_{ij}(\{T\}, d)T_j(d) = F_i(d). \tag{5.18}$$

Differentiating both sides and noting that $\{T\} = \{T_1, T_2, ...\}'$, we have

$$\left(\frac{\partial K_{ij}}{\partial T_k}\overset{*}{T}_k + \frac{\partial K_{ij}}{\partial d}\right)T_j + K_{ij}\overset{*}{T}_j = \frac{\partial F_i}{\partial d}, \tag{5.19}$$

which upon rearranging gives

$$\left(\frac{\partial K_{ij}}{\partial T_k}T_j + K_{ik}\right)\overset{*}{T}_k = F_i^{(pseudo)} := \frac{\partial F_i}{\partial d} - \frac{\partial K_{ij}}{\partial d}T_j. \tag{5.20}$$

Notice that the term in the parenthesis on the left hand side is the Jacobian defined in (3.9). Hence we can rewrite the equation as

$$J_{ik}\overset{*}{T}_k = F_i^{(pseudo)}, \tag{5.21}$$

where the Jacobian and the right hand side are evaluated at the solution of the last iteration. Note that (5.21) is a *linear* system of equations defining $\{\overset{*}{T}\}$. The sensitivities of the stiffness matrix and the load vector are respectively given by

$$\begin{aligned}\left[\frac{\partial K}{\partial d}\right] &= \int_{\Omega_s}\left(\left[\frac{\partial B}{\partial d}\right][\kappa][B]' + [B][\kappa]\left[\frac{\partial B}{\partial d}\right]' + [B][\kappa][B]'\nabla_x\cdot\boldsymbol{v}\right)\mathrm{d}\Omega \\ &+ \int_{\Omega_s}(\tilde{h}+\epsilon\sigma_B T^{(h)3})\left(\left\{\frac{\partial W}{\partial d}\right\}\{N\}' + \left\{\frac{\partial N}{\partial d}\right\}\{W\}' + \{W\}\{N\}'\nabla_x\cdot\boldsymbol{v}\right)\mathrm{d}\Omega \\ &+ \int_{\Omega_s} 3\epsilon\sigma_B T^{(h)2}\{T\}'\left\{\frac{\partial N}{\partial d}\right\}\{W\}\{N\}'\mathrm{d}\Omega \\ &+ \sum_{i=1}^{n_{ch}}\int_{\Gamma_f^{(i)}}\left[\left\{\frac{\partial W}{\partial d}\right\}([B]\gamma^{(i)}\{t^{(i)}\})' + \{W\}([B]\gamma^{(i)}\{t^{(i)}\})'\nabla_{\partial l}\cdot\boldsymbol{v}\right. \\ &\qquad\left. + \{W\}\left(\left[\frac{\partial B}{\partial d}\right]\gamma^{(i)}\{t^{(i)}\} + [B]\frac{\partial\gamma^{(i)}}{\partial d}\{t^{(i)}\} + [B]\gamma^{(i)}\left\{\frac{\partial t^{(i)}}{\partial d}\right\}\right)'\right]\mathrm{d}\Gamma, \end{aligned}\tag{5.22}$$

and

$$\begin{aligned}\left\{\frac{\partial F}{\partial d}\right\} &= \int_{\Omega_s}\left(\left\{\frac{\partial W}{\partial d}\right\}f + \{W\}\overset{*}{f} + \{W\}f\nabla_x\cdot\boldsymbol{v}\right)\mathrm{d}\Omega \\ &+ \int_{\Omega_s}(\tilde{h}T_\infty + \epsilon\sigma_B T_\infty^4)\left(\left\{\frac{\partial W}{\partial d}\right\} + \{W\}\nabla_x\cdot\boldsymbol{v}\right)\mathrm{d}\Omega \\ &+ \int_{\Gamma_q}\left(\left\{\frac{\partial N}{\partial d}\right\}q^{\prime\prime(p)} + \{N\}\overset{*}{q}^{\prime\prime(p)} + \{N\}q^{\prime\prime(p)}\nabla_{\partial l}\cdot\boldsymbol{v}\right)\mathrm{d}\Gamma. \end{aligned}\tag{5.23}$$

It should be noted that (5.23) can be obtained from (5.11) simply by replacing $\tilde{h}T_\infty$ with $\tilde{h}T_\infty + \epsilon\sigma_B T_\infty^4$. However, it is not sufficient to replace $\tilde{h}$ in (5.10) with $\tilde{h} + \epsilon\sigma_B T^{(h)3}$ to derive (5.22). An additional term in the third row appears since $\{\partial N/\partial d\}$ does not vanish in IGFEM. As before, (5.22) and (5.23) hold in the 3D case with Ω_s, $\{W\}$, $\nabla_x\cdot$ of the terms containing $\tilde{h}, \epsilon$ replaced with S_h, $\{N\}$ and the surface divergence, respectively.

Due to (5.21), the counterparts of (5.13) and (5.15) are respectively given by

$$[J^{(ff)}]\{\overset{*}{T}^{(f)}\} = \{F^{(pseudo,f)}\}, \tag{5.24}$$

and

$$[J^{(ff)}]'\{\Lambda^{(f)}\} = \{F^{(adj,f)}\}. \tag{5.25}$$

The sensitivity of the objective function can then by evaluated using (5.16). It is worth emphasizing that at every iteration of an optimization in which the sensitivity is required, the sensitivity calculation only needs to be performed once after the iterative procedure given in Section 3.2.1 terminates.

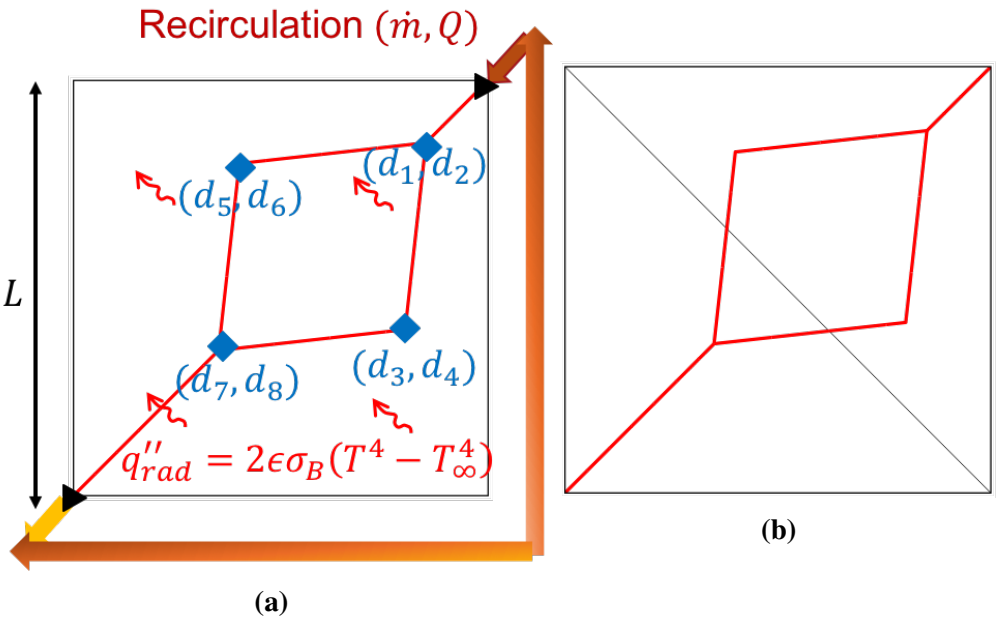

Figure 5.2 – (a) Verification setup for the sensitivity analysis of the nonlinear discretized weak form for the problems in Chapter 9. The inlet and outlet of the channel represented by the black triangles are fixed while the coordinates of the interior control point $(d_1, ..., d_8)$ are chosen as design parameters. (b) Non-conforming structured mesh used for the verification exercise.

In the remainder of this section, we verify the sensitivity analysis of the nonlinear discretized weak form with the finite difference method for the objective functions of interest in Chapter 9. The first objective function is given by

$$\theta_1 = ||(T^{(h)} - T_o)(\Gamma_f)||_p := \left(\int_{\Gamma_f} |T^{(h)} - T_o|^p \mathrm{d}\Gamma\right)^{\frac{1}{p}}, \tag{5.26}$$

which is the the p-norm of the temperature along the network offset by T_o. For this particular objective function, (5.7) and (5.8) becomes the following:

$$\{F^{(adj)}\} = \int_{\Gamma_f} p(\{N\}'\{T\} - T_o)^{p-1}\{N\}\mathrm{d}\Gamma, \tag{5.27}$$

and

$$R = \int_{\Gamma_f} \left[p(\{N\}'\{T\} - T_o)^{p-1} \left\{ \frac{\partial N}{\partial d} \right\}' \{T\} + (\{N\}'\{T\} - T_o)^p \nabla_l \cdot \boldsymbol{v} \right] \mathrm{d}\Gamma. \tag{5.28}$$

The second objective function is the inlet temperature of a single-inlet network defined as

$$\theta_2 = T_{in}. \tag{5.29}$$

In this case, $\{F^{(adj)}\}$ is a vector with all entries equal to zero except the entry corresponding to the inlet node, which equal unity, and $R = 0$.

Lastly, consider the pressure difference between nodes j and k as the objective function, i.e,

$$\theta_3 = \Delta P := P_j - P_k. \tag{5.30}$$

For simplicity, consider a single design parameter d. To obtain $\partial(\Delta P)/\partial d$, we differentiate the system of hydraulic equations (2.11) to obtain

$$[G] \left\{ \frac{\partial P}{\partial d} \right\} = - \left[\frac{\partial G}{\partial d} \right] \{P\} + \left\{ \frac{\partial S}{\partial d} \right\}. \tag{5.31}$$

Since the kinematic viscosity ν is evaluated at the average temperature of the network $\langle T \rangle_1 = (\int_{\Gamma_f} T^{(h)} \mathrm{d}\Gamma)/L_{ch}$, $\partial[G]/\partial d$ is given by

$$\frac{\partial [G]}{\partial d} = \frac{\partial [G]}{\partial \nu} \frac{\partial \nu}{\partial \langle T \rangle_1} \frac{\partial \langle T \rangle_1}{\partial d} + \sum_{i=1}^{n_{ch}} \frac{\partial [G]}{\partial L_i} \frac{\partial L_i}{\partial d}. \tag{5.32}$$

Thus, $\partial(\Delta P)/\partial d$ can be readily obtained by substituting (5.32) into (5.31) and solving the resulting linear system of equations.

The sensitivities of the objective functions θ_1, θ_2 and θ_3 defined above are verified with the central finite difference method using the setup shown in Figure 5.2a, which is specifically designed for Chapter 9. A recirculation boundary condition is prescribed, leading to a temperature difference between the inlet and outlet of $T_{in} - T_{out} = Q/(\dot{m}c_p)$. The heat added to the coolant Q is lost through radiation q''_{rad}. Parameter values associated with the setup can be found in Table 5.2a.

We select the coordinates of the interior control point of the channel d_1 and d_2 as design parameters, and define the relative difference between the sensitivity of the objective function θ_i obtained from the sensitivity analysis and the finite difference method (subscript FD) as

$$\varepsilon_{ij} = \frac{|\partial\theta_i/\partial d_j - (\partial\theta_i/\partial d_j)_{FD}|}{\partial\theta_i/\partial d_j}, \tag{5.33}$$

where $i = 1, 2, 3$ and $j = 1, 2$. We present the relative differences of the solutions computed on the non-conforming structured mesh (Figures 5.2b) in Table 5.2b. As evident from the last column of the table, the values from the sensitivity analysis agree with those from numerical differentiation within the range 10^{-7}–10^{-8}.

Table 5.2 – (a) Parameters for the setup shown in Figure 5.2. (b) Relative differences between the sensitivities of the objective functions θ_1, θ_2, and θ_3 ((5.26) with $T_o = 273.15$, (5.29) and (5.30)) computed from the sensitivity analysis of the nonlinear discretized weak form and those obtained from the central finite difference method with perturbation size 10^{-7}.

Parameter	Value
Solid thermal conductivity κ	78.8 $\mathrm{Wm^{-1}K^{-1}}$
Panel thickness t	1 mm
Surface emissivity ϵ	1
Sink temperature T_∞	50 K
Dissipated heat rate Q	80 W
Coolant flow rate $\dot{m}$	1.7827 g/s
Coolant specific heat capacity c_p	2711 $\mathrm{J/kg \cdot K}$
Coolant kinematic viscosity ν	Equation in Figure A.3d
L	0.1 m

(a)

Design parameter	Initial value	ε_{1j}	ε_{2j}	ε_{3j}
d_1	0.085	4.02e-8	6.09e-8	7.53e-12
d_2	0.085	1.35e-7	2.24e-7	5.54e-9
d_3	0.08	7.34e-9	3.04e-9	2.71e-9
d_4	0.04	1.21e-8	8.19e-9	3.29e-10
d_5	0.04	4.35e-8	2.51e-8	4.49e-9
d_6	0.08	1.35e-8	7.18e-9	4.44e-10
d_7	0.035	6.38e-7	2.87e-7	1.62e-8
d_8	0.035	5.71e-7	2.64e-7	1.46e-8

(b)

6 2D Gradient-Based Design of Actively Cooled Battery Composite Panels

This chapter is adapted from the article published in the *International Journal of Heat and Mass Transfer* [52], titled "Gradient-based design of actively cooled microvascular composites" by M. H. Y. Tan, A. R. Najafi, S. J. Pety, S. R. White and P. H. Geubelle.

6.1 Introduction

This chapter presents a validation of the numerical model developed in Chapter 2 and a single-objective gradient-based shape optimization scheme for microvascular composites used as battery cooling panels [105, 106]. Battery cooling is essential to extend the range of electric vehicles and prolong battery life [107]. For batteries with high energy density such as those in electric vehicles, liquid cooling is the most effective cooling method [108]. As shown in Figure 6.1a–c, a typical battery packaging for electric vehicles consists of stacks of battery cells separated by fiberglass or steel panels to provide structural protection and cooling plates to regulate battery temperature. Recently, a novel battery packaging described schematically in Figure 6.1d and e, in which a single microvascular composite provides both cooling and crash protection, has been proposed [106, 109]. The crash protection is superior to conventional battery packaging because the carbon fiber reinforced composite possesses high specific strength, stiffness as well as energy absorbing ability [110, 111].

In optimization studies of cooling panels, objective functions commonly considered are average temperature and standard deviation, a measure of temperature uniformity [20, 46]. Temperature uniformity is important because non-uniformity causes variations in reaction rates that lead to incomplete energy utilization and shorter battery life [107]. However, average temperature alone as an objective function is not sufficient to keep the maximum temperature in the panel low. Furthermore, as seen later, the average temperature is relatively insensitive to the channel design. Besides, small regions with high temperature akin to the appearance of areas with stress concentration in a compliance-based optimization [112] may also appear in the optimal design. This suggests that the maximum temperature be minimized rather than the average temperature. Unfortunately, the maximum temperature is not differentiable in a classical sense [113] and therefore conventional gradient-based optimizer cannot be used when the maximum temperature is chosen as the objec-

tive function. Instead, following a standard practice in stress-based optimization [114, 115, 112], the p-mean of the temperature with a sufficiently large p is used in this work.

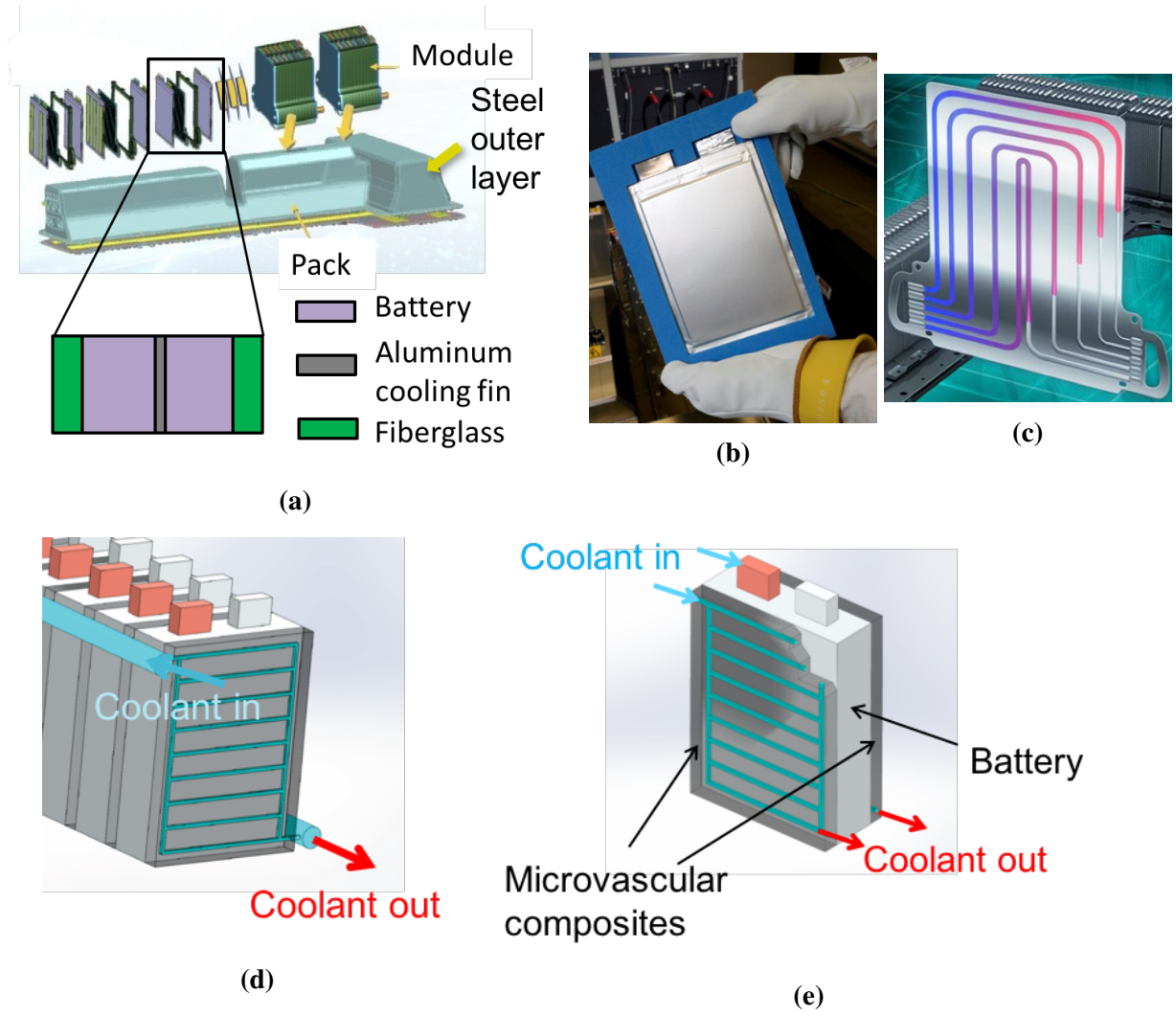

Figure 6.1 – (a) Chevrolt Volt battery packaging containing alternating layers of (b) Li-ion pouch cells and (c) aluminum cooling fins. Adapted from [116, 117, 118]. Schematic of actively cooled microvascular composite battery packaging (d) consisting of the unit cells (e) [106, 109].

This chapter is organized as follows: Starting in Section 6.2, we validate the dimensionally reduced models against more complex 3D, fully coupled FLUENT simulations and experiments performed by Stephen J. Pety. We then describe the optimization problem in Section 6.3. Lastly, we apply the IGFEM-based shape optimization scheme to optimize different parallel network designs defined by the number of branches and validate one of the optimized designs in Section 6.4.

6.2 Validation study

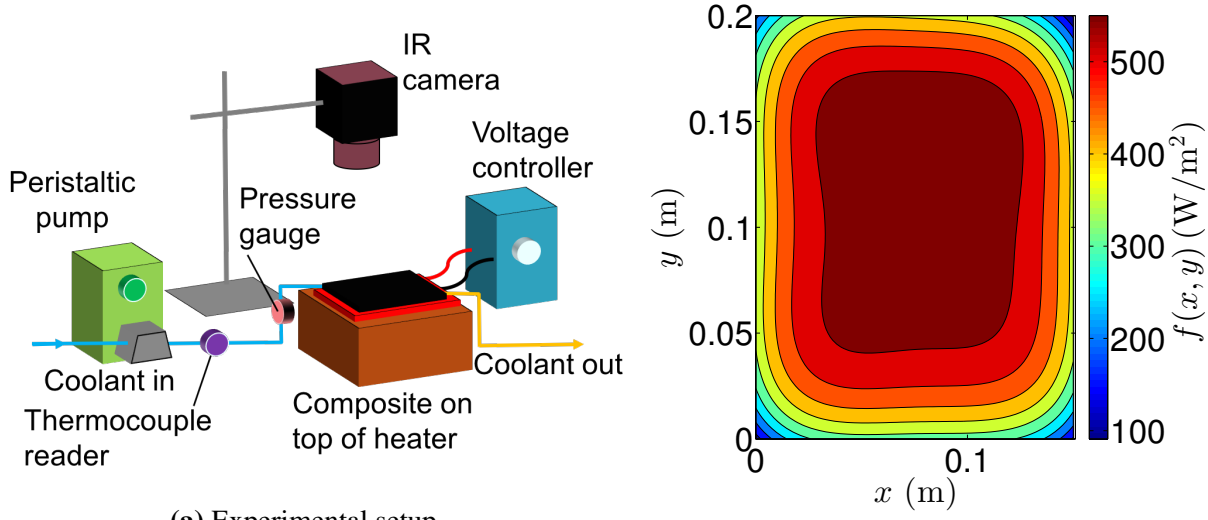

(a) Experimental setup.

(b) Experimental heat source.

Figure 6.2 – (a) Experimental setup for the heating of a microvascular composite panel with active-cooling. (b) Fourth-order polynomial fit (6.1) to the heat flux distribution.

Table 6.1 – Experimental conditions, coolant and composite thermal properties.

In-plane dimension L_x	150 mm
In-plane dimension L_y	200 mm
Panel thickness t	3 mm
Fin coefficient $\tilde{h}$	8 $\mathrm{Wm^{-2}K^{-1}}$
Ambient temperature T_∞	21 °C
Emissivity ϵ	0.97
Coolant density	1065 $\mathrm{kgm^{-3}}$ [20]
Coolant conductivity	0.419 $\mathrm{Wm^{-1}K^{-1}}$ [20]
Coolant heat capacity	3494 $\mathrm{Jkg^{-1}K^{-1}}$ [20]
Coolant flow rate	28.2 ml/min
Coolant inlet temperature	22 °C
In-plane conductivity	2.04 $\mathrm{Wm^{-1}K^{-1}}$
Out-of-plane conductivity	0.59 $\mathrm{Wm^{-1}K^{-1}}$

Experiments were performed on microvascular composite panels with the setup shown in Figure 6.2a and parameters presented in Table 6.1. A composite panel, shown schematically in Figure 6.3a, was heated from below by an electric heater with a heat distribution profile shown in Figure

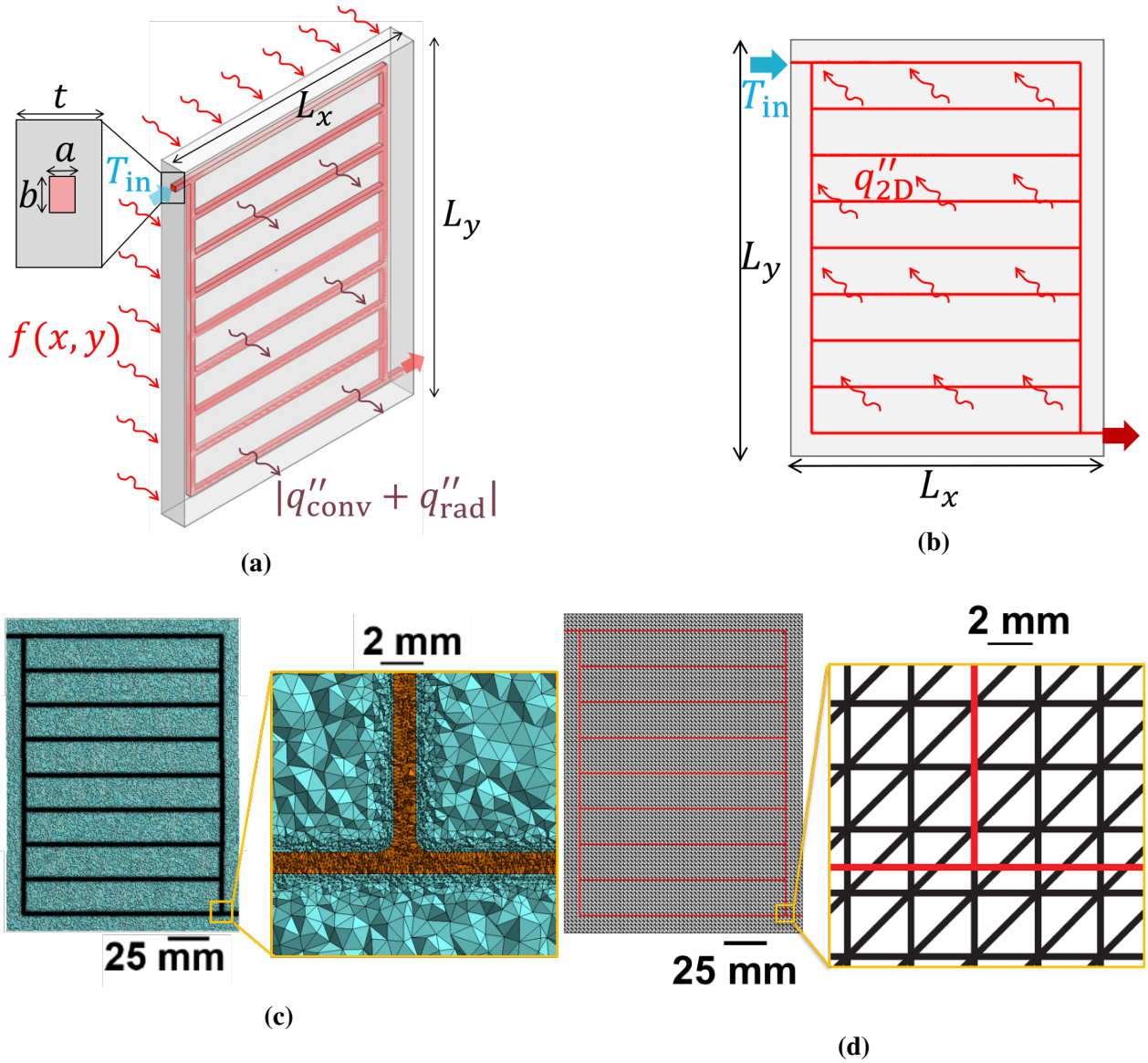

Figure 6.3 – (a) FLUENT setup and (b) IGFEM setup with $q''_{2D} = f(x,y) - \tilde{h}(T - T_\infty)$ for validation. Meshes used for the (c) FLUENT and (d) IGFEM simulations.

6.2b given by the following fourth order polynomial fit:

$$\begin{aligned} f(\boldsymbol{x}) = f(x,y) = 500(&0.2489 + 23.42x + 21.87y - 485.7x^2 - 16.96xy - 356.8y^2 \\ &+ 4317x^3 + 170.4yx^2 + 276.7y^2x + 2422y^3 \\ &- 14060x^4 - 791yx^3 - 490x^2y^2 - 972.2y^3x - 5849y^4)\,\mathrm{Wm}^{-2}. \end{aligned} \tag{6.1}$$

The spatial average of (6.1) is $\int_{\Omega_s} f(x,y)\mathrm{d}\Omega/|\Omega_s| \approx 500\,\mathrm{W/m}^2$, which represents the characteristic heat flux generated by adjacent battery pouches. A water ethylene/glycol coolant was pumped through the vascular network with a peristaltic pump and the resulting pressure drop across the

channel network was measured with pressure transducers. While the inlet temperature was determined with a thermocouple, the temperature distribution of the top surface of the panel was recorded with an infrared (IR) camera.

We apply $f(x, y)$ on the bottom face, allow convective and radiative heat loss from the top face and insulate the thin sides of the panel as shown in Figure 6.3a to simulate the conditions of the experiments in FLUENT. The convective heat loss is modeled as $q''_{\text{conv}} = -\tilde{h}(T - T_\infty)$, where $\tilde{h}$ is found by fitting simulation results to results from experiments [105, 106]. Using the Stefan-Boltzmann law for gray surfaces, the radiative heat loss is modeled as $q''_{\text{rad}} = -\epsilon\sigma_B(T^4 - T_\infty^4)$, where σ_B is the Stefan-Boltzmann constant. The emissivity of the matte black paint used on the panels, ϵ is provided by the vendor.

The thermal conductivities of the composite were calculated basd on the measured volume fraction of fiber (45%) and knowledge of thermal conductivities of the carbon fiber and epoxy as provided by the manufacturer. The in-plane conductivity was then calculated using a closed-form solution developed in [62] and the out-of-plane conductivity was calculated using a self-consistent model described in [119]. Further details on panel fabrication, testing and FLUENT simulations are presented in [105, 106, 13].

In this chapter, the IGFEM is used to solve the linearized weak form (2.6) on a 2D domain approximating the composite panel as shown in Figure 6.3b. An equivalent "2D" conductivity defined as $\kappa_{2\text{D}} = \kappa t$ is used in order to account for the approximation. Instead of a heat flux, a distributed heat source of strength $f(\boldsymbol{x})$ is applied in the interior of the domain. All sides of the domain are insulated except at the channel inlet, where $T_{\text{in}} = 22\,^\circ\text{C}$. The effective convection coefficient is given by $\tilde{h}_{eff} = \tilde{h} + 4\epsilon\sigma_B T_\infty^3 = 13.6\,\text{Wm}^{-2}\text{K}^{-1}$.

The hydraulic model presented in Section 2.5 is used to calculated the nodal pressures and the channel flow rates. All properties are assumed to be constant, except for the dynamic viscosity of the fluid (in Pa.s), given by ([120], p. 45)

$$\mu(T) = 0.0069 \left(\frac{T}{273.15}\right)^{-8.3}, \tag{6.2}$$

where the temperature T is expressed in K. The dynamic viscosity used for the hydraulics equations is evaluated at the average temperature of the domain, $\langle T \rangle_1 = \int_{\Omega_s} T^{(h)} \text{d}\Omega / |\Omega_s|$.

The mesh used by FLUENT for a network of parallel channels shown in Figure 6.3c contains a high concentration of elements in and near the channels to resolve the fluid velocities in the channel network. To achieve convergence in the average surface temperature and pressure drop, the number of elements needed exceeds 7 million. In contrast, the mesh for IGFEM in Figure 6.3d contains only 9600 elements, is uniform everywhere and does not need to conform to the channel geometry. The maximum computational time (excluding the time to create the channel

network) on a single thread is 1 minute for the bifurcating design with a 60×80 triangular mesh containing 9600 elements. In contrast, the mesh generation (excluding the creation of the channel geometry) in ANSYS and the FLUENT simulation take approximately seven hours to run on a single thread. Furthermore, creating a channel network consisting of lines is much simpler than creating a volumetric geometry of the channels.

The validation study was conducted for the parallel, bifurcating, spiral and serpentine channel networks shown in Figures 6.4a to 6.4d with total lengths of 1.54, 1.61, 1.46 and 1.35 m, respectively. To obtain the temperature distribution using FLUENT, we simulate the channels with uniform rectangular cross sections of width 1.02 mm and height 0.84 mm corresponding to the average channel dimensions measured experimentally. Comparison of the top surface temperatures from FLUENT and the IGFEM temperature distribution in Figure 6.4 shows excellent agreement. As shown in Table 6.2, the IGFEM results agree with FLUENT results within 1 °C. Moreoever, both simulations slightly underpredict the surface temperature measured experimentally as revealed in Figure 6.4. In all cases, the difference between simulation and experiment temperatures is less than 2 °C, which is within the uncertainty of the experiments.

Table 6.2 – Comparison of average temperatures $\langle T \rangle$ $(^\circ\mathrm{C})$ and maximum temperatures $T_{\max}$ $(^\circ\mathrm{C})$ from experiments, FLUENT and IGFEM, denoted respectively by the superscripts (E), (F) and (I). The top surface temperatures of experiments and FLUENT are used for comparison.

Design	$\langle T \rangle^{(E)}$	$\langle T \rangle^{(F)}$	$\langle T \rangle^{(I)}$	$T_{\max}^{(E)}$	$T_{\max}^{(F)}$	$T_{\max}^{(I)}$
Parallel	30.4	29.0	28.7	37.2	36.5	36.8
Bifurcating	29.8	28.8	28.4	34.0	33.0	32.9
Spiral	30.0	28.4	28.2	33.2	31.5	31.4
Serpentine	29.8	28.6	28.3	33.6	32.6	32.5

In Table 6.3, we compare the total pressure drops and standard deviations of the temperature defined as

$$\sigma_T = \left(\int_{\Omega_s} (T - \langle T \rangle)^2 \mathrm{d}\Omega / |\Omega_s| \right)^{1/2}. \tag{6.3}$$

All standard deviations agree within 10%. The pressure drops calculated using the simplified models agree with experiments to within 11% while the FLUENT pressure drops differ from experiments by at most 20%.

In order to simulate the pressure drop ΔP, we use the reduced dimensions of the cross section, defined as the average minus the standard deviation of the experimentally measured cross-sectional dimensions (0.94 mm$\times 0.8$ mm). The reduced dimensions are used because (i) the smaller cross sections contribute significantly to the pressure drop, as evident by the strong dependence on the diameter in (2.13) and (ii) better agreement between experiments and simulations are obtained

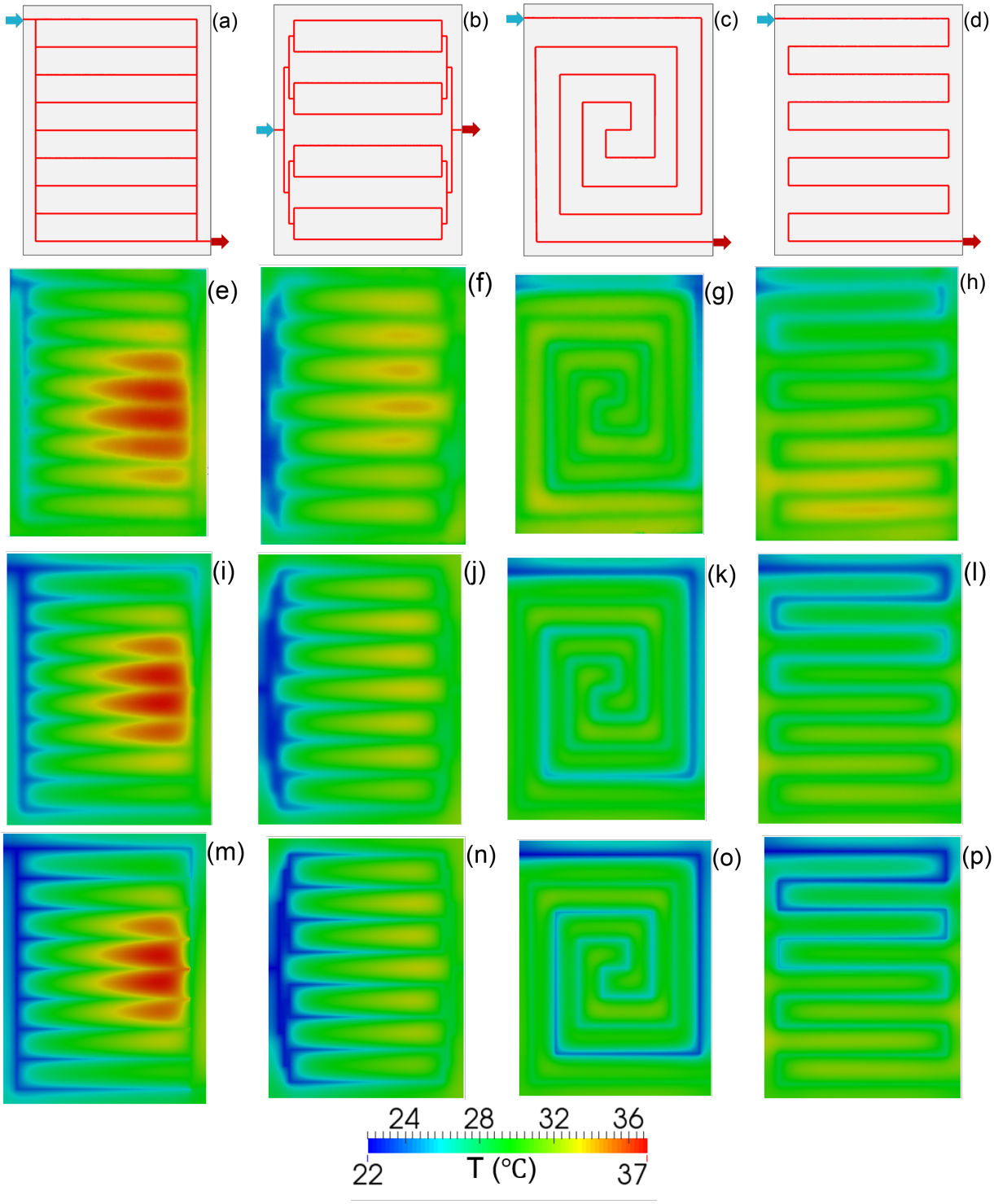

Figure 6.4 – (a) Parallel, (b) bifurcating, (c) spiral and (d) serpentine reference designs for the cooling of composite panels. (e)-(h) Experiment and (i)-(l) FLUENT top surface temperature distributions compared to (m)-(p) IGFEM temperature solutions.

Table 6.3 – Comparison of standard deviations of temperatures σ_T ($^\circ$C) (6.3) and pressure drops ΔP (kPa) from experiments, FLUENT and IGFEM, denoted respectively by the superscripts (E), (F) and (I).

Design	$\sigma_T^{(E)}$	$\sigma_T^{(F)}$	$\sigma_T^{(I)}$	$(\Delta P)^{(E)}$	$(\Delta P)^{(F)}$	$(\Delta P)^{(I)}$
Parallel	3.0	3.2	3.3	10.3	10.9	9.9
Bifurcating	2.4	2.5	2.5	8.0	8.6	7.4
Spiral	1.8	1.9	2.0	109	130	106
Serpentine	2.5	2.1	2.3	110	121	97.8

compared to that using the average dimensions. In the FLUENT simulations, the dynamics viscosity varies in the fluid according to (6.2). As shown in Table 6.3, the FLUENT simulations overestimate the pressure drops measured experimentally. However, due to the offseting effects of not accounting for the formation of the vortices at a branch or a bend in a channel [17, 18] and the use of the reduced dimensions, IGFEM underestimates the pressure drops measured experimentally.

6.3 Optimization problem

The formulation of the optimization problem is given by (5.1) with the channel control point chosen as design parameters and one objective function: the p-mean of the temperature field over the panel $\langle T(\Omega_s)\rangle_p$ written as $\langle T\rangle_p$ for brevity. We combine the IGFEM-based sensitivity analysis presented in Section 5.2 and gradient-based optimization algorithms available in MATLAB to solve the optimization problem. The interior-point [121] and sequential quadratic programming (SQP) [122] algorithms are found to be sufficiently robust for this work. Important parameters for these algorithms are given in Table 6.4. We have found that the SQP algorithm is more capable of producing solutions further from the initial guesses. As with all gradient-based optimization algorithms, we can only guarantee that a stationary solution (local minimum or saddle point) is found when certain conditions are met for a general well-posed optimization problem with nonlinear objective function and/or constraints [122]. To increase the chance of getting a solution close to the global optimum, we perform optimizations starting from many distinct initial designs.

Table 6.4 – Parameters for the MATLAB interior-point and sequential quadratic programming algorithms.

Algorithm	`TolFun`	`TolX`	`TolCon`	`InitBarrierParam`
Interior-point	1e-8	1e-10	1e-8	0.01
SQP	1e-6	1e-6	1e-6	Not applicable

6.4 Optimization of parallel network designs

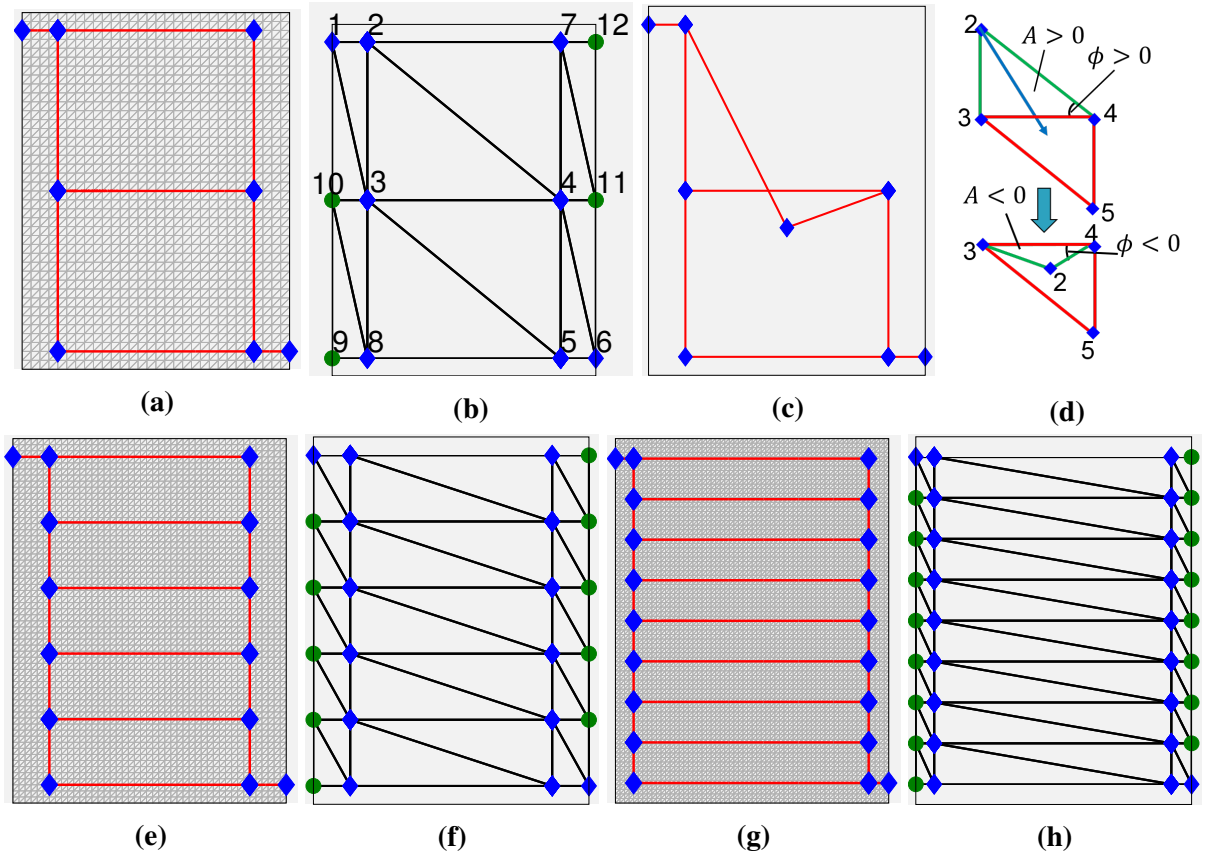

Figure 6.5 – (a) two-branch, (e) five-branch and (g) eight-branch parallel networks used as reference designs for comparison with optimal designs. (b), (f), (h) Corresponding nonlinear constraint triangles used to help prevent self-intersections as explained in Section 6.4.1. Examples of (c) self-crossing channel network and (d) nonlinear constraint violation.

In the remainder of this paper, we apply the shape optimization method to the parallel channel designs with different number of branches. Parallel designs with two, five and eight branches are presented in Figures 6.5a, 6.5e and 6.5g, respectively, together with the non-conforming structured mesh used for the optimization analysis. The problem setup is similar to that of Figure 6.3b except for the nature of the thermal loading applied to the battery cooling panel. To simulate more accurately the thermal load that a battery cooling panel would receive, no heat loss from the surface is assumed and a uniform heat source of 500 Wm^{-2} is applied. This represents the scenario where a panel is heated from both sides. The thermal conductivity of the composite is raised to 2.7 $\mathrm{Wm}^{-1}\mathrm{K}^{-1}$ to represent a composite with a higher fiber volume fraction of 60%, the inlet temperature is set at 27 °C and the inlet flow rate is 28.2 ml/min unless specified otherwise. The width and height of the channel cross section are set to 0.75 mm. These conditions are representative

of the heat flux, coolant temperature and coolant flow rate found in Chevy Volt cooling panels [20]. As indicated earlier, the design parameters are the locations of all control points indicated by blue diamonds in the figure, except the inlet and outlet control points, which are fixed. Thus the shape optimization problems described in Figures 6.5a, 6.5e and 6.5g involve 12, 24 and 36 design parameters, respectively. The bounding boxes for all design parameters are chosen as (in m) $\{0.005 \leq x \leq 0.145, 0.005 \leq y \leq 0.195\}$.

6.4.1 Geometrical constraints

One of the key constraints of the design problem is associated with the "self-crossing" of some of the channels, which renders the problem unphysical, as illustrated in Figure 6.5c. To address this issue, we apply a set of simple geometrical constraints to triangles constructed from the networks as shown in Figures 6.5b, 6.5f and 6.5h. Let ϕ and A respectively denote the interior angle and area of a triangle such as $\{2, 3, 4\}$ in Figure 6.5d. The geometrical constraints take the form: (i) $\sin\phi \geq \sin\phi_o$ for some $\phi_o \in [0, \pi/2]$ (typically, $\phi_o = 0.5°$) and (ii) $A \geq A_o$ (typically, $A_o = 0.001\times$area of domain). Mathematically, condition (ii) is redundant. However, numerically, it is needed when two vertices are very close together and calculation of $\sin\phi$ becomes inaccurate. The derivative of the above nonlinear constraints with respect to the design parameters can readily be found as the vertex locations are directly related to the design parameters.

6.4.2 Choice of p in p-mean temperature

As described earlier, the max function $T_{\max}(\boldsymbol{d}) = \max_{\boldsymbol{x}} T(\boldsymbol{x}, \boldsymbol{d})$ is not differentiable in the classical sense [113], and is typically replaced by a differentiable alternative such as the Kreisselmeier-Steinhauser function or the p-norm/p-mean in stress-based optimization [112, 114, 115]. Adopting the latter approach, we replace $T_{\max}(\boldsymbol{d})$ with $\langle T\rangle_p$, noting that $\lim_{p\to\infty}\langle T\rangle_p = T_{\max}(\boldsymbol{d})$ since $T(\boldsymbol{x}, \boldsymbol{d})$ is a continuous function of $\boldsymbol{x}$ and the domain is bounded and closed [123]. In general, $\langle T\rangle_p \leq T_{\max}(\boldsymbol{d})$ [123, 124]. However, there is no explicit relationship between $T_{\max}(\boldsymbol{d})$ and $\langle T\rangle_p$.

The choice of p is the result of a compromise: large values may cause $\langle T\rangle_p$ to be ill-conditioned or less smooth [112, 115], but small values may not allow $\langle T\rangle_p$ to capture reliably the trend in $T_{\max}(\boldsymbol{d})$, resulting in local regions of high temperature similar to regions of stress concentration in structural optimization problems [112, 115]. Based on our numerical observations and on recommended values for stress-based optimization [112], we adopt $p = 8$. It is worth mentioning here that to integrate (5.4) exactly over a triangle with $p = 8$, a 16-point Gauss-Dunavant quadrature [125] is required.

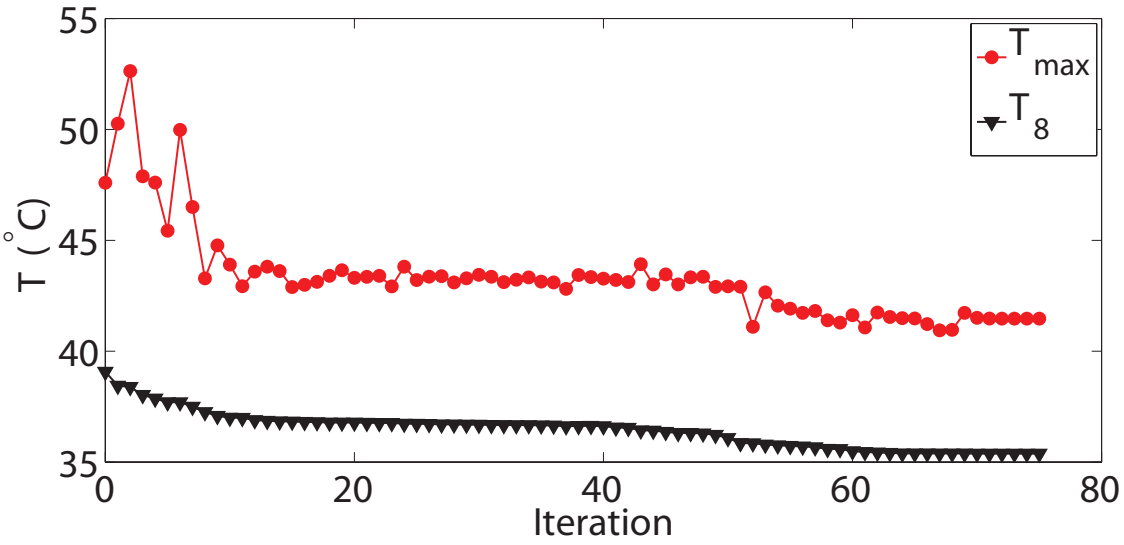

Figure 6.6 – Optimization history of the five-branch parallel design.

Figure 6.6 illustrates the optimization history of $\langle T \rangle_8$ and $T_{\max}$ for the five-branch parallel design study starting from the reference design, showing how $T_{\max}$ follows the overall downward trend of $\langle T \rangle_8$.

6.4.3 Optimal designs of branched networks

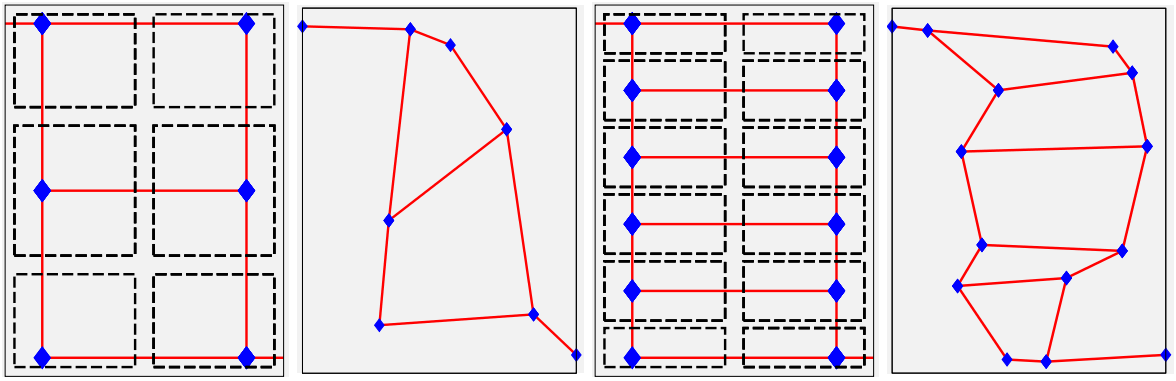

Figure 6.7 – Bounding boxes indicated by dash rectangles for generating random initial designs for (a) two and (c) five branches together with examples of initial designs ((b) and (d)).

Multiple potential optimal configurations are investigated by starting the optimization from more than 40 distinct designs for each number of branches. The initial designs are obtained by randomizing the initial positions of the control points within non-overlapping bounding boxes shown in

Figures 6.7a and 6.7c. Some of the initial designs are presented in Figures 6.7b and 6.7d.

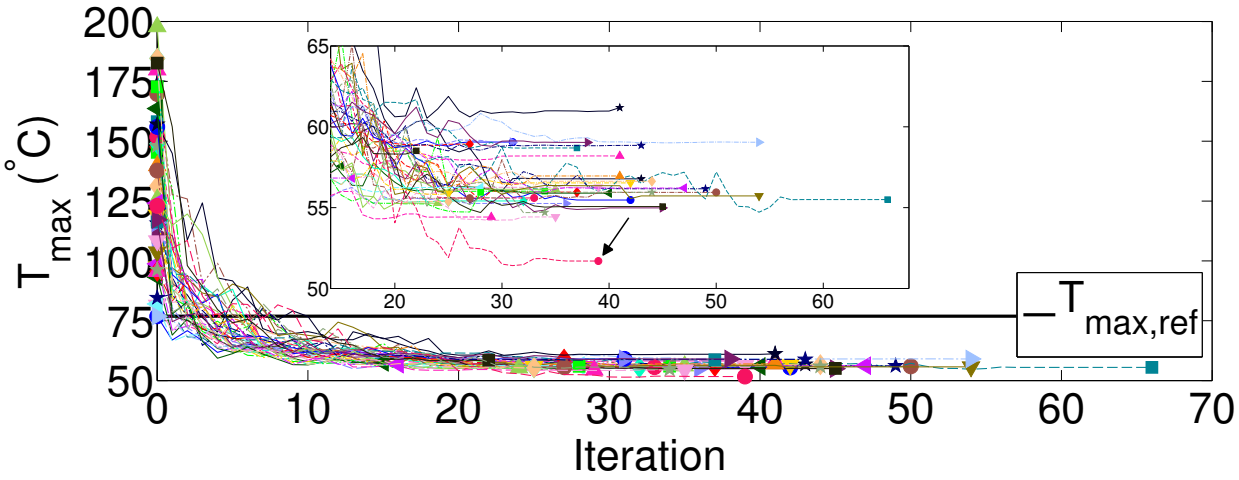

Figure 6.8 – Evolution of $T_{\max}$ during the shape optimization of the two-branch case. The inset presents a zoomed-in view of the maximum temperature associated with multiple local optimal configurations.

As apparent from the optimization histories for the two-branch case shown in Figure 6.8, the optimizer reduces $T_{\max}$ by more than 20 °C compared to the reference maximum temperature $T_{\max,\text{ref}}$ (represented by a horizontal line in the figure). Numerous optimal solutions are obtained, as shown in the inset by the various stationary values of $T_{\max}$. It should be noted that, due to round-off errors and various approximations in the algorithm (such as the approximate Hessian [122, 121]), optimal solutions with similar shapes may have slightly different objective function values and design parameter values, as also observed in [20] with the SQP algorithm in MATLAB. The "best optimal" configuration (in terms of $T_{\max}$) corresponds to the red circular point indicated by an arrow in Figure 6.8 with $T_{\max} = 51.7\,^{\circ}\text{C}$, and is shown in Figure 6.9b.

In Figure 6.9, we present the optimal designs for two, five and eight branches, together with the corresponding reference designs and temperature distributions. As apparent from these figures, the thermal performance of the optimal designs is greatly superior to that of the reference designs in terms of both maximum temperature and temperature uniformity. The predicted configuration depends strongly on the number of branches in the network: the optimal designs for two to six branches tend to adopt a more "vertical configuration" while those with seven to twelve branches appear to be diagonally oriented. For a low number of branches, it is reasonable to stretch the channels as long as possible to maximize area coverage. Hence, the vertically oriented design is preferred. However, the higher the number of branches, the lower the flow rate in each channel, which results in a more rapid temperature rise along the channel. Therefore, the optimal designs for high number of branches tend to have shorter channel segments, i.e., the diagonal orientation

is preferred. As shown in Figure 6.10a, the optimal designs tend to equalize the flow rates in the interior channels, thereby achieving a more uniform temperature field. This observation is consistent with that of an existing study [23], where it is shown that the "distributor" designs

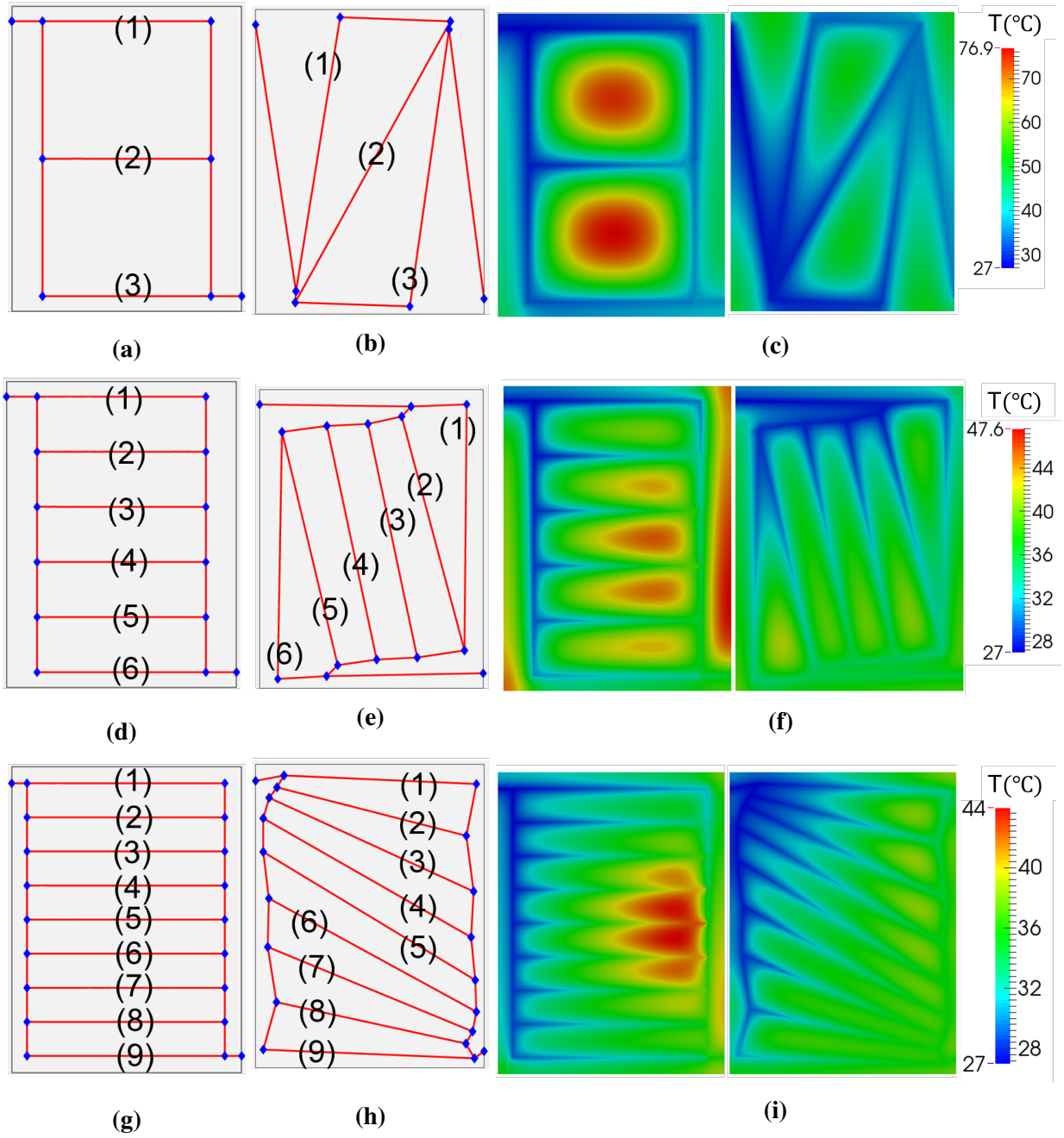

Figure 6.9 – Reference (a, d, g) and optimal (b, e, h) designs for two, five and eight branches. (c), (f) and (i): Temperature distributions corresponding to the optimal designs compared with the reference temperature distributions with the upper bound of the color bar set to the maximum temperature of the corresponding reference design.

with the most uniform flow distribution generally have the best performance in terms of maximum temperature difference and thermal resistance.

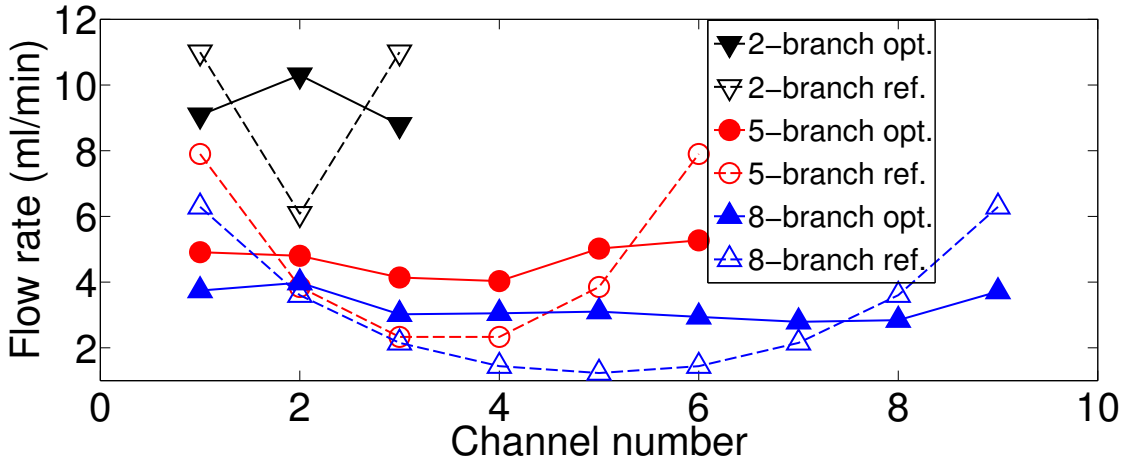

(a)

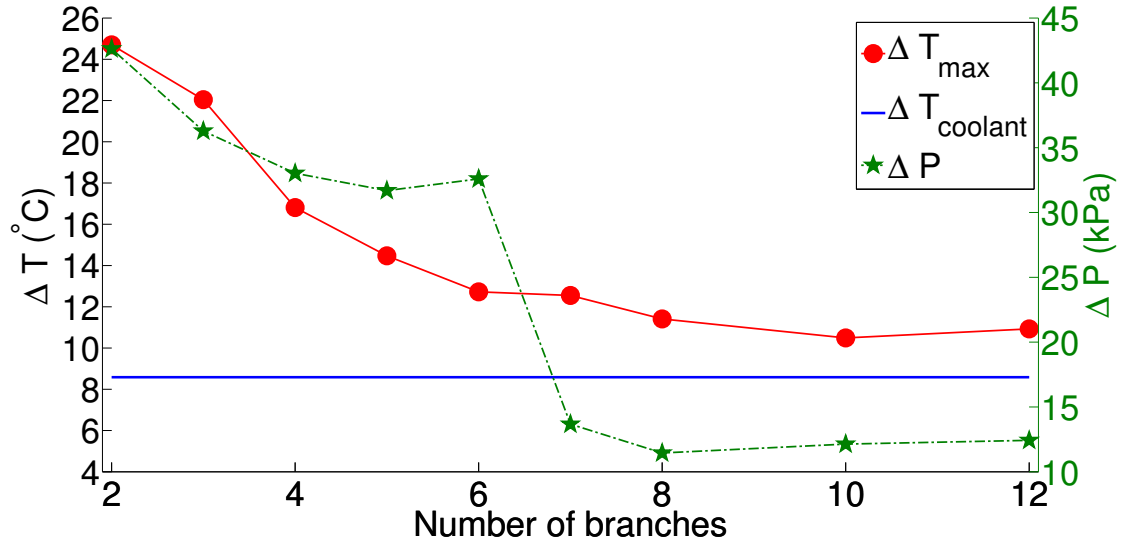

(b)

Figure 6.10 – (a) Flow rates in the interior channels of the two-, five-, and eight-branch reference and optimal designs, with the channel numbers shown in Figure 6.9. (b) Temperature difference $\Delta T = T_{\max} - T_{\text{in}}$ and pressure drop ΔP obtained for the optimal designs as a function of number of branches. The "optimum" temperature rise of the coolant $\Delta T_{coolant}$ is also shown for comparison.

Figure 6.10b shows that the reduction in the maximum temperature of the microvascular panel diminishes as the number of branches increases and saturates between eight to ten branches. As a reference, we have also plotted the expected "optimum" rise in coolant temperature, $\Delta T_{\text{coolant}} = Q/(\dot{m}c_p)$ if all the applied heat is absorbed by the coolant. This rise in temperature is also a lower bound for ΔT. At ten branches, the maximum temperature of the optimal design is only

1.5 °C above $\Delta T_{\text{coolant}}$. We also observe that the pressure drop needed to circulate the coolant is substantially higher for the vertically oriented optimal designs with six branches or less. The pressure drop appears to be the lowest for the eight branch design, beyond which ΔP increases slightly with the number of branches.

6.4.4 Effect of flow rate on optimal design

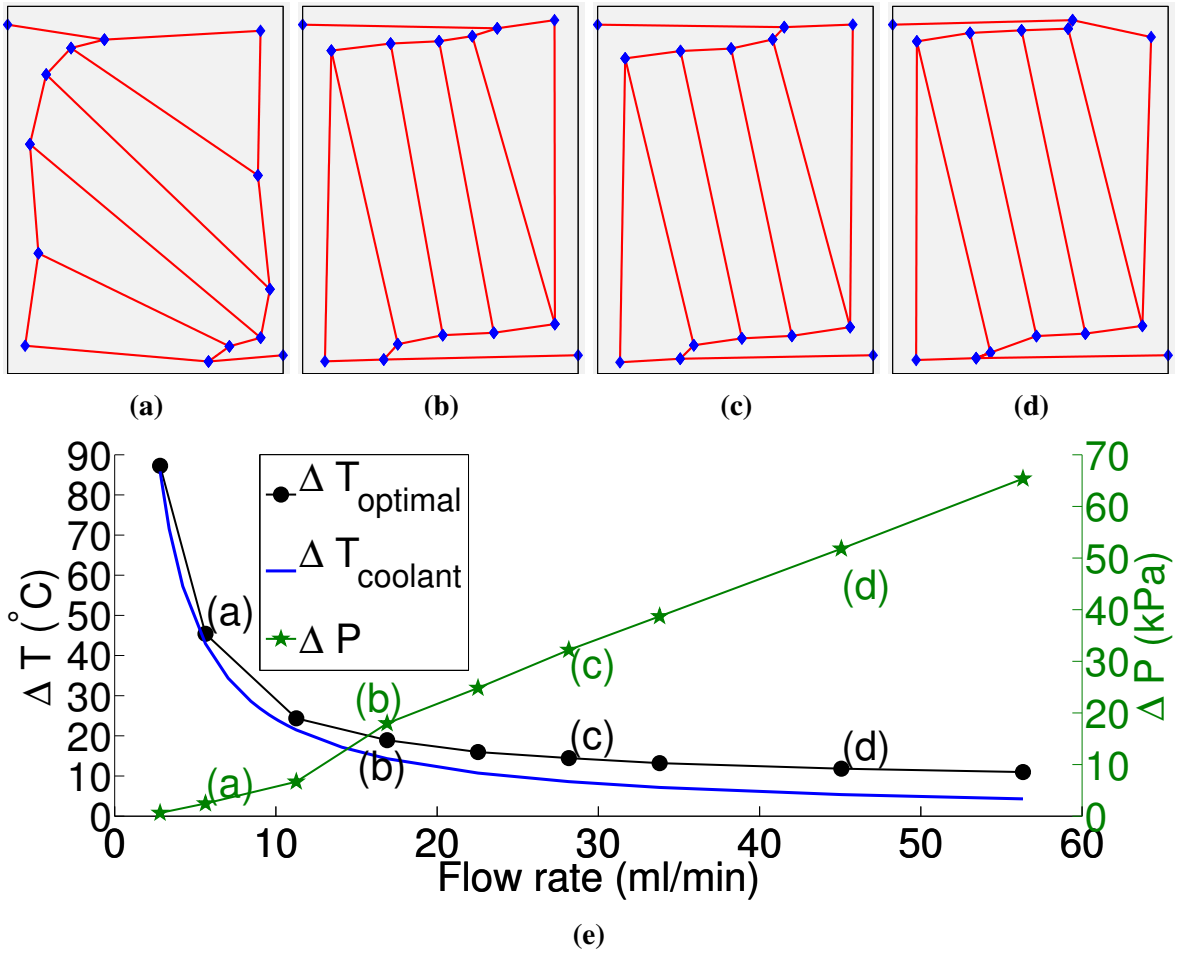

(e)

Figure 6.11 – Best optimal configurations for flow rates of (a) 5.63, (b) 16.9, (c) 28.2 and (d) 45.1 ml/min. Figure (e) presents the effect of the flow rate on the temperature difference $\Delta T = T_{\max} - T_{\text{in}}$ and pressure drop ΔP associated with the best optimal design. The "optimum" temperature rise of the coolant $\Delta T_{coolant}$ is also shown for comparison.

All the design results presented thus far are based on a constant flow rate of 28.2 ml/min. In this section, the effect of the flow rate on the design of the five-branch network is investigated by varying the flow rate from 2.82 to 56.3 ml/min. Some of the optimal designs are shown in Figures 6.11a to 6.11d. The transition from a diagonal design to a vertical design between 11.3

and 16.9 ml/min is consistent with the earlier observations: for low flow rates, the channels tend to be shorter to maximize their cooling effect.

As evident in Figure 6.11e, the thermal impact of the embedded network increases (i.e., $\Delta T = T_{\max} - T_{\text{in}}$ decreases) with increasing flow rate, but at a declining rate in a trend consistent with previous studies [21, 32, 14]. This trend is due to the positive correlation between ΔT and the temperature rise of the coolant $\Delta T_{\text{coolant}}$, itself linked to the flow rate through $\Delta T_{\text{coolant}} \sim Q/(\dot{m}c_p)$. The "cost" of circulating the coolant is illustrated through the evolution of the pressure drop ΔP, which, as expected, increases with the flow rate. However, it shows two distinct linear regions, with a transition corresponding to the flow rate at which the aforementioned transition from vertical to diagonal configurations takes place.

6.4.5 Validation of five-branch optimal design

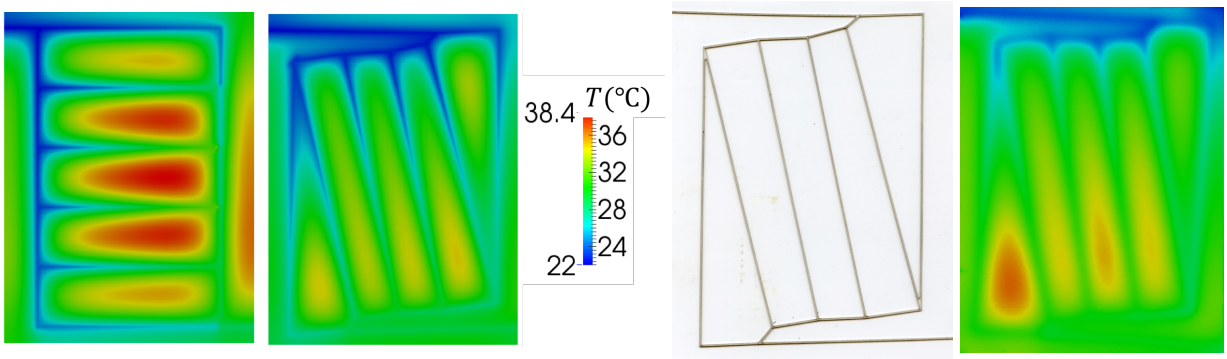

Figure 6.12 – Numerical temperature distributions of (a) the reference and (b) the optimal five-branch networks. (c) Laser-cut sacrificial template used to embed the optimal five-branch network in the composite panel for the validation study. (d) Experimentally-measured temperature distribution of the optimal network.

In this final section, we present a validation study of the five-branch optimal design under the thermal loading conditions described in the validation exercise of Section 6.2 and for the same flow rate of $28.2\,\text{ml}\,\text{min}^{-1}$. As shown in Figures 6.12a and 6.12b, the IGFEM temperature distribution of the optimal network is significantly more uniform than that of the reference network. The average and maximum temperatures of the optimal network are respectively 28.8 °C and 34.6 °C compared to 30.8 °C and 38.4 °C for the reference network. For this validation study, we have fabricated the optimal network by using the sacrificial template shown in Figure 6.12c [105, 106, 13]. The experimentally measured average and maximum temperatures are respectively 30.5 °C and 36.5 °C, which are slightly higher than the simulated values, but within experimental error. The

experimental standard deviation of 2.5 °C agrees closely with that of simulated value of 2.87 °C. On the other hand, the experimental pressure drop of 26.4 kPa is higher than the simulated value of 20.8 kPa, which is calculated using the hydraulic equation and the experimentally measured minimum cross section dimensions. One possible source of the discrepancy is the omission of additional pressure penalty at the corners of the channels in the hydraulics equations.

6.5 Conclusions

Dimensionally reduced thermal and hydraulic models were used to model the impact of an embedded channel network on the thermal field in a thin microvascular composite and the pressure drop needed to circulate the coolant. To facilitate the discretization of the many configurations analyzed in the design process, and to avoid issues associated with mesh distortion present in conventional finite-element-based shape optimization studies, an interface-enriched generalized finite element method (IGFEM) was used for the thermal solver, allowing for accurate and efficient solutions of the thermal problem with meshes that did not conform to the network configurations. A SUPG scheme was introduced to stabilize the IGFEM solution. The IGFEM solver was verified against nonlinear, fluid/thermal 3D FLUENT solutions, and validated against experimental measurements. By combining the thermal IGFEM solver with a gradient-based shape optimization scheme, we optimized the designs of parallel networks defined by a set of branched channels. To avoid self-intersection of the channels, a set of simple nonlinear constraints were incorporated in the design problem formulation, and each design analysis involved multiple initial configurations to address the presence of a large number of local optima.

The shape optimization studies led to configurations substantially different from the reference parallel channel configurations, with thermal performance greatly improved both in terms of reducing the maximum temperature and achieving a uniform temperature field. The predicted optimal designs showed shorter and longer channel segments for low and high number of branches, respectively. Consistent with the previous trend, we also found a transition from a design with shorter channels at low flow rates to one with longer channels at higher flow rates. Furthermore, we demonstrated that the simulation results of the five-branch optimal design agreed with experimental results. The method described here can be applied to a wide range of objective functions and constraints.

7 2D Multi-Objective Design of Battery Cooling Panels

This chapter is adapted from an article in preparation titled "Multi-objective design of microvascular panels for battery cooling applications" by M. H. Y. Tan, A. R. Najafi, S. J. Pety, S. R. White and P. H. Geubelle.

7.1 Introduction

This chapter focuses on the multi-objective design of microvascular composite panels proposed for battery cooling applications [105, 106]. The design objectives include the p-mean as a differentiable alternative to the maximum temperature, pressure drop and variance, as well as various operating constraints/conditions including pressure drop, pump power and localized heat sources. We begin this chapter by describing in Section 7.2 the optimization problems and techniques. In Section 7.3, we present designs optimized based on pressure drop across the network and p-mean of the temperature. Localized heat sources and pump power constraint are investigated in Section 7.4. Lastly, in Section 7.5, the cross-sectional sizes are considered as design parameters, and the resulting optimal design is validated with experiment.

7.2 Optimization problem

In this chapter, the multi-objective optimization problems are given by (5.1). Since the multi-objective vector $\boldsymbol{\theta}$ in the equation utlimately depends only on $\boldsymbol{d}$, we henceforth write $\boldsymbol{\theta} = \boldsymbol{\theta}(\boldsymbol{d})$. Let $\mathcal{F}$ be the set of feasible solutions to (5.1). As defined in [126], a solution $\boldsymbol{x} \in \mathcal{F}$ dominates another solution $\boldsymbol{y} \in \mathcal{F}$ if and only if $\theta_i(\boldsymbol{x}) \leq \theta_i(\boldsymbol{y})$ for every i, and $\theta_j(\boldsymbol{x}) < \theta_j(\boldsymbol{y})$ for at least one j. Further, if no other solution in $\mathcal{F}$ dominates $\boldsymbol{x}$, then $\boldsymbol{x}$ is Pareto optimal. The set of all such solutions is called the Pareto optimal set and the Pareto optimal front is the set of objective values corresponding to the solutions in the Pareto optimal set. While some studies define a Pareto point as a Pareto solution, we define a Pareto point as a point on the Pareto optimal front. For brevity, we omit "optimal" when using the foregoing terms.

7.2.1 Problem setup

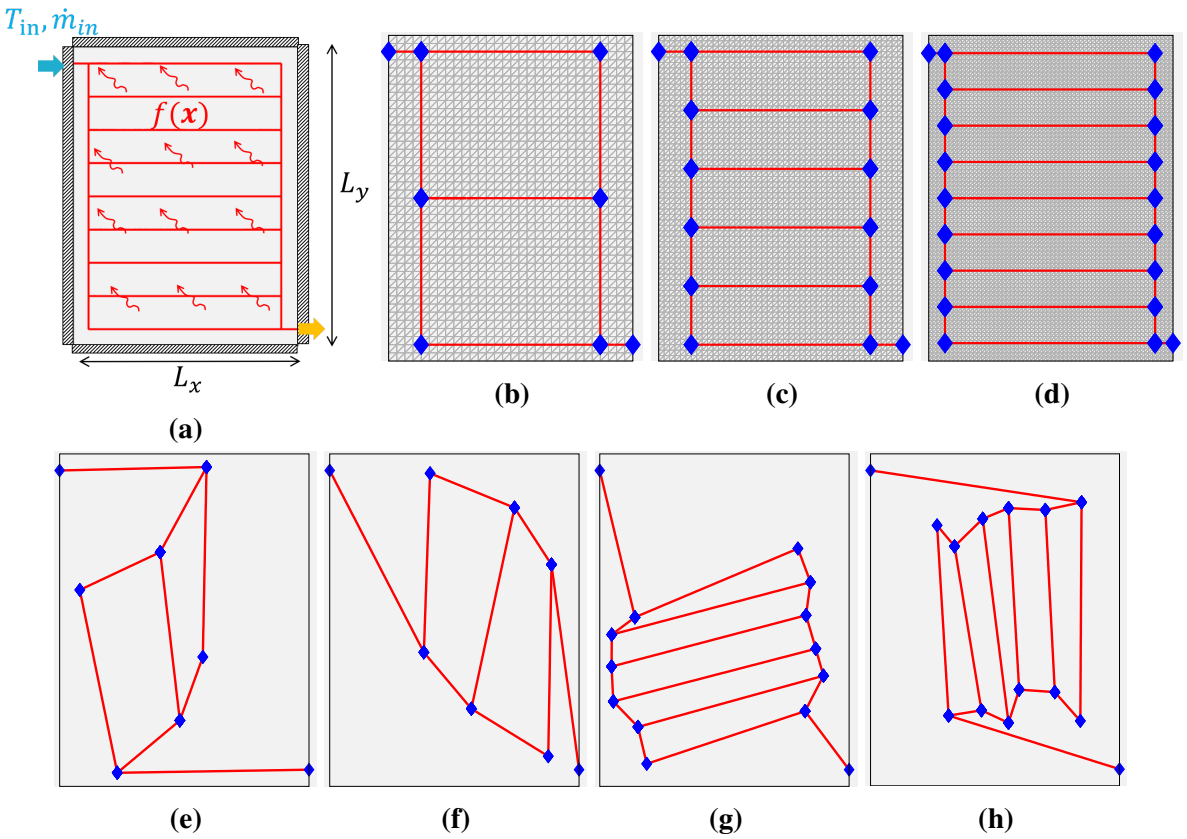

Figure 7.1 – (a) Channel design problem setup. Two-branch (b), five-branch (c) and eight-branch (d) reference networks with corresponding fixed background mesh. Examples of two-branch (e), (f) and five-branch (g), (h) initial designs.

The optimization problem setup shown in Figure 7.1a simulates the conditions experienced by a battery cooling panel in operation. A carbon fiber/epoxy matrix composite panel of size $L_x = 0.15$ m, $L_y = 0.2$ m is subject to a uniform thermal load of $f(\boldsymbol{x}) = 500\,\mathrm{Wm}^{-2}$ unless stated otherwise. The composite is assumed to be balanced plain-weave and hence has an isotropic in-plane conductivity. We set the thermal conductivity and thickness of the panel to be $2.7\,\mathrm{Wm}^{-1}\mathrm{K}^{-1}$ and 3 mm, respectively.

Embedded in the panel of Figure 7.1a is a parallel network with coolant entering the inlet near the top left corner at a temperature of $T_{\text{in}} = 27\,^{\circ}\mathrm{C}$ and exiting from the outlet near the bottom right corner. The parallel networks chosen to be optimized are the two-, five- and eight-branch networks shown in Figures 7.1b–7.1d with the corresponding non-conforming meshes. At least 48 initial designs for each case are used to address the problem of multiple local optima (see Figures 7.1e–7.1h). The geometrical constraints described in Chapter 6 are imposed to prevent the unphysical scenario of "self-crossing" of channels during the optimization.

Unless mentioned otherwise, the prescribed flow rate is $\dot{m}_{\text{in}} = 5 \times 10^{-4}$ kg/s (corresponding to a flow rate of 28.2 ml/min) at the inlet of the network and a zero reference pressure at the outlet. Under these boundary conditions, the system of hydraulics equations (2.11) is linear in $\{P\}$. Since the viscosity is assumed to be uniform across the channel network, the flow rates are independent of the viscosity. Hence the hydraulics equations are decoupled from the heat equation and the actual pressure drop can be obtained after the heat equation is solved.

However, when the pump power is prescribed, the hydraulics and heat equations are coupled if and only if the dynamic viscosity is temperature-dependent. Hence, we decouple the equations by fixing the viscosity at a reference temperature of 38 °C, approximately the lowest temperature achievable by our optimal designs. The choice of lowest possible temperature gives the highest possible viscosity and hence the lowest possible flow rates. The dynamic viscosity (6.2) and a density of $1065\,\mathrm{kg/m^3}$ yield a kinematic viscosity of $2.198 \times 10^{-6}\,\mathrm{m^2/s}$.

7.2.2 Generation of Pareto front

Various methods are available to generate the Pareto front [127, 128, 129, 130, 131]. In the gradient-based optimization problem at hand, we adopt two decomposition-based methods. The first approach is the ε-constraint method [130], which minimizes one objective function called the primary objective function while imposing the others as constraints. The original problem (5.1) is then converted to:

$$\begin{aligned} \min_{\boldsymbol{d}} \quad & \theta_1(\boldsymbol{d}), \\ \text{such that} \quad & \boldsymbol{g}(\boldsymbol{d}) \leq 0, \\ \text{and} \quad & \theta_i(\boldsymbol{d}) \leq \varepsilon_i, \quad i = 2, ..., n_o. \end{aligned} \tag{7.1}$$

The lower bound on ε_i can be obtained by performing single-objective optimization on θ_i. When ε_i is sufficiently close to its lower bound, the ε_i constraint becomes active. However, as ε_i increases, the constraint eventually becomes inactive. Although simple in its implementation, this method may not produce well-distributed points on the Pareto front.

To overcome this limitation, we adopt as the second approach a boundary intersection method called the normalized normal constraint (NNC) method [131]. The key idea of the method is to successively restrict $\mathcal{F}$ to generate well-distributed solutions along the Pareto front. As illustrated in Figure 7.2, the method in the bi-objective case can be summarized in two steps described next.

Step 1: Perform single-objective optimizations on θ_1 and θ_2. Let the resulting solutions be denoted by $\boldsymbol{d}^{1*}$ and $\boldsymbol{d}^{2*}$, respectively. Associated with these solutions are the end points of the Pareto front in the $\theta_1\theta_2$-plane: $(\theta_1(\boldsymbol{d}^{1*}), \theta_2(\boldsymbol{d}^{1*}))$ and $(\theta_1(\boldsymbol{d}^{2*}), \theta_2(\boldsymbol{d}^{2*}))$. Now, let us define the

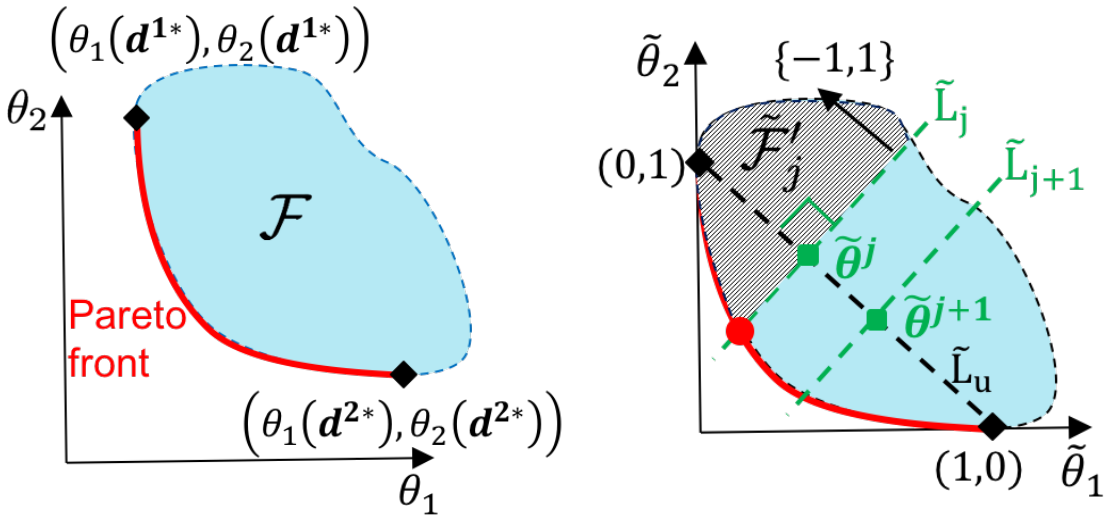

Figure 7.2 – Illustration of the normalized normal constraint method in the bi-objective case showing (a) the generation of the two end points of the Pareto front represented by the black diamonds, and (b) transformation to a normalized coordinate system followed by minimization of $\tilde{\theta}_2$ in the new feasible region $\tilde{\mathcal{F}}'_j$ to obtain a point (red circle) on the Pareto front.

normalized objective functions as

$$\begin{aligned} \tilde{\theta}_1 &= \frac{\theta_1(\boldsymbol{d}) - \theta_1(\boldsymbol{d}^{1*})}{\theta_1(\boldsymbol{d}^{2*}) - \theta_1(\boldsymbol{d}^{1*})}, \\ \tilde{\theta}_2 &= \frac{\theta_2(\boldsymbol{d}) - \theta_2(\boldsymbol{d}^{2*})}{\theta_2(\boldsymbol{d}^{1*}) - \theta_2(\boldsymbol{d}^{2*})}, \end{aligned} \tag{7.2}$$

and the vector of normalized objective functions as $\tilde{\boldsymbol{\theta}} = \{\tilde{\theta}_1, \tilde{\theta}_2\}$. In the $\tilde{\theta}_1\tilde{\theta}_2$-plane, the end points of the Pareto front are now $\tilde{\boldsymbol{\theta}}(\boldsymbol{d}^{1*}) = (0, 1)$ and $\tilde{\boldsymbol{\theta}}(\boldsymbol{d}^{2*}) = (1, 0)$.

Step 2: To obtain the j-th Pareto point, where $j = 2, ..., N-1$, we solve the following optimization problem:

$$\begin{aligned} \min_{\boldsymbol{d}} \quad & \tilde{\theta}_2(\boldsymbol{d}) \\ \text{such that} \quad & \boldsymbol{g}(\boldsymbol{d}) \leq 0, \\ \text{and} \quad & \{-1, 1\}' \left(\tilde{\boldsymbol{\theta}} - \tilde{\boldsymbol{\theta}}_{\boldsymbol{j}}\right) \geq 0, \end{aligned} \tag{7.3}$$

where

$$\tilde{\boldsymbol{\theta}}_{\boldsymbol{j}} := \frac{N-j}{N-1}(0, 1) + \frac{j-1}{N-1}(1, 0). \tag{7.4}$$

To understand the second constraint of (7.3), let us denote the line connecting the two end points of the Pareto front in the normalized coordinate system by $\tilde{\mathrm{L}}_{\mathrm{u}}$ as shown in Figure 7.2b. Also, let

$\tilde{\mathrm{L}}_{\mathrm{j}}$ be the line perpendicular to $\tilde{\mathrm{L}}_{\mathrm{u}}$ and passing through the point $\tilde{\boldsymbol{\theta}}_{\boldsymbol{j}}$. We observe that the second constraint restricts the solution to the side of the $\tilde{\mathrm{L}}_{\mathrm{j}}$ indicated by the vector $\{-1, 1\}$, leading to a smaller feasible region $\tilde{\mathcal{F}}'_j$. Minimization of $\tilde{\theta}_2$ in this new feasible region then produces a point on the Pareto front represented by the red circle in Figure 7.2b. Since $\tilde{\mathrm{L}}_{\mathrm{j}}$ is shifted in fixed increments along $\tilde{\mathrm{L}}_{\mathrm{u}}$ as j increases, uniformly distributed points on the Pareto front would be obtained. We note that the end point coordinates of $\tilde{\mathrm{L}}_{\mathrm{u}}$ are not critical for generating the interior points of the Pareto front. In fact, the role of $\tilde{\mathrm{L}}_{\mathrm{u}}$ is only to allow for more uniform distribution of the points on the Pareto front. After the points on the Pareto front in the normalized coordinate system are obtained, the obvious step is to transform the objective functions back into the original coordinate system.

Both (7.1) and (7.3) are solved with the MATLAB sequential quadratic programming (SQP) algorithm [122] using the gradients provided by the sensitivity analysis in Section 5.2, and with important parameters of the algorithm given in Table 6.4. Since the abovementioned methods do not guarantee the generation of Pareto solutions, a Pareto filter is also used as described in [131].

7.2.3 Objective functions

As indicated earlier, the primary objective function used in this work is a differentiable alternative to the maximum temperature, the p-mean of the temperature field over the panel $\langle T(\Omega_s)\rangle_p$ defined in Section 5.2 and written as $\langle T\rangle_p$ for convenience. We set $p = 8$, the choice of which has been discussed in Section 6.4.2. Another objective function considered here is the pressure drop across the network. We sometimes impose the pressure drop as a constraint instead of an objective function, i.e., $\Delta P \leq \Delta P_o$, where ΔP_o is the desired bound on the pressure drop.

The last objective function considered is the variance, used as a measure of temperature uniformity in [20, 46] and defined as

$$\sigma^2(T) = \frac{1}{|\Omega|}\left(\int_\Omega (T^{(h)} - \langle T\rangle_1)^2 \mathrm{d}\Omega\right). \tag{7.5}$$

This expression can be rewritten as

$$\sigma^2(T) = \langle T\rangle_2^2 - \langle T\rangle_1^2. \tag{7.6}$$

which allows the application of the sensitivity analysis described in Section 5.2.

When the variance is chosen as the objective function, we want to impose a constraint $T_{\max} \leq T_{\max,o}$. Unfortunately, this constraint cannot be handled by a gradient-based algorithm. Hence, as before, we replace $T_{\max}$ with $\langle T\rangle_p$. However, by doing so, we are left with the problem of

finding an upper bound on $\langle T \rangle_p$ corresponding to $T_{\max,o}$. To circumvent this issue, we correct for the difference between $T_{\max}$ and $\langle T \rangle_p$ in "real time" by adopting the algorithm proposed in [112]. Starting from an initial guess $c^{(0)}$, we impose the following constraint at each iteration $i = 1, ..., n$:

$$c^{(i)} \langle T \rangle_p \leq T_{\max,o}, \tag{7.7}$$

where $c^{(i)} = T_{\max}^{(i-1)} / \langle T \rangle_p^{(i-1)}$.

7.3 Optimization results related to pressure and temperature

7.3.1 Pressure-temperature Pareto front from ε-constraint method

To obtain the pressure-temperature Pareto front, we perform optimizations for different values of the upper bound of the pressure constraint P_o. The evolution of the optimal design for the two-branch network is shown in Figures 7.3a–7.3d for $P_o = 10, 30, 40, 50$ kPa. When P_o is small, the optimal designs have small total channel length with only one interior channel placed diagonally across the panel. As P_o increases to 50 kPa, the optimal design becomes vertically oriented with three diagonally oriented interior channels spanning the panel. The optimal designs of the five-branch case follows the same trend when P_o increases from 10 to 40 kPa as shown in Figures 7.3e and 7.3f. On the other hand, the eight-branch optimal design for $P_o = 10$ and 14 kPa are both diagonally oriented.

The pressure-temperature Pareto front is presented as a plot of maximum temperature versus the actual pressure drop in Figure 7.3i. Except for the eight-branch optimal design with P_o = 10 kPa, all optimal designs have lower maximum temperature compared with the reference designs. For all branches, the pressure constraint becomes active at lower P_o and inactive at higher P_o. However, the value of P_o beyond which the pressure constraint becomes inactive decreases with increasing number of branches. While the pressure constraint becomes inactive at $P_o = 40$ kPa for the two-branch case, this occurs at $P_o = 14$ kPa for the eight-branch case. Furthermore, the lower pressure constraint has a more detrimental effect on the performance of networks with higher number of branches. As evident from the plot, the pressure and temperature range accessible to the ε-constraint method is rather limited. As described next, this limitation can be overcome by the NNC method.

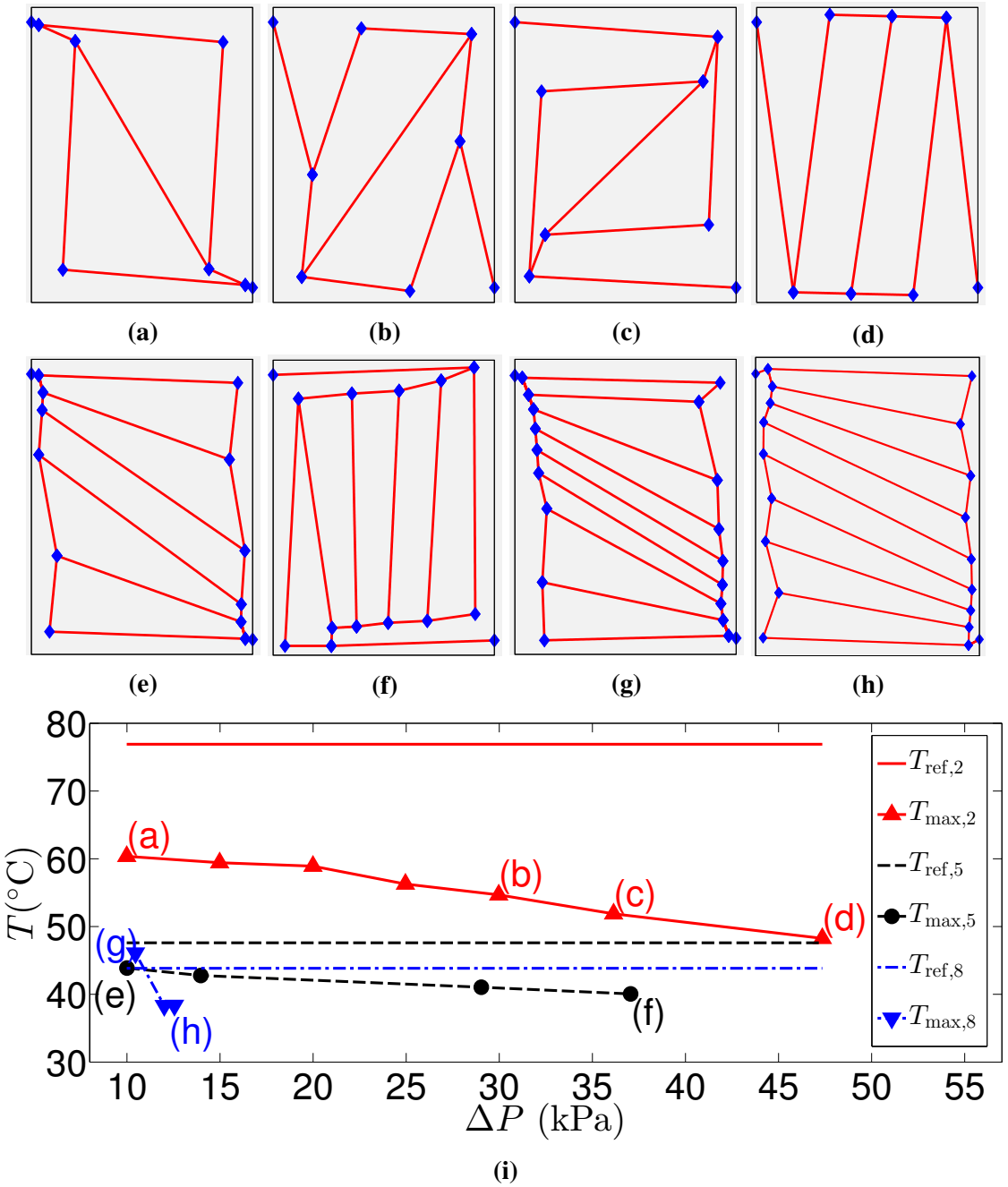

Figure 7.3 – (a)-(d) Two-branch optimal designs for $\Delta P \leq 10, 30, 40, 50$ kPa. (e) and (f) Five-branch optimal designs for $\Delta P \leq 10, 40$ kPa. (g) and (h) Eight-branch optimal designs for $\Delta P \leq 10, 14$ kPa. (i) Maximum temperature as a function of actual pressure drop for the two-, five- and eight-branch designs. The reference temperatures are also plotted for comparison.

7.3.2 Pressure-temperature Pareto front from NNC method

In the first step of the NNC, minimization of the pressure drop across a channel network results in all channels being very close together, with a collapse barely prevented by the geometrical

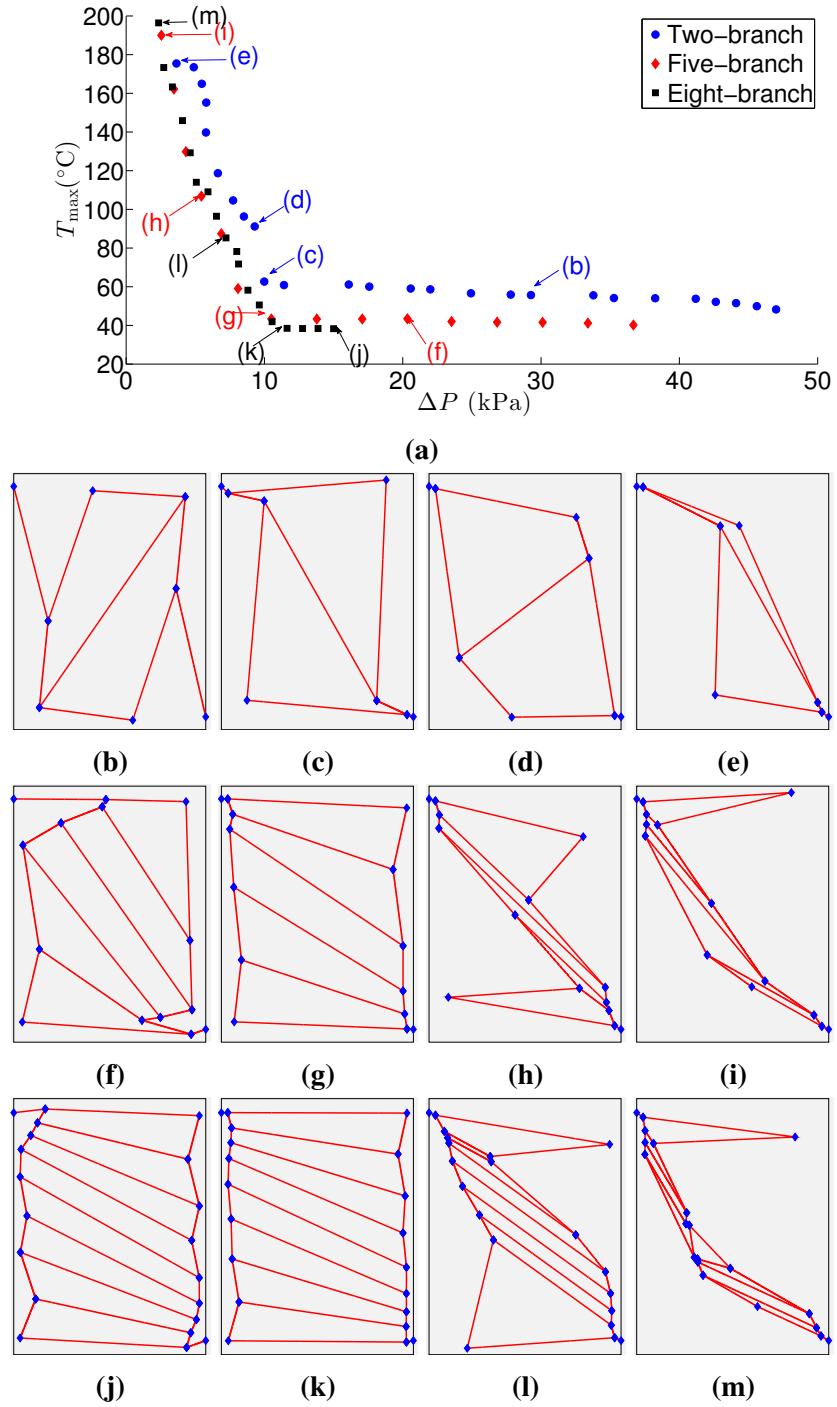

Figure 7.4 – (a) Tradeoff between $T_{\max}$ and ΔP represented by the Pareto fronts for the two-, five- and eight-branch networks, respectively. Some of the designs on the fronts are shown in (b)-(m). The two- and five-branch networks with the minimum value of $T_{\max}$ on the fronts are shown in Figures 7.3d and 7.3f.

constraints described in Chapter 6. When that happens, the numerical accuracy of the finite element method suffers unless elements cut by the channels are sufficiently refined. To address this issue, we constraint the area fraction of the channels to be greater than or equal to the area fraction of the appropriate reference network, which is 0.018, 0.027 and 0.038 for the two-, five- and eight-branch networks, respectively. This constraint is removed when generating other Pareto points. As explained in Section 7.2, the abovementioned modification does not affect the shape of the Pareto front except at the end point with the lowest pressure.

Figure 7.4a presents the pressure-temperature Pareto front for the two-, five- and eight-branch cases, where each interior point has been generated from one initial design corresponding to the point on the right. We note that the Pareto points with $T_{max} > 200\,^{\circ}\mathrm{C}$ are not included in Figure 7.4a as those points are of no interest to the designer. Also, since the Pareto front of the eight-branch network is characterized by a very short horizontal portion, we have imposed a minimum pressure constraint of 15 kPa to obtain the rightmost end point of the front, thus effectively extending the front to the right. For all branches, the fronts exhibit the same trend of a flat portion for larger pressure drop and a steep portion for smaller pressure drop. As the number of branches increases, the front is translated downwards with decreasing size. At the same time, the flat segment becomes more horizontal and the kink shifts slightly to the right. Note that this part of the front corresponds to the results shown in Figure 7.3i.

The optimal designs represented by some of the Pareto points are presented in Figure 7.4b–7.4m. The designs of the first two columns are consistent with those of Figures 7.3a–7.3h in reversed order. As the pressure drop is severely constrained, it is observed that the designs approach the theoretical minimum pressure design of a straight line between the inlet and outlet. On the other hand, as the pressure drop is allowed to be large, the network becomes significantly longer in length.

7.3.3 Minimization of variance

In this subsection, we consider the minimization of the variance (7.6) of the two-branch network subject to pressure and temperature constraints $T_{\max} \leq T_{\max,o}$ and $\Delta P \leq P_o$, where $T_{\max,o} = 60\,^{\circ}\mathrm{C}$ and $P_o = 20$ kPa. The maximum temperature constraint is imposed using (7.7). In Figures 7.5a and 7.5b, we show the optimal design with the lowest $T_{\max}$ and corresponding optimization history of the maximum temperature and the standard deviation (square root of variance). The optimal design maximum temperature and actual pressure drop are respectively 59.4 °C and 18.5 kPa, which satisfy the imposed constraints.

However, we note that the maximum temperature constraint algorithm did not work well from time to time due to the changing $c^{(i)}$ in (7.7), which sometimes led to failure in satisfying the

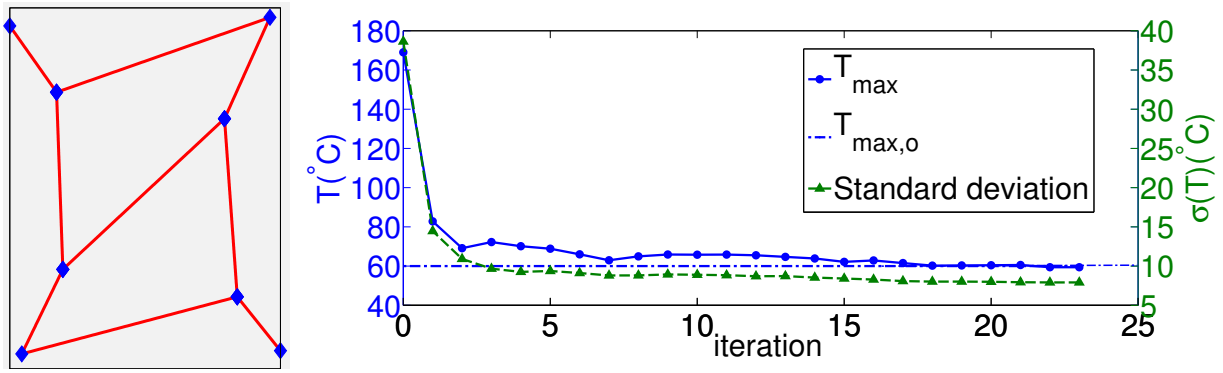

(a) **(b)**

Figure 7.5 – (a) Optimal design obtained with variance as objective function and constraints ($\Delta P \leq 20$ kPa, $T_{\max} \leq 60\,^{\circ}\mathrm{C}$) and (b) the corresponding optimization history.

constraint. Furthermore, the abovementioned minimization of the variance only resulted in designs that were marginally better in terms of variance compared with those arising from the minimization of $\langle T \rangle_p$. Therefore, the minimization of $\langle T \rangle_p$ is a better choice for producing designs with uniform temperature.

7.4 Optimization results related to operating constraints

7.4.1 Optimal designs with localized heat sources

Thermal management of lithium-ion batteries need to consider localized heating due to abuse events [132]. Furthermore, higher heat generation rates in experiments can cause concentration gradients in the electrolyte to develop, which then leads to localized heat generation [132]. Hence, the computational design tool developed in this dissertation allows for such heating to be considered. Provided that the distribution of the heat source can be approximated by a differentiable function, the sensitivity analysis described in Section 5.2 can be readily applied. For the purpose of demonstration, we define a heat source localized in n_r regions as

$$f(x,y) = \begin{cases} q_o'' \sum_{i=1}^{n_r} \left[1 - \left(\frac{x-x_i}{r_i}\right)^2\right]^2 \left[1 - \left(\frac{y-y_i}{r_i}\right)^2\right]^2 & |x-x_i| \leq r_i,\ |y-y_i| \leq r_i, \forall i \\ 0 & \text{otherwise,} \end{cases} \tag{7.8}$$

where $\int_\Omega f(x,y)\mathrm{d}\Omega = Q$. To satisfy the last equation, it can be readily shown that the equation $(256 q_o'' \sum_i r_i^2)/225 = Q$ must hold. We choose Q to be the total heat generated by the uniform heat source in this work, i.e., $Q = 15\,\mathrm{W}$.

As shown in Figures 7.6a and 7.6b, we consider two sets of parameters: (i) $x_1 = 0.075$ m, $y_1 = 0.1$ m, $r_1 = 0.04$ m corresponding to a localized heat source in the middle, and (ii) $x_1 = 0.04$ m, $y_1 = 0.04$ m, $x_2 = 0.11$ m, $y_2 = 0.16$ m, $r_1 = r_2 = 0.015$ m, corresponding to two heat sources localized near the bottom left and top right corners of the domain. Figures 7.6c to 7.6j compare the reference designs with the optimal designs for both cases. The reference designs fail to eliminate the hot spots as apparent in Figures 7.6d and 7.6h. In contrast, the thermal fields associated with the optimized designs in Figures 7.6f and 7.6j show that the hot spots are removed and the maximum temperatures are significantly reduced. Indeed, the maximum temperatures of the optimal designs are about 20 °C lower than those of the reference designs.

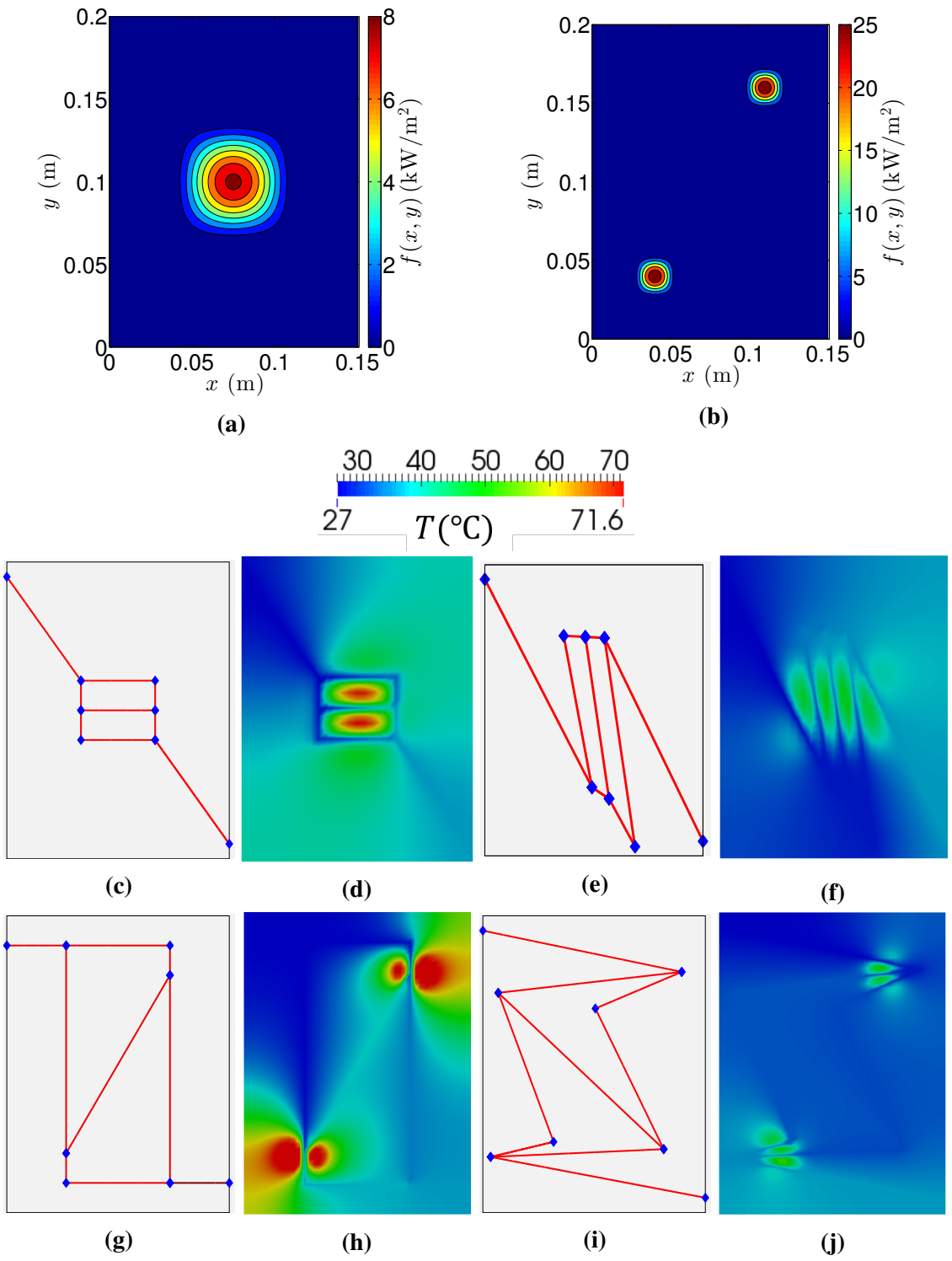

Figure 7.6 – Localized thermal loads on cooling panels represented by heat sources localized in the middle (a), and the top right and bottom left corners of the panel (b). Reference (c) and optimized (e) designs for heat source (a) and the associated temperature distributions (d) and (f). Reference (g) and optimal (j) designs for heat sources (b) with their corresponding thermal fields in (h) and (j).

7.4.2 Optimal designs with imposed pump power versus imposed flow rate

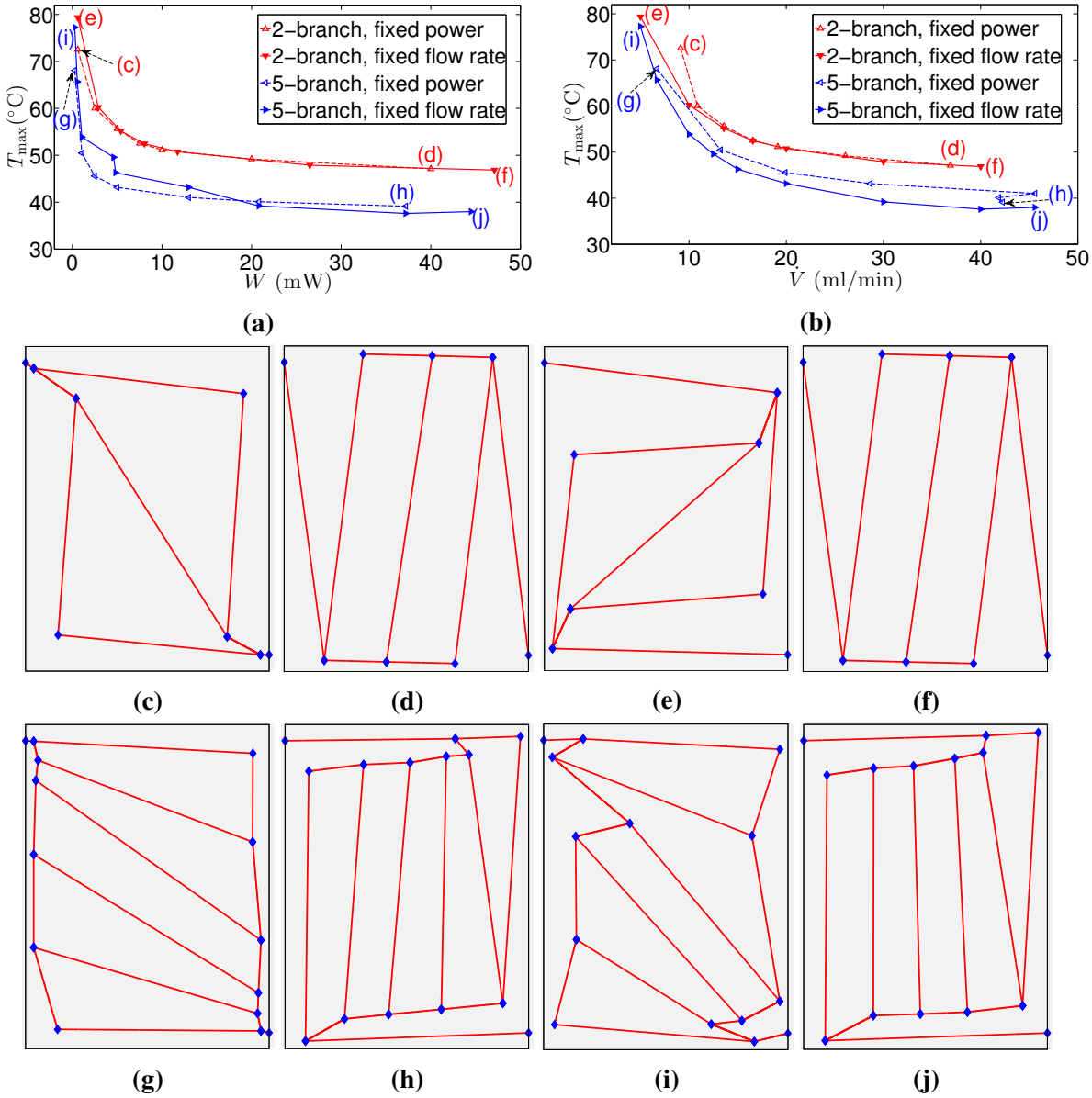

Figure 7.7 – Maximum temperatures of optimal designs as a function of (a) pump power and (b) flow rates, when the pump power or the flow rate is specified in the optimization. Designs optimized at low power (c), (g), and high power (d), (h). Designs optimized at low flow rates (e), (i), and high flow rates (f), (j).

Thus far, the optimization was done with a prescribed flow rate. In this subsection, we compare the optimal designs obtained with prescribed pump power to those derived by prescribing flow rates, both with constant viscosity evaluated at the reference temperature ($2.198 \times 10^{-6}\,\mathrm{m}^2/\mathrm{s}$ at 38 °C). Figure 7.7a (Figure 7.7b) shows the variation of the maximum temperature with respect to the

pump power (flow rate). At low power (flow rates), it is apparent that the fixed-power (fixed-flow-rate) optimal designs have lower maximum temperatures compared with the fixed-flow-rate (fixed-power) optimal designs. The optimal designs corresponding to low prescribed power (Figures 7.7c and 7.7g) are characterized by shorter channels since the prescribed power is akin to a pressure constraint.

For the two-branch case, the maximum temperature curves coincide with each other for high power (flow rates) as the fixed-power-optimal designs become identical to the fixed-flow-rate optimal designs (Figures 7.7d and 7.7f) for sufficiently large power (flow rates). On the other hand, the curves associated with the five-branch optimal designs are different, with the fixed-power optimal designs having higher maximum temperatures compared with the fixed-flow-rate optimal designs for $W \geq 20$ mW. This difference arises due to two reasons: (i) the optimized design at higher power (Figures 7.7h) is not exactly the same as the design at high flow rates (7.7j), and (ii) optimization at high prescribed power is not accompanied with higher flow rates as shown in Figure 7.7b. Upon closer examination of the five-branch fixed-power curve in that figure, it is evident that the flow rates of the last three points corresponding to optimization at power greater than 13 mW stagnates at about 42 ml/min, indicating that the flow rates chosen at high power are only locally optimal.

7.5 Cross-sectional area as design parameter

7.5.1 Optimal designs

In Section 7.3, Figure 7.4a showed that the pressure drop of the most "balanced" designs at the kinks (i.e., designs (c), (g) and (k) of Figure 7.4a) were rather insensitive to the number of branches. As shown next, the geometry of the channel cross sections can be introduced as design parameters to lower the pressure drop further. To faciliate the manufacturing of the optimal designs, we fix the height of the channels at 0.75 mm but allow the width to vary between 0.35 and 1.5 mm. We then minimize $\langle T \rangle_8$ of the eight-branch network subject to the contraints $\Delta P \leq 7$ kPa and $A_f \leq 0.041$, where A_f is the area fraction of the network and the upper bound corresponds to the area fraction of the fixed-cross-section optimal network in Figure 7.4k, for which $\Delta P = 10.6$ kPa. Figure 7.8a shows the variable-width optimal design together with the widths of its channels. The pressure constraint is satisfied, resulting in a subtantially lower pressure drop compared with that of the fixed-cross-section optimal design. The distribution of the diameters reveals that larger cross sections are favored for channels near the boundaries of the domain. This is reasonable because the pressure drop is reduced when more coolant is supplied through the shorter channels.

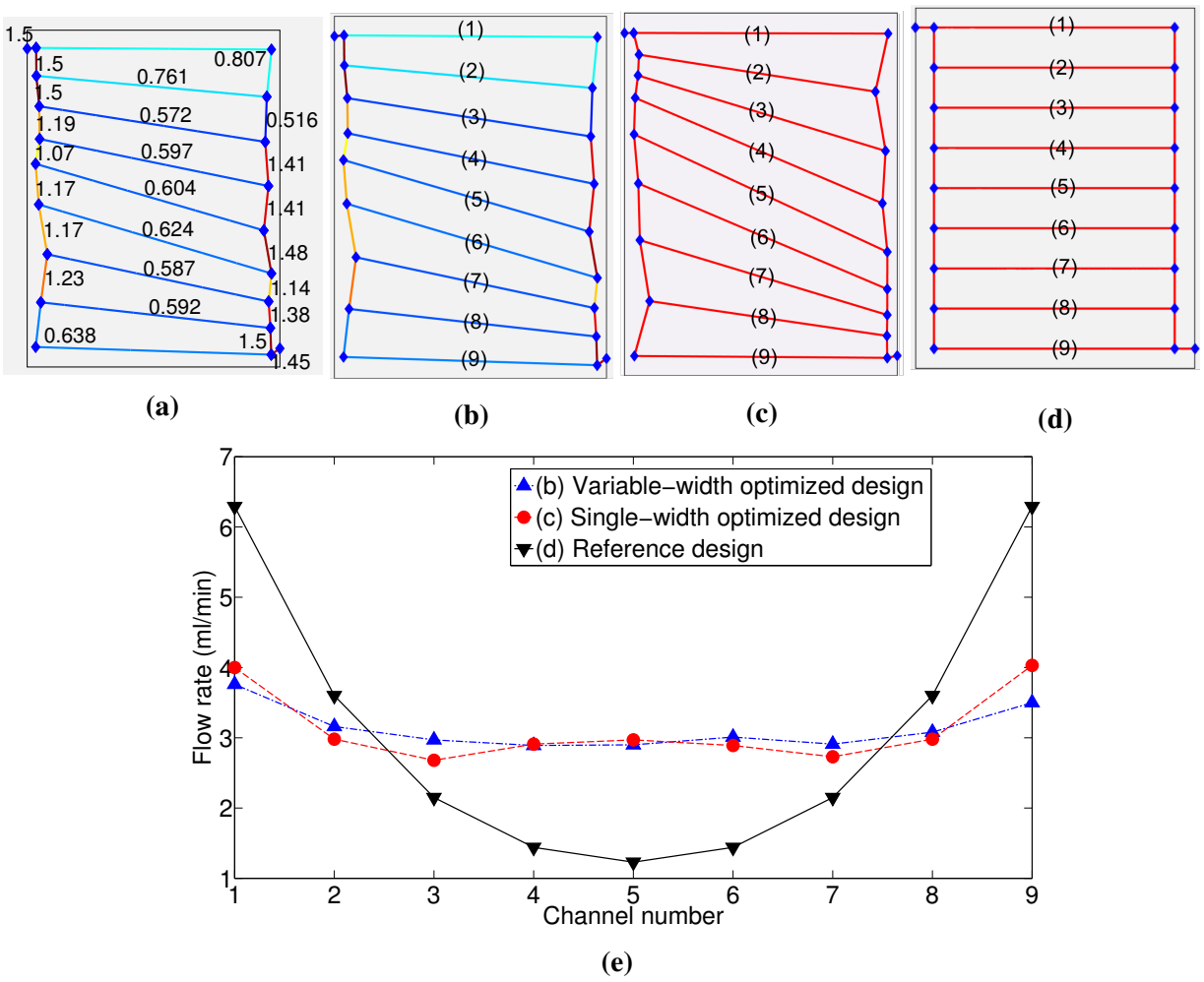

Figure 7.8 – Introducing the width of the channel rectangular cross sections as design variables allows further reduction in pressure drop and improves thermal performance compared with the fixed-cross-section case. (a) Widths in mm of the variable-width optimal design. (e) Flow rates in the nine interior channels for the variable-width optimal design (b) with $T_{\max} = 38.3\,^{\circ}\mathrm{C}$, $\Delta P = 7.0$ kPa and $A_f = 0.041$. (c) Fixed-cross-section optimal design (same as Figure 7.4k) with $T_{\max} = 41.9\,^{\circ}\mathrm{C}$, $\Delta P = 10.6$ kPa and $A_f = 0.041$. (d) reference design.

As shown in Figure 7.8e, both variable-width and fixed-cross-section optimal designs tend to equalize the flow rates in the interior channels labelled in Figures 7.8b and 7.8c. In contrast, the distribution of the corresponding flow rates of the reference network is rather non-uniform.

7.5.2 Validation

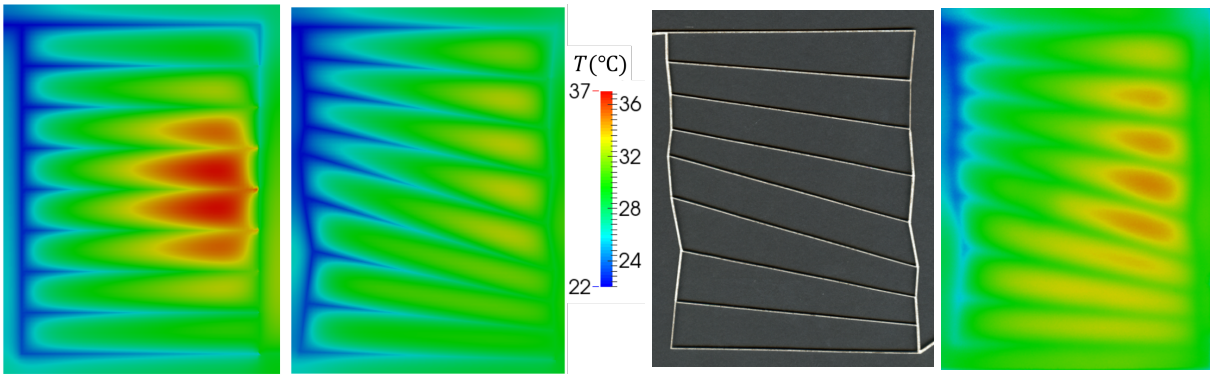

Figure 7.9 – Numerical temperature distributions associated with the reference eight-branch networks with fixed cross section (a) and the variable-width optimal eight-branch network (b). (c) Laser-cut sacrifical template used to embed the optimal eight-branch network in the composite panel for the validation study. (d) Experimentally measured temperature distribution of the optimized network.

In this last section, we present a validation study of the variable-width optimal design under the thermal loading conditions described in the validation study of Chapter 6 (Section 6.2) and for the same flow rate of 28.2 ml/min. The temperature of the optimized design shown in Figure 7.9b is significantly more uniform than that of the reference design shown in Figure 7.9a. While the average and maximum temperatures associated with the former are respectively 27.9 °C and 32.9 °C, those associated with the reference designs are 30.4 °C and 37.2 °C, respectively.

Using the laser-cut sacrifical template shown in Figure 7.9c, a microvascular composite panel with the optimized network was fabricated. While the experimentally measured thermal field shown in Figure 7.9d agrees with the simulated thermal field, the experimental average and maximum temperatures of 30 °C and 34.6 °C, respectively, agree with the simulated values within the uncertainty of the experiment. Furthermore, the experimental pressure drop of 9.0 kPa is well predicted by the simulated pressure drop of 8.15 kPa.

7.6 Conclusions

Using the 2D computational design tool, we considered two competing objective functions — p-mean of the temperature and pressure drop — in the optimization of parallel microchannel networks. The Pareto front of these competing objectives were generated using the ε-constraint method and the NNC method. The former method generated a front that showed a rather slow

decrease in maximum temperature with respect to pressure drop. This front turned out to be part of the complete front generated by the NNC method. The complete front showed two distinct regions separated by a kink. One region had a gentle slope that tended to a horizontal line as the pressure drop increased, consistent with that of the ε-constraint method. The other region was characterized by a steep slope that indicated a rapid rise in maximum temperature as the pressure was reduced. Another optimization using the variance of the thermal field as objective function was also considered.

We also optimized the designs in the presence of localized heat sources to simulate the conditions often encountered in reality. These optimal designs were superior to the "ad hoc" reference designs under these specific thermal loads. Optimization with prescribed pump power and constant fluid viscosity were also performed. However, the tendency of designs optimized at higher powers to operate at lower flow rates and the constant viscosity assumption placed power-based optimization at a disadvantage compared with the more versatile fixed-flow-rate optimization.

Next, we showed that the pressure drop of the network could be improved subtantially when the sizes of the channel cross sections were introduced as design parameters. Lastly, the variable-width optimal design was validated with experiment.

8 2D Design of Blockage-Tolerant Microvascular Cooling Networks

This chapter is adapted from an article in preparation titled "Design of blockage-tolerance microvascular cooling networks" by S. J. Pety, M. H. Y. Tan (co-first author), A. R. Najafi, P. Barnett, N. Sottos, P. H. Geubelle and S. R. White.

8.1 Introduction

Branched networks are pervasive in nature and show high resiliency against blockages. In modern leaves, nutrients can circumvent damaged regions of considerable sizes to reach downstream regions of the leaves [133]. In the brain of rodents, blood flow can bypass occlusions occuring in certain parts of the vascular system [134, 135, 136]. Studies have been conducted to replicate these natural occuring network using constructal theory [39, 41] or numerical optimization [133, 137, 138]. By postulating that natural flow systems evolve to reduce resistance to flow and networks, branches perpendicular to each other with diameter decreasing with branch level were obtained in the former approach. The latter approach modeled a vascular network as an electrical circuit consisting of resistors, with each resistor having a conductance that was related to the diameter of the represented channel. While the conductances of the resistors were chosen as design variables, the total dissipated power for different scenarios of single cut connection was chosen as the objective function to represent robustness against "damage". Tree-like networks that resembled vascular systems of modern leaves were obtained from the minimization process, thus substantiating the theory that such vascular architecture arises in nature to maximize resiliency against blockages.

While microchannel cooling greatly enhances heat transfer, it comes with the challenge of susceptibility to blockages caused by particulates in the fluid [139, 140]. Inspired by natural vascular systems, branched network designs have been considered to increase the redundancy of the cooling system [17] and shown to reduce loss in cooling performance due to blockages [141]. In addition to starting with a good network topology, we demonstrate in this chapter that we can further minimize the thermal effect of the blockages using the optimization tool developed in this dissertation to solve a minmax optimization problem. To faciliate blocking the channels in experiments, we design the microchannels for microvascular PDMS panels.

This chapter is organized as follows: We begin by validating the nonlinear and linearized thermal models (2.5) and (2.6) for a range of flow rates in Section 8.2. Section 8.3 describes two optimization problems of interest: (i) minimization of the p-norm of the temperature field as a differentiable representation of the maximum temperature and (ii) minimization of the maximum p-norm for different blockage scenarios. Using the sensitivity analysis of the linearized thermal model described in Chapter 5, we then solve the abovementioned optimization problems for grid-like networks with different nodal degrees used as measures of redundancy. Lastly, we compare and validate the performance of the optimized networks with and without blockages.

8.2 Validation study

A validation study was performed with the experimental setup shown in Figure 8.1a and described by the parameters presented Table 8.1. A PDMS panel, painted black and shown schematically in Figure 8.1b, was subject to localized heating from below by an electric heater. An aqueous ethylene glycol was pumped through the embedded microchannel network with a peristaltic pump and the resulting pressure drop across the network was measured with a pressure transducer. While the inlet temperature of the coolant was monitored with a thermocouple, the top surface temperature distribution of the panel was recorded with an infrared camera.

The setup of the IGFEM simulation is shown in Figure 8.1c, which involves a convective heat loss q''_{conv} and a radiative heat loss q''_{rad} to the environment. q''_{conv} and q''_{rad} are respectively modeled with the last two terms of (2.2). Both original and linearized versions of q''_{rad} described in Section 2.4 are used in this chapter. While the convection coefficient $\tilde{h}$ is found by fitting simulation results to experimental measurements [105, 106], the emissivity of the black paint used for the panel ϵ is obtained from the vendor. All sides of the domain except the network inlet are insulated and an inlet temperature of 22 °C is specified. Due to the 2D nature of the simulation, a conductivity of κt is used.

We use a grid-like network with a single inlet on the top-left side and a single outlet on the bottom-right side as shown in Figure 8.1c in this validation exercise. We assume that the viscosity of the fluid is uniform throughout the channels and takes the value at the average channel temperature. Due to this assumption, the mass flow rate in each channel is independent of the viscosity and hence independent of temperature. The hydraulic model is therefore decoupled from the thermal model, and the pressure drop can be obtained after the solution of the thermal problem. A lower bound of the pressure drop is obtained using an average rectangular cross section with width and thickness (a_{ave}, b_{ave}) respectively equal to the averages of the experimentally measured widths and thicknesses of the channel cross sections at various locations. On the other hand, an upper

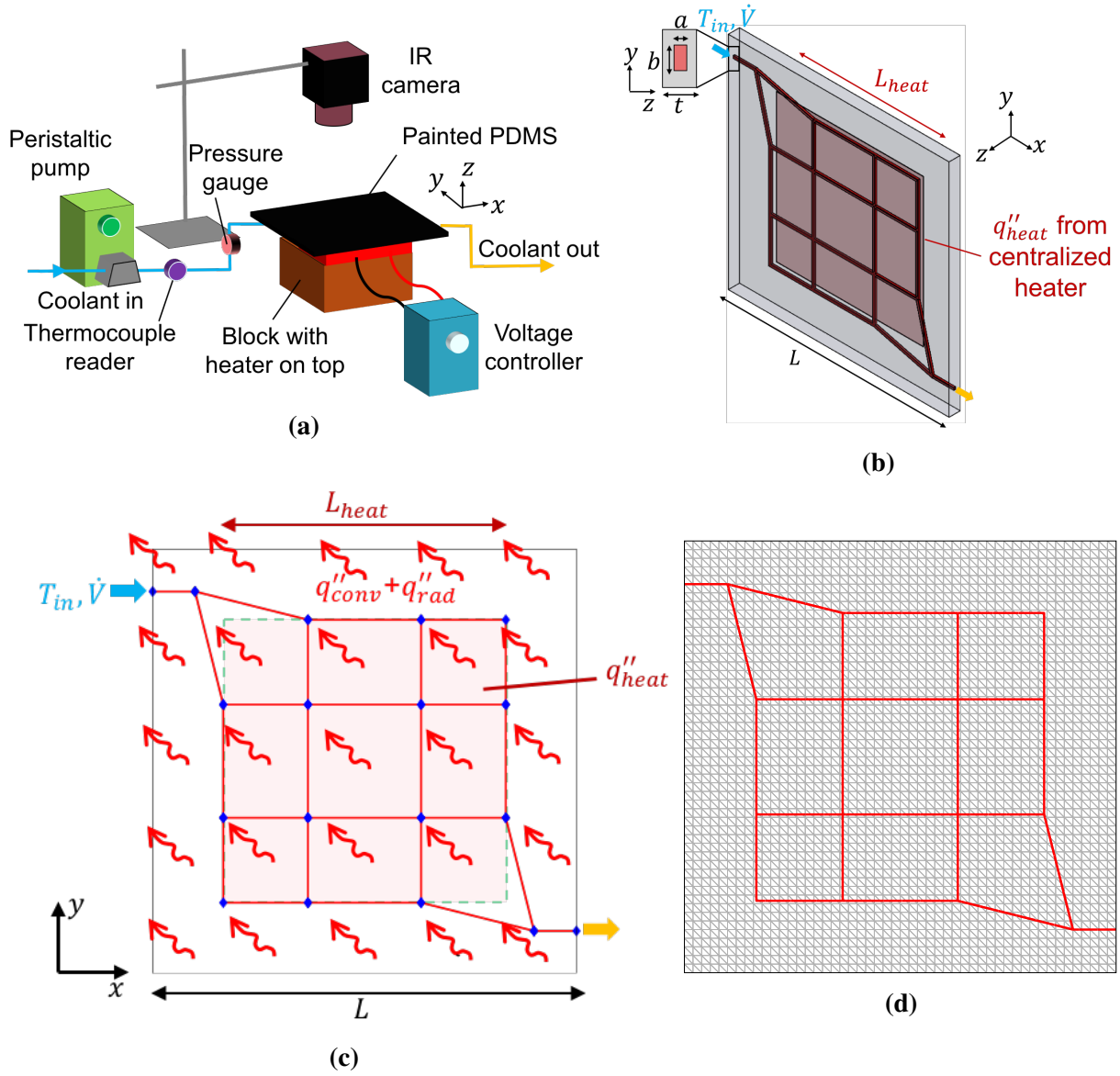

Figure 8.1 – (a) Experimental setup for the heating of an actively cooled microvascular PDMS panel (b). (c) IGFEM setup and (d) structured mesh used for the IGFEM simulations.

bound of the pressure drop is obtained using the minimum cross-sectional dimensions (a_{min}, b_{min}) consisting of the average width and thickness minus their respective standard deviations.

Throughout this chapter, a structured mesh with 40 divisions in both the x- and y- directions as shown in Figure 8.1d is found to be sufficiently accurate. The Newton-Raphson termination tolerance ε is fixed at 10^{-6}.

Temperature distribution resulting from the nonlinear model shown in Figure 8.2a agrees relatively well with the experimental temperature distribution shown in Figure 8.2b. A more detailed comparison of the simulated and experimental maximum temperatures and pressure drops for a

Table 8.1 – Parameters of validation study.

Parameter	Value
Boundary conditions	
Heater power q''_{heat}	2000 Wm^{-2}
Heater size L_{heat}	50 mm
Convection coefficient $\tilde{h}$	15 $\mathrm{Wm}^{-2}\mathrm{K}^{-1}$
Emissivity for top face ϵ	0.97
Ambient temperature T_∞	22 °C
Sample dimensions in mm	
Panel width or height L	75
Panel thickness t	3.8
Solid	PDMS
Thermal conductivity κ	0.27 $\mathrm{Wm}^{-1}\mathrm{K}^{-1}$ [142]
Channel cross section in mm	
Average width b_{ave}	0.81
Average thickness a_{ave}	0.55
Minimum width b_{min}	0.68
Minimum thickness a_{min}	0.53
Coolant	Water-ethylene glycol
Total flow rate $\dot{V}$	≤ 56.4 ml/min
Inlet temperature T_{in}	22 °C
Outlet pressure	0
Density ρ	1065 $\mathrm{kg\,m}^{-3}$ [20]
Viscosity μ	$0.0069(T/273)^{-8.3}$ $\mathrm{kg\,m}^{-1}\mathrm{s}^{-1}$ ([120], p. 45)
Specific heat capacity c_p	3494 $\mathrm{J\,kg}^{-1}\mathrm{K}^{-1}$ [20]

range of flow rate is presented in Figure 8.3. As shown in Figure 8.3a, the maximum temperature obtained with the linear model consistently overestimates that of the nonlinear model with decreasing difference as the flow rate increases. The differences at the flow rates of 1.5 and 28.2 ml/min are 1.46 and 0.64 °C, respectively. Furthermore, excluding the no flow case, the experimental temperature differs from those of the linear and nonlinear models by at most 2.9 and 2.3 °C, respectively, which are within the uncertainty of the experiment. Hence, in the design study described later in Section 8.3, we develop an optimization scheme exploiting the linear model to improve efficiency, and postprocess the optimized designs with the nonlinear model for improved accuracy.

As apparent from Figure 8.3b, the experimental pressure drop is contained within the lower and upper bounds of the simulated pressure drop obtained respectively with the average and minimum cross-sectional dimensions. However, the upper bound appears to be significantly more accurate. Hence for the remainder of this chapter, the simulated pressure drops for the minimum cross-sectional dimensions are reported unless specified otherwise.

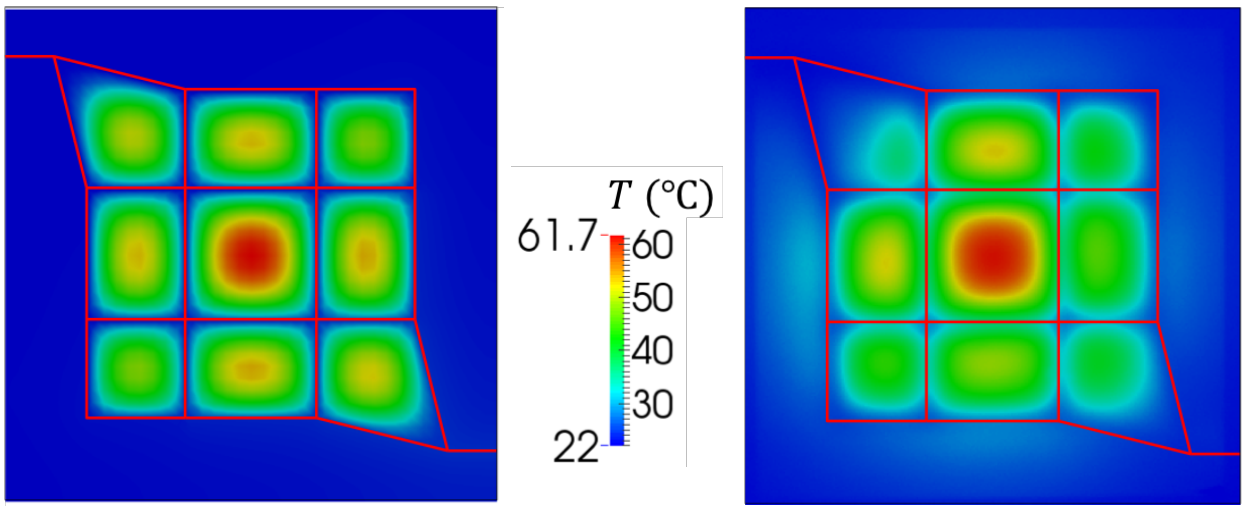

(a) **(b)**

Figure 8.2 – (a) IGFEM and (b) experimental temperature distributions at a flow rate of 28.2 ml/min with maximum temperatures 61.7 and 58.9 °C, respectively.

In Figure 8.4, we compare the simulated and experimental coolant temperature rise ΔT_c, and cooling efficiency defined as $\eta = \dot{m}c_p\Delta T_c/(q''_{heat}L^2_{heat})$. Although the coolant temperature rise decreases with flow rate, the mass flow rate increases faster, thus increasing the cooling efficiency. However, the cooling efficiency saturates at about 76–78% for flow rates higher than 28.2 ml/min. This is due to the resistance associated with the absorption of the heat by the coolant, which scales with $1/(\dot{m}c_p)$, dropping below other thermal resistances in the system. At all flow rates tested here, the simulated ΔT_c and η agree well with that of experiment.

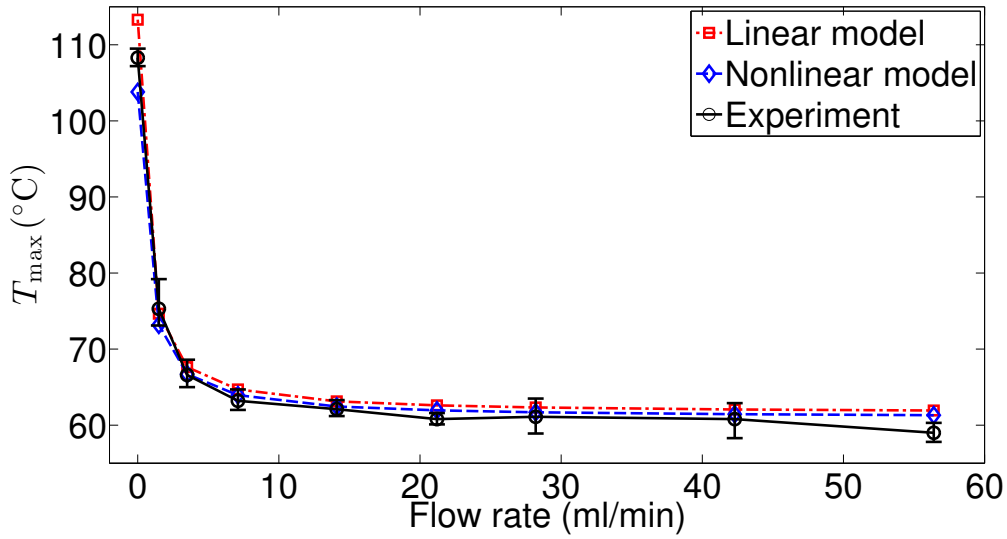

(a)

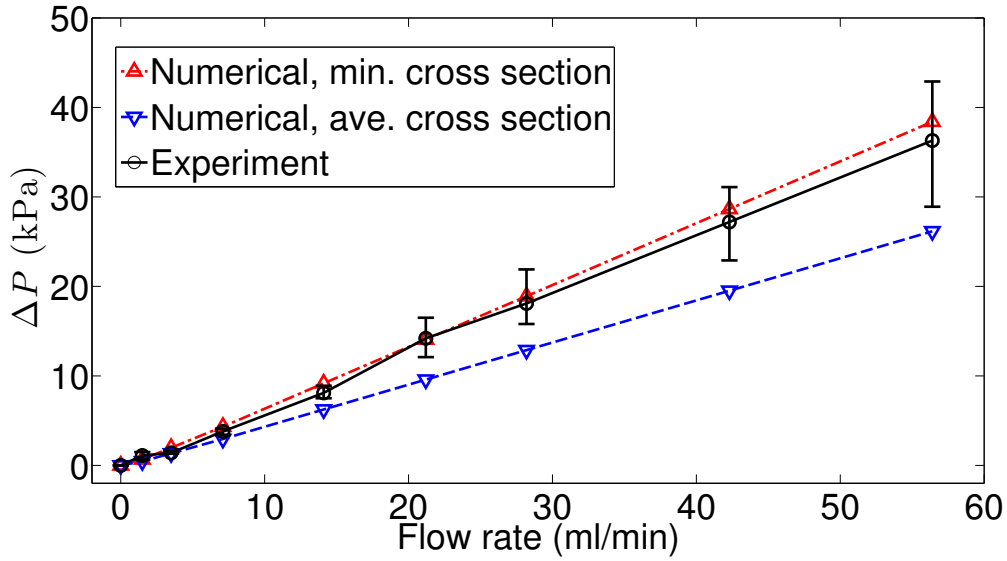

(b)

Figure 8.3 – (a) Maximum temperatures associated with the $D4$ R network in Figure 8.1c computed from the linear and nonlinear thermal models compared against the corresponding experimental measurements. (b) Simulated lower and upper bounds of the pressure drop across the network obtained respectively from the average and minimum channel cross sections compared with experimental measurements.

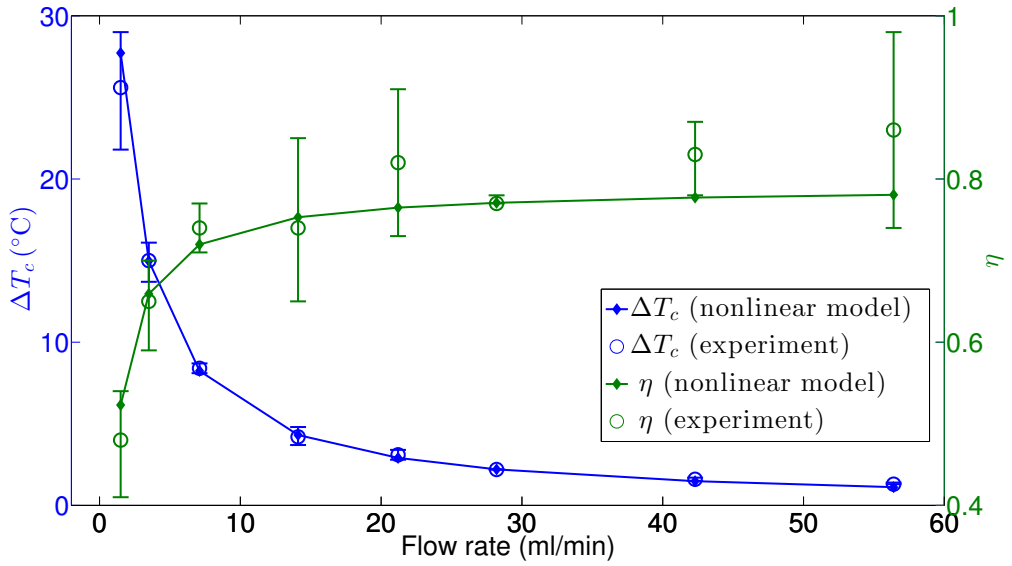

Figure 8.4 – Simulated and experimentally measured coolant temperature rise ΔT_c and the computed thermal efficiency η defined in the text.

8.3 Optimization study

8.3.1 Optimization problem

We now combine the IGFEM-based sensitivity analysis for the linear thermal model described in Chapter 5 (Section 5.2) and the MATLAB sequential quadratic programming (SQP) algorithm [122] to solve two optimization problems described next. The important parameters used for the SQP algorithm are given in Table 6.4. An objective function of primary importance in cooling is the maximum temperature. However, since it is not differentiable, we replace it with the differentiable p-norm $\|T^{(h)}\|_p$, where p is sufficiently large to represent the behavior of the maximum temperature. Based on previous work [52], we choose $p = 8$. We note here that the subsequent discussion is not limited to that particular value of p. Denoting the design parameters by $\boldsymbol{d} = \{d_1, ..., d_{n_d}\}$ and the nodal coordinates of the mesh by $\boldsymbol{X}$, the optimization problem, hereafter referred to as O_0, is given by

$$\begin{aligned} \min_{\boldsymbol{d}} \quad & \|T^{(h)}\|_p(\boldsymbol{X}(\boldsymbol{d}), \boldsymbol{d}), \\ \text{such that} \quad & \boldsymbol{g}(T^{(h)}(\boldsymbol{X}(\boldsymbol{d}), \boldsymbol{d}), \boldsymbol{X}(\boldsymbol{d}), \boldsymbol{d}) \leq 0, \end{aligned} \tag{8.1}$$

where $\boldsymbol{g} \leq 0$ is a vector of constraints and $T^{(h)}(\boldsymbol{X}(\boldsymbol{d}), \boldsymbol{d})$ is obtained from the finite element method.

Let $\boldsymbol{b}$ be a bit vector with n_{ch} entries where 1 on the ith position means that the ith channel is blocked and 0 otherwise. Let $\mathcal{B}$ be a finite set of bit vectors $\{\boldsymbol{b}^{(1)}, \boldsymbol{b}^{(2)}, ..., \boldsymbol{b}^{(n_\mathcal{B})}\}$ representing $n_\mathcal{B}$ blockage scenarios. The problem of designing for blockage tolerance can be thought of as the minimization of the worst "damage" resulting from predetermined blockage scenarios. One quantification of the "damage" is the maximum temperature in the domain, which is replaced with $\|T^{(h)}\|_p$, where p is also set to 8. The optimization problem can then be formulated as

$$\begin{aligned} \min_{\boldsymbol{d}} \max_{\boldsymbol{b} \in \mathcal{B}} \quad & \|T^{(h)}\|_p(\boldsymbol{b}, \boldsymbol{X}(\boldsymbol{d}), \boldsymbol{d}), \\ \text{such that} \quad & \boldsymbol{g}(T^{(h)}(\boldsymbol{X}(\boldsymbol{d}), \boldsymbol{d}), \boldsymbol{X}(\boldsymbol{d}), \boldsymbol{d}) \leq 0, \end{aligned} \tag{8.2}$$

where the first argument after the p-norm emphasizes that it is a function of the bit vector. The seemingly formidable optimization problem (8.2) can be converted into the following simpler optimization problem [143, 144], referred to as O_j, where $j > 0$ is the maximum number of blockages in $\mathcal{B}$:

$$\begin{aligned} \min_{\boldsymbol{d}, z} \quad & z \\ \text{such that} \quad & \|T^{(h)}\|_p(\boldsymbol{b}, \boldsymbol{X}(\boldsymbol{d}), \boldsymbol{d}) - z \leq 0, \quad \forall \boldsymbol{b} \in \mathcal{B} \\ \text{and} \quad & \boldsymbol{g}(T^{(h)}(\boldsymbol{X}(\boldsymbol{d}), \boldsymbol{d}), \boldsymbol{X}(\boldsymbol{d}), \boldsymbol{d}) \leq 0. \end{aligned} \tag{8.3}$$

Let us denote the design obtained from the O_i optimization and operated in the blockage scenario $\boldsymbol{b}$ by $O_i(\boldsymbol{b})$. Let $\boldsymbol{c}$ to be a bit vector with only unity entries. Thus $O_i(\boldsymbol{c})$ means a design operating in the ideal scenario of clear channels. For a given design, define $\boldsymbol{w}$ as a bit vector that maximizes the maximum temperature over $\mathcal{S}$, i.e., $\boldsymbol{w} = \arg\max_{\boldsymbol{b}\in\mathcal{S}} T_{\max}(\boldsymbol{b})$. Then $O_i(\boldsymbol{w})$ is a design derived from the O_i optimization and operated in the worst case scenario of $\mathcal{S}$. Note that $\boldsymbol{w}$ for one design is not the same as that of another design though the notation does not explicitly indicate that dependence. We summarize the design notations in Table 8.2.

Table 8.2 – Summary of design notations.

Notation	Description
$O_i(\boldsymbol{c})$	O_i optimized design operating with clear channels
$O_i(\boldsymbol{w})$	O_i optimized design operating in the worst blockage scenario among a finite set of blockage scenarios
$R(\boldsymbol{c})$	Reference design operating with clear channels
$R(\boldsymbol{w})$	Reference design operating with the worst blockage scenario among a finite set of blockage scenarios
Dn	Degree-n design

In the remainder of this chapter, we apply the shape optimzation scheme to the grid-like designs with nodal degrees ranging from 2 to 6 as shown in Figures 8.5a–e, using the same parameters as the validation study presented in Section 8.2 and a flow rate of 28.2 ml/min. The nodal degree, defined as the number of channels incident upon any of the interior nodes indicated by the green squares, is a measure of the redundancy of the network. For brevity, we refer to a degree-n design by Dn.

Throughout the optimization process, the inlet and outlet channel nodes are fixed. Only interior nodes are allowed to move within the central region delineating the heater as shown in Figure 8.6a. While the movement of the two corner nodes represented as gray circles is restricted in a small region around their respective corners, the edge nodes indicated by the blue diamonds are allowed to move within rectangular regions around their respective edges. For example, the top right corner node is confined in the bounding box $\{62.5 \leq x \leq 72.5\,\mathrm{mm}, 62.5 \leq y \leq 72.5\,\mathrm{mm}\}$ represented by the dashed gray box in Figure 8.6b. On the other hand, the bounding box associated with the two upper edges nodes is $\{2.5 \leq x \leq 72.5\,\mathrm{mm}, 62.5 \leq y \leq 72.5\,\mathrm{mm}\}$ shown as the blue dashed box in Figure 8.6c.

To adress the "self-crossing" of some of the channels, which renders the problem unphysical, we apply geometrical constraints to the triangles constructed from the channels as shown in Figure 8.6d. The constraints are (i) the interior angles of the triangles $> 10^\circ$ and (ii) the area of each triangle $> 0.001\times$ area of domain. At least 48 distinct initial designs such as those shown in Figures 8.6e and f, which are generated by shuffling the control points within non-overlapping

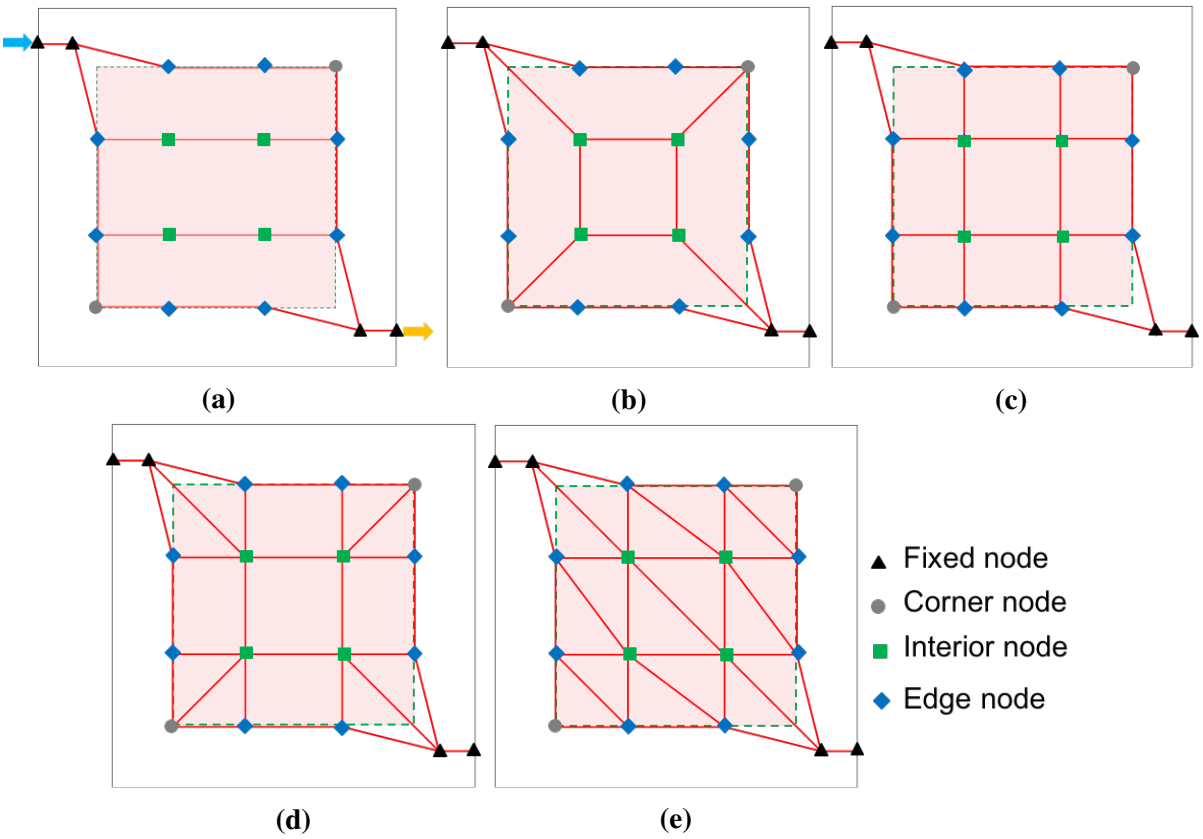

Figure 8.5 – (a)–(e) $D2$–$D6$ network designs and the different types of nodes of the networks described in the text.

bounding boxes, are used to investigate a wide range of potential optimal configurations.

We consider the collection of blockages $\mathcal{B}$ to consist of single-channel or double-channel blockages that exclude the inlet and outlet channels. The number of possible single-channel blockages scenarios ranges from 16 to 31 for the $D2$ and $D6$ designs, respectively. We consider double-channel blockages only for the $D6$ design, where the total number of scenarios is 465.

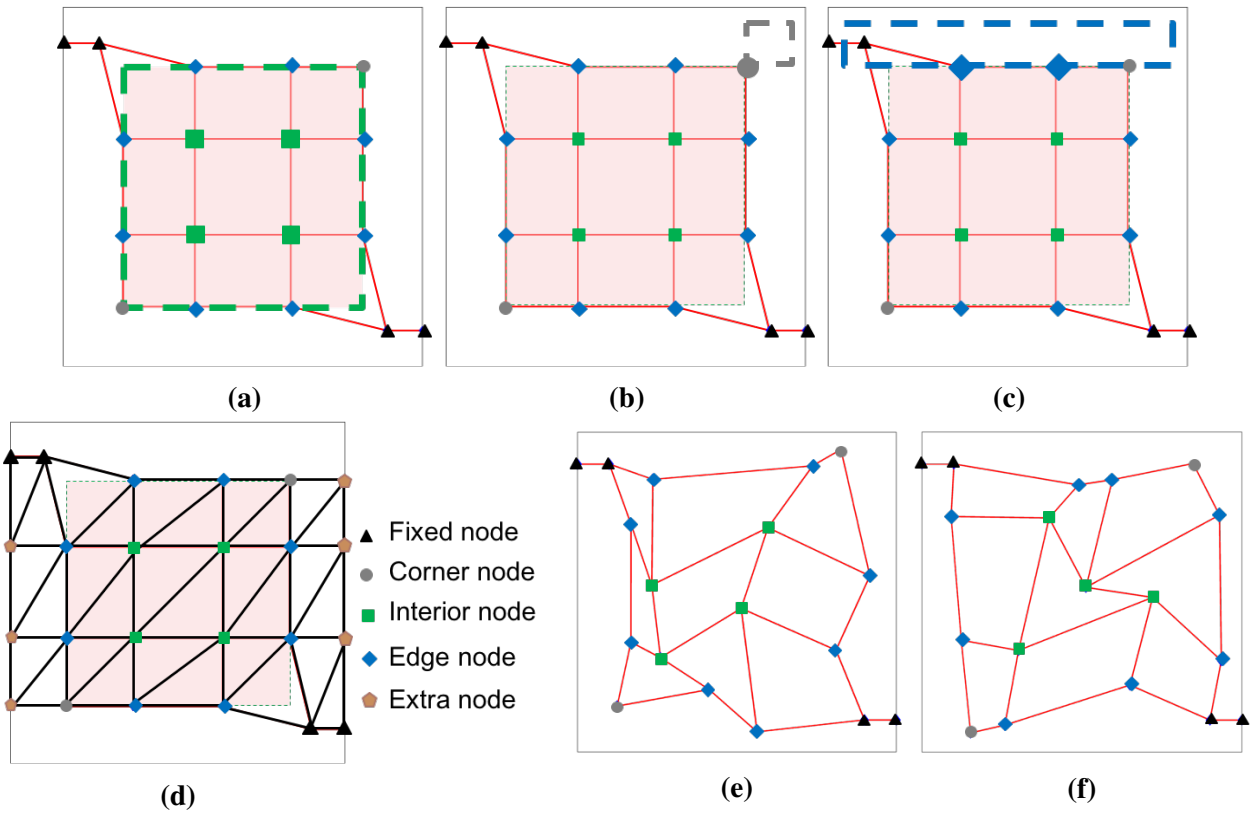

Figure 8.6 – Bounding boxes associated with the interior nodes (a), the top right corner node (b) and the two upper edge nodes (c). (d) Triangles for imposing geometrical constraints. Initial $D4$ designs (e) and (f).

8.3.2 Optimized designs for different degrees

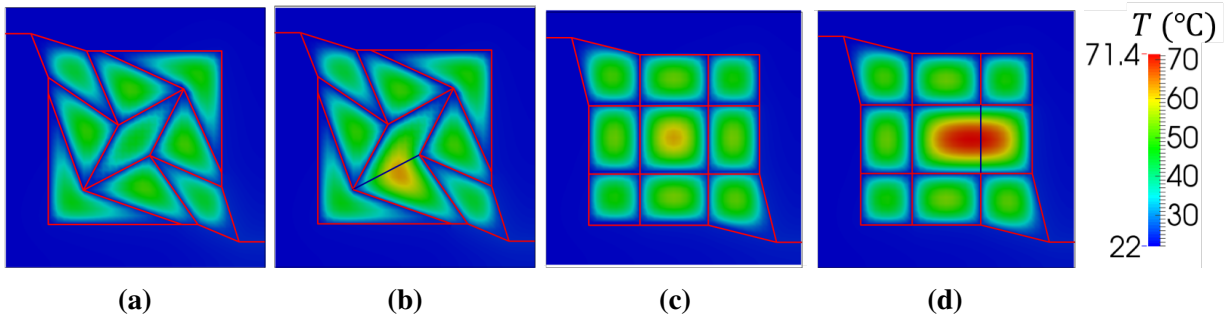

Figure 8.7 – (a), (b) Temperature field of the $D4$ O_1 designs in the worst-case and ideal scenarios ($\boldsymbol{w}$ and $\boldsymbol{c}$ in Table 8.2) compared with (c), (d) reference designs in the corresponding scenarios.

Figure 8.7 shows the thermal fields associated with the $D4$ O_1 design resulting from the above-mentioned choice of $\mathcal{B}$ and the $D4$ R design in the ideal scenario $\boldsymbol{c}$ and the worst-case scenario $\boldsymbol{w}$.

While the maximum temperatures of $O_1(\boldsymbol{c})$ and $O_1(\boldsymbol{w})$ are respectively 48.4 and 59.9 °C, the corresponding maxima for $R(\boldsymbol{c})$ and $R(\boldsymbol{w})$ are significantly higher at 61.7 and 71.4 °C, respectively. The associated pressure drops in the same order are 16.2, 16.6, 18.9 and 19.7 kPa. As expected, for both designs, the pressure drop increases when a single blockage occur.

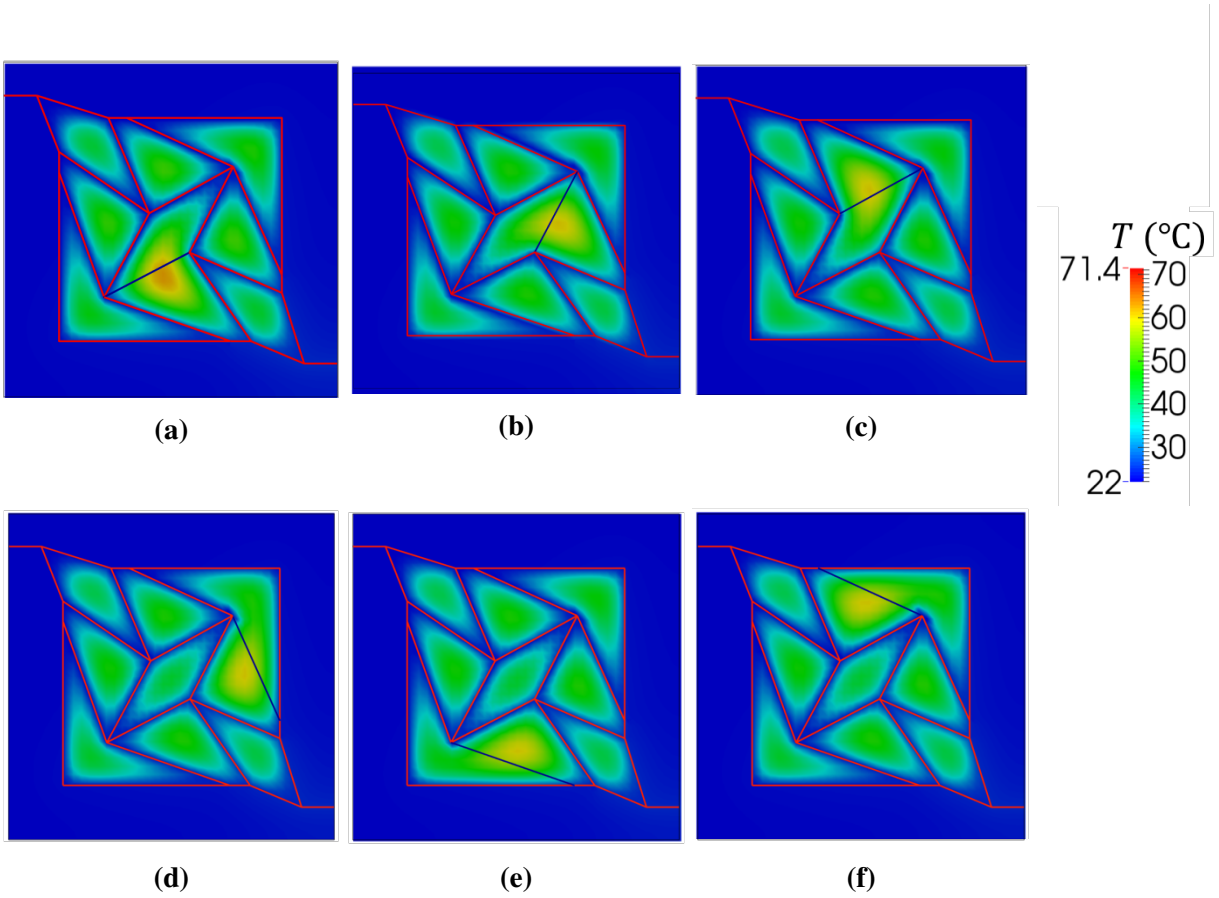

Figure 8.8 – (a)–(f) Temperature fields resulting from different single-blockage scenarios for the $D4$ O_1 design in descending order of maximum temperature starting from the worst-case Figure 8.7b.

To support the claim that Figure 8.7b is indeed the worst-case in the set $\mathcal{B}$, we show in Figure 8.8 the temperature distribution associated with the worst case together with those for five other scenarios of the 24 possible scenarios in $\mathcal{B}$ ranked by the maximum temperature in descending order. In addition to the substantially lower maximum temperature compared with the $D4$ R design, the closely spaced maximum temperatures of 59.92, 59.91, 59.78, 59.61, 59.54, 59.45 °C for the worst six scenarios demonstrate its blockage-tolerant performance.

We further compare the blockage-tolerant thermal performance of the designs resulting from the O_1 optimization (8.3) with those obtained from the O_0 formulation (8.1). Figure 8.9 shows the $D2$ to $D6$ O_0 designs in the leftmost two columns and the corresponding O_1 designs in the

rightmost two columns. By comparing the first and third columns, we observe that the thermal performance of the O_0 designs is better than that of the O_1 designs in the ideal scenario but with less distinguishable difference at higher nodal degrees. However, as apparent from the hot spots in the second and fourth columns, the loss in performance due to a blockage in the $\boldsymbol{w}$ scenario is significantly more severe for the O_0 designs.

The maximum temperatures corresponding to the different designs and scenarios are presented in Figure 8.10. Except for the $O_0(\boldsymbol{c})$ case, the maximum temperature decreases monotonously with nodal degree. The small increase from $D2$ to $D3$ for the $O_0(\boldsymbol{c})$ case is due to the additional effect of nodal connectivity, i.e., the choice of neighbouring nodes for an interior node. For example, the top left interior node of the $D3$ network presented in Figure 8.5 could have been connected horizontally to the another node instead of the fixed node. If all interior nodes of the $D3$ network were connected horizontally to other nodes instead of the fixed nodes and the corner nodes, the $D2$ network would have been a subset of the $D3$ network, and one would expect the maximum temperature to decrease. As previously alluded to in Figure 8.9, while the O_0 designs perform better than the O_1 designs for clear channels, their performance deteriorates substantially for single-channel blockages. Furthermore, the loss in performance in terms of maximum temperature gained increases as the nodal degree decreases.

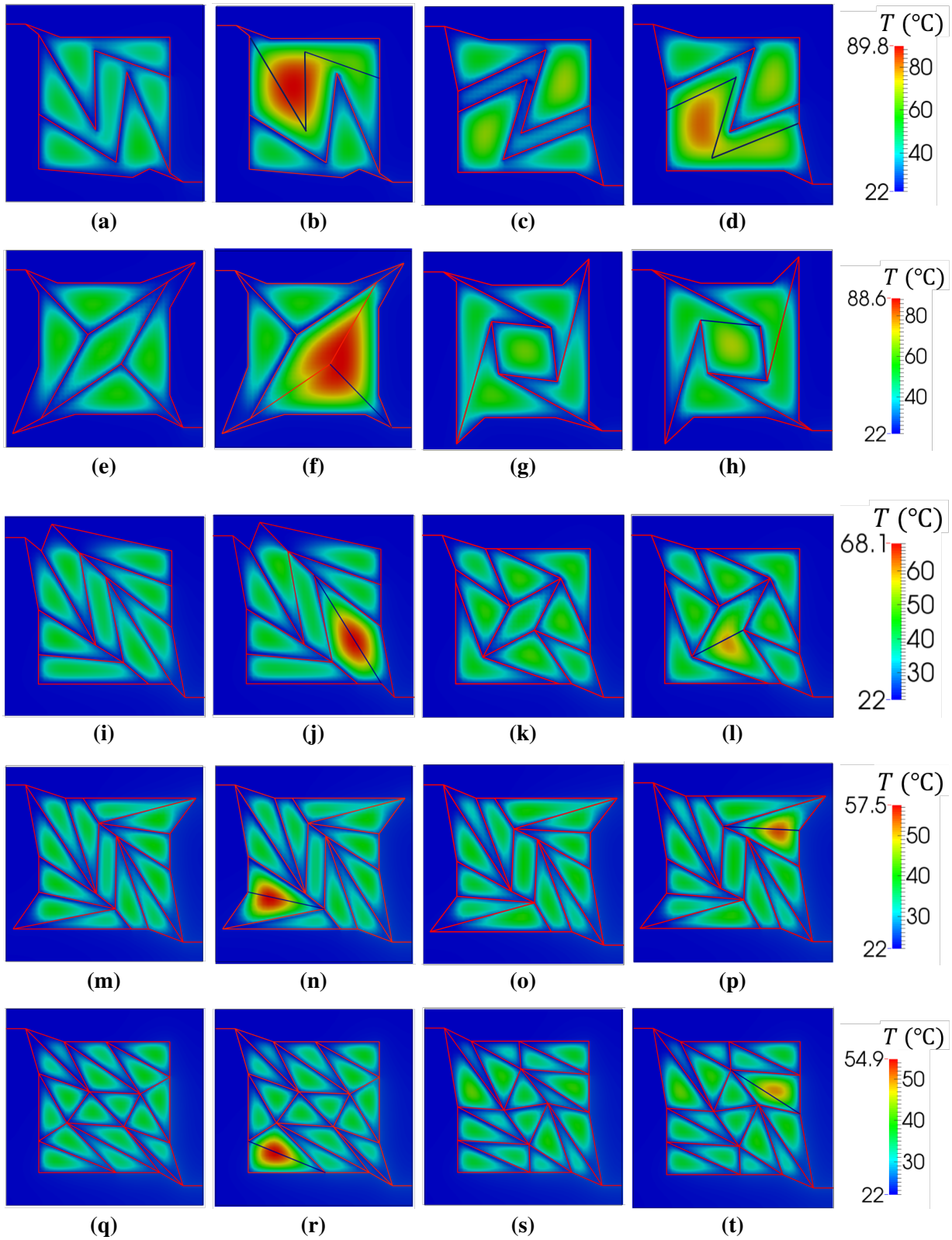

Figure 8.9 – Leftmost two columns respectively show O_0 designs in the worst-case and ideal scenarios ($\boldsymbol{w}$ and $\boldsymbol{c}$ in Table 8.2). Rightmost two columns respectively show O_1 designs in the same scenarios. The nodal degree increases from 2 (top row) to 6 (bottom row).

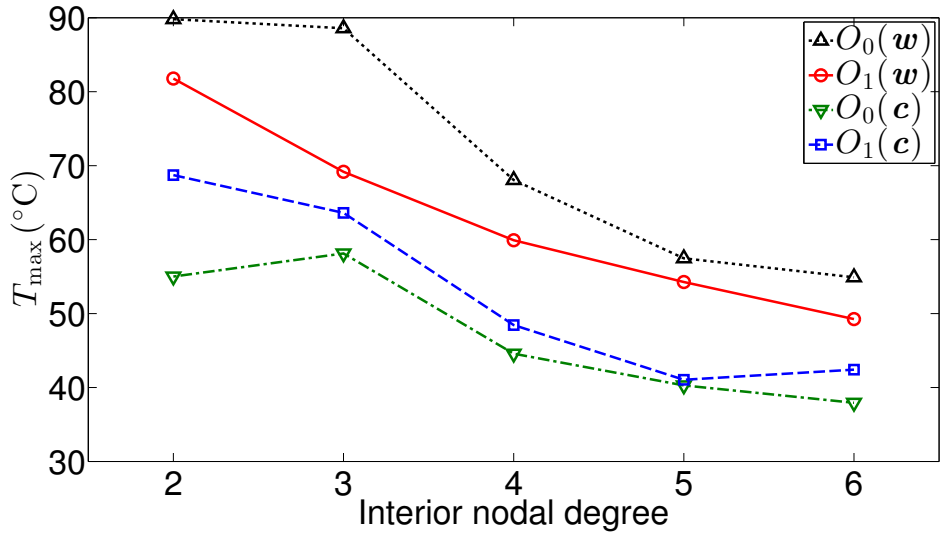

Figure 8.10 – Maximum temperature as a function of nodal degree corresponding to the Figure 8.9 optimized designs O_0 and O_1 in the worst-case and ideal scenarios ($\boldsymbol{w}$ and $\boldsymbol{c}$ in Table 8.2).

8.3.3 Optimized designs with different number of blockages

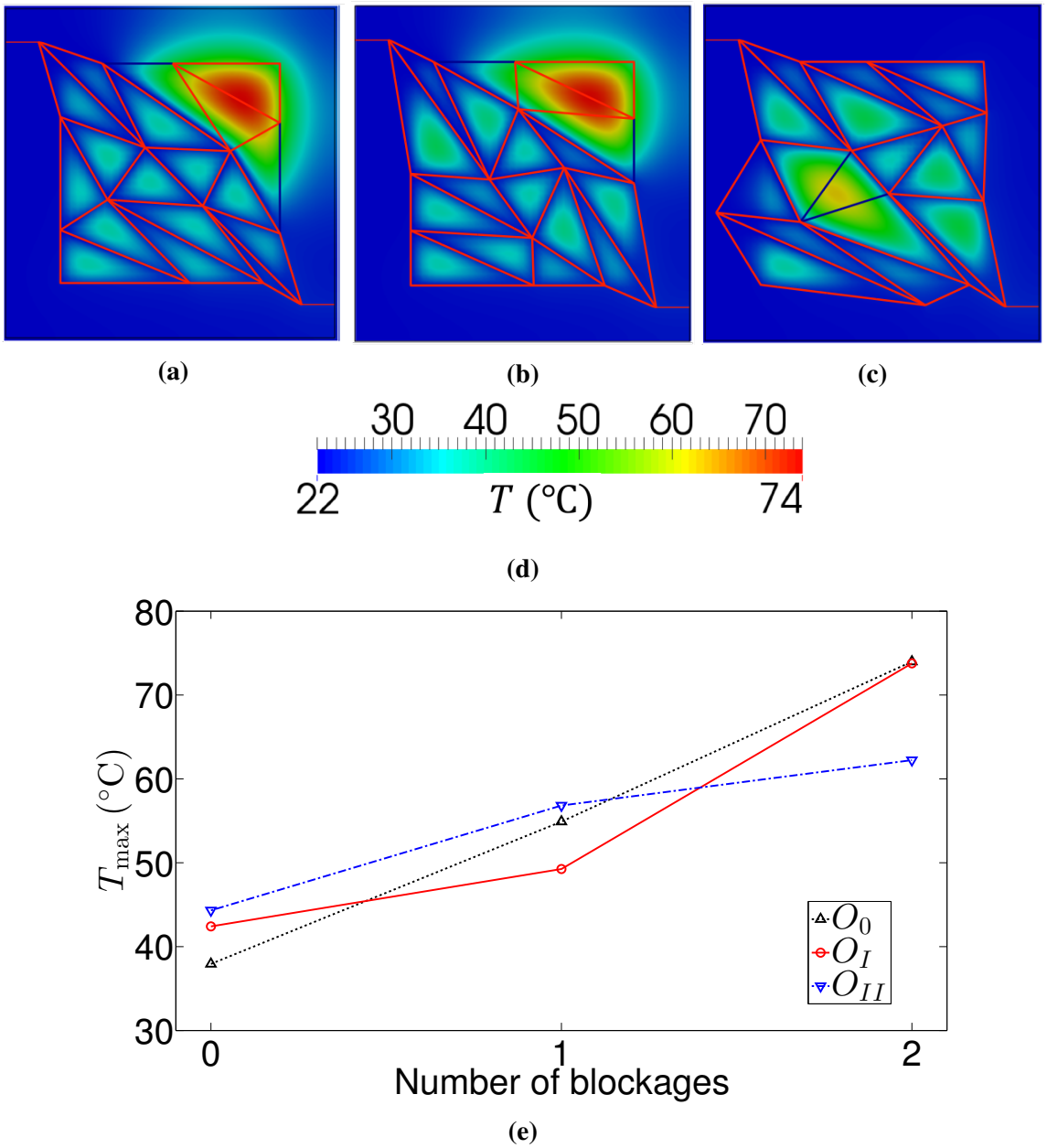

Figure 8.11 – Temperature fields associated with the $D6$ $O_0(\boldsymbol{w})$ (a), $O_1(\boldsymbol{w})$ (b) and $O_2(\boldsymbol{w})$ (c) designs. (d) The maximum temperatures associated with the three designs in the ideal scenario of clear channels, and worst case scenarios of different number of blockages.

Thus far, the designs have been optimized considering single-channel blockages. In this section, we demonstrate the generality of the optimization scheme described in this work by optimizing the $D6$ design for resiliency against double-channel blockages. Fig. 8.11c shows the design optimized considering double-channel blockages and the thermal field associated with the worst-case of sce-

nario. The thermal field shows substantially lower temperature compared with the thermal fields associated with the $D6$ O_0 and O_1 designs shown in Fig. 8.11a and b.

Fig. 8.11 shows the maximum temperatures resulting from the three designs in the no blockage scenario, and worst-case scenarios of single-blockage and double-blockages. As expected, the designs have the lowest maximum temperatures in the scenarios for which they are optimized.

8.3.4 Validation of optimized designs

In this final section, we present a validation study of the $D2, D4$ and $D6$ O_1 designs in the no blockage and worst-case single-blockage scenarios under the same thermal loading conditions as the validation exercise of Section 8.2 for a single flow rate of 28.2 ml/min. As apparent in Figure 8.12, the experimentally measured thermal fields in the second and fourth columns agree well with those simulated with IGFEM. A detailed comparison of the maximum temperatures in Figure 8.13a shows that for both $D4$ and $D6$ designs, the simulated maximum temperatures agree with those measured experimentally. However, the experimental temperatures for the the $D2$ design are lower than those predicted by IGFEM by about 4–5 °C. This discrepancy may be due to the increase in convection coefficient $\tilde{h}$ with temperature and the heat loss through the sides of the panels, which are not considered in the model. We also observe in Figure 8.13b that the pressure drop decreases with the nodal degree as expected. Moreover, except for the experimental pressure drops across the $D4$ network in the ideal scenario, the experimental pressure drops lie within the simulated lower and upper bounds.

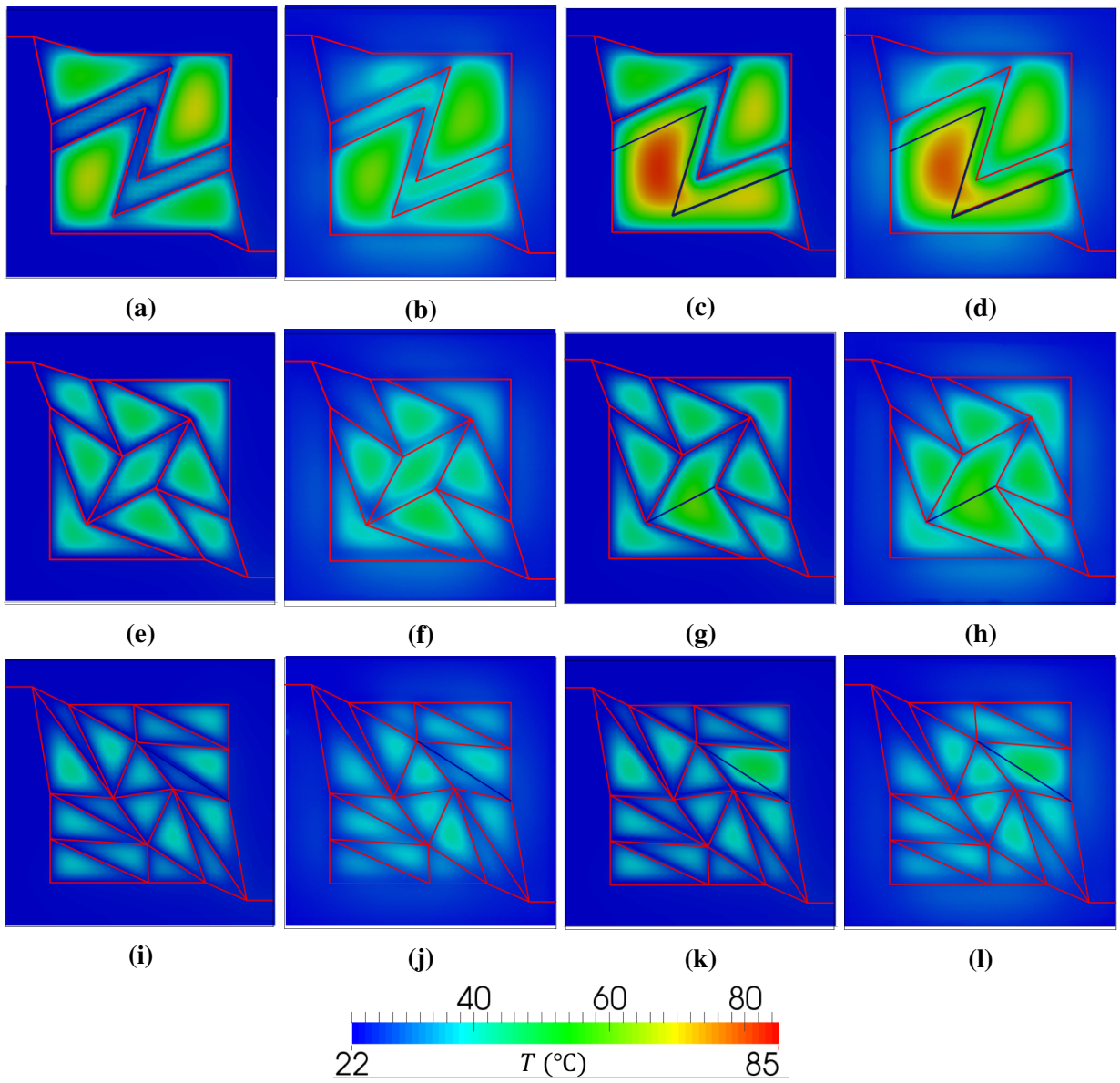

Figure 8.12 – Leftmost two columns respectively show the simulated and experimental temperature fields associated with the $D2$, $D4$ and $D6$ O_1 designs when the channels are clear. Rightmost two columns are the simulated and experimental temperature fields associated with the worst-case single-blockage scenario.

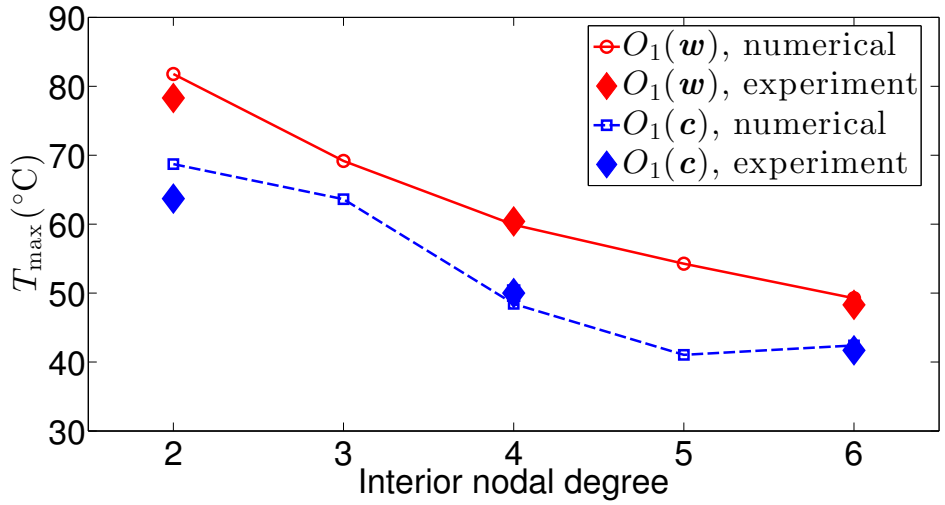

(a)

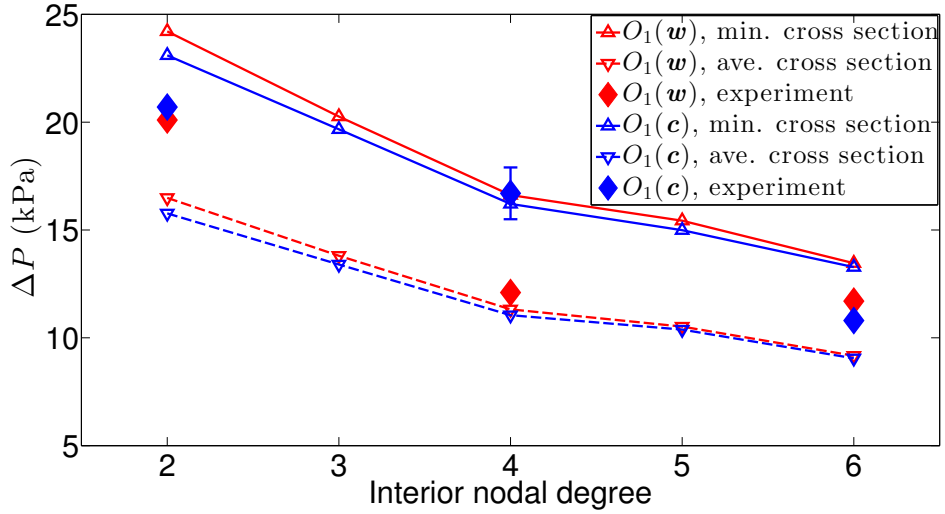

(b)

Figure 8.13 – Simulated and experimental maximum temperatures (a) and pressure drops (b) associated with the O_1 designs in the scenarios of worst-case single-blockage and clear channels ($\boldsymbol{w}$ and $\boldsymbol{c}$ in Table 8.2).

8.4 Conclusions

In this chapter, we have validated the interface-enriched generalized finite element method solutions of the dimensionally reduced thermal and hydraulic models of microvascular PDMS panels. Two approaches were adopted to handle the effect of radiation in the validation exercise: (i) linearization of the radiation term resulting in a linear system of equations and (ii) solving the nonlinear equation using the Newton-Raphson method. Both approaches were found to be sufficiently accurate compared with experimental observations.

Taking advantage of the linear model, the associated IGFEM-based sensitivity analysis and the sequential quadratic programming method, we optimized the microchannel networks for two design objectives: (i) a differentiable representation of the maximum temperature (p-norm of temperature) and (ii) a representation of the blockage-tolerance. While the first objective resulted in a conventional single-objective optimization problem (O_0), the second objective gave rise to a minmax problem. The complicated minmax problem was then reduced to a simpler single-objective optimization problem (O_1). Both types of optimization were applied to design grid-like networks with different nodal degrees, which were used to quantify the redundancy of the networks. While the O_0 optimization resulted in designs that had better thermal performance when the channels were clear, the O_1 designs, which were optimized for single-blockage scenarios, were shown to be substantially more resilient in those blockage scenarios. The loss in thermal performance of the O_0 designs became more substantial as the degree of redundancy decreased. We then demonstrated the generality of the blockage-tolerant design scheme with the optimization of the degree-6 design with double-channel blockages. Lastly, the simulated maximum temperatures and pressure drops of the O_1 designs were validated against experimental measurements.

9 2D Design of Microvascular Composite Panels for Radiative Cooling of Nanosatellites

This chapter is adapted from an article in preparation titled “Design of Microvascular Composite Radiator Panels for Nanosatellites” by M. H. Y. Tan, D. Bunce, A. Ghosh and P. H. Geubelle.

9.1 Introduction

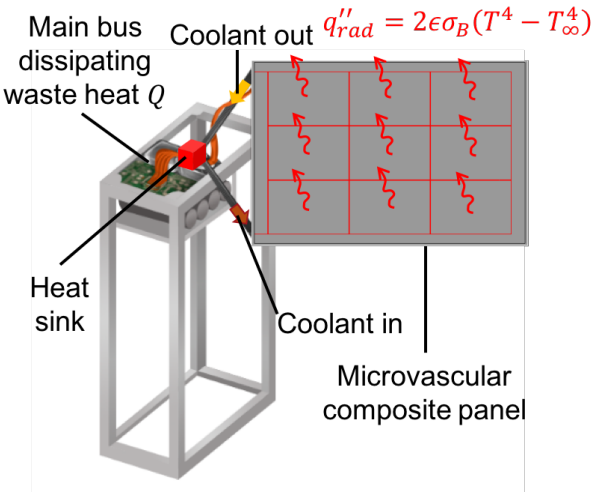

Figure 9.1 – Schematic of a microvascular composite panel attached to a nanosatellite. Adapted from [145].

Nanosatellites are categorized as satellites weighing between 1 and 10 kg [146]. The widely adopted CubeSat standards, which were introduced in 2000 [147], have led to a surge in nanosatellites developed for various applications including education, research and technology demonstration [146]. A nanosatellite of interest in this study is shown schematically in Figure 9.1, with payloads (not shown in the figure) supported by the main bus that contains subsystems such as transponders, computing chips and energy storage. From time to time, high-power functions such as electric propulsion and communication require the satellite to operate in “burst” mode, where significantly amount of heat is dissipated. During idleness, minimal heat is generated to prevent extremely low temperatures. Hence, a dynamic cooling system that can adapt to the variation in dissipated heat is required.

Recently, actively cooled microvascular composite panels have been proposed as radiators due to the flexibility of adjusting their effective thermal properties by changing the flow rate of the coolant [145]. A key challenge associated with this technology is the design of the embedded microchannel networks to keep the coolant temperature at appropriate levels for the range of generated heat during satellite operation. This chapter applies the gradient-based optimization scheme consisting of the sensitivity analysis for the nonlinear dimensionally reduced thermal model developed in Section 5.3 with the sequential quadratic programming method [122] to address this challenge. We begin by describing the operating conditions and design constraints of the nanosatellite of interest in Section 9.2. We then benchmark the solution of the nonlinear dimensionally reduced thermal model in Section 9.3 with ANSYS FLUENT simulations. In Section 9.4, we propose two optimization formulations to satisfy the design contraints, using grid-like networks of different grid densities as base designs. The feasibility of the resulting optimized designs are assessed for a wide range of operating conditions in Section 9.5. To close the loop, we verify in Section 9.6 the performance of an optimized design with ANSYS FLUENT. Lastly, we develop in Section 9.7 analytical expressions for the coolant temperatures.

9.2 Operating conditions and design constraints

The proposed cooling system consists of a heat sink used to gather waste heat from the subsystems, a coolant reservoir, and an electronically controlled pump that circulates the coolant through the heat sink and the microvascular panel. During the burst mode of the satellite, the rate of dissipated heat in the main bus Q is estimated to be 80 W. When idle, the subsystems are expected to generate about 20 W of waste heat.

In orbit, the only mode of heat transfer between the panel and the surrounding is radiation. The panel exchanges radiation with three sources: the Sun, Earth and albedo (solar radiation reflected from Earth). In practice, the sources are simplified to be a sink enclosure with temperature equivalent to the total heat flux received by the panel [148]. Let the heat fluxes received from the Sun, Earth and albedo be denoted by q''_S, q''_E and q''_a, respectively. The equivalent sink temperature of both large faces of the panel is defined as [148]

$$T_\infty = \left(\frac{q''_S + q''_E + q''_a}{\sigma_B} \right)^{\frac{1}{4}}, \tag{9.1}$$

where q''_S, q''_E and q''_a depend on factors such as orientation with respect to the Sun and Earth, orbital elevation and surface coating of the panel. An average sink temperature of 50 K is targeted in this study, though significant variation in the sink temperature is expected along the satellite orbit. This

variation is considered in the design assessment described in Section 9.5.3.

Table 9.1 – Operating conditions, and constraints on coolant temperatures and pressure drop of interest in this study.

Variable	Value or constraint
Rate of dissipated heat Q	20 – 80 W
Equivalent sink temperature T_∞	50 K
Coolant inlet or maximum temperature T_{in}	≤ 75 °C
Coolant minimum temperature $T_{c,min}$	≥ -45 °C
Pressure drop across network ΔP	≤ 2 atm

A summary of the operating conditions and constraints is shown in Table 9.1. The coolant temperature at the inlet of the panel T_{in}, which is close to maximum temperature of the heat sink, should be kept below 80 °C at all times to protect the electronics in the main bus. Given an allowance of about 5 °C to account for the inaccurary of numerical models and departure from ideal conditions, this value is reduced to 75 °C. During periods of low activity, the minimum coolant temperature should be greater than the coolant freezing temperature. These two requirements necessitate the use of a coolant with high specific heat capacity and very low freezing point. 50/50 aqueous ethylene glycol was initially considered due to its high specific heat capacity (averaging 3.38 kJ/kg K over the operating temperature range) but was later found to be susceptible to freezing. The minimum coolant temperature based on the numerical study described hereafter is found to be around -40 °C, which is substantially lower than the aqueous ethylene glycol freezing point of -34 °C. In this study, Dynalene HC-50, whose relevant properties are presented in Appendix A.5, is chosen as the coolant due to its substantially lower freezing point (less than -55 °C) and a relatively high specific heat capacity (about 2.71 kJ/kg K). Given an allowance of 10 °C, the lower bound of the the minimum coolant temperature $T_{c,min}$ is set to -45 °C. We note that it is beneficial to impose a higher lower bound for $T_{c,min}$ due to the rapid rise in coolant viscosity as the temperature approaches the freezing point, which leads to a much greater pressure drop. Noting that the pressure drop must be kept below the maximum pump pressure, we set the upper bound of the pressure drop to be 2 atm in this study.

9.3 Comparison with FLUENT – reference design

In this section, we compare the IGFEM solution against that of ANSYS FLUENT v15.0 using the simulation setups shown in Figure 9.2. A pitch-based carbon fiber composite panel with a surface emissivity assumed to be unity is used. We impose radiative boundary conditions on the two largest panel faces in the FLUENT simulations with equal emissivities and sink temperatures.

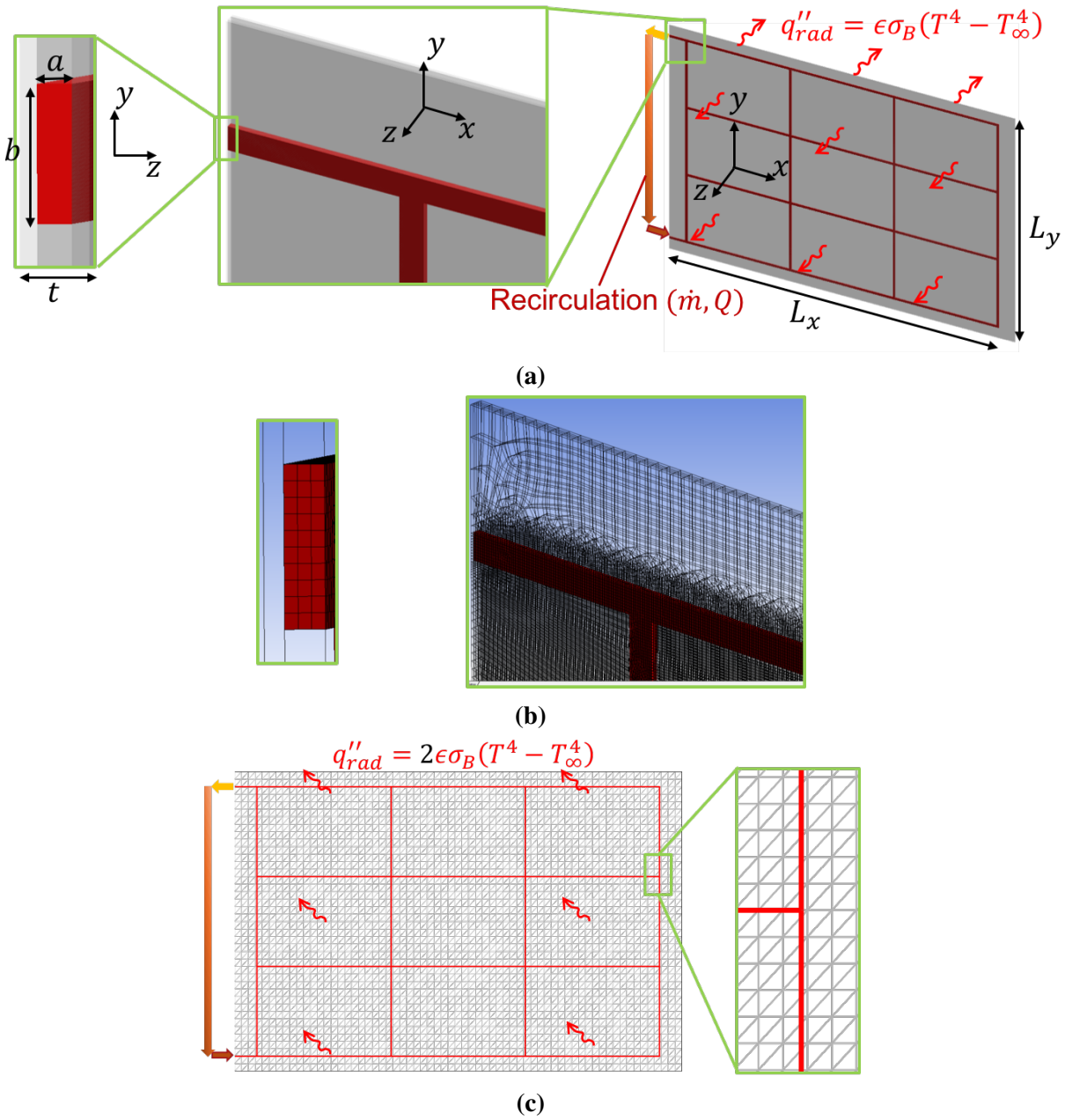

Figure 9.2 – (a) Panel containing a reference microchannel network with rectangular cross section simulated in 3D ANSYS FLUENT on a conforming mesh (b). (c) Setup for the 2D IGFEM simulation solved on a non-conforming structured mesh.

The same radiative boundary condition is imposed in the IGFEM simulation but with a factor of two to account for radiation from both faces. Values of the boundary conditions, the dimensions of the panel and channel cross section, and the solid properties are shown in Table 9.2.

An $N_x \times N_y$ reference grid-like microchannel network, where N_x and N_y respectively denote the number of divisions in the x- and y- directions, is used in this study. For this particular design,

$N_x = N_y = 3$. In both simulations, a recirculation boundary condition (which can be enabled through the Text User Interface in FLUENT) with heat source Q and mass flow rate $\dot{m}$ is prescribed. As a convenience to the reader, we define an equivalent volume flow rate $\dot{V}$ calculated from the prescribed mass flow rate using an average coolant density of 1337 $\mathrm{kg/m^3}$. Given a coolant specific heat capacity c_p, the recirculation boundary condition gives rise to a difference between inlet and outlet temperatures of

$$T_{in} - T_{out} = \frac{Q}{\dot{m} c_p}. \tag{9.2}$$

Dynalene HC-50 is chosen as the coolant, with its temperature-dependent properties shown in Figure A.3 of the appendix and average property values over the range -50 to 100 °C given in Table A.4. The hydraulic model employed by IGFEM simulations assumes constant heat capacity and uniform kinematic viscosity, which respectively take the average value in Table A.4 and the value at the average temperature of the coolant. Two sets of simulations are performed with FLUENT: one with the temperature-dependent properties (FLUENT I) and another with average properties of the coolant (FLUENT II) similar to the IGFEM.

Table 9.2 – Parameters for IGFEM and FLUENT benchmark study shown in Figure 9.2.

Parameter	**Value**
Boundary conditions	
Sink temperature T_∞	50 K
Heat dissipated Q	20 – 80 W
Prescribed mass flow rate $\dot{m}$	0.891 and 1.7827 g/s
Equivalent volume flow rate at average coolant density $\dot{V}$	40 and 80 ml/min
Dimensions	
Panel width L_x	0.3 m
Panel height L_y	0.2 m
Panel thickness t	1 mm
Channel width b	2 mm
Channel height a	0.5 mm
Solid	Pitch-based carbon fiber composite
Emissivity ϵ	1
Thermal conductivity κ	78.8 $\mathrm{W/m \cdot K}$

As shown in Figures 9.3a–c, the temperature fields obtained from the three simulations agree at a flow rate of 80 ml/min and $Q = 80$ W. However, discrepancy between the FLUENT I and IGFEM simulations is observed in Figures 9.3d and f. The source of this discrepancy can be deduced from the agreement between the FLUENT II and IGFEM simulations as shown in Figures 9.3e and f, which points to the coolant property assumptions underlying the hydraulic model.

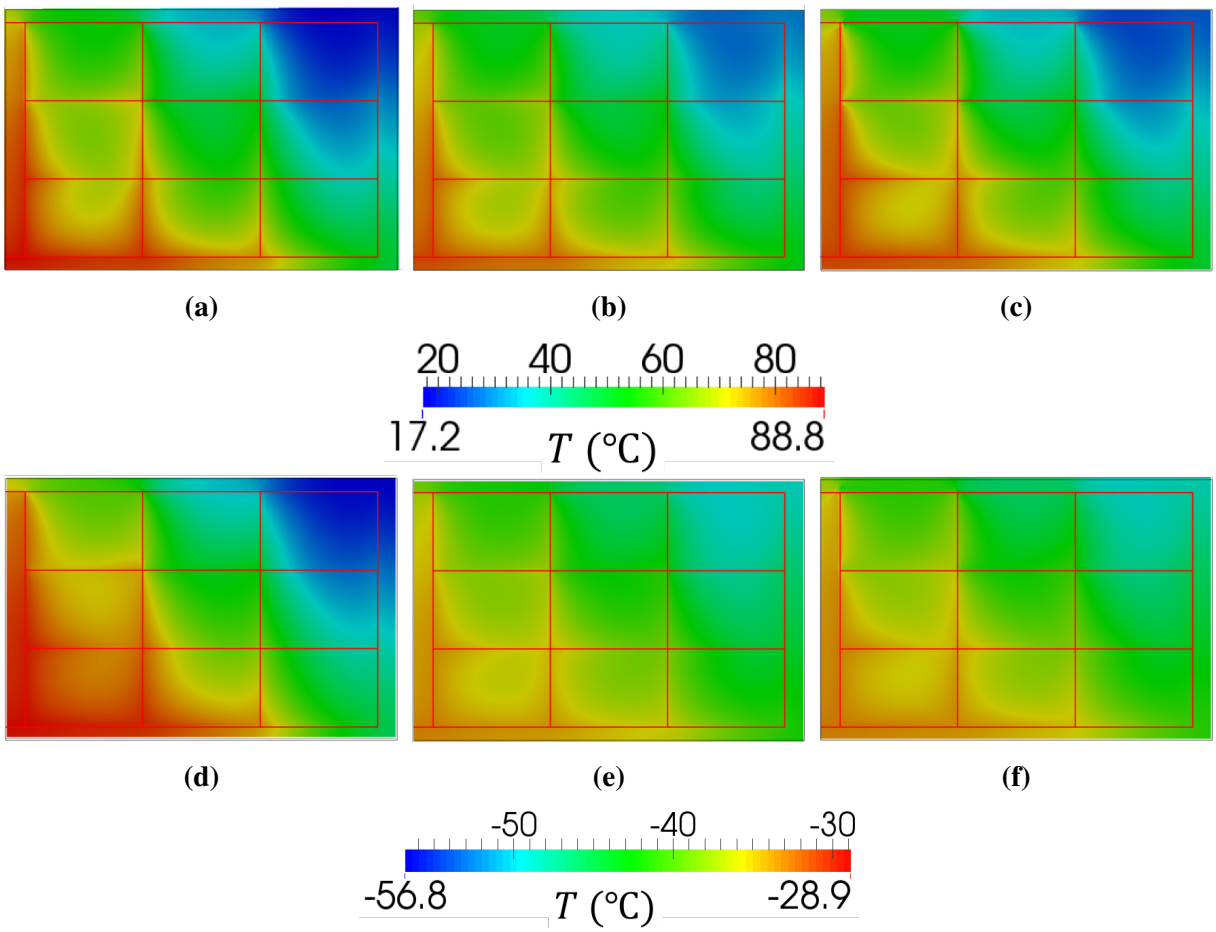

Figure 9.3 – Thermal fields associated with the 3×3 reference design obtained with (a) FLUENT I, (b) FLUENT II and (c) IGFEM simulations at $Q = 80$ W and $\dot{V} = 80$ ml/min. (d)–(f) Thermal fields obtained from the same simulations at $Q = 20$ W and the same flow rate.

A detailed comparison of the coolant inlet temperatures T_{in}, outlet temperatures T_{out}, average temperatures $T_{c,ave}$, minimum temperatures $T_{c,min}$ and pressure drops ΔP resulting from the FLUENT I and IGFEM simulations are presented in the left column of Figure 9.4, and the corresponding absolute differences ($\Delta^{(FI)}\Phi = \Phi^{(F)} - \Phi^{(I)}$, where Φ is an arbitrary variable) shown in the right column. It is observed that IGFEM underestimates the inlet and outlet temperatures but overestimates the minimum coolant temperature. While these differences are within 7 °C at a higher flow rate of 80 ml/min, it increases to roughly 20 °C at a lower flow rate of 40 ml/min. At the same time, the IGFEM pressure drop overestimates the FLUENT pressure drops with substantially greater discrepancy at the lowest Q of 20 W. The better agreement at higher flow rates is expected since the coolant temperature field becomes more uniform as the flow rate increases.

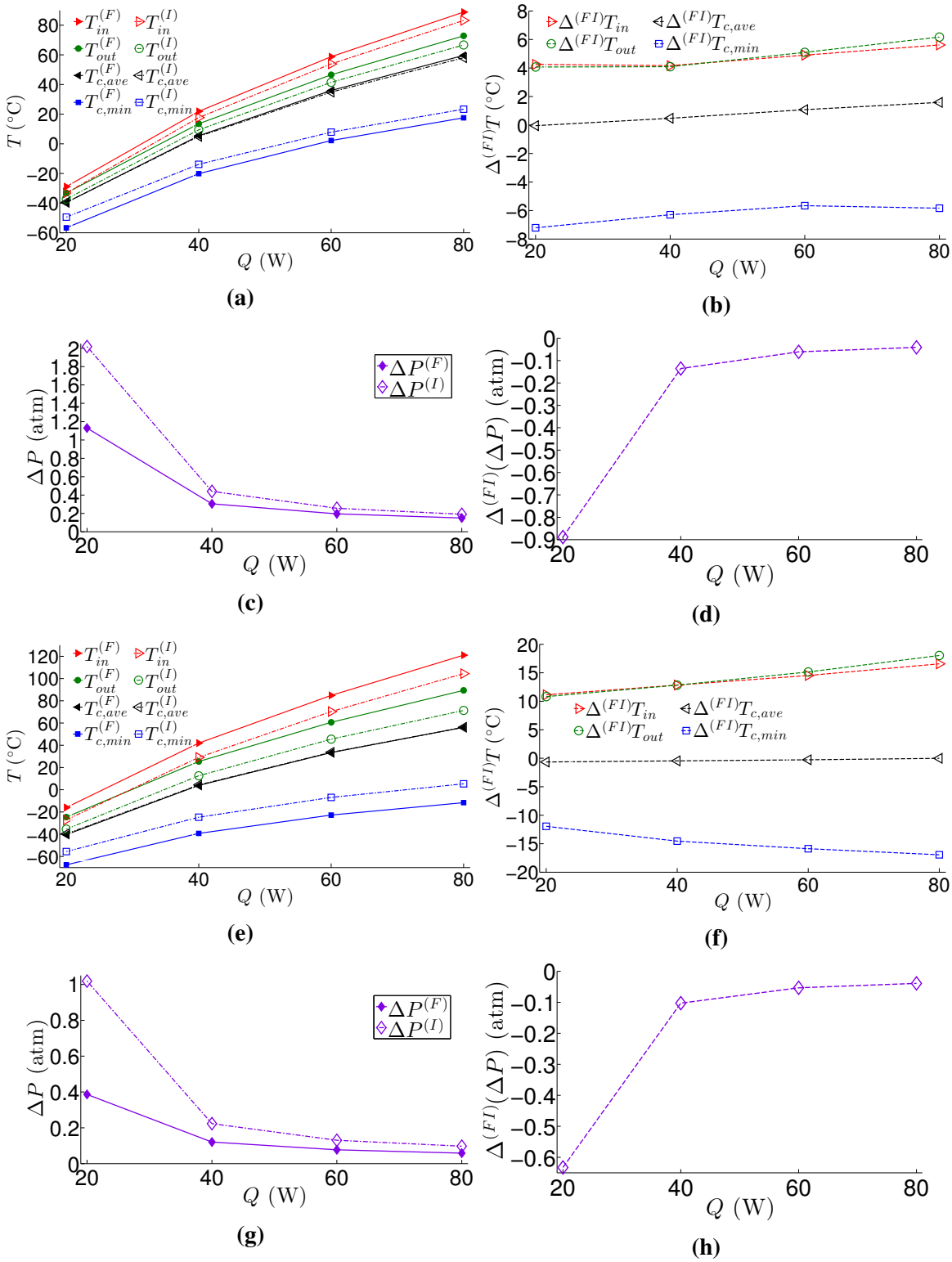

Figure 9.4 – FLUENT I (superscript F) coolant temperatures and pressure drops associated with the 3×3 reference design compared with those of IGFEM (superscript I) at flow rates of (a), (c) 80 ml/min and (e), (g) 40 ml/min with corresponding absolute differences shown in the right column.

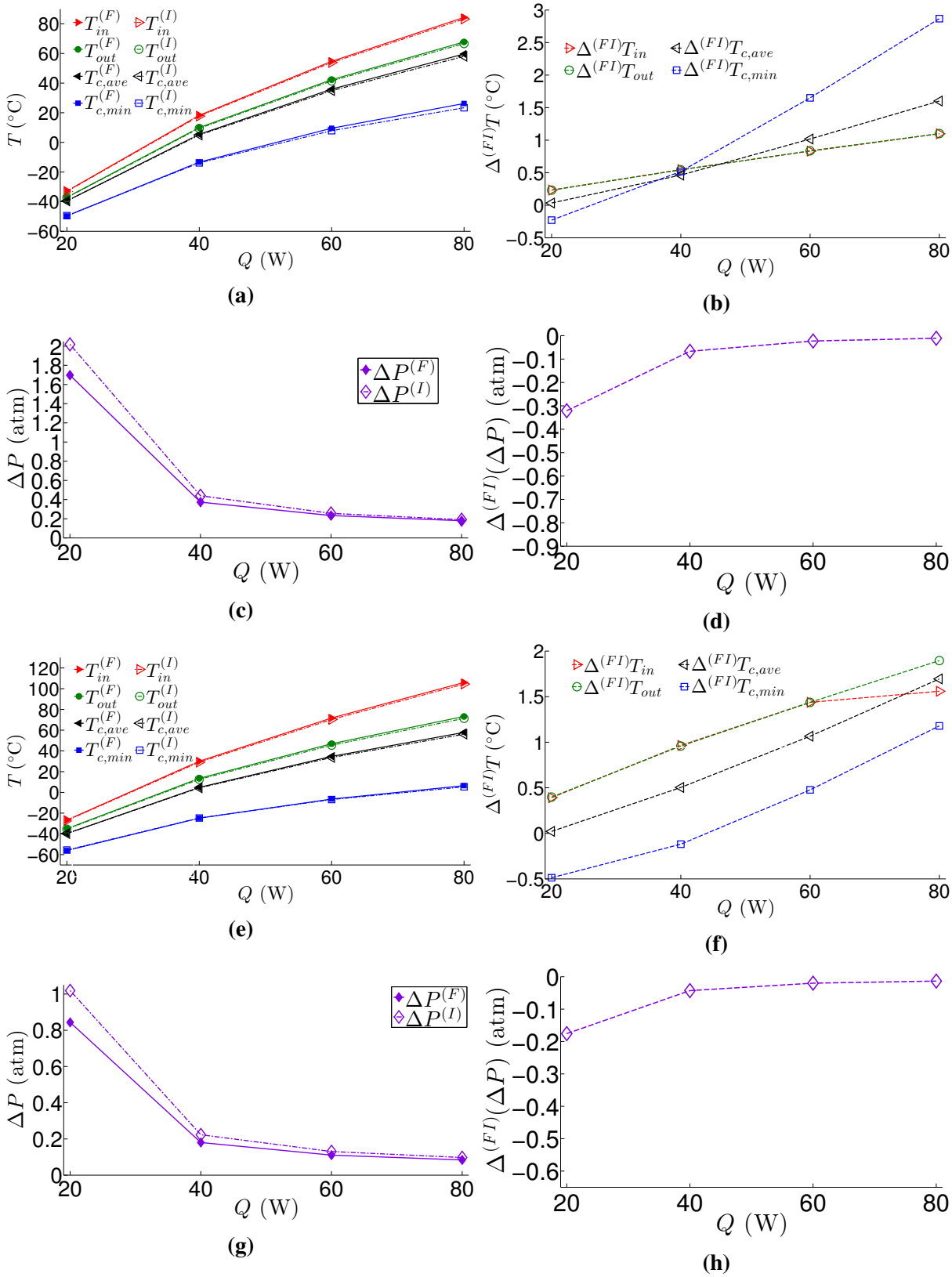

Figure 9.5 – Same description as Figure 9.4 for the FLUENT II and IGFEM simulations.

Figure 9.5 compares the coolant temperatures and pressure drops resulting from the FLUENT II and IGFEM simulations, showing that much better agreement would be obtained if the coolant properties were constant. The coolant temperatures differ by at most 3 °C and the IGFEM pressure drops differ by at most 0.3 atm. In fact, additional FLUENT simulations (not shown here) with constant uniform density, heat capacity and thermal conductivity but temperature-dependent viscosity show that the strong dependence of the viscosity on temperature is the dominant source of discrepancy. This benchmarking exercise for the reference design demonstrates that the aforementioned assumptions on coolant properties lead to substantial loss in accuracy. However, we show in Section 9.6 that this is not true for certain optimized designs.

9.4 Optimization formulations and setup

9.4.1 General formulation

Denote the objective function, the temperature field in *Kelvin*, the nodal coordinates of the mesh and the design parameter vector respectively by $\theta, T, \boldsymbol{X}$ and $\boldsymbol{d}$. Let us represent nonlinear constraints that only depend on $\boldsymbol{d}$ by the functions $\boldsymbol{g}$ and nonlinear constraints that also depend on T by the functions Θ_j, where $j = 1, ..., n_\Theta$. The general optimization problem can be formulated as

$$\begin{aligned} \min_{\boldsymbol{d}} \quad & \theta(T(\boldsymbol{X}(\boldsymbol{d}), \boldsymbol{d}; Q_0, \dot{m}_0), \boldsymbol{X}(\boldsymbol{d}), \boldsymbol{d}), \\ \text{such that} \quad & \boldsymbol{g}(\boldsymbol{d}) \leq 0, \\ \text{and} \quad & \Theta_j(T(\boldsymbol{X}(\boldsymbol{d}), \boldsymbol{d}; Q_j, \dot{m}_j), \boldsymbol{X}(\boldsymbol{d}), \boldsymbol{d}) \leq 0, \;\; j = 1, ..., n_\Theta, \end{aligned} \tag{9.3}$$

where dependence of the temperature field on the two parameters, dissipated heat Q_j and mass flow rate $\dot{m}_j$, is emphasized in its argument. We note that different dissipated heats Q_j and mass flow rates $\dot{m}_j$ are possible. Two formulations with specific choices of θ and Θ_j referred to as the O_T and O_P formulations, respectively, are considered next.

9.4.2 O_T formulation

This formulation intends to maximize the minimum coolant temperature. However, the objective function is not differentiable since the location of the minimum is unknown a priori. Hence, we use (5.26) (the p-norm of the channel temperature field offset by a sufficiently large constant T_o) as a differentiable alternative, where T_o is chosen such that $T \leq T_o$ on the channel network Γ_f. Minimizing this objective function effectively reduces the difference between the channel temper-

Table 9.3 – Parameters for O_T formulation.

Parameter	Value
Sink temperature and panel length	
T_∞	50 or 150 K
L_x	0.2, 0.25 or 0.3 m
Objective function	(5.26)
p	8
T_o	273.15 K
Q_0	20 W
$\dot{m}_0$	1.7827 g/s
Constraint 1	$\Theta_1 = T_{in} - T_{upp} \leq 0$
Q_1	80 W
$\dot{m}_1$	1.7827 g/s
T_{upp} for $T_\infty = 50$ K, $L_x = 0.2$ m	103 °C
T_{upp} for $T_\infty = 50$ K, $L_x = 0.25$ m	83 °C
T_{upp} for $T_\infty = 50$ K, $L_x = 0.3$ m	70 °C
T_{upp} for $T_\infty = 150$ K, $L_x = 0.3$ m	71 °C

ature field and T_o. Due to the choice of T_o, the intended effect of maximizing the minimum coolant temperature is achieved when p is sufficiently large. As before, p is chosen as 8. The objective function (5.26) is evaluated at $Q_0 = 20$ W, where the channel temperature field is substantially lower than 273.15 K. Hence, T_o is fixed at 273.15 K. We choose the largest flow rate at our disposal, i.e., $\dot{m}_0 = 1.7827$ g/s (80 ml/min). We note that the subsequent discussion is not limited to particular choices of the parameters.

Furthermore, we impose a constraint on the inlet temperature of the coolant $T_{in} \leq T_{upp}$, i.e, we set $\Theta_1 = T_{in} - T_{upp}$ in (9.3). Based on the discussion in Section 9.2, we choose $Q_1 = 80$ W. To improve our chance of getting a feasible solution, we set $\dot{m}_1 = 1.7827$ g/s. The upper bound of the inlet temperature T_{upp} is decreased by trial and error until few feasible solutions are found. This process yields final values of T_{upp} shown in Table 9.3 for different panel lengths L_x defined in Figure 9.2 and the equivalent sink temperatures T_∞.

The pressure drop is not constrained but determined in the postprocessing step. If the pressure drop exceeds the maximum pump pressure, the channel cross section can be enlarged to reduce the pressure drop substantially. We note that the detrimental effect of larger cross sections on structural performance does not factor into the design since the panel is not intended for load-bearing. If for some reason the pressure drop cannot be reduced in this manner to satisfy the pressure constraint, the formulation described next can be considerd.

9.4.3 O_P formulation

Table 9.4 – Parameters for O_P formulation.

Parameter	Value
Sink temperature and panel length	
T_∞	50 K
L_x	0.3 m
Objective function	$\theta = \Delta P$
Q_0	20 W
$\dot{m}_0$	1.7827 g/s
Constraint 1	$\Theta_1 = T_{in} - T_{upp} \leq 0$
Q_1	80 W
$\dot{m}_1$	1.7827 g/s
T_{upp}	70 °C
Constraint 2	$\Theta_2 = T_{low} - T_{out} \leq 0$
Q_1	20 W
$\dot{m}_1$	1.7827 g/s
T_{low}	-40 °C

This formulation minimizes the pressure drop of the network and constraints the inlet and outlet temperatures of the coolant, i.e, $\theta = \Delta P$, $\Theta_1 = T_{in} - T_{upp} \leq 0$ and $\Theta_2 = T_{low} - T_{out} \leq 0$. One drawback of this formulation is that the minimum coolant temperature does not necessarily occur at the outlet. Hence, to increase the chance of satisfying the minimum coolant temperature constraint, the lower bound on the outlet temperature needs to be increased by trial and error until few feasible solutions are found. This process yields $T_{low} = -40$ °C. The parameters for this formulation is summarized in Table 9.4.

9.4.4 Optimization setup

The optimization setup is similar to that shown in Figure 9.2c with different $N_x \times N_y$ grid-like designs shown in Figure 9.6 considered for the optimization study. Except for Section 9.7, where panel lengths of $L_x = 0.2$, 0.25 and 0.3 m are simulated, the default panel length is 0.3 m. The coordinates of the control points of the channels except those at the inlet and outlet are selected as the design parameters, leading to 12, 18, 32 and 50 design parameters for the 2×1, 2×2, 3×3 and 4×4 grids, respectively. The movable control points are not allowed to be within a distance 5 mm $(L_x/60)$ from the edges of the panel.

A key constraint to this design problem is associated with the "self-crossing" of the channels, which renders the problem unphysical. To deal with this issue, geometrical constraints are applied

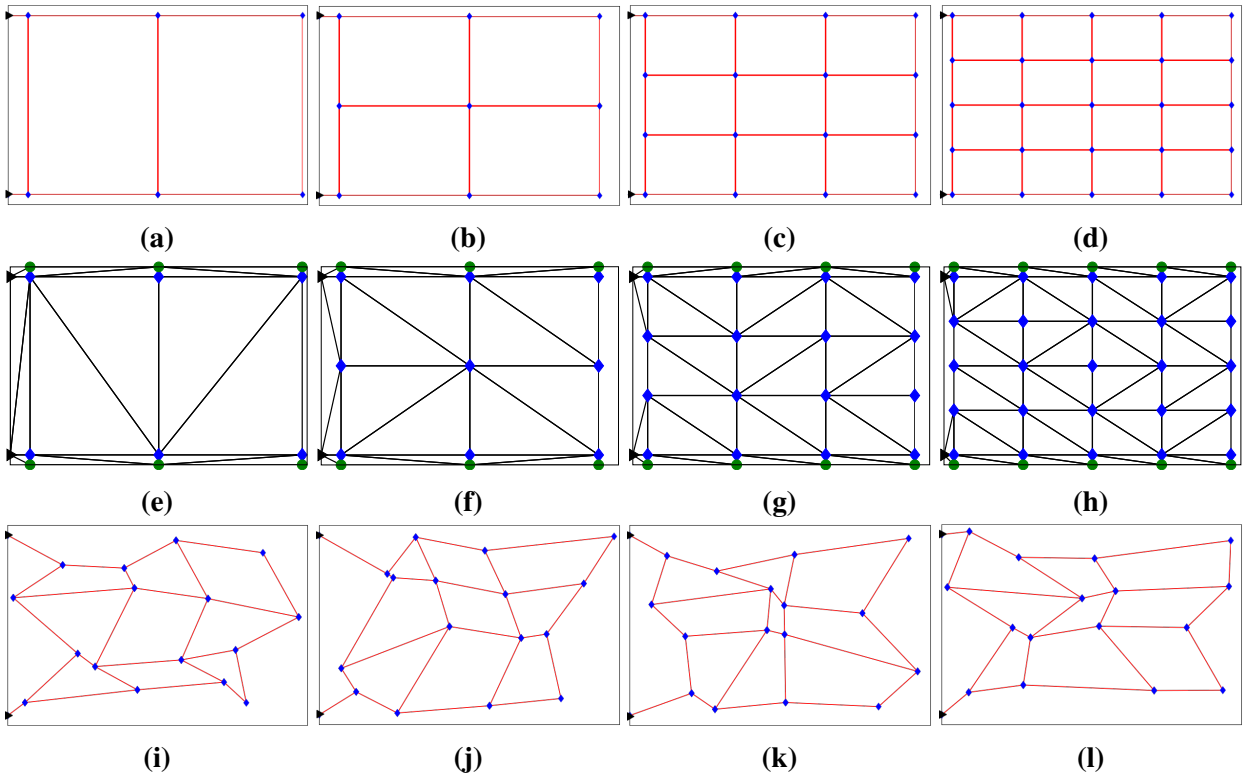

Figure 9.6 – (a)–(d) 2×1, 2×2, 3×3 and 4×4 reference designs with fixed and movable control points indicated by black triangles and blue diamonds, respectively. (e)–(h) Triangles used to imposed geometrical constraints on the designs with additional control points (green circles) introduced for the triangles. (i)–(l) Initial 3×3 designs .

to the triangles constructed based on the geometry of the microchannels as shown in Figure 9.6. The geometrical constraints impose the conditions that (i) the interior angles of a triangle are bounded between ϕ_o and $180 - \phi_o$ degrees and (ii) the area of each triangle is greater than A_o. ϕ_o is set to be 1° for triangles with control points along the panel edges and 10° for other triangles. A_o is chosen to be $0.001\times$ the panel area.

For each set of optimization, at least 48 distinct initial designs obtained by shuffling the control points within non-overlapping bounding boxes are used to get solutions that are closer to the global optima. Some of the initial designs for the 3×3 configuration are shown in Figure 9.6.

9.5 Optimized designs and feasibility study

9.5.1 Optimized designs

In Figure 9.7, we compare the performance of the 3×3 designs derived from the O_T and O_P optimizations with the corresponding reference design. The inlet temperatures of the O_T and O_P designs are respectively 13 and 8 °C lower than that of the reference design, while the minimum coolant temperatures are 10 and 5 °C higher, respectively. A desirable charateristic of the O_T design is that $T_{c,min}$ occurs exactly at the outlet as shown in the inset of Figure 9.7b. Although the same cannot be said of the O_P design, the location of the minimum coolant temperature of the design is closer to the outlet compared with that of the reference design. As evident in Figure 9.7b, the O_P design has the smallest pressure drop. Since the pressure drop is not considered in the O_T optimization, it has the largest pressure drop among the three designs considered here. However, we note that the larger pressure drop can be remedied by using significantly lower flow rates (20–30 ml/min) as demonstrated in a feasibility study (Section 9.5.2) or enlarging the channel cross section as pointed out earlier. The feasibility study also shows that O_P design needs to be operated at flow rates of at least 80 ml/min to satisfy the minimum coolant temperature constraint.

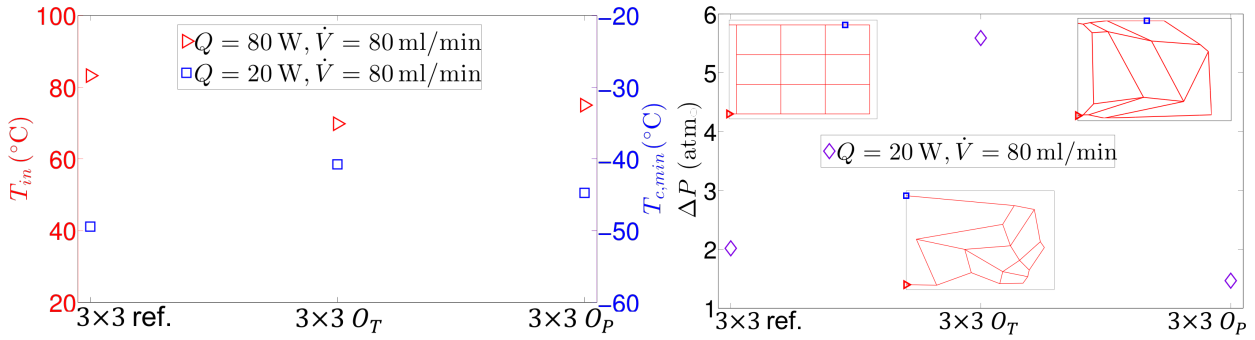

Figure 9.7 – (a) Inlet temperature T_{in}, minimum coolant temperature $T_{c,min}$, and (b) pressure drop ΔP associated with the 3×3 reference, O_T and O_P designs shown in the inset of (b). The locations of the maximum and minimum coolant temperatures are respectively indicated by the red triangles and blue squares on the designs.

The O_T designs for different grid densities presented in Figures 9.8a–d show that the optimized designs favor longer outlet channels and the concentration of channels at the bottom right of the panel. Branching is avoided near the outlet to prevent rapid drop in coolant temperature due to small flow rates. At the same time, the top right corner of the panel is avoided since the temperature is lowest in that region as shown in Figure 9.3. If only the minimum coolant temperature at low Q is considered in the optimization process, an optimized design would contain channels that are

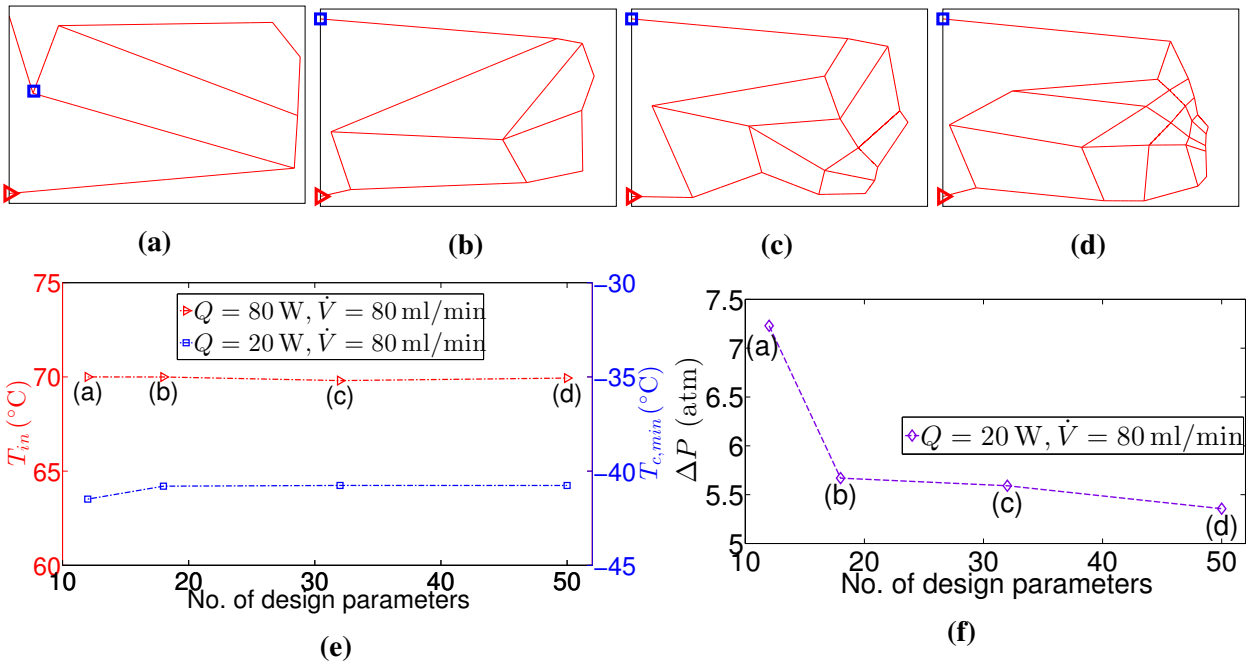

Figure 9.8 – (a)–(d) 2×1, 2×2, 3×3 and 4×4 O_T designs with the locations of the maximum and minimum coolant temperatures indicated by the red triangles and blue squares, respectively, on the designs. (e) Inlet temperature T_{in}, minimum coolant temperature $T_{c,min}$, and (f) pressure drop ΔP for different number of design parameters associated with the designs.

concentrated near the inlet, where the temperature is highest. However, due to another competing constraint on the maximum coolant temperature, a compromise between the coolest top right and warmest bottom left regions is reached, i.e., the channels are concentrated in the bottom right region.

We also observe in Figure 9.8e that the thermal performance of the panel is almost unchanged despite the increasing number of design parameters associated with higher grid densities. While the pressure drop shows remarkable reduction from the 2×1 to 2×2 grids as shown in Figure 9.8f, much less reduction is obtained as the grid density increases further. The observed trend is due to the dominant contribution of the significantly longer outlet channel to the pressure drop across the network arising from the need to maximize the minimum coolant temperature. Therefore, the improvement in pressure drop associated with the denser grids is significantly reduced.

9.5.2 Different dissipated heat rates and flow rates

In the remainder of this chapter, we perform a detailed study of the performance and feasibility of the 3×3 designs for different dissipated heat rates and flow rates using the IGFEM solver. Temperatures and pressure drops are computed for $20 \le Q \le 80$ W and $5 \le \dot{V} \le 80$ ml/min at

increments of 5 W and 5 ml/min, respectively, leading to a total of 208 sample points. The outputs are then interpolated using the MATLAB function `interp2` to generate the smooth contour plots shown in Figures 9.9–9.11.

Figure 9.9a–c show the maximum and minimum coolant temperatures (T_{in}, $T_{c,min}$), and the pressure drop (ΔP) associated with the 3×3 reference design. As evident from the figures, while T_{in} decreases with $\dot{V}$ for a given Q, $T_{c,min}$ increases with $\dot{V}$, implying that higher flow rates are better for both temperatures. As expected, both temperatures increase with Q for a fixed $\dot{V}$. On the other hand, ΔP decreases with Q for a given $\dot{V}$ due to the drop in viscosity accompanying the rise in temperature.

Let us define the feasible region as $\mathcal{F} = \{(Q, \dot{V}) | T_{in} \leq T_{upp}, T_{c,min} \geq T_{low}, \Delta P \leq P_{upp}\}$, where as stated earlier, $T_{upp} = 75$ °C, $T_{low} = -45$ °C and $P_{upp} = 2$ atm. Also, define the indicator function as

$$I(Q, \dot{V}) = \begin{cases} 1 \ \ \forall (Q, \dot{V}) \in \mathcal{F}, \\ 0 \ \ \text{otherwise.} \end{cases} \tag{9.4}$$

The indicator function associated with the 3×3 reference design is presented in Figure 9.9d, where the curves due to the constraints on T_{in} (blue dash-dot curve) and $T_{c,min}$ (red dash-dot curve), and the maximum $\dot{V}$ (80 ml/min) delineate the boundary of the feasible region. The region shows that the design fails to meet the design requirement for $Q \geq 75$ W or $Q \leq 22.4$ W. We note that due to the underestimation of T_{in} and overestimation of $T_{c,min}$ as shown in Section 9.3, the actual range of allowable Q is expected to be narrower than that predicted by IGFEM.

The same study done for the 3×3 O_T design is shown in Figure 9.10. While the pressure drop across the 3×3 reference design is less than the maximum pressure for all Q and $\dot{V}$ of interest, the maximum pressure indicated by the black dash curve in Figure 9.10c is exceeded by the 3×3 O_T design at sufficiently low Q and high $\dot{V}$. Hence, in addition to the temperature constraint curves and the maximum $\dot{V}$, the feasible region shown in Figure 9.10d is also restricted by the pressure constraint. However, since the cooling system allows for flow rate adjustment, the design is able to operate at $Q = 80$ W at flow rates greater than 55 ml/min and $Q = 20$ W at flow rates between 20–30 ml/min.

The parameter sweep for the 3×3 O_P design is presented in Figure 9.11. Similar to the reference design, the pressure constraint curve does not appear in Figure 9.11c since the pressure drop of this optimized design is lower than that of the reference design. However, unlike the reference design, this design satisfies the temperature constraints at $Q = 20$ and 80 W only when the coolant is pumped through at the largest flow rate of 80 ml/min.

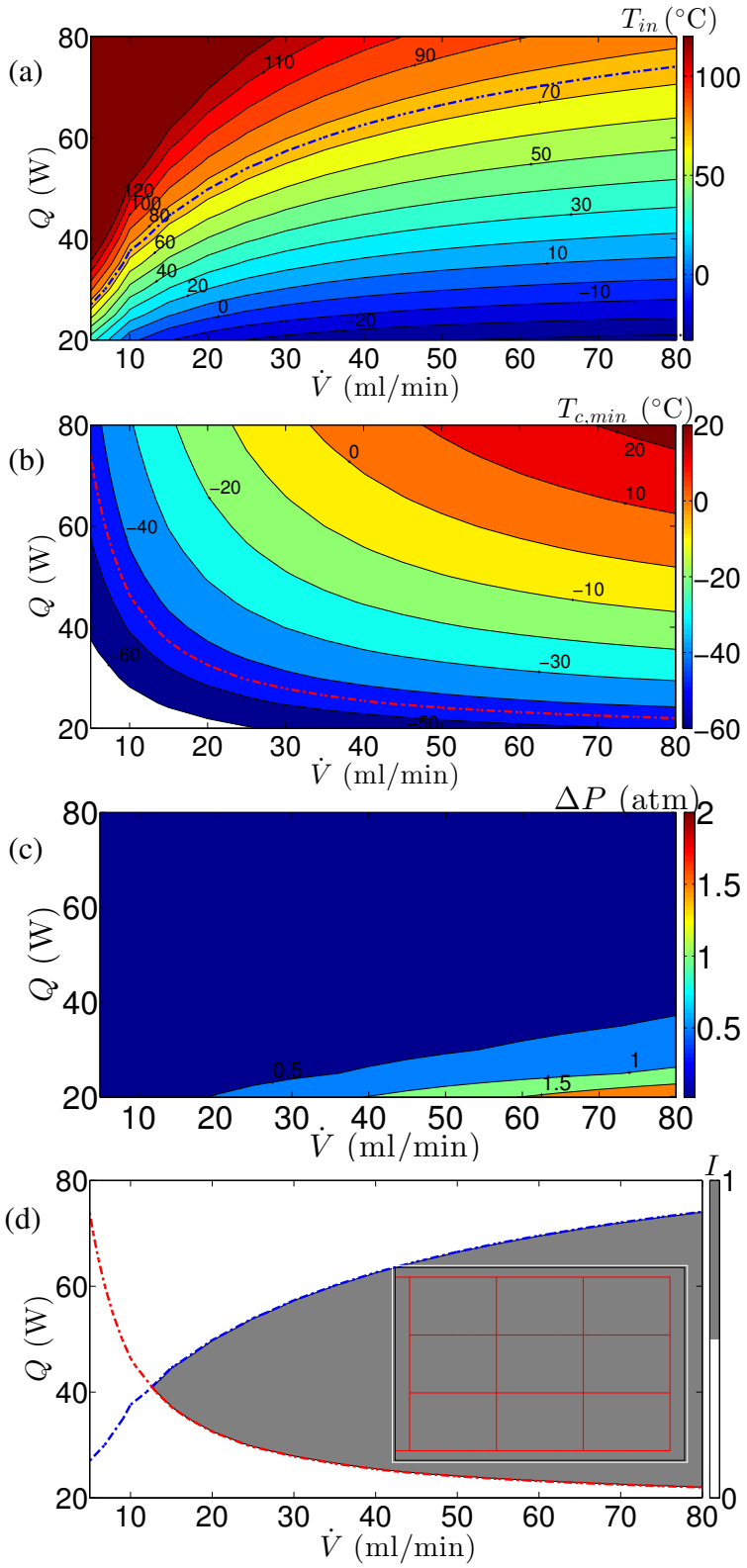

Figure 9.9 – (a)–(c) Temperatures and pressure drop associated with the 3×3 reference design. The constraints on the inlet temperature (75 °C) and minimum coolant temperature (-45 °C) are shown by the blue and red dash-dot curves, respectively. (d) Indicator function showing constraint satisfaction in the shaded region.

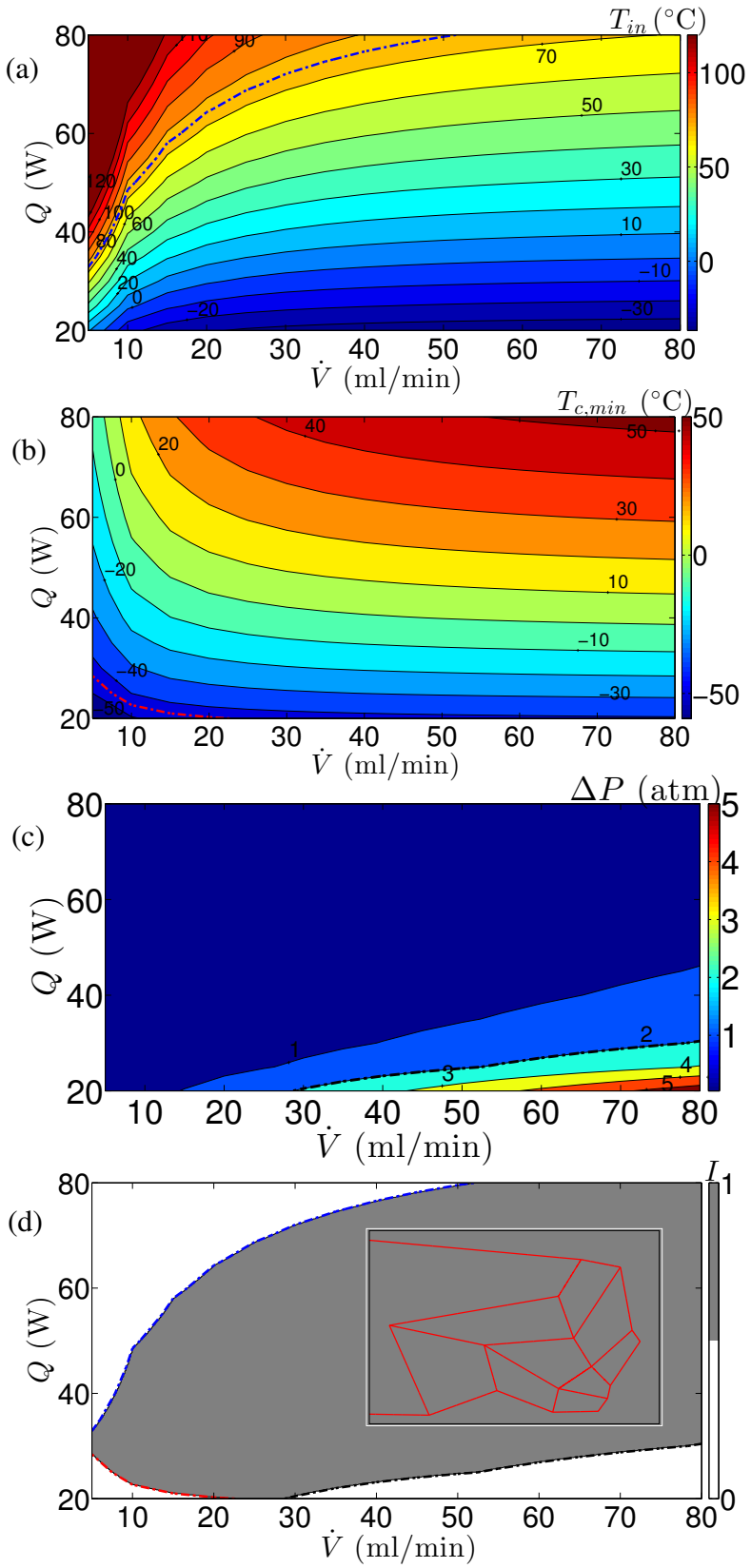

Figure 9.10 – Same description as Figure 9.9 for the 3×3 O_T design with the maximum allowable pressure drop (2 atm) indicated by the black dash-dot curve in (c).

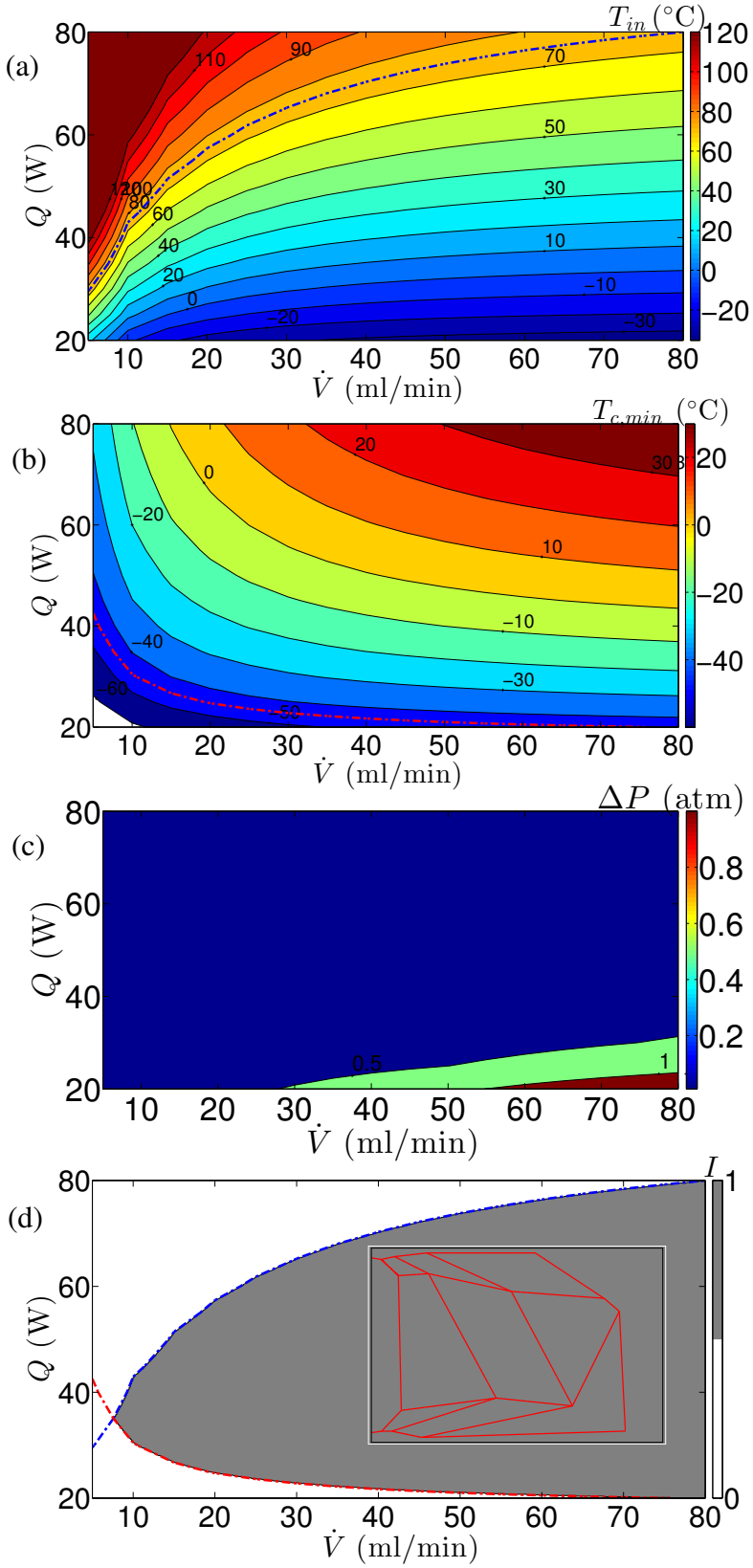

Figure 9.11 – Same description as Figure 9.9 for the 3×3 O_P design.

9.5.3 Different sink temperatures

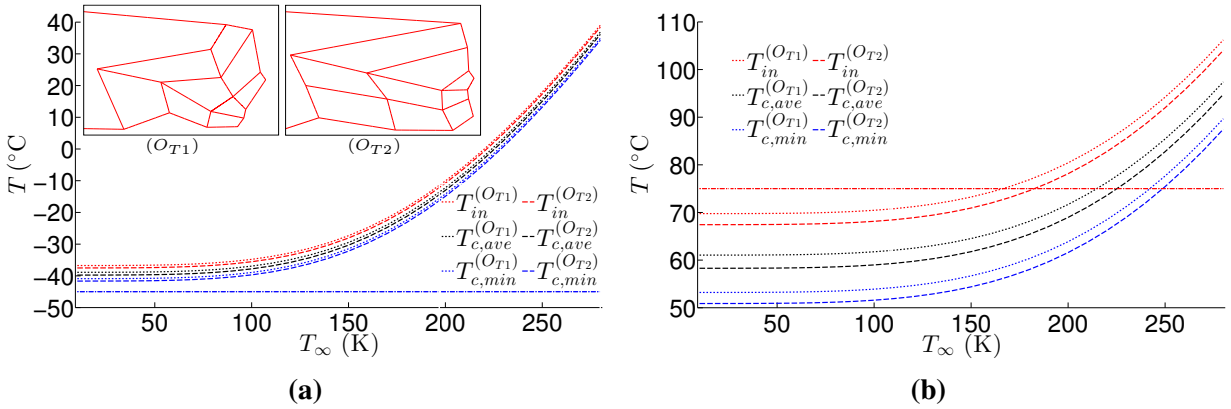

Figure 9.12 – Coolant temperatures associated with the 3×3 designs optimized at $T_\infty = 50$ K (denoted by O_{T1} and also referred to as O_T previously) and $T_\infty = 150$ K (denoted by O_{T2}) at (a) $Q = 20$ W and (b) $Q = 80$ W, and the same flow rate of 80 ml/min. The optimized designs are shown in the inset of (a).

Due to the variation in environmental radiation along the satellite orbit, it is important to study the performance of the designs at different sink temperatures T_∞. For that reason, we also optimize the 3×3 design at a higher sink temperature of 150 K, resulting in the O_{T2} design shown in the inset of Figure 9.12a. The 3×3 design optimized at 50 K and shown earlier is now also called the O_{T1} design. At $Q = 20$ W and 80 ml/min, the minimum coolant temperatures of both designs are a few degrees above the lower temperature constraint of -45 °C even as T_∞ approaches 0 K as shown in Figure 9.12a. A closer inspection reveals that the minimum coolant temperatures of the O_{T1} design is about 1 degree above that of the other design. On the other hand, Figure 9.12b shows that both designs satisfy the maximum coolant temperature constraint of 75 °C when operated at 80 W and 80 ml/min provided T_∞ is sufficiently low, i.e., $T_\infty \leq 168$ and 182 K for the O_{T1} and O_{T2} designs, respectively.

9.6 Comparison with FLUENT – optimized design

Using the same setup described in Section 9.3, we compare the IGFEM solution for the 3×3 O_T design against that of the ANSYS FLUENT simulation at the flow rates 80 and 20 ml/min. The full temperature-dependent properties of the coolant are simulated in the FLUENT simulations, while the assumptions on the coolant properties described earlier continue to be used in the IGFEM simulations. Comparison of Figure 9.13a and Figure 9.3a reveals that the temperature distribution associated with the optimized design at $Q = 80$ W and $\dot{V} = 80$ ml/min is significantly more

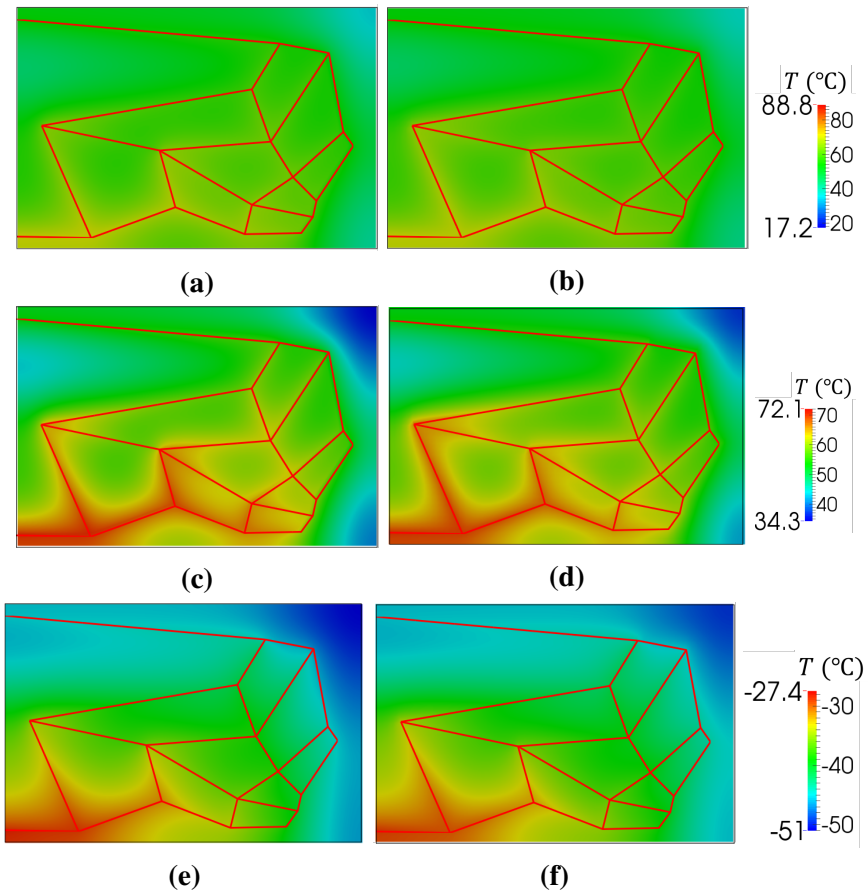

Figure 9.13 – Thermal fields associated with the 3×3 O_T design obtained with (a) FLUENT and (b) IGFEM simulations at $Q = 80$ W and $\dot{V} = 80$ ml/min, and plotted on the same scale as Figures 9.3a–c. Thermal fields (c) and (d) are respectively the same as (a) and (b) but plotted on a scale adapted to the maximum and minimum temperatures of the panel. (e) and (f) Temperature distributions at $Q = 20$ W and $\dot{V} = 80$ ml/min.

uniform compared with that resulting from the reference design. As shown in Figures 9.13c–f, temperature fields plotted on scales adapted to the maximum and minimum panel temperatures reveal very good qualitative agreement between the FLUENT and IGFEM simulations at $\dot{V} = 80$ ml/min, and at both high and low dissipated heat ($Q = 80$ and 20 W).

We present in Figure 9.14 a detailed comparison of the coolant temperatures and pressure drop at various Q, and at high and low flow rates ($\dot{V} = 80$ and 20 ml/min). The minimum and maximum coolant temperatures differ by at most 2.5 °C at 80 ml/min, and 3.5 °C at 20 ml/min, which are much lower than the errors associated with the reference design shown in Figures 9.4b and f. On the other hand, the FLUENT pressure drop is consistently overestimated by IGFEM, with improved agreement at higher Q and substantially higher accuracy compared with that of the reference design. We note that for design purposes, consistent overestimation of the pressure drop is preferred over consistent underestimation or random error direction.

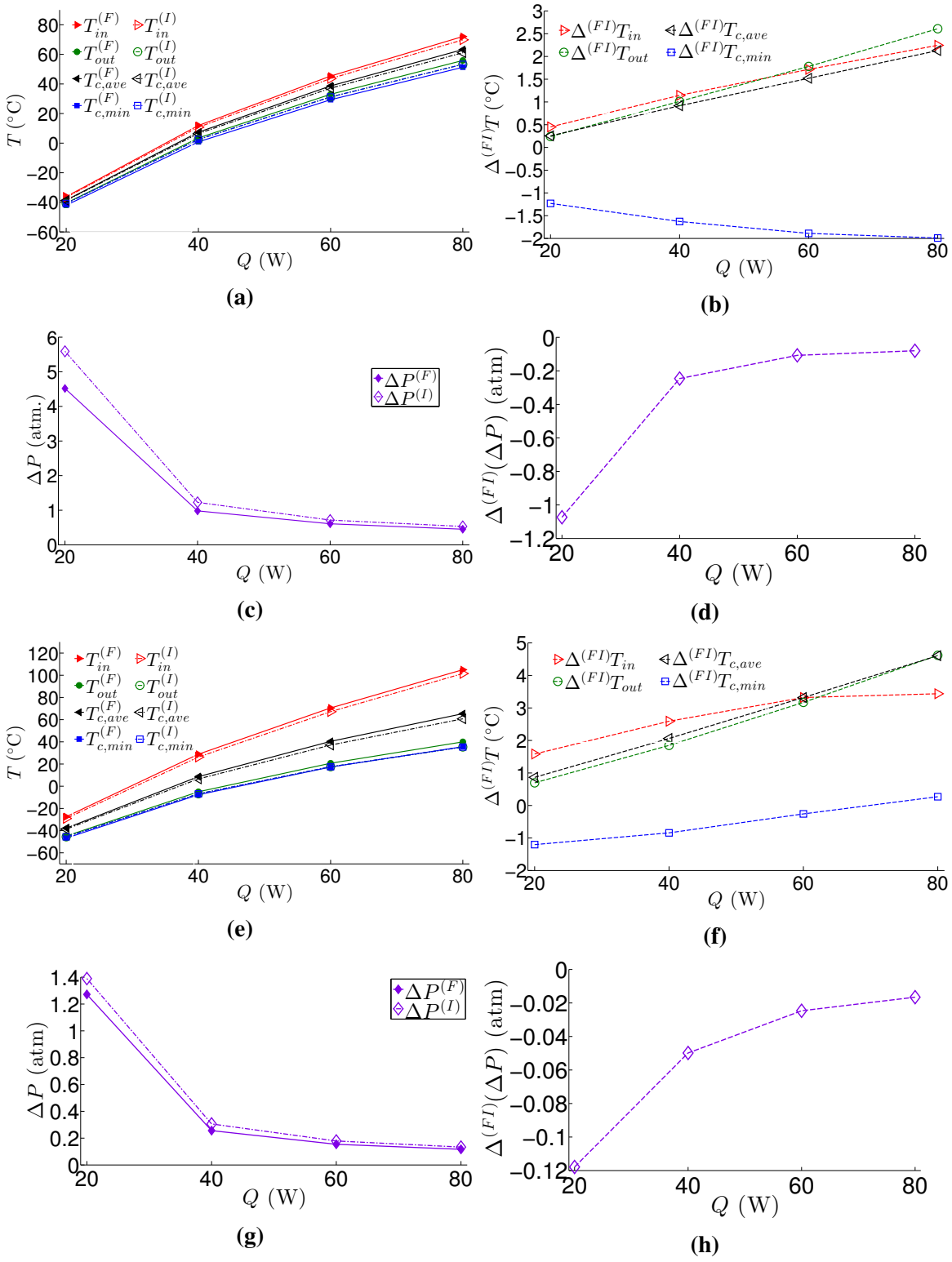

Figure 9.14 – FLUENT (superscript F) coolant temperatures and pressure drops associated with the 3×3 O_T design compared with those of IGFEM (superscript I) at flow rates of (a), (c) 80 ml/min and (e), (g) 20 ml/min with corresponding absolute differences shown on the right column.

9.7 Analytical estimates of panel and coolant temperatures

Based on results from the previous sections, we derive analytical estimates of the panel and coolant temperatures to facilitate the design process. The derivation begins by considering a *perfectly* conductive body of uniform surface emissivity ϵ and total surface area $|S|$ with a heat source Q in its interior, and contained in an enclosure with temperature T_∞. At equilibrium, the temperature in the body is uniform and given by

$$T_{pc} = \left(\frac{Q}{\epsilon \sigma_B |S|} + T_\infty^4 \right)^{1/4}. \tag{9.5}$$

Now, consider the same body subject to identical conditions but with a *finite* thermal conductivity. By conservation of energy, the surface temperature of the body satisfies the following equation:

$$\int_S \epsilon \sigma_B (T^4 - T_\infty^4) \mathrm{d}S = Q, \tag{9.6}$$

which is rearranged to yield the following equation for the 4-mean of the surface temperature:

$$\langle T \rangle_4 := \left(\frac{1}{|S|} \int_S T^4 \mathrm{d}S \right)^{1/4} = \left(\frac{Q}{\epsilon \sigma_B |S|} + T_\infty^4 \right)^{1/4} = T_{pc} \tag{9.7}$$

Since $|S|$ is finite, we also have for $0 < m \leq n \leq \infty$ [124],

$$\langle T \rangle_m \leq \langle T \rangle_n. \tag{9.8}$$

Denote the average and maximum surface temperatures of the body by T_{ave} and T_{max}, respectively. Then, $\langle T \rangle_1 = T_{ave}$ and $\langle T \rangle_\infty = T_{max}$. Using (9.7) and (9.8), we arrive at

$$T_{ave} \leq T_{pc} \leq T_{max}. \tag{9.9}$$

Let the body be a thin rectangular microvascular panel. Then, $T_{max} = T_{in}$, and to a very good approximation, $|S| = 2L_x L_y$. In all simulations of this study, we find that $T_{ave} \approx T_{pc}$. Hence, we have the following lower bound of T_{in}:

$$T_{ave} \approx T_{pc} \leq T_{in}. \tag{9.10}$$

The abovementioned lower bound can be improved by considering the solid-coolant interaction. Assuming a fully developed heat flow, conservation of energy applied to the heat transfer between

solid and coolant yields

$$\frac{\kappa_f \mathrm{Nu}}{D_h}\tilde{p}\int_{\Gamma_f}(T_m(\boldsymbol{x})-T_w(\boldsymbol{x}))\mathrm{d}\boldsymbol{x}=Q.. \tag{9.11}$$

where $\tilde{p}$ is the cross section perimeter and other symbols were defined in Chapter 2. Rearranging (9.11), we obtain the average coolant temperature as follows:

$$T_{c,ave}:=\frac{1}{L_{ch}}\int_{\Gamma_f}T_m(\boldsymbol{x})\mathrm{d}\boldsymbol{x}=\frac{1}{L_{ch}}\int_{\Gamma_f}T_w(\boldsymbol{x})\mathrm{d}\boldsymbol{x}+\frac{D_hQ}{\kappa_f\mathrm{Nu}\tilde{p}L_{ch}}, \tag{9.12}$$

where the first term on the right hand side is the average wall temperature of the channels. For a design with sufficiently uniform temperature distribution, the term can be approximated by T_{ave}, the average surface temperature of the panel, which is in turn approximated well by T_{pc}. Therefore, we obtain the following estimate for the average coolant temperature:

$$\begin{aligned}T_{c,ave}&\approx T_{pc}+\frac{D_hQ}{\kappa_f\mathrm{Nu}\tilde{p}L_{ch}}\\&=\left(\frac{Q}{2\epsilon\sigma_BL_xL_y}+T_\infty^4\right)^{1/4}+\frac{D_hQ}{\kappa_f\mathrm{Nu}\tilde{p}L_{ch}}.\end{aligned} \tag{9.13}$$

Let us now assume a monotonic or near monotonic decrease in coolant temperature from the inlet to the outlet. We note that this assumption is equivalent to the assumption that the minimum coolant temperature occurs near or at the outlet, and is valid only for certain designs such as the O_T designs shown in Section 9.2. With this assumption , $T_{c,ave}$ can be approximated as

$$T_{c,ave}\approx\frac{1}{2}(T_{in}+T_{out}) \tag{9.14}$$

Combining (9.2), (9.13) and (9.14), we arrive at a tighter lower bound for T_{in} given by

$$\begin{aligned}T_{in}&\approx T_{c,ave}+\frac{1}{2}(T_{in}-T_{out})\\&=\left(\frac{Q}{2\epsilon\sigma_BL_xL_y}+T_\infty^4\right)^{1/4}+\frac{D_hQ}{\kappa_f\mathrm{Nu}\tilde{p}L_{ch}}+\frac{Q}{2\dot{m}c_p}.\end{aligned} \tag{9.15}$$

In addition, we obtain the following estimated upper bound for $T_{c,min}$:

$$\begin{aligned}T_{c,min}&\approx T_{out}\approx T_{c,ave}-\frac{1}{2}(T_{in}-T_{out})\\&=\left(\frac{Q}{2\epsilon\sigma_BL_xL_y}+T_\infty^4\right)^{1/4}+\frac{D_hQ}{\kappa_f\mathrm{Nu}\tilde{p}L_{ch}}-\frac{Q}{2\dot{m}c_p}.\end{aligned} \tag{9.16}$$

We note that the bounds (9.15) and (9.16) are valid only when the assumption $T_{c,min}\approx T_{out}$ holds.

To validate the analytical estimates, we optimize the 3×3 designs embedded in panels of different lengths $L_x = 0.2$, 0.25 and 0.3 m, resulting in the designs shown in Figure 9.15a–c, where the last design was presented in previous sections. Figure 9.15d shows upper and lower temperature curves corresponding to those of perfectly conductive panels computed with (9.5) at $Q = 80$ and 20 W, respectively. The average temperatures (not shown in the figure) of the microvascular composite panels containing various designs are closely approximated by these curves.

By substituting $\kappa_f = 0.505\,\mathrm{W}/(\mathrm{m}\cdot\mathrm{K})$ (Table A.4), $\mathrm{Nu} = 2.94$ (corresponding to that of a rectangular cross section in this study subject to constant axial and uniform peripheral wall heat flux [58]) and the length of the optimized design shown in Figure 9.15b or c ($L_{ch} = 1.70$ m) into the analytical estimates (9.15) and (9.16), we generate the solid curves $T_{in}^{(A)}$ and $T_{c,min}^{(A)}$ shown in Figure 9.15d. We note that the discussion related to this figure remains valid with other choice of L_{ch} since L_{ch} only affects the second term of these estimates, which has the smallest magnitude in these cases, and the lengths of the 3×3 reference and optimized designs are quite similar (1.46 – 1.83 m). It is observed that $T_{in}^{(A)}$, evaluated at $Q = 80$ W, $\dot{V} = 80$ ml/min, is significantly higher than the upper T_{pc} curve. However, $T_{c,min}^{(A)}$, which is evaluated at $Q = 20$ W and $\dot{V} = 80$ ml/min, is much closer to the lower T_{pc} curve due to the significantly smaller contributions of the last two terms of (9.16) at lower Q and their opposite signs. Given the constraints on the coolant temperatures represented by the upper and lower horizontal lines in Figure 9.15d, it appears that only a narrow range of panel length centered around $L_x = 0.3$ m has the potential to satisfy both constraints.

This prediction is confirmed by Figure 9.15e, where T_{in} at $Q = 80$ W and $\dot{V} = 80$ ml/min, and $T_{c,min}$ at $Q = 20$ W and $\dot{V} = 80$ ml/min of the reference and optimized designs are shown. It is evident that only the 3×3 optimized design of the $L_x = 0.3$ m panel satisfies the temperature constraints. We also observe that the coolant temperatures of the optimized designs are significantly improved over those of the corresponding reference designs. Moreover, they agree well with the analytical estimates $T_{in}^{(A)}$ and $T_{c,min}^{(A)}$.

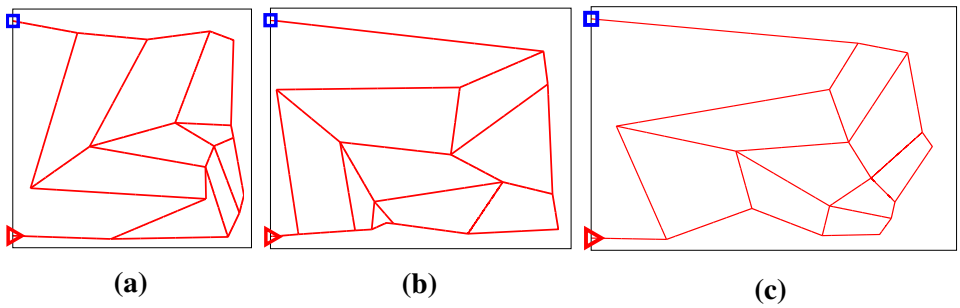

(a) (b) (c)

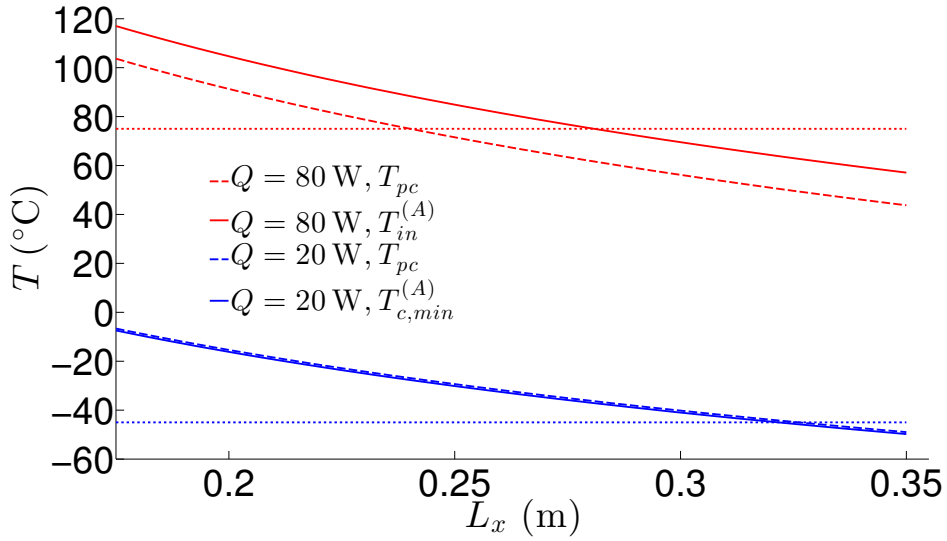

(d)

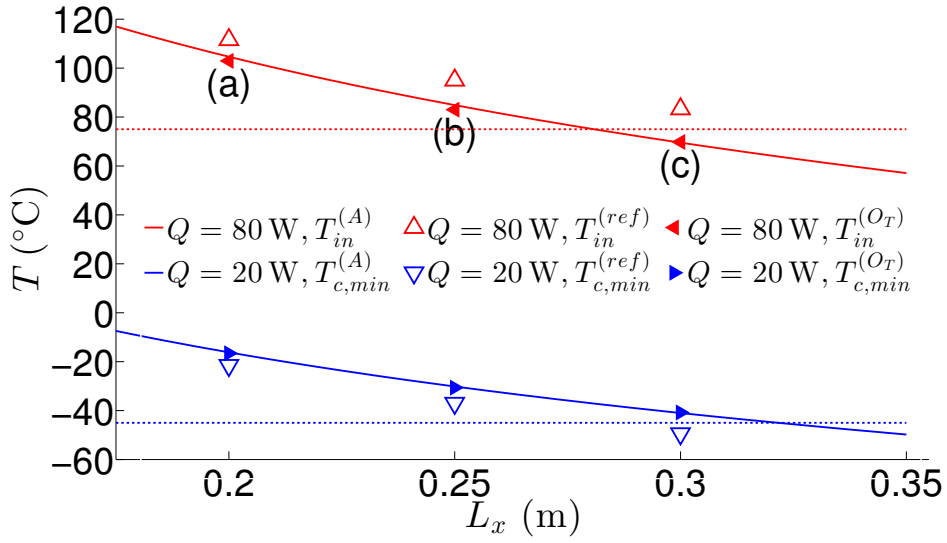

(e)

Figure 9.15 – (a)–(c) 3×3 O_T designs for panel lengths $L_x = 0.2$, 0.25 and 0.3 m, with total channel lengths $L_{ch} = 1.59, 1.70, 1.70$ m, respectively. (d) Temperatures of perfectly conductive panels T_{pc} given by (9.5) and analytical estimates (superscript A) given by (9.15) and (9.16) evaluated at $\dot{V} = 80$ ml/min and $L_{ch} = 1.70$ m. Maximum and minimum temperature constraints (75 and -45 °C) are shown as horizontal lines. (e) Inlet and minimum coolant temperatures of the panels compared with the analytical estimates.

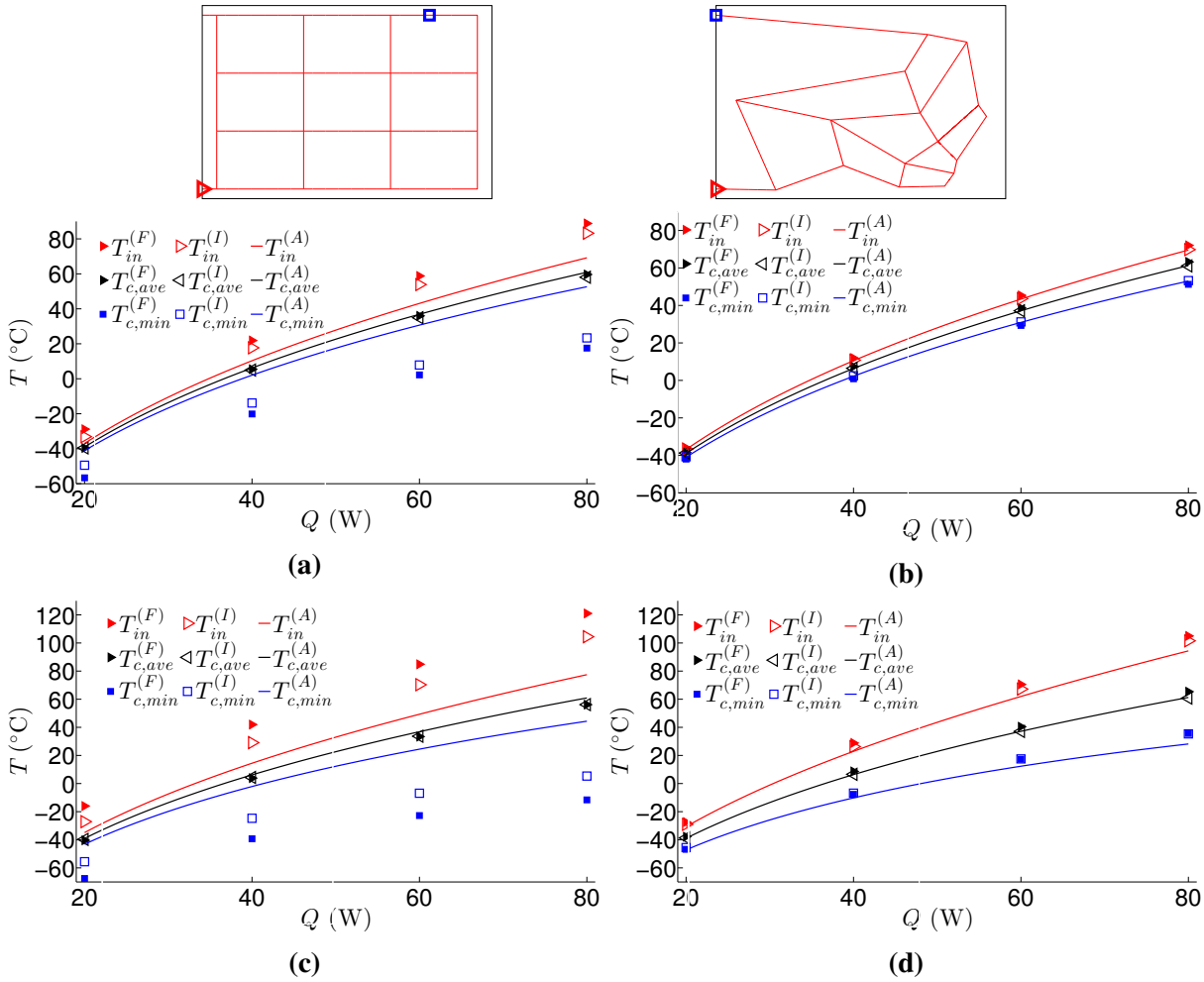

Figure 9.16 – (a), (c) Coolant temperatures associated with the 3×3 reference design of the $L_x = 0.3$ m panel for (a) $\dot{V} = 80$ and (c) $\dot{V} = 40$ ml/min computed using FLUENT (superscript F), IGFEM (superscript I) and analytical estimates (superscript A) given by (9.15) and (9.16). Coolant temperatures for the 3×3 O_T design at the flow rates (b) $\dot{V} = 80$ and (d) $\dot{V} = 20$ ml/min.

The analytical estimates (9.13), (9.15) and (9.16) are also benchmarked against the coolant temperatures computed with FLUENT and IGFEM simulations as shown in Figure 9.16. It is apparent from Figures 9.16a ($\dot{V} = 80$ ml/min) and 9.16c ($\dot{V} = 40$ ml/min) that only (9.13) is accurate for the reference design. The estimates (9.15) and (9.16) are inaccurate because the key assumption of near monotonic decrease in coolant temperature from inlet to outlet is violated by the reference design. However, for the optimized design, we observe good agreement between the analytical estimates and simulated coolant temperatures as evident in Figures 9.16b ($\dot{V} = 80$ ml/min) and 9.16d ($\dot{V} = 20$ ml/min) since the assumption is well satisfied.

9.8 Conclusions

In this chapter, a design scheme for nanosatellite microvascular composite radiator panels has been developed. The design problem involved three primary constraints: (i) keeping the coolant temperature at the network inlet sufficiently low when radiating the highest amount of dissipated heat, (ii) maintaining sufficiently high coolant temperature throughout the network when dissipating minimal heat, and (iii) ensuring that the maximum pump pressure was not exceeded when attempting to satisfy constraint (ii).

The computational design tool developed in this dissertation was used to satisfy these design constraints. Underyling this design tool was a dimensionally reduced thermal model with the nonlinear Stefan-Boltzmann law, and a hydraulic model assuming constant heat capacity and uniform kinematic viscosity. The solution of these models was obtained using the Newton-Raphson algorithm and the IGFEM, and compared against that of ANSYS FLUENT simulations. Discrepancy was found in the coolant temperatures and pressure drops associated with the reference design. Based on agreement of the solutions when the coolant properties were constant in the FLUENT simulations, the source of this discrepancy was determined to be the specific assumptions on coolant properties behind the hydraulic model, which were not satisfied by the reference design due to large variation in the coolant temperature. The large variation was manifested in the appearance of the minimum coolant temperature far from the network outlet.

In anticipation of better agreement for optimized designs, we formulated two optimization problems that allowed the design constraints to be satisfied. The first formulation (O_T) involved (i) replacing the original problem of maximizing the non-differentiable minimum coolant temperature with the minimization of the differentiable p-norm of the difference between the coolant temperature and a sufficiently large constant value, and (ii) imposing an upper bound constraint on the inlet temperature of the coolant. The other formulation (O_P) consisted of (i) minimizing the pressure drop across the network subject to (ii) an upper bound constraint on the coolant inlet temperature, and (iii) a lower bound constraint on the coolant outlet temperature. Employing the gradient-based optimization scheme developed in this dissertation, we then solved the optimization problems for grid-like designs of different grid densities. Optimized designs resulting from both formulations possessed substantially lower inlet temperature and higher minimum coolant temperature compared with the reference design. Furthermore, the minimum coolant temperature associated with the O_T designs occured near or at the outlet. Results from the O_T optimization also revealed that the inlet and minimum coolant temperatures were almost unchanged with grid densities, and the pressure drop decreased little at higher grid densities. As expected, the O_P design had the lowest pressure drop compared with the O_T and reference designs.

Next, we performed a detailed evaluation of some of the reference and optimized designs for a

range of dissipated heat rates, flow rates and sink temperatures. Given the range of available flow rates, the evaluation showed that reference design could not satisfy the coolant temperature constraints at lower and higher heat rates required by the design specification. On the other hand, both O_T and O_P designs satisfied the design constraints when appropriate flow rates were used. Examination of thermal solutions associated with two O_T designs optimized at different sink temperatures also revealed that the minimum coolant temperature remained above the required minimum temperature even at very low sink temperature. However, the maximum temperature constraint could not be satisfied when the sink temperature was too high.

Allowing for temperature-dependent coolant properties, we validated a selected O_T design against FLUENT simulations. Very good agreement between FLUENT and IGFEM solutions was found, hence justifying the IGFEM assumptions on the coolant properties for optimized designs. Examination of the thermal field associated with the optimized design revealed substantial uniformity compared with that resulting from the reference design.

Lastly, we developed analytical lower bound of the inlet temperature and upper bound of the minimum coolant temperature for designs satisfying the key assumption of near monotonic variation in coolant temperature between the inlet and outlet of the network. The coolant temperatures of the O_T designs, which satisfied this assumption, showed very good agreement with the analytical estimates. These analytical estimates are therefore expected to be useful for designing microvascular composite panel radiators for nanosatellites in the future.

10 3D Gradient-Based Design

This chapter is adapted from a recently submitted article titled "3D dimensionally reduced modeling and gradient-based optimization of microchannel cooling networks" by M. H. Y. Tan and P. H. Geubelle.

10.1 Introduction

In this chapter, we apply the optimization scheme developed in Chapter 5 to the 3D computational design of microvascular panels with parallel curved microchannels. Due to the importance of parallel straight channels as optimal designs for higher flow rates, we also present in Section 10.5 a semi-analytical model of the maximum temperature of a microvascular plate with parallel straight channels.

10.2 Optimization setup

We combine the 3D thermal solver described in Chapter 4 and the sensitivity analysis presented in Section 5.2 together with the sequential quadratic programming (SQP) algorithm in MATLAB [122] to solve the single-objective optimization problem given by (5.1) with $n_o = 1$. The objective function of interest is the maximum temperature in the domain, which is replaced with the p-norm of the temperature as a differentiable alternative. We set $p = 8$ for reasons explained in Section 6.4.2. Since the maximum temperature always occur at the domain boundary $\partial\Omega$ in this chapter, we consider $\langle T(\partial\Omega)\rangle_p$, i.e., the p-norm over $\partial\Omega$.

The optimization method is applied to the problem shown in Figure 10.1, which involves a single channel described by a quadratic B-spline. The boundary conditions are the same as those used in Sections 4.4 and 4.5 except that periodic boundary conditions are imposed on the two faces with normals in the y-direction to capture the presence of multiple parallel channels in the microvascular plate. The thermal conductivity is set to 0.6 $\mathrm{Wm^{-1}K^{-1}}$ to approximate more closely that of a woven composite [32]. For each optimization, the flow rate is fixed at a value between 0.5–20 ml/min, and three values of the width W (0.01, 0.02 and 0.04 m) are considered to represent

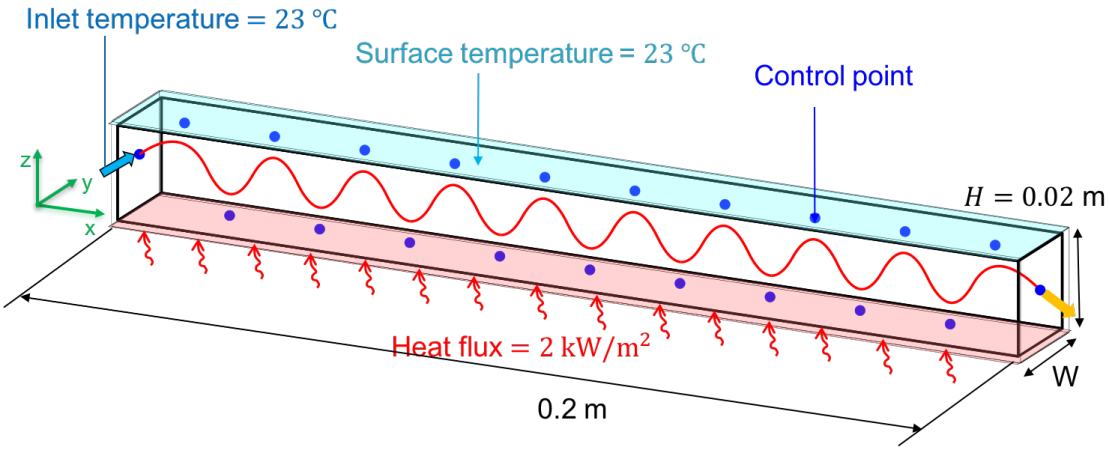

Figure 10.1 – Schematic of the optimization problem showing a section of a microvascular plate with parallel microchannels described by a set of control points used as design variables. The two end faces are insulated while periodic boundary conditions are applied along the front and back faces.

different spacings between channels.

Either the z-coordinates (see Section 10.3) or both the y- and z-coordinates (see Section 10.4) of the 21 control points of the quadratic B-spline are chosen as design parameters. The expression of the velocities of the intersection points between a quadratic B-spline and a face of a tetrahedral element required for the evaluation of the sensitivity is given in Appendix A.6. The control points are restricted to move within bounding intervals such that the minimum allowable distance to the four largest faces is $\sim H/7$, which represents the manufacturing constraint of avoiding channels too close to the surface. For each set of conditions, up to 48 distinct channel designs produced by shuffling the control points within the bounding intervals are used as initial guesses.

10.3 Control points allowed to move in the z-direction only

In this section, only the z-coordinates of the control points are chosen as design parameters, i.e., the microchannel is constrained to the midplane $y = W/2$, resulting in 21 design parameters. The optimal designs are compared in Figure 10.2 with a straight channel design, which is known to be optimal at sufficiently high flow rates [31]. At a low flow rate of 0.5 ml/min, an optimal undulating design is obtained (Figure 10.2b) consistent with [31]. Two key reasons give rise to this design. Firstly, the flow rate is not high enough to convect the heat via the coolant directly to the outlet. Hence the heat absorbed by the coolant needs to be "deposited" at the cold surface before the coolant temperature becomes too high. Secondly, since the channel is not in close proximity to

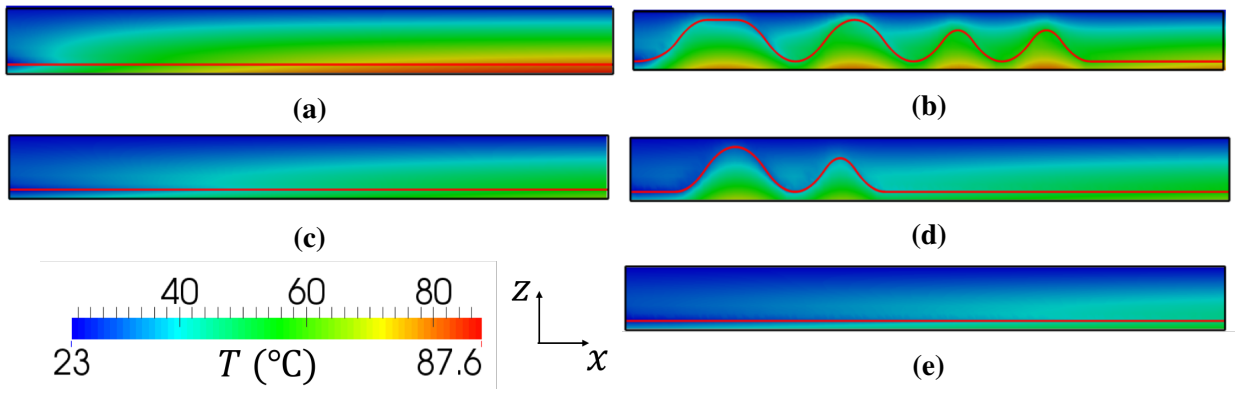

Figure 10.2 – Temperature distribution on the middle plane $y = W/2$ for the straight and optimal designs, and $W = 0.02$ m. At a flow rate of 0.5 ml/min, the maximum temperatures of the straight (a) and optimal (b) designs are respectively 87.6 °C and 81.8 °C. At 2 ml/min, the maximum temperatures of the corresponding designs (c) and (d) are respectively 72.5 °C and 71.5 °C . At 4 ml/min, the optimal design (e) is the straight design with maximum temperature 63.7 °C.

.

the surface where the heat flux is applied, less heat is absorbed by the coolant, thus slowing the rise in coolant temperature. As apparent from Figure 10.2d, the waviness in the optimal design diminishes at an intermediate flow rate of 2 ml/min. At a flow rate of 4 ml/min, the optimal design is a straight channel consistent with [31].

The designs are optimized for different domain widths $W = 0.01, 0.02$ and 0.04 m and compared with the straight design for flow rates ranging from 0.5 ml/min to 8 ml/min, corresponding to dimensionless values of the flow rates $\dot{m}^* = \dot{m}c_p/(\kappa\pi L) = 0.08225$ and 1.32 in Figure 10.3. The maximum temperature of the straight design is close to that of the optimal designs even for very low rates. When the flow rate is 4 ml/min ($\dot{m}^* = 0.658$) or larger, the straight design is optimal. Due to the importance of the straight channel design, we have developed a semi-analytical expression for predicting the associated maximum temperature in Section 10.5.

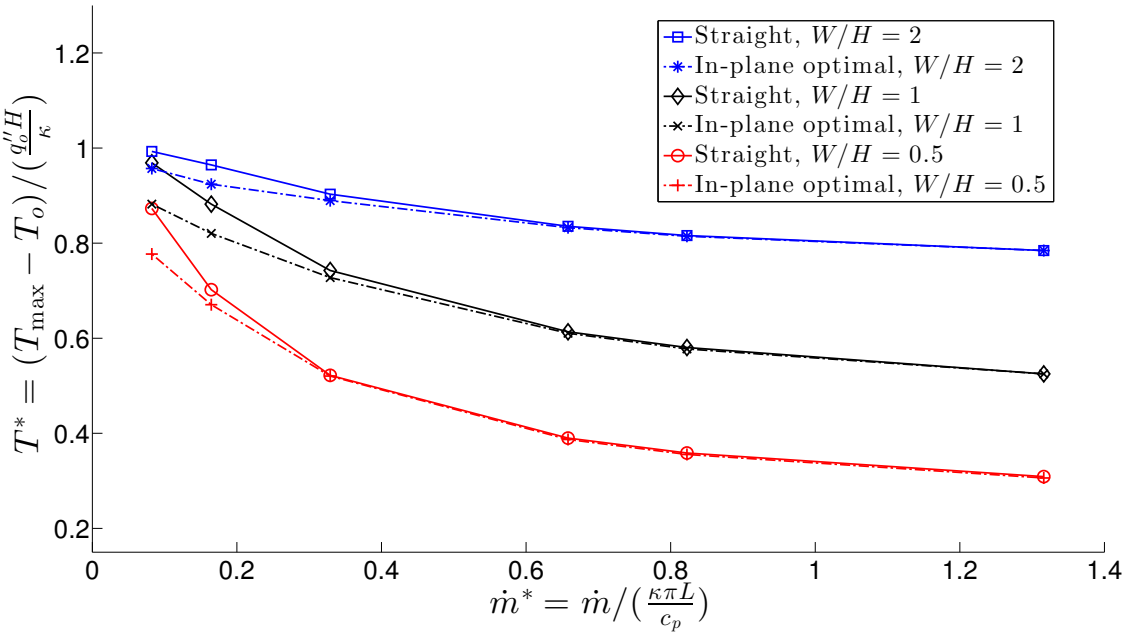

Figure 10.3 – Performance of the straight channel configuration compared with that of the optimal designs: maximum temperature vs. mass flow rate. Note that $T^* = 1$ corresponds to the maximum temperature in the absence of cooling ($\dot{m}^* = 0$).

10.4 Control points allowed to move in the y- and z-directions

Both the y- and z- coordinates are chosen as design parameters in this section, leading to 42 design parameters. The optimal designs at a flow rate of 20 ml/min and for $W = 0.01, 0.02, 0.04$ m are presented in Figure 10.4. In all cases, the optimal designs tend to stay close to the bottom face where the heat flux is applied, as evident in Figures 10.4a, d and g. When the domain width is small, i.e., $W = 0.01$ m, the optimal design exhibits little waviness in the y-direction as apparent in Figure 10.4c. However, the waviness becomes more pronounced as seen in Figures 10.4f and i for the larger widths 0.02 and 0.04 m, respectively.

In Figure 10.5, the maximum temperatures of the optimal designs are compared with the in-plane optimal designs obtained in Section 10.3. Evidently, allowing the control points to move more freely reduces the maximum temperature of the optimal design further, with greater reduction for larger domain widths.

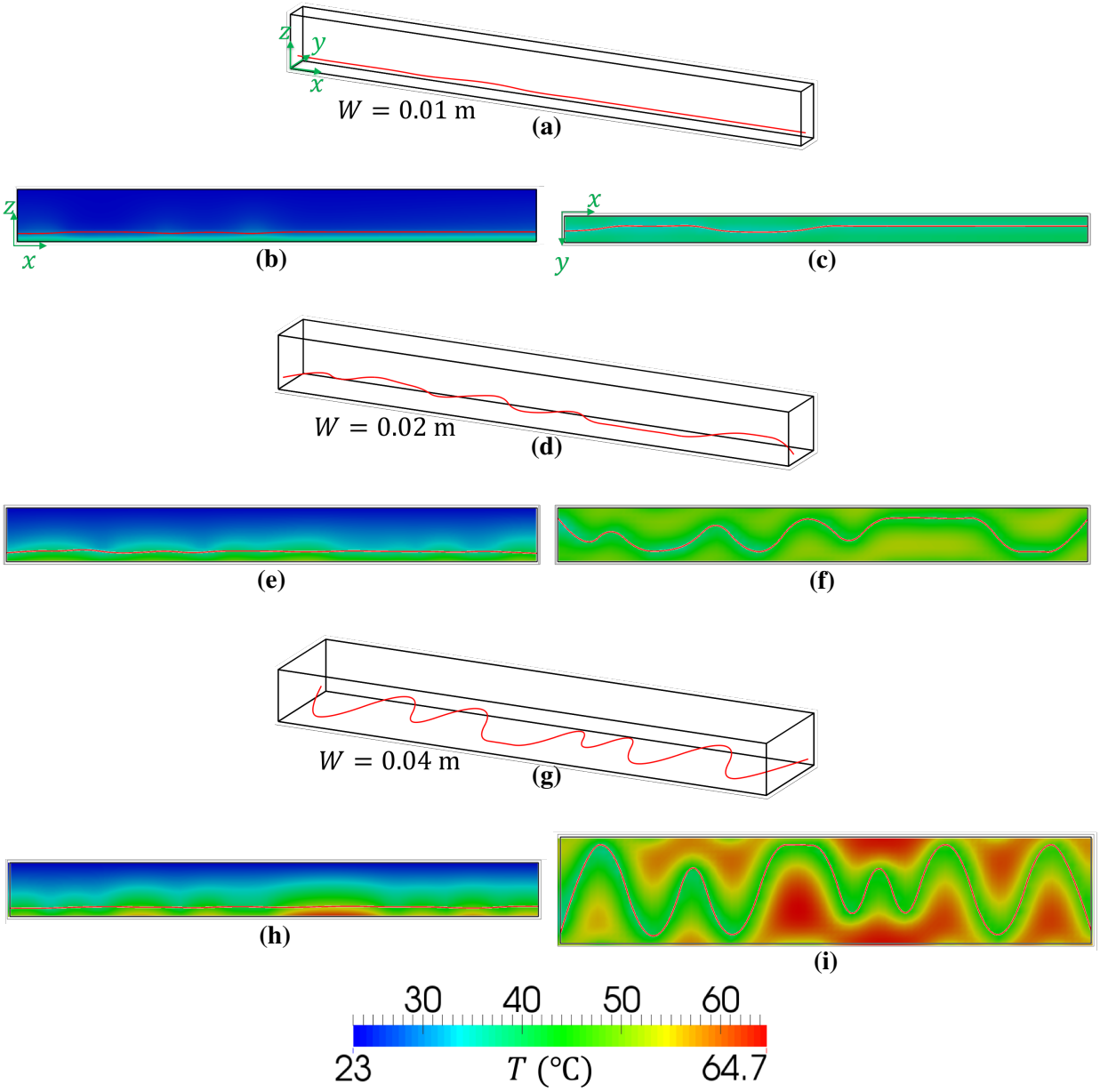

Figure 10.4 – Optimal designs (a), (d), (g) for different widths W of the periodic domain at a flow rate of 20 ml/min obtained using the y- and z-coordinates of the control points as design parameters. Figures (b), (e), (h): temperature field of the optimal designs on the $y = 0$ plane with the superimposed front views of the designs. Figures (c), (f), (i): temperature solution for the optimal designs on the $z = 0$ plane with the superimposed bottom views of the designs.

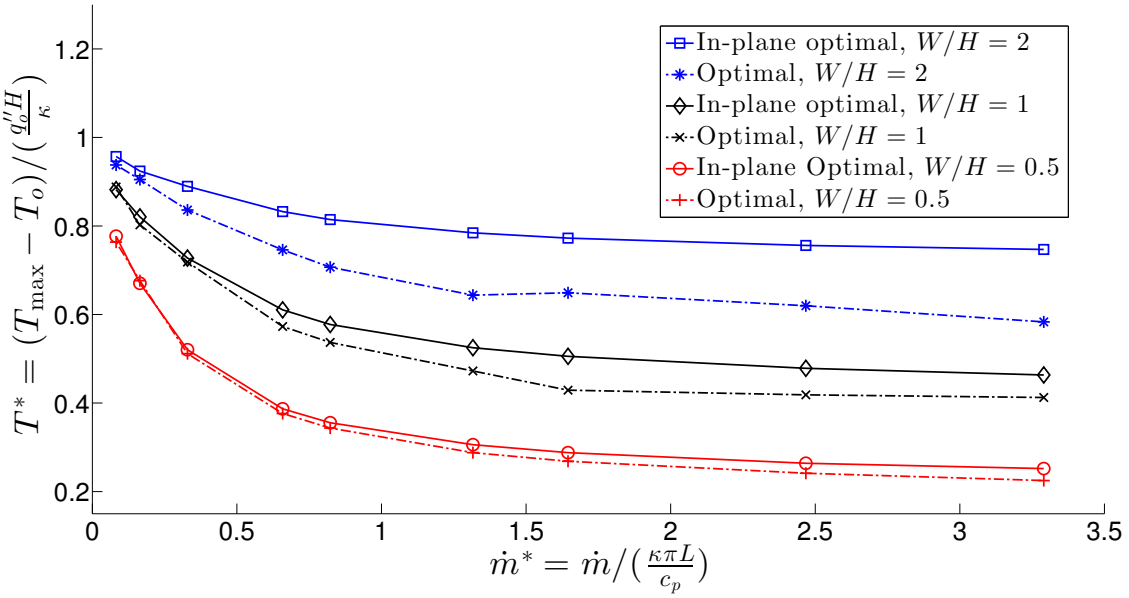

Figure 10.5 – Maximum temperature of the optimal designs obtained by allowing the control points to move in both the y- and z-directions (Section 10.4) compared with that obtained by only allowing movement in the z-direction (Section 10.3) as a function of the mass flow rate.

10.5 Theoretical estimate of $T_{\max}$ in microvascular panels with straight microchannels

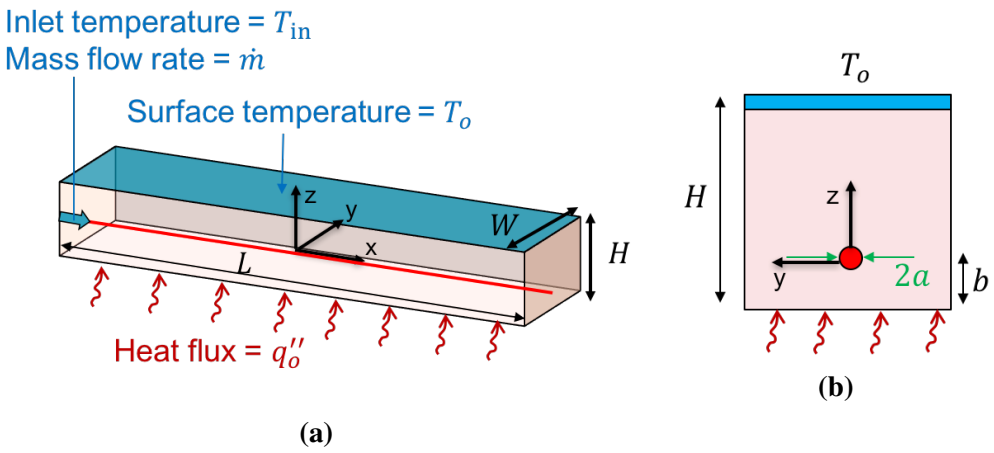

Figure 10.6 – Perspective (a) and side views (b) of the problem setup for the analytical model of the temperature in the microvascular panel, with the definition of the geometric and thermal loading parameters.

In this section, we derive a semi-analytical model to predict the temperature in a microvascular panel with embedded straight parallel channels of radius a as shown Figure 10.6. A thermal load q_o'' is applied along the bottom face while the top face is fixed at temperature T_o. Periodic boundary conditions are imposed along the front and back faces whereas the remaining end faces are insulated. The model starts by generalizing (4.6) to

$$T(x,y,z) = G(r_c)\left(x + \frac{r_c}{2\pi}\log\frac{r}{a}\right) + T_{in} + \frac{q_o''}{\kappa}l(x,y,z), \tag{10.1}$$

where $r_c = \frac{\dot{m}c_p}{\kappa}$, G is a function of r_c, $l(x,y,z)$ is a correction term for the far-field solution and $r = \sqrt{y^2+z^2}$. Imposing the boundary condition $T(L,0,H-b) = T_o$, we have

$$G(r_c) = \frac{T_o - T_{in} - \frac{q_o'' l_o}{\kappa}}{L + \frac{r_c}{2\pi}\log\frac{H-b}{a}}, \tag{10.2}$$

where $l_o = l(L,0,H-b)$. Let us rewrite (10.2) as

$$G(r_c) = \frac{C_1}{L + C_2 r_c}, \tag{10.3}$$

where C_1 and C_2 are parameters independent of r_c.

Using (10.1), the maximum temperature in the domain obtained at $(x,y,z) = (L, W/2, -b)$ is

given by

$$T_{max} = G(r_c)\left(L + \frac{r_c}{2\pi}\log\frac{r_b}{a}\right) + T_{in} + \frac{q_o''}{\kappa}l_b, \tag{10.4}$$

where $r_b = \sqrt{\frac{W^2}{4} + b^2}$ and $l_b = l(L, W/2, -b)$. In the absence of the channel, $T_{max} = \frac{q_o'' H}{\kappa} + T_o$. Therefore, from (10.3) and (10.4),

$$C_1 = \frac{q_o''(H - l_b)}{\kappa} + \Delta T_o, \tag{10.5}$$

where $\Delta T_o = T_o - T_{in}$.

Let $\Delta T_{coolant}$ be the difference between the outlet and inlet temperatures of the coolant. Define the size of the zone of influence of the channel as

$$D_z := \frac{r_c \kappa \Delta T_{coolant}}{q_o'' L}. \tag{10.6}$$

Then, along the channel, we get for large flow rates, i.e., for large r_c,

$$\frac{\partial T}{\partial x} \approx \frac{q_o'' D_z}{\kappa r_c}. \tag{10.7}$$

From (10.1), $\frac{\partial T}{\partial x} \approx G(r_c)$. Therefore, at large flow rates,

$$G(r_c) \approx \frac{q_o'' D_z}{\kappa r_c}, \tag{10.8}$$

and from (10.3),

$$G(r_c) \approx \frac{C_1}{C_2 r_c}. \tag{10.9}$$

Equating the right hand sides of (10.8) and (10.9), and using (10.5), we get

$$C_2 = \frac{H - l_b}{D_z} + \frac{\kappa}{q_o'' D_z}\Delta T_o. \tag{10.10}$$

Combining (10.3), (10.5) and (10.10) yields

$$G(r_c) = \frac{\frac{q_o''(H-l_b)}{\kappa} + \Delta T_o}{L + \left(\frac{H-l_b}{D_z} + \frac{\kappa}{q_o'' D_z}\Delta T_o\right) r_c}. \tag{10.11}$$

For the remainder of this section, let $T_o = T_{in}$, which implies $\Delta T_o = 0$. Therefore, (10.11) simplifies to

$$G(r_c) = \frac{q_o''}{\kappa}\frac{H - l_b}{L + \frac{H-l_b}{D_z} r_c}, \tag{10.12}$$

and (10.4) becomes

$$T_{max} = \frac{q_o''}{\kappa} \frac{H - l_b}{L + \frac{H-l_b}{D_z} r_c} \left(L + \frac{r_c}{2\pi} \log \frac{r_b}{a} \right) + T_{in} + \frac{q_o''}{\kappa} l_b. \tag{10.13}$$

Two model parameters, D_z and l_b, are yet to be determined. l_b is found by numerical fitting to be proportional to W with the proportionality constant given later. Let us now consider the size of the zone of influence D_z. When the flow rate is small, $\Delta T_{coolant} \approx \frac{q_o''}{\kappa}(H - b)$ since the outlet temperature would be close to the temperature of the solid at that location in the absence of the channel. Hence, from the definition of D_z in (10.6),

$$D_z = \frac{H - b}{L} r_c = \frac{H - b}{L} \frac{\dot{m} c_p}{\kappa}, \tag{10.14}$$

i.e, the size of the zone of influence is proportional to the flow rate for small flow rates. For large flow rates and $W/H << 1$ or $H/W << 1$, we expect

$$D_z = \min(W, H). \tag{10.15}$$

Let us introuce the dimensionless flow rate as

$$\dot{m}^* = \frac{\dot{m} c_p}{\kappa \pi L}. \tag{10.16}$$

Figure 10.7a shows how the zone of influence changes with $\dot{m}^*$ for three different widths of the domain, $W = 0.5H, H$ and $2H$. For small flow rates, the slope agrees well with the small flow rate zone of influence (10.14) as shown in the inset. For the cases $W = 0.5H$ and $W = 2H$, the simulated zone of influence tends to values consistent with (10.15) at large flow rates. Also shown in the same figure are exponential models of the form

$$D_z = D_{z,\infty} \left[1 - \exp\left(-\frac{H - b}{L} \frac{r_c}{D_{z,\infty}} \right) \right], \tag{10.17}$$

where $D_{z,\infty} = \min(W, H)$. The exponential models agree with (10.14) and (10.15), but exhibits significantly faster transition to the large flow rate zone of influence. The zone of influence at large flow rates cannot be predicted accurately by (10.15) when $W = H$ since both W and H simultaneously determine its size. However, we note that the case $W >> H$ is the most important case since microvascular composites are typically manufactured with thicknesses significantly smaller than the other dimensions. Hence, in an "optimized" microvascular composite with straight channels, i.e., one for which the zones of influence of the channels are not spaced too far apart or overlapping, the spacing between the channels are approximately H.

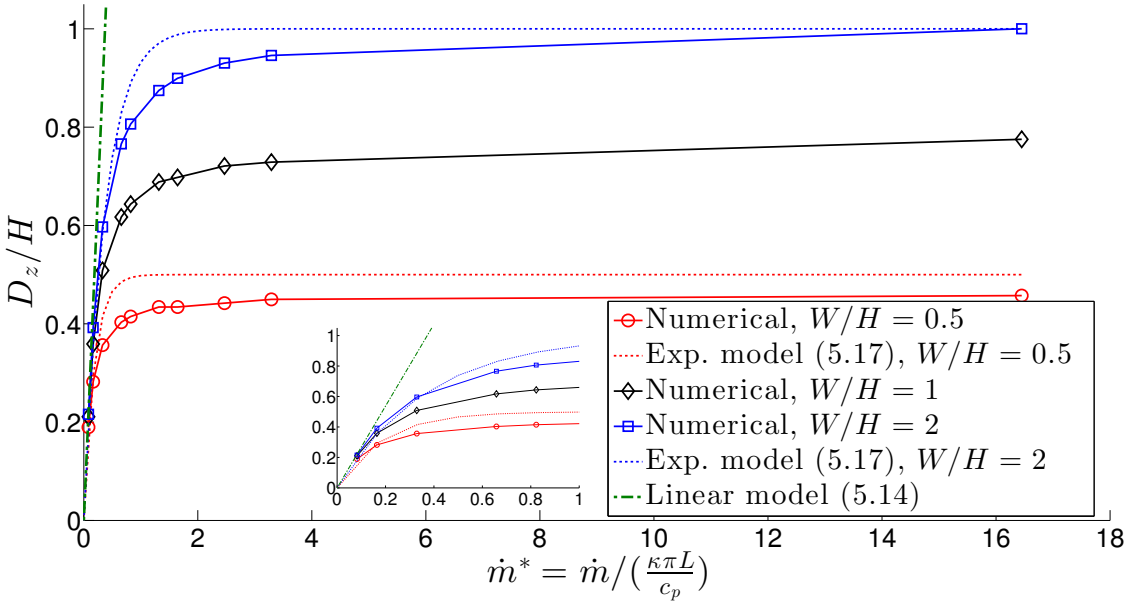

(a)

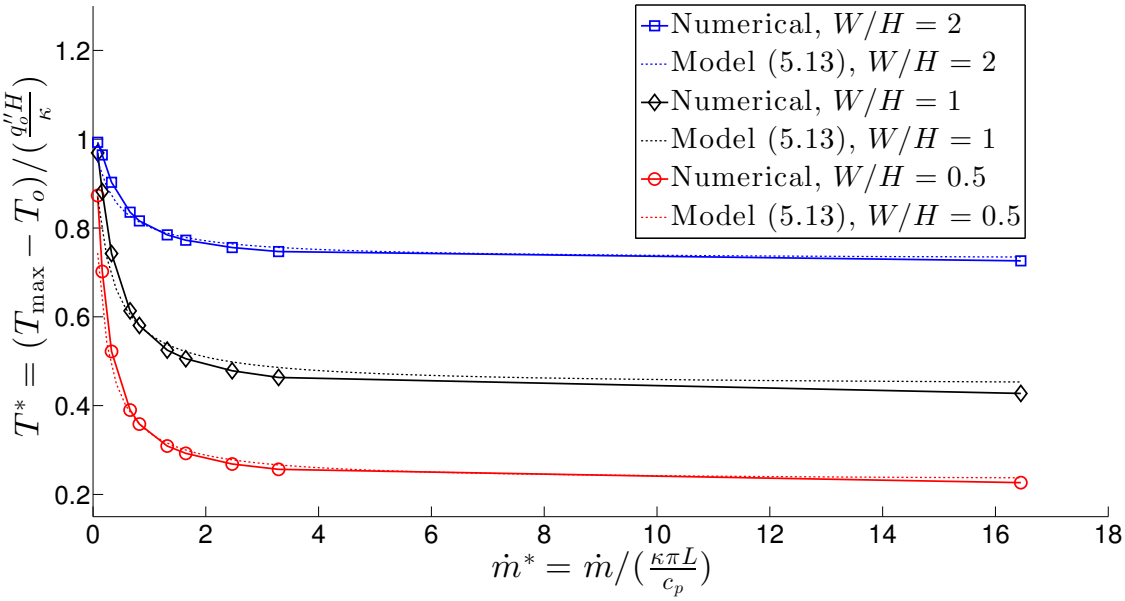

(b)

Figure 10.7 – (a) Size of the zone of influence and (b) maximum temperature as a function of mass flow rate: comparison between numerical and analytical solutions.

The aforementioned expression of the zone of influence in fact provides the average size of the zone of influence over the length of the channel. To accurately predict the maximum temperature, which occurs at the channel outlet, we need the zone of influence at the outlet. As shown hereafter, using the average zone of influence at large flow rates to approximate the outlet zone of influence results in an accurate prediction of the maximum temperature. On the other hand, using the actual

average zone of influence results in an unphysical linear increase in maximum temperature at small flow rates as predicted by (10.13).

Let us define the dimensionless maximum temperature as

$$T^* = \frac{(T_{max} - T_o)\kappa}{q_o'' H}. \tag{10.18}$$

The simulated T^* for straight channels decreases in a manner shown in Figure 10.7b consistent with other studies [21, 32]. With $l_b = 0.07W$, $D_z = 0.0155$ obtained numerically for $W = H$ and $D_z = \min(W, H)$ otherwise, the model (10.13) agrees well with the simulated value of T^*.

10.6 Conclusions

In this chapter, we have combined the 3D IGFEM thermal solver described in Chapter 4, the IGFEM-based sensitivity analysis summarized in Chapter 5 and the SQP algorithm to optimize the shape of parallel curved microchannels in a microvascular panel. The exercise has demonstrated two main advantages of the IGFEM: its ability to capture the discontinuous gradient for many configurations with a single non-conforming mesh, and to avoid mesh distortion as the channel geometry evolved. In the optimization problems, a differentiable alternative of the maximum temperature (the p-norm of the temperature) of a microvascular material embedded with a quadratic B-spline channel was minimized with the control points of the channel chosen as the design parameters. By restricting the channel to evolve in a plane, we showed that the optimal designs were consistent with a previous study, i.e., the optimal designs were oscillatory and straight for lower and higher flow rates, respectively. More complex and efficient optimal designs were then obtained by using additional coordinates of the control points as design parameters.

Finally, for a plate with embedded parallel straight channels, we proposed a semi-analytical model based on the concept of the zone of influence to predict the maximum temperature associated with the dimensionally reduced model. Good agreement was found between the analytical and numerical maximum temperatures.

11 Concluding Remarks and Future Work

11.1 Key contributions

This thesis has focused on the formulation, implementation, verification and validation of a novel gradient-based design tool for microchannel cooling networks. The key contributions of this work can be summarized as follows:

- A 2D non-uniform rational B-splines (NURBS)-based interface-enriched generalized finite element method (IGFEM) was developed to solve the thermal fields associated with panels containing branched network of curved microchannels on a non-conforming mesh. Convergence studies performed with the method of manufactured solution showed optimal convergence and accuracy comparable to that of standard finite element method. The problems devised for the convergence studies are novel.

- The convergence issue associated with the thermal model in 3D was addressed with a method adapted from wire-based electromagnetics, which involved modifying the thermal conductivity of the elements surrounding the microchannels. The IGFEM solution resulting from this modification showed significantly faster convergence to a solution compared with one without modification. Furthermore, we showed that the modified IGFEM solution agreed with that of the significantly more complex ANSYS FLUENT simulation and yielded up to two orders of magnitude of speed-up.

- We developed IGFEM-based sensivitiy analyses for both linear and nonlinear thermal models, where the nonlinearity of the latter arises from the Stefan-Boltzmann law of radiation. These sensitivity analyses were then combined with existing gradient-based algorithms to optimize microchannel cooling networks used in three main applications.

- First application: 2D design of electric vehicle battery cooling panels.

  - We performed single-objective optimization of parallel networks using the p-norm of the temperature field as a differentiable alternative to the maximum temperature of the panel. Transitions in the optimal designs were observed as the number of branches

of the networks and flow rates were varied. The optimal designs showed subtantially lower maximum temperatures and greater temperature uniformity compared with those of the reference designs.

  - We performed multi-objective optimization of parallel networks, in which the Pareto fronts of maximum temperature and pressure associated with different number of branches of the networks were generated using an existing method called the nornalized normal constraint method. Various other optimizations involving variance of the temperature field, microchannel diameters as design parameters, localized heat sources and prescribed pump power were also considered.
  - We designed grid like networks with different degrees of redundancy in PDMS panels for blockage tolerance. The problem of designing for blockage-tolerance was formulated as a minmax problem, which was then converted to a simpler single-objective optimization problem. The designs optimized in this manner demonstrated significantly better thermal performance in the worst case of predetermined blockage scenarios compared with designs optimized assuming clear channels, with increasing difference in performance as the degree of redundancy decreased.

- Second application: 2D design of actively cooled panel radiators for nanosatellites. The solution associated with the nonlinear thermal model was extensively benchmarked against that of ANSYS FLUENT. Conditions for the agreement of the solutions were established. Two optimization problems were formulated and solved using the optimization scheme developed for the nonlinear thermal model to satisfy the constraints on the radiator coolant temperatures and pressure drop across the network. The first problem involved the minimization of the p-norm of the difference between the coolant temperature and a sufficiently large constant as a differentiable alternative to the maximization of the minimum coolant temperature. Another formulation minimized the pressure drop across the network. Both designs satisfied the constraints when appropriate flow rates depending on dissipated heat rate were used. Accurate analytical estimates of the coolant temperatures associated with designs satisfying a key assumption were derived.

- Third application: 3D design of actively cooled microvascular composite panels. Curved parallel channels described by B-splines were optimized. Expected optimized designs were obtained at lower and higher flow rates, and new optimized designs for different spacings of the channels were obtained. A semi-analytical model of the maximum temperature of microvascular panels containing parallel straight channels was also developed.

11.2 Future work

A potential research direction is the development of more accurate dimensionally reduced models. To capture the solid temperature more accurately, a number of possible approaches can be taken. Instead of a thermal model that is based on the mixed-mean temperature, one that relates the heat transfer to the wall temperature of the channels is worth exploring. An example of such a model is given in Appendix A.7. To capture both solid and fluid temperatures accurately, two degrees of freedom per node representing the wall and mixed mean temperatures can be used. The degrees of freedom can then be coupled with (2.3), which holds pointwise along the channels. While a constant Nusselt number assumption simplifies the coupling, the accuracy requires further investigation. If found inaccurate, methods to compute the Nusselt number based on location, Reynolds number and Prandtl number need to be developed.

When the fluid temperature changes substantially along the channels as in the case of certain designs for microvascular satellite panels (Chapter 9), two-way coupling of the dimensionally reduced thermal and fluid models needs to be implemented. The coupling is required since the mass flow rates in (2.2) depends on the kinematic viscosity, which varies significantly along the network due to large variation in fluid temperature. Although pump power has been imposed in this work (Section 7.4.2), the implementation assumes *temperature-independent* viscosity. However, implementation of the two-way coupling would allow the pressure drop or pump power to be prescribed while allowing for *temperature-dependent* viscosity.

Gradient-based topology optimization can be developed to automate the design process further by obviating the need for a base design. Instead of the typical approach of having a single mesh that describes both fluid and solid, a grid instead of a mesh for the fluid as described in [29] can be used. Associated with each segment of the grid is a density design variable that is related to the diameter via an interpolation function rather than a set of discrete diameters. Filtering techniques need to be developed to reduce excessive details in the optimized designs. Another possible solution to excessive details is the manual simplification of the optimized design followed by application of the shape optimization tool developed in this work to further improve the design. The development of the sensitivity analysis for the topology optimization is also a worthwhile intellectual pursuit.

In 3D gradient-based design, geometrical constraints supplementing the bounding boxes need to be developed to provide more freedom to the control points while addressing the "self-crossing" of the channels. This additional freedom would produce designs substantially more different than the initial designs. Optimization of branched networks can also be explored in the future. These advanced applications come with the challenge of a more robust and efficient NURBS curve-triangular face intersection finder than that provided by the SINTEF spline library [149]. Furthermore, the creation of more complex 3D networks can be facilitated by the creation of a graphical

user interface tool similar to the one created for 2D (Figure A.2 of the appendix).

A number of other applications can be explored. For example, applications with high heat flux or in particular, microvascular composites for hypersonic vehicles where heat flux as high as hundreds of $\mathrm{kW/m^2}$ are encountered [14]. Another example is turbine blade cooling, where temperatures up to 1200–1450 °C [150] and convection coefficients as large as 500–1700 $\mathrm{W/(m^2K)}$ [151] are common. Since the fluid in the microchannels is expected to operate in the turbulent regime in turbine applications [33], the effect of turbulence on the model accurary requires careful study. Lastly, cooling with gases in extreme temperature environment is another possible application.

A Appendix

A.1 Overview of implementation

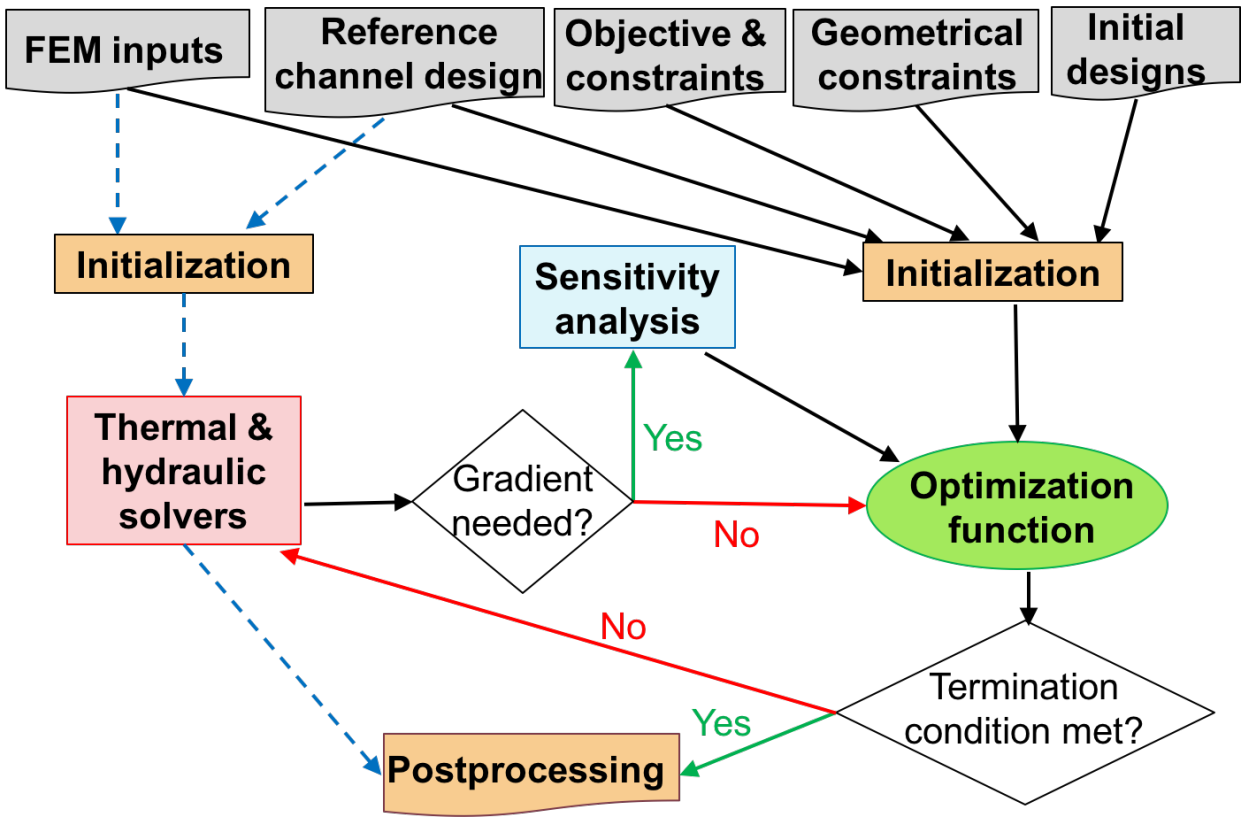

Figure A.1 – Overview of the design tool showing two applications: analysis of individual channel design and gradient-based optimization of a collection of initial designs indicated by the dashed and solid arrows, respectively.

In this section, we present a high-level description of the design tool implementation. As shown in the flow chart of Figure A.1, the implementation consists of three major processing units: **Thermal & hydraulic solvers**, **Sensitivity analysis** and **Optimization function**. The route represented by dashed arrows in the flow chart shows that **Thermal & hydraulic solvers** can be used as a standalone processing unit for the thermal and hydraulic analyses of an individual microchannel design. This application only needs data from two input units: (i) the unit containing convectional FEM

input information such as the mesh, boundary conditions, solver termination tolerance etc. (**FEM inputs**) and (ii) the geometry of the channel design and coolant properties (**Reference channel design**). A graphical user interface tool shown in Figure A.2 used to create 2D microchannel networks is provided as a convenience to the user. While the hydraulic solver has only been implemented in MATLAB as it constitute a neglible fraction of the computational time, two major parts of the thermal solver — assembly, and intersection search between a channel and an edge/face of the mesh— have been written in C++ using the Armadillo C++ linear algebra library [152]. In addition, the intersection search component calls functions from the SINTEF spline library [149] and the assembly component allows for the use of OpenMP for parallel execution. The functions associated with assembly and intersections search can be called in MATLAB as if they were built-in functions via the MEX application programming interface provided by MATLAB.

Another more important application of the design tool, i.e., gradient-based optimization follows the route represented by the solid arrows. This application combines **Thermal & hydraulic solvers** with the other two major processing units (**Sensitivity analysis** and **Optimization function**). Three additional sources of data are required: (i) objective function and constraints (**Objective & constraints**), (ii) geometry of triangles used to prevent "self-crossing" of channels (**Geometrical constraints**) and (iii) a collection of channel designs used as starting guesses for the optimization (**Initial designs**). Just like the assembly of the IGFEM equations, the assembly of the equations for sensitivity analysis has been implemented in C++ using the Armadillo library. **Optimization function** uses the MATLAB built-in function `fmincon`, which implements a number of powerful optimization methods such as interior-point and sequential quadratic programming. Cluster-based scripts have been written to run the optimization of the initial designs in multiple instances of MATLAB independently, thus allowing for many initial designs to be optimized at an efficiency higher than that associated with shared memory parallel programming.

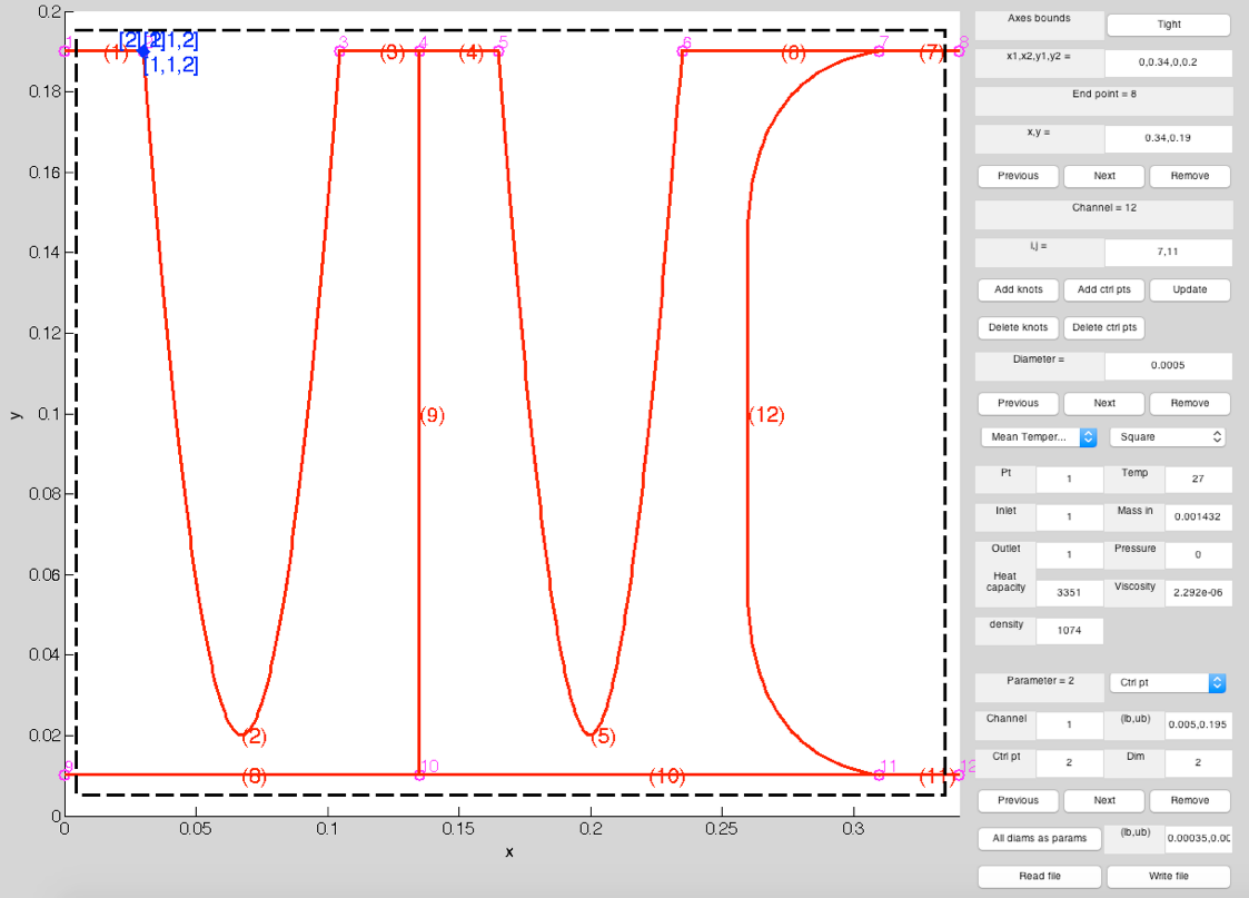

Figure A.2 – Graphical user interface for facilitating the creation of 2D channel networks.

A.2 NURBS description of channels

Table A.1 – Knot vectors and control points for the numerical integration study in Section 3.3.5. The last two NURBS curves are circular arcs of radii 1.6 and 8, respectively.

n	p	Knot vector	Control points	Weights
4	2	{0,0,0,0.5,1,1,1}	(0,0), (0.3,0.25), (0.7,0.05), (1.0,0.0)	1,1,1,1
5	3	{0,0,0,0,0.5,1,1,1,1}	(0,0), (0.2,0.2), (0.5,0.05), (0.8,0.15), (1.0,0.0)	1,1,1,1,1
3	2	{0,0,0,1,1,1}	(0,0), (0.5,0.1645), (1,0)	1,0.950,1
3	2	{0,0,0,1,1,1}	(0,0), (0.5,0.03131), (1,0)	1,0.998,1

Table A.2 – Knot vectors and control points for Verification Problem 2. The microchannels are described by different degree NURBS, p and different number of control points, n. The coordinates are expressed in terms of the charateristic length L. All weights are unity.

n	p	Knot vector	Channel	Control points
2	1	{0,0,1,1}	1	(0.50,0), (0.50,0.50)
			2	(0.50,0.50), (0,0.50)
			3	(0.50,0.50), (1,0.50)
			4	(0.50,0.50), (0.50,1)
3	2	{0,0,0,1,1,1}	1	(0.50,0), (0.50,0.25), (0.50,0.50)
			2	(0.50,0.50), (0.25,0.50), (0,0.50)
			3	(0.50,0.50), (0.75,0.50), (1,0.50)
			4	(0.50,0.50), (0.50,0.75), (0.50,1)
4	3	{0,0,0,0,1,1,1,1}	1	(0.50,0), (0.50,0.15), (0.50,0.35), (0.50,0.50)
			2	(0.50,0.50), (0.35,0.50), (0.15,0.50), (0,0.50)
			3	(0.50,0.50), (0.65,0.50), (0.85,0.50), (1,0.50)
			4	(0.50,0.50), (0.50,0.65), (0.50,0.85), (0.50,1)

Table A.3 – Knot vectors and control points for Application Problem 3 expressed in terms of the charateristic length L. All weights are unity.

Channel	Knot vector	Control points
A	{0,0,1,1}	(0,0.300), (0.110,0.255)
B	{0,0,1,1}	(0.890,0.255), (1,0.200)
1	{0,0,0,1,2,3,3,3}	(0.110,0.255), (0.300,0.500), (0.500,0.325), (0.700,0.500), (0.890,0.255)
2	{0,0,0,1,2,3,3,3}	(0.110,0.255), (0.300,0.375), (0.500,0.250), (0.700,0.375), (0.890,0.255)
3	{0,0,0,1,2,3,3,3}	(0.110,0.255), (0.300,0.125), (0.500,0.250), (0.700,0.125), (0.890,0.255)
4	{0,0,0,1,2,3,3,3}	(0.110,0.255), (0.300,0), (0.500,0.175), (0.700,0), (0.890,0.255)

A.3 Sensitivity of weight function

The derivative of the weight function with respect to a design parameter is given by

$$\left\{\frac{\partial W}{\partial d}\right\} = \left\{\frac{\partial N}{\partial d}\right\} + \frac{1}{2}\sum_{i=1}^{n_{ch}}\left(\frac{\partial h_e^{(i)}}{\partial d}[B]\{t^{(i)}\} + h_e^{(i)}\left[\frac{\partial B}{\partial d}\right]\{t^{(i)}\} + h_e^{(i)}\,[B]\left\{\frac{\partial t^{(i)}}{\partial d}\right\}\right), \tag{A.1}$$

where

$$\frac{\partial h_e^{(i)}}{\partial d} = -\frac{h_e^{(i)2}}{2}\sum_{j=1}^{n_n}\text{sign}\left(\{B_j\}'\{t^{(i)}\}\right)\left(\left\{\frac{\partial B_j}{\partial d}\right\}'\{t^{(i)}\} + \{B_j\}'\left\{\frac{\partial t^{(i)}}{\partial d}\right\}\right), \tag{A.2}$$

and

$$\{B_j\} = \left\{\frac{\partial N_j}{\partial x}, \frac{\partial N_j}{\partial y}\right\}'. \tag{A.3}$$

A.4 Sensitivity of mass flow rate

To obtain $\partial\gamma^{(i)}/\partial d = c_p\partial\dot{m}^{(i)}/\partial d$, we first need to obtain $\partial P_j/\partial d$, i.e, the derivative of the nodal pressures with respect to a design parameter. Differentiating the system of hydraulics equations (2.11), we have

$$[G]\left\{\frac{\partial P}{\partial d}\right\} = -\left[\frac{\partial G}{\partial d}\right]\{P\} + \left\{\frac{\partial S}{\partial d}\right\}, \tag{A.4}$$

which is reminiscent of the pseudo-force equation (5.9). If nodes j, k are the end nodes of channel i, the derivative of its mass flow rate is

$$\frac{\partial\dot{m}^{(i)}}{\partial d} = g^{(i)}\text{sign}(P_j - P_k)\left(\frac{\partial P_j}{\partial d} - \frac{\partial P_k}{\partial d}\right). \tag{A.5}$$

A.5 Dynalene HC-50 coolant properties

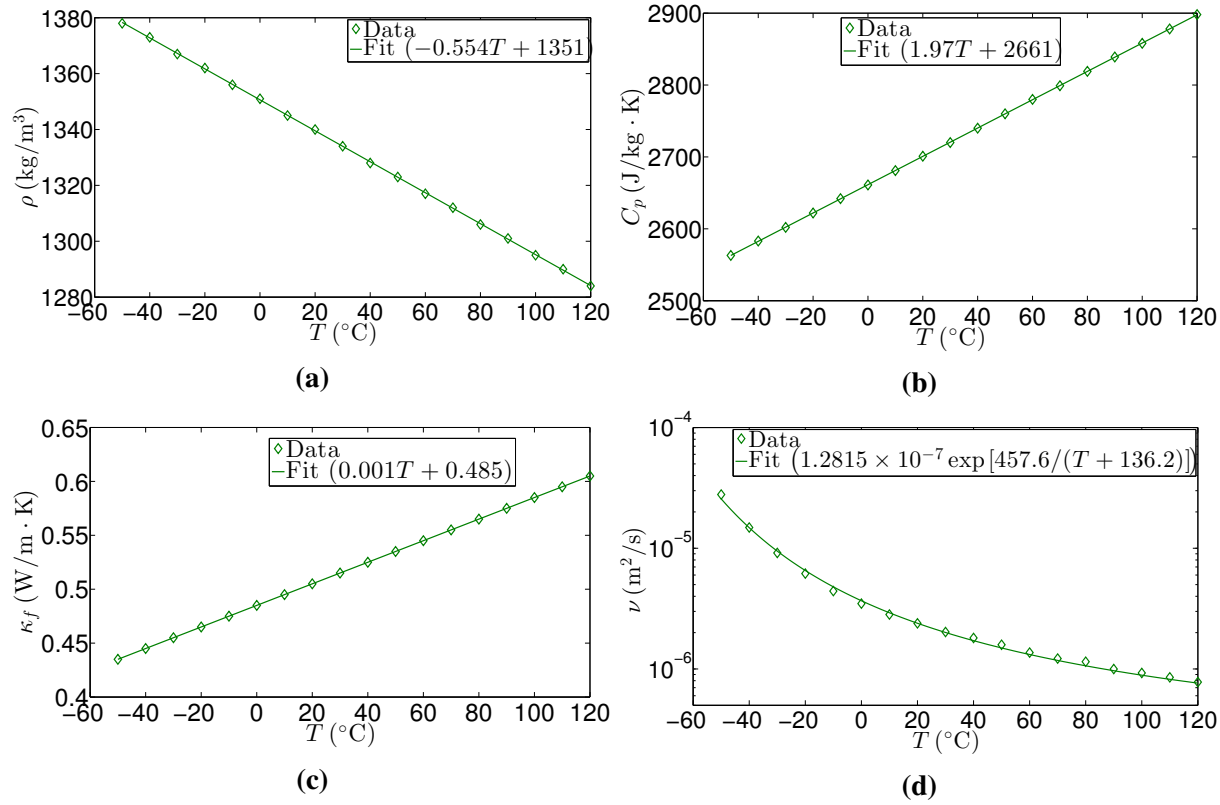

Figure A.3 – Dynalene HC-50 density (a), heat capacity (b), thermal conductivity (c) and kinematic viscosity (d).

Table A.4 – Average Dynalene HC-50 coolant properties over the temperature range -50 to 100 °C.

Property	Value
Density $(\mathrm{kg/m^3})$	1337
Heat capacity $(\mathrm{J/kg \cdot K})$	2711
Thermal conductivity $(\mathrm{W/m \cdot K})$	0.505

A.6 Velocity of intersection between a B-spline curve and a triangular face

Let the number of control points of a B-spline curve be n_{cpt}. Denoting the j-th control point of the B-spline curve by (C_{1j}, C_{2j}, C_{3j}) and the associated basis function by $N_j(\xi)$, the i-th component

of the physical coordinates on the curve corresponding to the parametric coordinate ξ is given by

$$x_i(\xi) = \sum_{j=1}^{n_{cpt}} C_{ij} N_j(\xi). \tag{A.6}$$

Let us suppose that the face of interest of an element is contained in the plane with normal (n_1, n_2, n_3) described by the equation $n_i x_i = b$, where Einstein summation is implied. If the B-spline curve intersects the face, then the parametric coordinate corresponding to the interesection ξ_I satisfies

$$n_i C_{ij} N_j(\xi_I) = b, \tag{A.7}$$

where, upon differentiation with respect to a control point coordinate C_{ij}, we have

$$\frac{\partial \xi_I}{\partial C_{ij}} = -\frac{n_i N_j(\xi_I)}{n_k C_{kl} N_l'(\xi_I)}, \tag{A.8}$$

provided the denominator does not vanish, i.e, when no segment of the curve lies in the same plane as the face. In the degenerate case where the denominator vanishes, some nodes shared by the face are moved by a small distance to eliminate the degeneracy following the strategy described in [85].

Since the physical coordinates of the intersection is $x_i(\xi_I) = C_{ij} N_j(\xi_I)$, the i-th component of the velocity with respect to the control point coordinate C_{kl} is given by

$$\frac{\partial x_i}{\partial C_{kl}} = \delta_{ik} N_l(\xi_I) + C_{ij} N_j'(\xi_I) \frac{\partial \xi_I}{\partial C_{kl}}, \tag{A.9}$$

where $\partial \xi_I / \partial C_{kl}$ is defined in (A.8).

Other than the abovementioned degenerate case, another case that can cause the velocity to be ill-defined happens when the curve passes through an edge of the face. In that situation, a small perturbation of the control point would result in more than one intersection. When that happens, a small adjustment of the nodes in the vicinity is performed so that the curve passes through the interior of the face.

A.7 Alternative dimensionally reduced thermal model

In the absence of branching, an alternative thermal model presented in this section is more accurate than the model (2.1). We hereafter refer to the two models as the constant heat flux and mean temperature models, respectively. Based on the temperature solution of a steady laminar flow in a circular tube with prescribed wall heat flux derived by Siegel et al. [153], the constant heat flux

model is expressed in terms of the wall temperature of the channel. In this section, we reproduce the main steps of the derivation as a convenience to the reader, describe how the constant heat flux model can be applied to this work and compare the solutions of the two thermal models against the FLUENT solution.

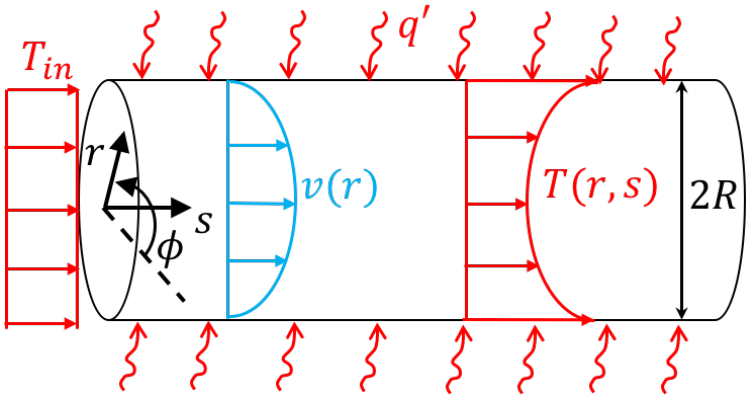

Figure A.4 – Circular tube with laminar flow subject to a constant thermal load on its wall.

Consider the problem shown in Figure A.4. The derivation starts by assuming fully developed hydrodynamic flow, hence implying that only the axial velocity of the flow is non-vanishing. This axial velocity is given by the well-known Poiseuille solution:

$$v(r) = \bar{v}\left(1 - \frac{r^2}{R^2}\right), \tag{A.10}$$

where $\bar{v}$ and R are respectively the mean axial velocity and radius of the channel.

Let us define the dimensionless radial and axial coordinates, Prandtl and Reynolds numbers as $r^* = r/R$, $s^* = s/R$, $\mathrm{Pr} = \rho c_p \nu/\kappa_f$ and $\mathrm{Re} = 2\bar{v}R/\nu$, respectively. Assuming steady and axisymmetric heat flow, and negligible dissipation, we can write the energy equation as

$$\mathrm{PrRe}(1 - r^{*2})\frac{\partial T}{\partial s^*} = \frac{1}{r^*}\frac{\partial}{\partial r^*}\left(r^*\frac{\partial T}{\partial r^*}\right) + \frac{\partial^2 T}{\partial s^{*2}}. \tag{A.11}$$

Applying the method of separation of variables, we can express the temperature field as $T(r^*, s^*) = R(r^*)S(s^*)$. The energy equation (A.11) therefore reduces to

$$S_n(s) = \exp\left(\frac{-\beta_n^2}{\mathrm{PrRe}}s^*\right), \tag{A.12}$$

and the Sturm-Liouville differential equations

$$\frac{\mathrm{d}^2 R_n}{\mathrm{d}r^{*2}} + \frac{1}{r^*}\frac{\mathrm{d}R_n}{\mathrm{d}r^*} + R_n\beta_n^2(1 - r^{*2}), \tag{A.13}$$

where $n = 1, .2, ..., R_n$ is an eigenfunction of (A.13) and β_n^2 is an eigenvalue associated with R_n.

Based on the solution of (A.13) given in [153], one can readily show that the energy transfer per unit length of the tube is given by

$$q' = h(s^*)(T(1, s^*) - T_{in}), \tag{A.14}$$

where

$$h(s) = 2\pi\kappa_f \left[\frac{11}{6} \frac{s^*}{\mathrm{PrRe}} + \sum_{n=1}^{\infty} C_n R_n(1) \exp\left(\frac{\beta_n^2}{\mathrm{PrRe}} s^* \right) \right]^{-1}. \tag{A.15}$$

C_n, β_n^2 and $R_n(1)$ can be obtained by imposing the appropriate boundary conditions, and values of the terms up to $n = 7$ can be found in [153]. In the constant heat flux model, the above expression (A.14) with T in lieu of $T(1, s^*)$ together with the line Dirac delta function replace the first term of (2.2) for a single channel.

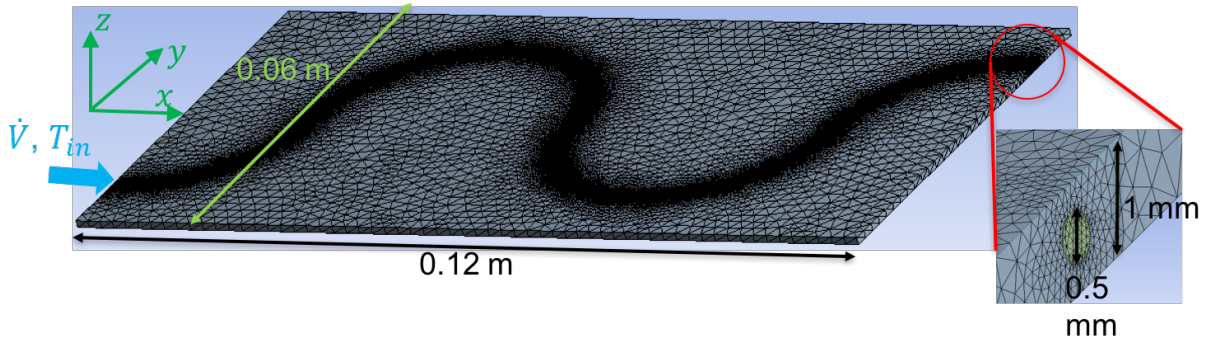

(a)

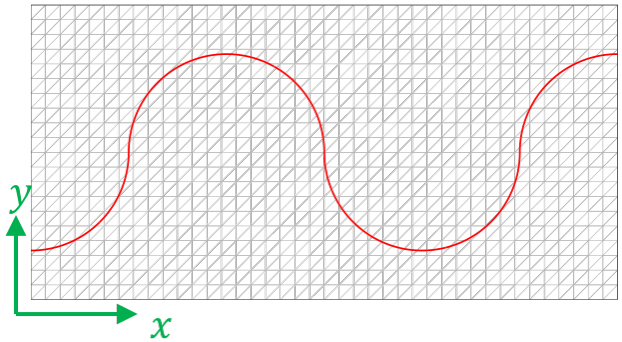

(b)

Figure A.5 – (a) FLUENT and (b) IGFEM meshes for a panel embedded with a curved microchannel consisting of circular arcs of radius 0.02 m.

To validate the constant heat flux model, we used a setup similar to that described in Section 6.4, but with a panel of length 0.12 m and width 0.06 m containing a curved channel design with circular cross section shown in Figure A.5a. The coolant was circulated at a flow rate of $\dot{V} = 4.69$

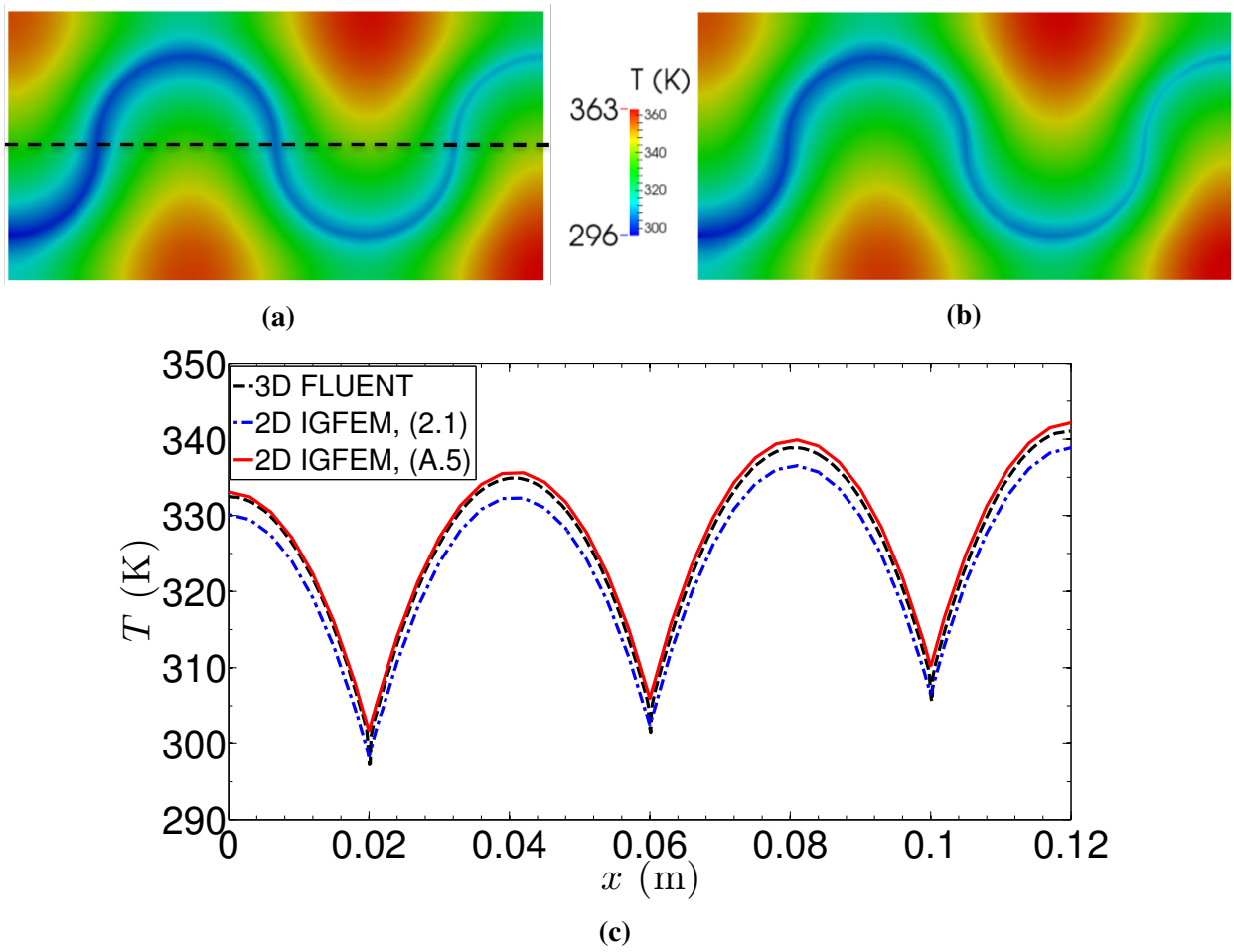

Figure A.6 – Thermal fields obtained from FLUENT (a) and IGFEM solution of the constant heat flux model (b). (c) Temperature solutions associated with the mean temperature and constant heat flux models compared with that of FLUENT along the black dashed line indicated in (a).

ml/min and an inlet temperature of $T_{in} = 296$ K was prescribed. The ANSYS FLUENT simulation was solved on a conforming mesh containing 2 million elements by Stephen J. Pety, whereas the IGFEM solutions were obtained on a non-conforming mesh with 1600 elements as shown in Figure A.5b.

Figures A.6a and b show that the temperature field associated with the constant heat flux model agrees well with that obtained from the FLUENT simulation. A closer examination of the temperature variation along the black dashed line ($y = 0.03$ m) on the top face of the panel reveals better agreement between the constant heat flux model and FLUENT compared with the mean temperature model. Further work is required to extend the constant heat flux model to other cross-sectional geometries and branched networks of channels.

References

[1] K. K. Chawla. *Composite Materials*, chapter 1, page 5. Springer, 2012.

[2] R. F. Gibson. A review of recent research on mechanics of multifunctional composite materials and structures. *Composite Structures*, 92:2793–2810, 2010.

[3] A. D. B. L. Ferreira, P. R. O. Nóvoa, and A. T. Marques. Multifunctional material systems: a state-of-the art review. *Composite Structures*, 151:3–35, 2016.

[4] C. J. Hansen. *Recent Advances in Smart Self-Healing Polymers and Composites*, chapter Microvascular-based self-healing materials, pages 129–157. Woodhead Publishing Series, 2015.

[5] L. Christodoulou and J. D. Venables. Multifunctional material systems: the first generation. *The Journal of The Minerals, Metals and Materials Society*, 55(12):39–45, 2003.

[6] N. W. Hagood and A. A. Bent. Development of piezoelectric fiber composites for structural actuation. In *AIAA 34th Structures, Structural Dynamics and Materials Conference*, 1993.

[7] J. P. Thomas, M. A. Qidwai, P. Matic, R. K.Everett, A. S. Gozdz, M. T. Keennon, and J. M. Grasmeyer. Structure-power multifunctional materials for UAV's. In Anna-Maria R. McGowan, editor, *Smart Structures and Materials 2002: Industrial and Commercial Applications of Smart Structures*, volume 4698, pages 160–170, 2002.

[8] C. Thill, J. Etches, I. Bond, K. Potter, and P. Weaver. Morphing skins. *The Aeronautical Journal*, 112(1129):117–139, 2008.

[9] S. R. White, N. R. Sottos, P. H. Geubelle, J. S. Moore, M. R. Kessler, S. R. Sriram, E. N. Brown, and S. Viswanathan. Autonomic healing of polymer composites. *Letters to Nature*, 409:794–797, 2001.

[10] D. Therriault, S. R. White, and J. A. Lewis. Chaotic mixing in three-dimensional microvascular networks fabricated by direct-write assemble. *Nature Materials*, 2:265–271, 2003.

[11] K. S. Toohey, N. R. Sottos, J. A. Lewis, J. S. Moore, and S. R. White. Self-healing materials with microvascular networks. *Nature Materials*, 6:581–585, 2007.

[12] A. P. Esser-Kahn, P. R. Thakre, H. Dong, J. F. Patrick, V. K. Vlasko-Vlasov, N. R. Sottos, J. S. Moore, and S. R. White. Three-dimensional microvascular fiber-reinforced composites. *Advanced Materials*, 23:3654–3658, 2011.

[13] R. C. R. Gergely, S. J. Pety, B. P. Krull, J. F. Patrick, T. Q. Doan, A. M. Coppola, P. R. Thakre, N. R. Sottos, J. S. Moore, and S. R. White. Multidimensional vascularized polymers using degradable sacrificial templates. *Advanced Functional Materials*, 25:1043–1052, 2015.

[14] A. M. Coppola, L. Hu, P. R. Thakre, M. Radovic, I. Karaman, N. R. Sottos, and S. R. White. Active cooling of a microvascular shape memory alloy-polymer matrix composite hybrid material. *Advanced Engineering Materials*, 18(7):1145–1153, 2016.

[15] D. B. Tuckerman and R. F. W. Pease. High-performance heat sinking for VLSI. *Electron Device Letters, IEEE*, 2(5):126–129, 1981.

[16] R. J. Phillips. Microchannel heat sinks. *The Lincoln Laboratory Journal*, 1(1):31–48, 1988.

[17] S. M. Senn and D. Poulikakos. Laminar mixing, heat transfer and pressure drop in tree-like microchannel nets and their application for thermal management in polymer electrolyte fuel cells. *Journal of Power Sources*, 130:178–191, 2004.

[18] D. Haller, P. Woias, and N. Kockmann. Simulation and experimental investigation of pressure lost and heat transfer in microchannel networks containing bends and T-junctions. *International Journal of Heat and Mass Transfer*, 52:2678–2689, 2009.

[19] J. Choi, Y. H. Kim, Y. Lee, K. J. Lee, and Y. Kim. Numerical analysis on the performance of cooling plates in a PEFC. *Journal of Mechanical Science and Technology*, 22:1417–1425, 2008.

[20] A. Jarrett and I. Y. Kim. Design optimization of electric vehicle battery cooling plates. *Journal of Power Sources*, 196:10359–10368, 2011.

[21] J. C. Kurnia, A. P. Sasmito, and A. S. Mujumdar. Numerical investigation of laminar heat transfer performance of various cooling channel designs. *Applied Thermal Engineering*, 31:1293–1304, 2011.

[22] S. M. Baek, S. H. Yu, J. H. Nam, and C. J. Kim. A numerical study on uniform cooling of large-scale PEMFCs with different coolant flow field designs. *Applied Thermal Engineering*, 31:1427–1434, 2011.

[23] B. Ramos-Alvarado, P. Li, H. Liu, and A. Hernandez-Guerrero. CFD study of liquid-cooled heat sinks with microchannel flow field configurations for electronics, fuel cells and concentrated solar cells. *Applied Thermal Engineering*, 31:2494–2507, 2011.

[24] C. Xu and T. S. Zhao. A new flow field design for polymer electrolyte-based fuel cells. *Electrochemistry Communications*, 9:497–503, 2007.

[25] J. H. Nam, K.-J. Lee, S. Sohn, and C.-J. Kim. Multi-pass serpentine flow-fields to enhance under-rib convection in polymer electrolyte membrane fuel cells: Design and geometrical characterization. *Journal of Power Sources*, 188:14–23, 2009.

[26] A. P. Manso, F. F. Marzo, J. Barranco, X. Garikano, and M. Garmendia Mujika. Influence of geometric parameters of the flow fields on the performance of a PEM fuel cell. a review. *International Journal of Hydrogen Energy*, 37:15256–15287, 2012.

[27] B. D. Kozola, L. A. Shipton, V. K. Natrajan, K. T. Christensen, and S. R. White. Characterization of active cooling and flow distribution in microvascular polymers. *Journal of Intelligent Material Systems and Structures*, 21:1147–1156, 2010.

[28] D. M. Phillips, M. R. Pierce, and J. W. Baur. Mechanical and thermal analysis of microvascular networks in structural composite panels. *Composites: Part A*, 42:1609–1619, 2011.

[29] A. M. Aragón, K. J. Smith, P. H. Geubelle, and S. R. White. Multi-physics design of microvascular materials for active cooling applications. *Journal of Computational Physics*, 230:5178–5198, 2011.

[30] S. Soghrati, P. R. Thakre, S. R. White, N. R. Sottos, and P. H. Geubelle. Computational modeling and design of actively-cooled microvascular materials. *International Journal of Heat and Mass Transfer*, 55:5309–5321, 2012.

[31] S. Soghrati, A. R. Najafi, J. H. Lin, K. M. Hughes, S. R. White, N. R. Sottos, and P. H. Geubelle. Computational analysis of actively-cooled 3D woven microvascular composites using a stabilized interface-enriched generalized finite element method. *International Journal of Heat and Mass Transfer*, 65:153–164, 2013.

[32] A. M. Coppola, A. S. Griffin, N. R. Sottos, and S. R. White. Retention of mechanical performance of polymer matrix composites above the glass transition temperature by vascular cooling. *Composites Part A: Applied Science and Manufacturing*, 78:412–423, 2015.

[33] J. C. Snyder, C. K. Stimpson, K. A. Thole, and D. Mongillo. Build direction effects on additively manufactured channels. *Journal of Turbomachinery*, 138:051006, 2016.

[34] K. L. Kirsch and K. A. Thole. Heat transfer and pressure loss measurements in additively manufactured wavy microchannels. In *Proceedings of ASME Turbo Expo*, 2016.

[35] R. J. Phillips. Forced-convection, liquid-cooled, microchannel heat sinks. Master's thesis, Massachusetts Institute of Technology, 1987.

[36] J. H. Ryu, D.H. Choi, and S.J. Kim. Three-dimensional numerical optimization of a manifold microchannel heat sink. *International Journal of Heat and Mass Transfer*, 46:1553–1562, 2003.

[37] S. J. Kim. Methods for thermal optimization of microchannel heat sinks. *Heat Transfer Engineering*, 25(1):37–49, 2004.

[38] A. Husain and K.-Y. Kim. Shape optimization of microchannel heat sink for microelectronics cooling. *IEEE Transactions on Components and Packaging Technologies*, 31:322–330, 2008.

[39] A. Bejan. Constructal-theory network of conducting paths for cooling a heat generating volume. *International Journal of Heat and Mass Transfer*, 40:799–816, 1997.

[40] A. Bejan. From heat transfer principles to shape and structure in nature: constructal theory. *Journal of Heat Transfer*, 122(3):430–449, 2000.

[41] A. Bejan and S. Lorente. Constructal theory of generation of configuration in nature and engineering. *Journal of Applied Physics*, 100:041301, 2006.

[42] M. P. Bendsøe and N. Kikuchi. Generating optimal topologies in structural design using a homogenization method. *Computer Methods in Applied Mechanics and Engineering*, 71:197–224, 1988.

[43] O. Sigmund and J. Petersson. Numerical instabilities in topology optimization: A survey on procedures dealing with checkerboards, mesh-dependencies and local minima. *Structural Optimization*, 16:68–75, 1998.

[44] A. Gersborg-Hansen, M. P. Bendsøe, and O. Sigmund. Topology optimization of heat conduction problems using the finite volume method. *Structural and Multidisciplinary Optimization*, 31:251–259, 2006.

[45] E. M. Dede. Multiphysics topology optimization of heat transfer and fluid systems. In *Proceedings of the COMSOL Conference Boston*, 2009.

[46] T. Matsumori, T. Kondoh, A. Kawamoto, and T. Nomura. Topology optimization for fluid-thermal interaction problems under constant input power. *Structural and Multidisciplinary Optimization*, 47:571, 2013.

[47] K. Yaji, T. Yamada, S. Kubo, K. Izui, and S. Nishiwaki. A topology optimization method for a coupled thermal-fluid problem using level set boundary expressions. *International Journal of Heat and Mass Transfer*, 81:878–888, 2015.

[48] A. Klarbring, J. Petersson, B. Torstenfelt, and M. Karlsson. Topology optimization of flow networks. *Computer Methods in Applied Mechanics and Engineering*, 192:3909–3932, 2003.

[49] A. M. Aragón, J. K. Wayer, P. H. Geubelle, D. E. Goldberg, and S. R. White. Design of microvascular flow networks using multi-objective genetic algorithms. *Computer Methods in Applied Mechanics and Engineering*, 197:4399–4410, 2008.

[50] A. M. Aragón, R. Saksena, B. D. Kozola, P. H. Geubelle, K. T. Christensen, and S. R. White. Multi-physics optimization of three-dimensional microvascular polymeric components. *Journal of Computational Physics*, 233:132–147, 2013.

[51] M. H. Y. Tan, M. Safdari, A. R. Najafi, and P. H. Geubelle. A NURBS-based interface-enriched generalized finite element scheme for the thermal analysis and design of microvascular composites. *Computer Methods in Applied Mechanics and Engineering*, 283:1382–1400, 2015.

[52] M. H. Y. Tan, A. R. Najafi, S. J. Pety, S. R. White, and P. H. Geubelle. Gradient-based design of actively-cooled microvascular composite panels. *International Journal of Heat and Mass Transfer*, 103:594–606, 2016.

[53] W. Qu and I. Mudawar. Analysis of three-dimensional heat transfer in micro-channel heat sinks. *International Journal of Heat and Mass Transfer*, 45:3973–3985, 2002.

[54] D. Liu and S. V. Garimella. Analysis and optimization of the thermal performance of microchannel heat sinks. *International Journal of Numerical Methods for Heat and Fluid Flow*, 15(1):7–26, 2005.

[55] A. R. Najafi, A. M. Coppola, S. Soghrati, N. R. Sottos, S. R. White, and P. H. Geubelle. Microvascular composite skin panels for hypersonic aircraft. In *AIAA SciTech*, 2014.

[56] A. M. Aragón, C. A. Duarte, and P. H. Geubelle. Generalized finite element enrichment functions for discontinuous gradient fields. *International Journal for Numerical Methods Engineering*, 82:242–268, 2009.

[57] W. M. Kays and M. E. Crawford. *Convective Heat and Mass Transfer*. McGraw-Hill, 1993.

[58] R. K. Shah and A. L. London. *Laminar Flow Forced Convection in Ducts*, chapter 2 and 7, page 20 and 200. Academic Press, 1978.

[59] H. H. Winter. *AIChEMI Modular Instruction*, volume 7 of *Series C*, chapter C7.4 Viscous dissipation term in energy equations, pages 27–34. American Institute of Chemical Engineers, 1987.

[60] A. Bejan. *Convective Heat Transfer*, chapter 3 Laminar duct flow, page 113. John Wiley and Sons, 4 edition, 2013.

[61] A. N. Brooks and T. J. R. Hughes. Streamline upwind/Petrov-Galerkin formulations for convection dominated flow with particular emphasis on the incompressible Navier-Stokes equation. *Computer Methods in Applied Mechanics and Engineering*, 32:199–259, 1982.

[62] Q.-G. Ning and T.-W. Chou. Closed-form solutions of the in-plane effective thermal conductivities of woven-fabric composites. *Composite Science and Technology*, 55:41–48, 1995.

[63] C. A. Brebbia and A. J. Ferrante. *Computational Hydraulics*. Butterworths, 1983.

[64] M. Bahrami, M. M. Yovanovich, and J. R. Culham. Pressure drop of fully-developed, laminar flow in microchannel of arbitrary cross-section. *Journal of Fluids Engineering*, 128:1036–1044, 2006.

[65] P. O'Hara, C. A. Duarte, and T. Eason. Generalized finite element analysis of three-dimensional heat transfer problems exhibiting sharp thermal gradients. *Computer Methods in Applied Mechanics and Engineering*, 198:1857–1871, 2009.

[66] A. Combescure, A. Gravouil, D. Grégoire, and J. Réthoré. X-FEM a good candiate for energy conservation in simulation of brittle dynamic crack propagation. *Computer Methods in Applied Mechanics and Engineering*, 197:309–318, 2008.

[67] C. A. Duarte, I. Babuška, and J. T. Oden. Generalized finite element mmethod for three-dimensional structural mechanics problems. *Computers and Structures*, 77:215–232, 2000.

[68] C. Daux, N. Moës, J. Dolbow, N. Sukumar, and T. Belytschko. Arbitrary branched and intersecting cracks with the extended finite element method. *International Journal for Numerical Methods Engineering*, 48:1741–1760, 2000.

[69] J. M. Melenk and I. Babuška. The partition of unity finite element method: Basic theory and applications. *Computer Methods in Applied Mechanics and Engineering*, 139:289–314, 1996.

[70] I. Babuška and J. M. Melenk. The partition of unity method. *International Journal for Numerical Methods Engineering*, 40:727–758, 1997.

[71] T.-P. Fries and T. Belytschko. The extended/generalized finite element method: An overview of the method and its applications. *International Journal for Numerical Methods Engineering*, 84:253–304, 2010.

[72] C. A. Duarte, L.G. Reno, and A. Simone. A high-order generalized FEM for through-the-thickness branched cracks. *International Journal for Numerical Methods Engineering*, 72:325–351, 2007.

[73] N. Moës, M. Cloirec, P. Cartraud, and J.-F. Remacle. A computational approach to handle complex microstructure geometries. *Computer Methods in Applied Mechanics and Engineering*, 192:3163–3177, 2003.

[74] S. Soghrati, A. M. Aragón, C. A. Duarte, and P. H. Geubelle. An interface-enriched generalized FEM for problems with discontinuous gradient fields. *International Journal for Numerical Methods Engineering*, 89:991–1008, 2012.

[75] S. Soghrati and P. H. Geubelle. A 3D interface-enriched generalized finite element method for weakly discontinuous problems with complex internal geometries. *Computer Methods in Applied Mechanics and Engineering*, 217-220:46–57, 2012.

[76] S. C. Olugebefola, A. M. Aragón, C. J. Hansen, A. R. Hamilton, B.D. Kozola, W. Wu, Philippe H. Geubelle, J. A. Lewis, N. R. Sottos, and S. R. White. Polymer microvascular network composites. *Journal of Composite Materials*, 44:2587–2603, 2010.

[77] K. W. Cheng and T. P. Fries. Higher-order XFEM for curved strong and weak discontinuities. *International Journal for Numerical Methods Engineering*, 82:564–590, 2010.

[78] D. F. Rogers. *An Introduction to NURBS with Historical Perspective*. Morgan Kaufmann Publishers, 2011.

[79] L. Piegl and W. Tiller. *The NURBS Book*. Springer, 1997.

[80] T. J. .R. Hughes, J. A. Cottrell, and Y. Bazilevs. Isogeometric analysis: CAD, finite element, NURBS, exact geometry and mesh refinement. *International Journal for Numerical Methods Engineering*, 194:4135–4195, 2005.

[81] J. A. Cottrell, T. J. R. Hughes, and Y. Bazilevs. *Isogeometric Analysis: toward Integration of CAD and FEA*. John Wiley and Sons, 2009.

[82] R. Sevilla, S. Fernández-Méndez, and A. Huerta. NURBS-enhanced finite element method (NEFEM). *Archives of Computational Methods in Engineering*, 18:441–484, 2011.

[83] G. Haasemann, M. Kästner, S. Prüger, and V. Ulbricht. Development of a quadratic finite element formulation based on the XFEM and NURBS. *International Journal for Numerical Methods Engineering*, 86:598–617, 2011.

[84] G. Legrain. A NURBS enhanced extended finite element approach for unfitted CAD analysis. *Computational Mechanics*, 59:913–929, 2013.

[85] A. R. Najafi, M. Safdari, D. A. Tortorelli, and P. H. Geubelle. A gradient-based shape optimization scheme using an interface-enriched generalized FEM. *Computer Methods in Applied Mechanics and Engineering*, 296:1–17, 2015.

[86] W. G. Habashi, J. Dompierre, Y. Bourgault, D. Ait-Ali-Yahia, M. Fortin, and M.-G. Vallet. Anisotropic mesh adaptation: towards user-independent, mesh-independent and solver-independent CFD. Part I: general principles. *International Journal for Numerical Methods in Fluid*, 32:725–744, 2000.

[87] D. W. Marquardt. An algorithm for least-squares estimation of nonlinear parameters. *Journal of the Society for Industrial and Applied Mathematics*, 11:431–441, 1963.

[88] T. J. .R. Hughes, A. Reali, and G. Sangalli. Efficient quadrature for NURBS-based isogeometric analysis. *Computer Methods in Applied Mechanics and Engineering*, 199:301–313, 2010.

[89] J. M. Lane and R. F. Riesenfeld. A theoretical development for the computer generation and display of piecewise polynomial surfaces. *IEEE Transactions on Pattern Analysis and Machine Intelligence*, 2:35–46, 1980.

[90] P. A. Koparkar and S. P. Mudur. A new class of algorithms for the processing of parametric curves. *Computer-aided Design*, 15:41–45, 1983.

[91] T. W. Sederberg and S. R. Parry. Comparison of three curve intersection algorithms. *Computer-aided Design*, 18:58–63, 1986.

[92] T. W. Sederberg and T. Nishita. Curve intersection using Bézier clipping. *Computer-aided Design*, 22:538–549, 1990.

[93] L. V. Miegroet and P. Duysinx. Stress concentration minimization of 2D filets using X-FEM and level set description. *Structural and Multidisciplinary Optimization*, 33:425, 2007.

[94] S. Kim, S. Lorente, and A. Bejan. Vascularized materials: tree-shaped flow architectures matched canopy to canopy. *Journal of Applied Physics*, 100:063525, 2006.

[95] C. D'Angelo. Finite element approximation of elliptic problems with Dirac measure terms in weighted spaces: Applications to one- and three-dimensional coupled problems. *SIAM Journal on Numerical Analysis*, 50(1):194–215, 2012.

[96] C. D'Angelo and A. Quarteroni. On the coupling of 1D and 3D diffusion-reaction equations: application to tissue perfusion problems. *Mathematical Models and Methods in Applied Sciences*, 18:1481, 2008.

[97] L. Cattaneo and P. Zunino. Computational models for fluid exchange between microcirculation and tissue interstitium. *Network and Heterogeneous Media*, 9(1):135–159, 2014.

[98] L. Cattaneo and P. Zunino. A computational model of drug delivery through microcirculation to compare different tumor treatments. *International Journal for Numerical Methods in Biomedical Engineering*, 30:1347–1371, 2014.

[99] L. Cattaneo and P. Zunino. *Numerical Investigation of Convergence Rates of the FEM Approximation of 3D-1D Coupled Problems*, volume 103 of *Lecture Notes in Computational Science and Engineering*, chapter Numerical Mathematics and Advanced Applications, pages 727–734. Springer, 2014.

[100] R. Gracie and J. R. Craig. Modelling well leakage in multilayer aquifer systems using the extended finite element method. *Finite Elements in Analysis and Design*, 46:504–513, 2010.

[101] C. Ladubec, R. Gracie, and J. Craig. An extended finite element method model for carbon sequestration. *International Journal for Numerical Methods Engineering*, 102:316–331, 2014.

[102] H. Wu and A. C. Cangellaris. Efficient finite element electromagnetic modeling of thin wires. *Microwave and Optical Technology Letters*, 50(2):350–354, 2007.

[103] S.-H. Lee and J.-M. Jin. Fast reduced-order finite-element modeling of lossy thin wires using lumped impedance elements. *IEEE Transactions on Advanced Packaging*, 33(1):212–218, 2010.

[104] N. H. Kim and Y. Chang. Eulerian shape design sensitivity analysis and optimization with a fixed grid. *Computer Methods in Applied Mechanics and Engineering*, 194:3291–3314, 2005.

[105] S. J. Pety, N. R. Sottos, and S. R. White. Actively cooled battery packaging using microvascular composites. In *Proceedings of the 19th International Conference on Composite Materials (ICCM 19)*, 2013.

[106] S. Pety, M. H. Y. Tan, A. R.. Najafi, P. H. Geubelle, N. Sottos, and S. R. White. Microvascular composites for intergrated battery packaging and cooling. In *Proceedings of the Society of Engineering Science 51st Annual Technical Meeting*, 2014.

[107] A. A. Pesaran. Battery thermal mangement in EVs and HEVs. In *Advanced Automotive Battery Conference*, 2001.

[108] G. H. Kim and A. A. Pesaran. Battery thermal management system design modeling. In *22nd International Battery, Hybrid and Fuel Cell Electric Vehicle Conference and Exhibition*, 2006.

[109] S. J. Pety, M. H. Y. Tan, A. R. Najafi, P. R. Barnett, N. R. Sottos, P. H. Geubelle, and S. R. White. Carbon fiber composites with 2D microvascular networks for battery cooling. *In preparation*.

[110] J. Obradovic, S. Boria, and G. Belingardi. Lightweight design and crash analysis of composite frontal impact energy absorbing structures. *Composite Structures*, 94:423–430, 2012.

[111] D. H.-J. A. Lukaszewicz. *Advanced Composite Materials for Automotive Applications: Structural Integrity and Crashworthiness*, pages 99–127. John Wiley and Sons, 2014.

[112] C. Le, J. Norato, T. Bruns, C. Ha, and D. Tortorelli. Stress-based topology optimization for continua. *Structural and Multidisciplinary Optimization*, 41:605–620, 2010.

[113] F. H. Clarke. *Optimization and Nonsmooth Analysis*, chapter 2, page 47. Society for Industrial and Applied Mathematics, 1990.

[114] R. J. Yang and C. J. Chen. Stress-based topology optimization. *Structural Optimization*, 12:98–105, 1996.

[115] P. Duysinx and O. Sigmund. New developments in handling stress constraints in optimal material distribution. *American Institute of Aeronautics and Astronautics*, 98-4906:1501–1509, 1998.

[116] General Motors. GM Exec: Gen 3 Voltec battery to have shortened lifespan, simpler shape, and be offered in smaller ranges. `http://gm-volt.com/category/battery/page/4/`, March 2010.

[117] General Motors. Report reveals lithium-ion battery prices already dropping steeper than expected. `http://gm-volt.com/category/battery/page/4/`, March 2010.

[118] General Motors. Spark EV versus Volt battery. `http://gm-volt.com/2013/08/02/spark-ev-versus-volt-battery/`, August 2013.

[119] R. Rolfes and U. Hammerschmidt. Transverse thermal conductivity of CFRP laminates: a numerical and experimental validation of approximation formulae. *Composite Science and Technolo*, 54:45–54, 1995.

[120] A. Jarrett. Multi-objective design optimization of electric vehicle battery cooling plates considering thermal and pressure objective functions. Master's thesis, Queen's University, 2011.

[121] R. H. Byrd, J. C. Gilbert, and J. Nocedal. A trust region method based on interior point techniques for nonlinear programming. *Mathematical Programming*, 89:149–185, 2000.

[122] P. T. Boggs and J. W. Tolle. Sequential quadratic programming. *Acta Numerica*, 4:1–51, 1995.

[123] W. Rudin. *Real and Complex Analysis*, chapter 3, pages 61–71. McGraw-Hill, 1987.

[124] G. B. Folland. *Real Analysis*, chapter 6, page 186. John Wiley and Sons, 1999.

[125] D. A. Dunavant. High degree efficient symmetrical Gaussian quadrature rules for the triangle. *International Journal for Numerical Methods Engineering*, 21:1129–1148, 1985.

[126] P. A. N. Bosman. On gradients and hybrid evolutionary algorithms for real-valued multiobjective optimization. *IEEE Transactions on Evolutionary Computation*, 16:51–69, 2012.

[127] Q. Zhang and H. Li. MOEA/D: A multiobjective evolutionary algorithm based on decomposition. *IEEE Transactions on Evolutionary Computation*, 11:712–731, 2007.

[128] A. Jaszkiewicz. On the performance of multi-objective genetic local search on the 0/1 knapsack problem. *IEEE Transactions on Evolutionary Computation*, 6:402–412, 2002.

[129] K. Deb, S. Agrawal, A. Pratap, and T. Meyarivan. A fast and elitist multiobjective genetic algorithm: NSGA-II. *IEEE Transactions on Evolutionary Computation*, 6:182–197, 2002.

[130] B. J. Ritzel, J. W. Eheart, and S. Ranjithan. Using genetic algorithms to solve a multiple objective groundwater pollution containment problem. *Water Resources Research*, 30:1589–1603, 1994.

[131] A. Messac, A. Ismail-Yahaya, and C. A. Mattson. The normalized normal constraint method for generating the Pareto frontier. *Structural and Multidisciplinary Optimization*, 25:86–98, 2003.

[132] T. M. Bandhauer, Srinivas Garimella, and Thomas F. Fuller. A critical review of thermal issues in lithium-ion batteries. *Journal of The Electrochemical Society*, 158(3):R1–R25, 2011.

[133] E. Katifori, G. J. Szöllősi, and M. O. Magnasco. Damage and fluctuations induce loops in optimal transport networks. *Physical Review Letters*, 104:048704, 2010.

[134] C. B. Schaffer, B. Friedman, N. Nishimura, L. F. Schroeder, P. S. Tsai, F. F. Ebner, P. D. Lyden, and D. Kleinfeld. Two-photon imaging of cortical surface microvessels reveals a robost redistribution in blood flow after vascular occlusion. *PLOS Biology*, 4(2):258–270, 2006.

[135] P. Blinder, A. Y. Shih, C. Rafie, and D. Kleinfeld. Topological basis for the robust distribution of blood to rodent neocortex. *PNAS*, 107(28):12670–12675, 2010.

[136] P. Blinder, P. S. Tsai, J. P. Kaufhold, P. M. Knutsen, H. Suhl, and D. Kleinfeld. The cortical angiome: an interconnected vascular network with noncolumnar patterns of blood flow. *Nature Neuroscience*, 16:889–897, 2013.

[137] S. Bohn and M. O. Magnasco. Structure, scaling, and phase transition in the optimal transport network. *Physical Review Letters*, 98:088702, 2007.

[138] F. Corson. Fluctuations and redundancy in optimal transport networks. *Physical Review Letters*, 104:048703, 2010.

[139] S. G. Kandlikar. High flux heat removal with microchannels—a roadmap of challenges and opportunities. *Heat Transfer Engineering*, 26(8):5–14, 2005.

[140] R. S. Bunker. Gas turbine cooling: moving from macro to micro cooling. In *Proceedings of ASME Turbo Expo*, 2013.

[141] X.-Q. Wang, A. S. Mujumdar, and C. Yap. Numerical analysis of blockage and optimization of heat transfer performance of fractal-like microchannel nets. *Transactions of the ASME*, 128:38–45, 2006.

[142] R. Gulotty, M. Castellino, P. Jagdale, A. Tagliaferro, and A. A. Balandin. Effects of functionalization on thermal properties of single-wall and multi-wall carbon nanotube-polymer nanocomposites. *ACS Nano*, 7(6):5114–5121, 2013.

[143] A. D. Waren, L. S. Lasdon, and D. F. Suchman. Optimization in engineering design. *Proceedings of the IEEE*, 55(11):1885–1897, 1967.

[144] C. Charalambous and A. R. Conn. An efficient method to solve the minimax problem directly. *SIAM Journal on Numerical Analysis*, 15(1):162–187, 1978.

[145] D. T. Bunce, K. P. Bassett, A. R. M. Ghosh, P. R. Barnett, D. M. Haken, S. Vrkljan, R. Jagannatha, T. Silva, V. L. Coverstone, B. D. Yost, J. R. Feller, and E. F. Agasid. Microvascular composite radiators for small spacecraft thermal management systems. In *30th Annual AIAA/USU Conference on Small Satellites*, 2016.

[146] J. Bouwmeester and J. Guo. Survey of worldwide pico- and nanosatellite missions, distributions and subsystem technology. *Acta Astronautica*, 67:854–862, 2010.

[147] H. Heidt, J. Puig-Suari, A. S. Moore, S. Nakasuka, and R. J. Twiggs. Cubesat: A new generation of picosatellite for education and industry low-cost space experimentation. In *14th Annual/USU Conference on Small Satellites*, 2000.

[148] R. D. Karam. *Satellite Thermal Control for Systems Engineers*, chapter 4 Heating fluxes, pages 78–79. AIAA, 1998.

[149] SINTEF, ICT, Department of Applied Mathematics, Norway. The SINTEF Spline Library. `https://www.sintef.no/projectweb/geometry-toolkits/downloads/`.

[150] J.-C. Han. Turbine blade cooling studies at Texas A&M University: 1980-2004. *Journal of Thermophysics and Heat Transfer*, 20(2):161–187, 2006.

[151] G. S. Azad, J.-C. Han, and S. Teng. Heat transfer and pressure distributions on a gas turbine blade tip. *Journal of Turbomachinery*, 122(4):717–724, 2000.

[152] C. Sanderson and R. Curtin. Armadillo: a template-based C++ library for linear algebra. *Journal of Open Source Software*, 1:26, 2016.

[153] R. Siegel, E. M. Sparrow, and T. M. Hallman. Steady laminar heat transfer in a circular tube with prescribed wall heat flux. *Applied Scientific Research*, 7(Section A):386–391, 1958.